

AD-A125 348

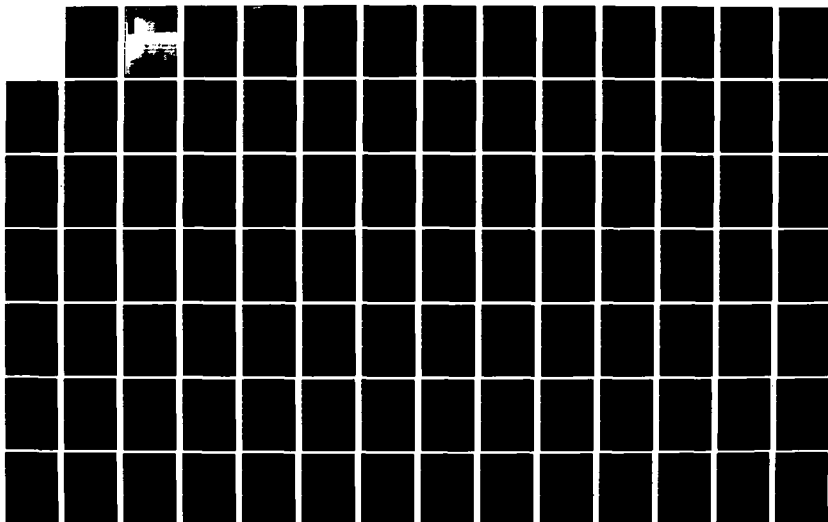
SIMULATION OF DISTRIBUTED-EMISSION AND INJECTED-BEAM
CROSSED-FIELD AMPLIF. (U) HARRIS SAI INC ANN ARBOR MI
D H MACGREGOR ET AL. APR 80 AFOSR-TR-80-0554
F49628-77-C-0091

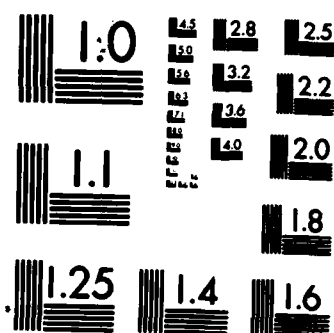
1/3

UNCLASSIFIED

F/G 9/1

NL





MICROCOPY RESOLUTION TEST CHART
NATIONAL BUREAU OF STANDARDS-1963-A

AFOSR-TR-80-0554

1

AD A125340

AMPLIFICATION OF DISTRIBUTED-EMISSION AND
LIMITED-BEAM-CROSSED-FIELD AMPLIFIERS

PART I

WAVELENGTH ELECTRON GUN

FOR OFFICE OF SCIENTIFIC RESEARCH

TECHNICAL REPORT

1977-1980

SECRET
MAR 7 1983
A

APRIL 1980

Approved for public release;
distribution unlimited.

83 03 04 099

UNCLASSIFIED

SECURITY CLASSIFICATION OF THIS PAGE (When Data Entered)

REPORT DOCUMENTATION PAGE		READ INSTRUCTIONS BEFORE COMPLETING FORM
1. REPORT NUMBER AFOSR-TR-80-0554	2. GOVT ACCESSION NO. AD-A125340	3. RECIPIENT'S CATALOG NUMBER
4. TITLE (and Subtitle) Simulation of Distributed-Emission and Injected-Beam Crossed-Field Amplifiers Part II: The Crossed-Field Electron Gun.		5. TYPE OF REPORT & PERIOD COVERED Final Technical Report March 1, 1977-Feb. 29, 1980
7. AUTHOR(s) Dr. Donald M. MacGregor Dr. Thomas P. Fontana and Dr. Joseph E. Rowe		6. PERFORMING ORG. REPORT NUMBER
9. PERFORMING ORGANIZATION NAME AND ADDRESS Harris SAI, Inc. 611 Church Street Ann Arbor, MI 48104		8. CONTRACT OR GRANT NUMBER(s) F49620-77-C-0091
11. CONTROLLING OFFICE NAME AND ADDRESS Air Force Office of Scientific Research Building 410 Bolling AFB, D.C. 20332		10. PROGRAM ELEMENT, PROJECT, TASK AREA & WORK UNIT NUMBERS 61102-F 2305/c1
14. MONITORING AGENCY NAME & ADDRESS (if different from Controlling Office)		12. REPORT DATE April 1980
		13. NUMBER OF PAGES 195
		15. SECURITY CLASS. (of this report) Unclassified
		15a. DECLASSIFICATION/DOWNGRADING SCHEDULE
16. DISTRIBUTION STATEMENT (of this Report) Approved for public release; distribution unlimited.		
17. DISTRIBUTION STATEMENT (of the abstract entered in Block 20, if different from Report)		
18. SUPPLEMENTARY NOTES		
19. KEY WORDS (Continue on reverse side if necessary and identify by block number) Injected-beam CFA Electron dynamics Crossed-field amplifier Electron gun Microwave tubes Computer simulation		
20. ABSTRACT (Continue on reverse side if necessary and identify by block number) Numerical models developed for the crossed-field electron gun predict the current and the beam shape and stability for varied voltages or magnetic field. These programs use a deform- able triangular mesh to reproduce the realistic electrode boundaries. A static iterative analysis predicts beam currents about 5 percent higher than measured for a short Kino gun, but is not		

DD FORM 1 JAN 73 1473

EDITION OF 1 NOV 65 IS OBSOLETE

UNCLASSIFIED

SECURITY CLASSIFICATION OF THIS PAGE (When Data Entered)

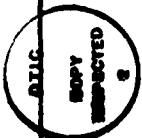
20.

stable for long cathodes with returning electrons. However, the alternative time-dependent method predicts a stable, well-defined beam in both cases.

Excess shot noise in a long-cathode crossed-field gun is believed to be due to cycloiding electrons which return to the cathode from well beyond the potential minimum. Of three theories compared here, only the Ho and Van Duzer model includes these electrons and predicts an instability. With added shot noise the computer simulation may be capable of reproducing the effect.

Experimental measurements have been obtained by subcontract for a Northrop gridded crossed-field gun. The two-dimensional time-dependent analysis, which ignores the grids, predicts the beam current with good order-of-magnitude agreement. A macroscopic cathode model uses the cathode electric field and the local charge to limit the emission at each time step, with results verified by Child's Law. A three-dimensional charge-free solution demonstrates the field at the grid. This study has established the essential theory and program structures for the planned complete gun simulation in three dimensions.

Accession For	
NTIS GRA&I	<input checked="" type="checkbox"/>
DTIC TAB	<input type="checkbox"/>
Unannounced	<input type="checkbox"/>
Justification	
By	
Distribution/	
Availability Codes	
Scale and/or	
Special	
Dist	
A	



UNCLASSIFIED

TABLE OF CONTENTS

	<u>Page</u>
I. INTRODUCTION	1
A. Research Objectives	1
B. Status of the Research Effort	2
C. Summary	4
II. STATE OF THE ART OF SIMULATION OF THE DISTRIBUTED-EMISSION CFA	5
III. TUBE DATA	14
IV. ASSUMPTIONS AND APPROXIMATIONS	16
V. CATHODE EMISSION	19
A. Introduction	19
B. Secondary Emission	19
C. Control of the Emitted Charge	21
D. Approximations of the Emission Model	22
E. Algorithm for Control of Emission	24
F. Test Results	26
1. Child's Law	26
2. Secondary Emission	26
VI. PARTICLE TRAJECTORIES	33
A. Basic Algorithm	33
B. Predictor	35
C. Corrector	36
D. Test Results	37
E. Proposed Development	37
1. Time-Centered Trajectory Calculation	40
2. RF Field Calculation	41
VII. SPACE-CHARGE FIELDS	42
A. Solution of Poisson's Equation	42
B. Charge Per Rod	43
C. Self-Magnetic Field	44
VIII. THE EQUIVALENT NETWORK FOR THE RF CIRCUIT	46
A. Introduction	46
B. Comparison with Other Models	46

	<u>Page</u>
C. Forms of Network	47
D. Oscillation Conditions	51
IX. THE MODULATOR	52
A. Line Type and Hard Tube Modulators	52
B. Equivalent Circuits	52
C. Typical Parameters	54
D. Stabilizing Effect of the Load Line	56
X. DESCRIPTION OF THE NUMERICAL SOLUTION	57
XI. RESULTS OF THE SIMULATIONS	62
A. QKS1842 Backward-Wave CFA	62
1. High-Power Mode	67
2. Low-Power Mode	75
3. Results at Constant Voltage	75
B. SFD-261 Forward-Wave CFA	75
C. QKS1319 Forward-Wave CFA	88
D. Cathode Phenomena	91
E. RF Oscillation and Mode Boundary	97
F. Computational Error	103
G. Comparison of QKS1842 with other Distributed-Emission Crossed-Field Amplifiers	105
XII. PROGRAM REQUIREMENTS	108
A. Number of Simulation Particles	108
B. Time Step	112
C. Length of Run	114
D. Computing Time and Storage	114
XIII. CONCLUSIONS AND RECOMMENDATIONS FOR FURTHER WORK	117
REFERENCES	123
APPENDIX A: DATA FOR THE RAYTHEON QKS1300 AMPLITRON	127
APPENDIX B: DATA FOR THE RAYTHEON QKS1842 CFA	129
APPENDIX C: DATA FOR THE VARIAN SFD-261 CFA	139
APPENDIX D: DATA FOR THE RAYTHEON QKS1319 CFA	146
APPENDIX E: DATA FOR THE RAYTHEON QKS1705 CFA	169

	<u>Page</u>
APPENDIX F: DATA FOR THE RAYTHEON QKS1840 CATHODE-CIRCUIT CFA	176
APPENDIX G: MEASURED SECONDARY-EMISSION CHARACTERISTICS OF CATHODE SURFACES	184
APPENDIX H: CIRCUIT THEORY FOR THE DECFA	191
APPENDIX I: THEORY OF THE RF NETWORK	203
APPENDIX J: THE CYLINDRICAL BRILLOUIN STREAM	223
APPENDIX K: PROGRAM OUTPUT INFORMATION	227
APPENDIX L: EXAMPLE OF PROGRAM OUTPUT	229
APPENDIX M: PROFESSIONAL PERSONNEL, INTERACTIONS, AND PUBLICATIONS	246

AIR FORCE OFFICE OF SCIENTIFIC RESEARCH (AFSC)
 NOTICE
 This report is the property of the AFSC and is loaned to you. It is to be used for the purpose for which it was loaned and is not to be distributed outside of your organization.
 MATTHEW J. [illegible]
 Chief, Technical Information Division

LIST OF ILLUSTRATIONS

<u>Figure</u>		<u>Page</u>
1	Continuous-Cathode Distributed-Emission Crossed-Field Amplifier	6
2	Mesh Elements at the Cathode in the DECFA Simulation	25
3	Anode Current Computed for Varian Forward- Wave DECFA for Varying Degrees of Smoothing at Cathode	28
4	RF Output Power Computed for Varian Forward- Wave CFA for Varying Degrees of Smoothing at Cathode	29
5	Charge Distribution Computed with one Electric Field Evaluation per Time Step	38
6	Charge Distribution Computed with Two Electric Field Evaluations per Time Step	39
7	General Equivalent Network for DECFA Slow- Wave Circuit	48
8	Simple Equivalent Network	49
9	Equivalent Circuit for the DECFA Modulator	53
10	General Flow Chart for DECFA Analysis Program	58
11	Beam Profile Computed in QKS1842 High- Power Mode	64
12(a)	Beam Profiles Computed in QKS1842 Low- Power Mode	65
12(b)	Beam Profiles Computed in QKS1842 Low- Power Mode	66
13	Irregular Charge Distribution Computed in QKS1842 with Unsmoothed Secondary Emission and 9,576 Interacting Particles	68

LIST OF ILLUSTRATIONS (continued)

<u>Figure</u>		<u>Page</u>
14	Computed and Measured Results for QKS1842 Backward-Wave Amplifier in High-Power Mode	69
15	RF Output Power Computed Over 91 RF Periods in QKS1842 High-Power Mode	72
16	Anode Current Computed Over 92 RF Periods in the QKS1842 High-Power Mode	73
17	RF Power and Phase Computed Around the QKS1842 in the High-Power Mode	74
18	RF Output Power Computed Over 250 Periods in QKS1842 Low-Power Mode	76
19	Anode Current Computed Over 250 Periods in QKS1842 Low-Power Mode	77
20	Computed and Measured Results for QKS1842 Backward-Wave Amplifier in Low-Power Mode	78
21	RF Output Power Computed in the QKS1842 CFA at 24.3 kV and 0.4114 T with 10,000-rod Model and Full Secondary Emission	79
22	Anode Current Computed in the QKS1842 CFA at 24.3 kV and 0.4114 T with 10,000-rod Model and Full Secondary Emission	80
23	Computed and Measured Results for SFD-261 Forward-Wave Amplifier	83
24	RF Output Power Computed in SFD-261 Forward-Wave CFA	84
25	Anode Current Computed in SFD-261 Forward-Wave CFA	85
26	Beam Profile Computed in SFD-261 Forward-Wave DECFA	86
27	RF Power and Phase Computed Around the SFD-261 DECFA	89
28	Beam Profile Computed in Forward-Wave QKS1319 DECFA Close to Emission Limit	90

LIST OF ILLUSTRATIONS (continued)

<u>Figure</u>		<u>Page</u>
29	Computed and Measured Results for QKS1319 Forward-Wave Amplifier	92
30	RF Output Power Computed in QKS1319 DECFA With Magnetic Field Raised to 0.13 T	93
31	RF Power and Phase Distributions Computed in QKS1319 DECFA as Averages Over 14 Periods	99
32	RF Output Power Computed for Varian Forward-Wave DECFA	110
33	Anode Current Computed for Varian Forward-Wave DECFA	111
G.1	Measured Secondary-Emission Coefficient Versus Primary Impact Energy for Platinum and Cermet Cathodes	185
G.2	Secondary-Emission Measurements for Beryllium Oxide	187
G.3	Secondary-Emission Coefficient of Magnesium Oxide and Gold Surface	189
H.1	Portion of CFA Equivalent Network	196
I.1	Strapped Vane Line as a Backward-Wave RF Circuit	216
I.2	Comparison of Exact Values and Single Space Harmonic of RF-Circuit Fields in QKS1842 at Radius 9.2 mm.	219
I.3	Comparison of Exact Values and Single Space Harmonic of RF-Circuit Fields in QKS1842 at Radius 9.6 mm	220
I.4	Comparison of Exact Values and Single Space Harmonic of RF-Circuit Fields in Sever Region of QKS1842.	221

LIST OF TABLES

		<u>Page</u>
1	Comparison of Distributed-Emission Crossed-Field Amplifier Models	9
2	Distributed-Emission Crossed-Field Amplifiers for Which Harris SAI has Experimental Data	15
3	Computed Results for Varian Forward-Wave CFA with Varied Smoothing of Cathode Emission; Averages over 18 RF Periods	30
4	Axial Self-Magnetic Field	45
5	Modulator Data Used for DECFA Simulation	55
6	Computed and Measured Results for Three Distributed-Emission Crossed-Field Amplifiers	63
7	Computed and Measured Results for QKS1842 Backward-Wave Amplifier in High-Power Mode	70
8	Computed and Measured Results for QKS1842 Backward-Wave Amplifier in Low-Power Mode	81
9	Computed and Measured Results for SFD-261 Forward-Wave Amplifiers	87
10	Computed and Measured Results for QKS1319 Forward-Wave Amplifier	94
11	Cathode Characteristics Computed in Distributed-Emission Crossed-Field Amplifiers	95
12	Computed Results for QKS1842 DECFA with Platinum and Cermet Cathodes Compared over 30 RF Periods	98
13	Computed and Measured Oscillation Conditions	101
14	Parameters for Four Distributed-Emission Crossed-Field Amplifiers	106
15	Particle Numbers Required in CFA Simulations	109

LIST OF TABLES (continued)

		<u>Page</u>
16	Time Steps Used in DECFA Simulations	113
17	Computing Time for DECFA Simulation on Harris 550 Computer	115
18	Capabilities of the Harris SAI DECFA Model	118

SECTION I

INTRODUCTION

For the past five years, Harris SAI, Inc., Ann Arbor, Michigan, has been developing advanced computer-aided simulations of crossed-field amplifiers. Since March 1, 1977, Harris SAI has been supported in this effort by the Air Force Office of Scientific Research under Contract No. F49620-77-C-0091. This Final Technical Report covers the entire period of the contract: March 1, 1977 through February 20, 1980.

The report is in two parts. Part I (this volume) describes the work on the distributed-emission crossed-field amplifier. Part II describes the parallel effort on the injected-beam crossed-field amplifier.

A. Research Objectives

Crossed-field amplifiers are commonly used to produce microwave power in transportable systems where light weight, compactness, high efficiency, and peak power of kilowatts or megawatts are required.^{1,2} Radar and electronic countermeasure systems are examples. In existing distributed-emission CFA's, it is desirable particularly to raise the gain and efficiency and extend the bandwidth over which the tube will both start and operate in the desired mode.

The present research program involves the development of advanced computer-aided design techniques and experimental verification of the theory. This work will lead to a better understanding of crossed-field interaction mechanisms and provide a guide for design improvements. The computer will then be available to provide valuable design information with a minimum of costly experimentation.

Harris SAI has studied the distributed-emission crossed-field amplifier (DECFA) and injected-beam crossed-field amplifier (IBCFA) in parallel efforts. The primary objectives of the DECFA work were as follows.

(1) To develop a computer simulation of the distributed-emission crossed-field amplifier applicable to both forward- and backward-wave devices.

(2) To verify the program using experimental data for production tubes under normal operating conditions.

(3) To test the capability of the model for predicting the operational limits of a tube, such as the bandwidth and the upper and lower current mode boundaries.

(4) To investigate transient behavior and possible models for the modulator to improve understanding of starting conditions.

(5) To incorporate the option of an asymmetrical cathode.

B. Status of the Research Effort

A computer model has been developed for both forward-wave and backward-wave DECFA's. This program is believed to be the first to simulate successfully a backward-wave CFA. This cylindrical model of the reentrant CFA cross-section includes the vane RF circuit, a secondary-emitting cathode, and an external modulator. The modulator has proven to be important in stabilizing the model. Earlier work showed a "runaway" effect of current and RF power, a problem that has now been overcome. An improved cathode emission model appears to reproduce well the observed phenomena of backbombardment and emission limitation of the tube current.

Experimental data have been obtained for production tubes, the backward-wave Raytheon QKS1842 and QKS1705, the forward-wave Varian SFD-261 and Raytheon QKS1319, and the cathode-driven QKS1840. The measurements on the QKS1319 were made by Raytheon Company under

a subcontract to Harris SAI. Simulations of the QKS1842, SFD-261 and QKS1319 tubes have been performed at their midband frequencies. Generally there is reasonable agreement with measurement, although the power balance is not yet satisfactory for the forward-wave tubes. The anode current and RF output power are now typically 7 percent and 41 percent, respectively, higher than measured in the forward-wave tubes and up to 25 percent below the measured values in the backward-wave tube. However, it is believed that only minor adjustments to the RF network model and the trajectory calculations are now needed to improve these quantitative results.

It is noteworthy that the multiple operating modes and high cathode backbombardment power actually observed in the QKS1842 are predicted by the simulation. The observed oscillation of the QKS1319 at current levels above 30A is also correctly predicted.

In late 1979 the program was installed on the Harris 550 computer which made large blocks of CPU time economically available. The program was tested with up to 27,900 rods and the results showed consistency with those of the usual 7,000-rod program. It was concluded that higher resolution than provided by the 7,000-rod model is not necessary. The off-center cathode (as in the production SFD-261 tube) will be incorporated in a future model by making a perturbation to the direct radial electric field. Time restrictions also precluded a study of transient effects, but the present program has the capability for simulating starting and turn-off with a modulator of either line or hard-tube type.

This study has succeeded in establishing the basic modeling techniques for the beam, the cathode, the RF network in forward-wave or backward-wave tubes, and the modulator. Only minor refinements, chiefly to the trajectory calculations, are now needed to provide a program of use to the engineer for design purposes.

C. Summary

Existing DECFA programs and their limitations are compared in Section II. Section III and Appendices A-G give the details of the tube data that Harris SAI has compiled during this study, and that are needed to perform a simulation. The major assumptions and approximations of the model are listed in Section IV, and Sections V through IX provide a description of the model. The computations involve, principally:

- primary and secondary emission at the cathode (Section V);
- particle trajectories (Section VI);
- space-charge fields (Section VII);
- the RF network (Section VIII);
- the modulator (Section IX);

Details of the circuit equations are given in Appendices H-J. Section X gives a more detailed description of the numerical procedure. The results of the simulations of three tubes are presented in Section XI, which includes a brief discussion of the design of the QKS1842. The computer requirements are explained in Section XII. A typical run now requires about 20 CPU hours on the Harris 550 minicomputer, but more efficient trajectory calculations are planned which may halve this time. A brief explanation of the program output information is given in Appendix K, and Appendix L reproduces the printed results from a typical run.

The professional personnel who assisted in this work are acknowledged in Appendix M.

SECTION II
STATE OF THE ART OF SIMULATION OF
THE DISTRIBUTED-EMISSION CFA

For over twenty years various workers have attempted to model the distributed-emission crossed-field amplifier with only partial success. Like the magnetron, this tube (Figure 1) presents modeling difficulties because of its interdependent parts (cathode, reentrant beam, RF circuit, modulator) all of which must be treated simultaneously.

Rigid-beam models of CFA's and magnetrons^{3,4} provide useful qualitative pictures but limited quantitative design information. Of the two types of computer simulation now in use, the rectangular single-wavelength model⁵⁻¹⁷ treats only forward-wave tubes, while the present Harris SAI model treats the entire tube as a cylindrical interaction region and can treat both forward-wave and backward-wave devices. It is based on an earlier program by Dombrowski and Price,¹⁸ but the cathode model, space-charge field calculations, trajectory calculations and the RF network all have been extensively developed by Harris SAI and the variable anode voltage from the modulator has been added. A similar cylindrical model is being used to study high-power relativistic magnetrons at the Naval Research Laboratory.¹⁹

Although the cylindrical coordinate system requires a more complex trajectory calculation than that for rectangular geometry, a clear advantage is that the measured magnetic field can be used directly. The rectangular model requires an empirical reduction of the magnetic field to lower the Hartree voltage.¹¹ Significant advantages of the Harris SAI cylindrical model are (1) the RF circuit model which can treat both forward-wave and backward-wave networks with equal ease, and (2) the realistic

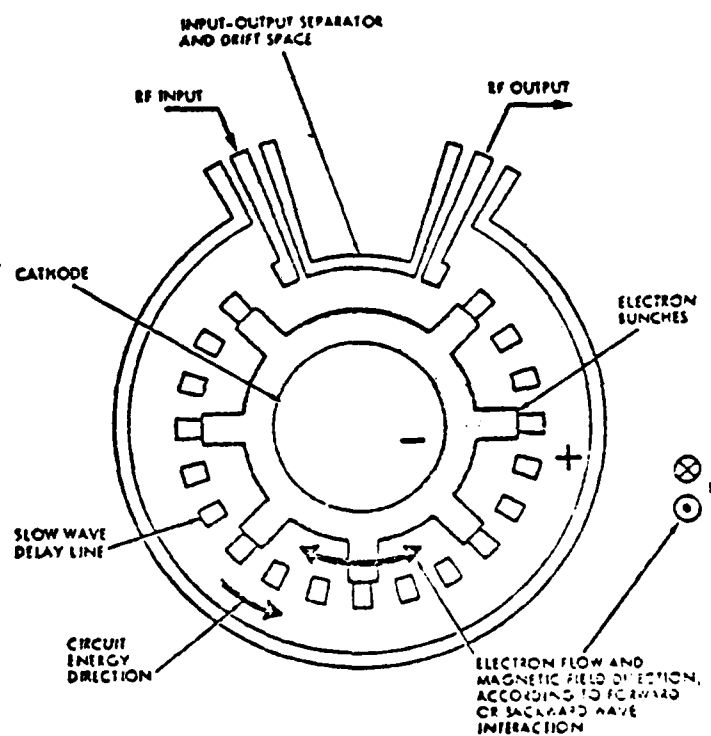


Figure 1. Continuous-cathode distributed-emission crossed-field amplifier. (After Skowron)

angular boundary condition which represents the reentrant beam as a continuous electron stream as in the actual tube. Both features are essential in simulating a backward-wave amplifier correctly.¹³

In the rectangular model study performed by Harris SAI for Lincoln Laboratory,^{12,13} backward-wave interaction was simulated (a) by moving the reference frame in the direction opposite to the beam from RF input to RF output, and (b) by moving the reference frame with the beam from RF output to RF input. It was shown that method (a) gives the beam dynamics incorrectly because the beam modulation at the input is computed immediately following the sever region, whereas the actual beam has the modulation produced by the RF interaction between the output and the input. Hence the computed current and RF output power are too low. Method (b) requires a prior estimate of both the RF output power and the "hot" phase delay of the RF voltage. Trials showed that the behavior of the beam is sensitive to both of these quantities. The value of RF drive power derived varied by a factor of 2 or more, with corresponding phase variations, in successive passes around the tube. In addition, that older model needed double the interaction impedance relative to the measured value to obtain sufficient RF interaction.

In the present cylindrical model, the network equations are identical for both forward-wave and backward-wave circuits: only the signs of the voltages on even-numbered vanes are changed to enable the beam to "see" a backward-traveling wave. Since the entire cylindrical region is viewed at every time step, the particles move in the realistic transient RF fields from all the vanes. The only difference between the forward-wave and backward-wave calculations is the larger number of RF periods required for the latter to reach saturation while RF current induced by the beam at the RF input (where the beam modulation is greatest) is fed back along the RF circuit to the RF output. Transient calculations with ideal spokes of charge demonstrate this effect.

The features of the cylindrical and rectangular DECFA models are compared in Table 1.

The RF network is a unique feature of the Harris SAI CFA analysis. While the NRL magnetron program is relativistically correct and uses a full solution of Maxwell's equations, the simple vane boundaries used do not reproduce the measured phase delay or interaction impedance of a CFA. Typical CFA circuits such as the backward-wave strapped vane line and interdigital line or the forward-wave stub-supported helix and meander line require a three-dimensional analysis to give their total electromagnetic field. However, the present quasistatic equivalent network is fully adequate for a two-dimensional model.

Although all previous simulations have assumed a fixed anode voltage (the "short-circuited diode" approximation), the nonzero impedance of the modulator allows the CFA voltage to fluctuate with the beam current. These fluctuations are too rapid or too small to be observed experimentally, but are essential in the simulation. Both the Harris SAI CFA model and the NRL magnetron model now impose a load-line constraint that limits the anode current by reducing the voltage as the current rises. This has proved necessary to ensure a stable RF solution.

In the "cathode-driven CFA" a gain of up to 30 dB has been obtained by forming the secondary-emission cathode into a slow-wave structure, on which the RF drive signal is applied.²⁰ (See Appendix F.) Litton Industries have developed a rectangular model of this device.¹⁵⁻¹⁷ However, that program gives limited resolution. The model uses a space charge array having 26 axial points and 11 radial points, and allows only 192 particles per RF wavelength. It also, more significantly, neglects recirculated charge at the RF input and ignores backward power flow on the RF circuits. The realistic direct field is included from the cathode vanes, but only a single space harmonic of the RF field is present in the Litton program.

TABLE 1

COMPARISON OF DISTRIBUTED-EMISSION
CROSSED-FIELD AMPLIFIER MODELS

Cylindrical Model

1. Model interaction region covers entire cylindrical reentrant tube.
2. Interaction region is stationary.
3. Reentrancy of the tube supplies the boundary condition at the ends of the interaction region. The mode of beam interaction (number of spokes of charge around the tube) develops automatically: no one mode is selected by the user.
4. The trajectory equations use cylindrical polar coordinates.
5. The measured magnetic field is supplied directly to the model.

Rectangular Model

1. A rectangular interaction region covers a single retarded RF wavelength only.
2. The interaction region moves around the tube at the cold RF phase velocity.
3. The beam distribution is forced to be periodic over the interaction region. Only a single beam mode is treated with the periodicity of the user-selected interacting space harmonic.
4. The curvature of the anode is neglected.
5. The magnetic field used in the model is artificially set lower than the measured value to maintain the ratio of the anode voltage to the Hartree voltage.

TABLE 1 (cont.)

- | | |
|--|--|
| <p>6. The RF fields are given by a Green's function for the actual anode vane structure. Network circuit equations give the transient solution for the vane voltages. All space harmonics and all time harmonics are included automatically.</p> | <p>6. Only a single interacting space harmonic is included at the drive frequency. The vane circuit is replaced by an equivalent transmission line. The time distribution of the induced current is approximated by the spatial distribution over the interaction wavelength.</p> |
| <p>7. The solution for a backward-wave network is obtained from that for a forward-wave network just by changing the signs of the voltage and current on alternate vanes.</p> | <p>7. For backward-wave interaction the reference frame must move with the beam. The RF output power is supplied and the drive power derived. The signs of the impedance and attenuation in the transmission line equations are opposite to the forward-wave signs.</p> |
| <p>8. At present, 10,000 rods of charge and a 257 (angular) x 33 (radial) space-charge array cover 15 RF wavelengths around the tube.</p> | <p>8. About 4,000 rods of charge and a 99 x 51 space-charge array cover one RF wavelength. The resolution of the rectangular model is greater than in the cylindrical model because of the larger array. Cost considerations, not inherent model limitations, are the reason for the difference.</p> |

TABLE 1 (cont.)

- | | |
|---|---|
| <p>9. The secondary-emission coefficient can be specified as a function of primary impact energy. Up to 120 emission sites cover the circular cathode (over 15 to 20 RF wavelengths). Options of time smoothing of the secondary charge and space-charge limitations are included to reduce the fluctuations at each emission site.</p> | <p>9. There are 96 secondary-emission sites per RF wavelength in the Varian model, where time smoothing is performed in the moving reference frame, and Child's Law limiting is included. The Litton model reemits every incident primary rod with a new charge obtained from the secondary-emission coefficient.</p> |
| <p>10. The anode-cathode voltage is variable in time and controlled by an external modulator circuit which reduces the voltage in response to an increase of current.</p> | <p>10. The anode-cathode voltage is constant.</p> |
| <p>11. The present program requires about 260,000 32-bit words of CPU memory. One pass around the tube (15 RF periods) with 7,000 particles requires about 13,500 CPU seconds on an IBM 360/67 computer.</p> | <p>11. The Harris SAI version of the rectangular model uses an estimated 60,000 32-bit words of CPU memory. One pass around the tube requires approximately 1,200 CPU seconds on an IBM 360/67 computer.</p> |

In order that the computer program be useful for design it is important to correlate the theoretical results with experimental measurements for a range of conditions in different tubes. Fairly good agreement (anode current about 20 percent below the measured value and RF output power about 15 percent too low) has been reported by Varian Associates¹¹ for a space-charge-limited cathode concentric with the anode. The Varian model, however, shows variations of ± 8 percent of the mean anode current and RF power over successive passes around the tube. That model has also been tested for the production SFD-261 CFA in which the cathode is noncylindrical, and on a tube with a tapered vane pitch. The computed power grows less rapidly along the circuit than observed in the instrumented tubes. For the Litton program there are no published comparisons with measurement.

The primary aim of these simulations is to predict the operating anode current and RF output power. However, the tube designer also needs to know the range of conditions under which the CFA can start and operate without oscillation or interfering modes, and under which the cathode will supply sufficient current.

Starting conditions have been studied using ballistic theory^{13,14,21} and with space charge²² but the steady-state assumption of the latter model is probably not realistic. The space-charge forces modify the trajectories significantly,¹⁴ making the full simulation necessary. The Harris SAI program can include both the formation of the beam and the buildup of voltage due to a line-type modulator, on an accelerated time scale.

Useful tests of the cathode-emission model are its ability to predict the backbombardment power, to form a stable steady-state charge hub, to predict the backbombardment power with RF drive, and to demonstrate the limits of available cathode current as the anode current is increased. Both Harris SAI and Varian originally used an unsmoothed emission model in which each primary

charge generated secondary charge computed from the impact energy. However, subsequent anomalous results have shown the need for some form of smoothing to suppress excess charge, since the space-charge mesh cannot resolve the local potential minimum. The Varian model uses time smoothing and applies a simple Child's Law emission limit using the first mesh interval as an elemental diode. It has not succeeded in reproducing emission limits. Harris SAI uses an improved model, originally developed for a thermionic cathode in the NRL magnetron study. Here both the local electric field and the charge near the cathode limit the emission. The present application to secondary emission is new. Initial results described in this report are qualitatively well supported by observations of backbombardment power and emission limitation.

Mode boundaries have not been predicted in any published analysis. As the first step, the Harris SAI program now shows the threshold RF output power for oscillation due to reverse-directed power flow on the circuit. It also gives a reasonable estimate of the RF drive power required to suppress this oscillation.

SECTION III

TUBE DATA

A considerable amount of experimental tube data has been obtained by Harris SAI during the present and earlier studies. Table 2 compares the six tubes for which data have been obtained; those data are listed in Appendices A-F. The secondary-emission characteristics of the four cathode materials are given in Appendix G.

The following quantities must be supplied by the engineer for performing a simulation:

- Circuit type (forward-wave or backward-wave), and number of active vanes;
- Magnetic field;
- Tube dimensions, i.e. width in the magnetic-field direction, anode and cathode radii, shape of cathode if eccentric or not cylindrical, pitch of vane circuit, vane spacing on the anode;
- Frequency and operating band;
- Operating voltage;
- RF drive power;
- Circuit cold-test measurements of phase delay per pitch, interaction impedance at the vane tips and attenuation per pitch;
- Secondary emission of cathode as a function of primary impact energy;
- Estimate of operating current;
- Type of modulator (line or hard-tube).

These quantities are listed on the forms used for Appendices B-F.

TABLE 2
DISTRIBUTED-EMISSION CROSSED-FIELD AMPLIFIERS
FOR WHICH HARRIS SAI HAS EXPERIMENTAL DATA

Manufacturer	Tube Designation	Forward-Wave or Backward-Wave Amplifier	Cathode Material	Notes
Raytheon Company	QKS1300	Backward-Wave	Thermionic emitter	See Appendix A. Data used only for program development.
Raytheon Company	QKS1842	Backward-Wave	Cermet (Tungsten-Thoria), platinum or gold with magnesium oxide	See Appendix B.
Varian Associates	SFD-261	Forward-Wave	Beryllium Oxide	See References 10 and 11 and Appendix C.
Raytheon Company	QKS1319	Forward-Wave	Beryllium Oxide	Measurements made under subcontract to Harris SAI, Inc. See Appendix D.
Raytheon Company	QKS1705	Backward-Wave	Not Known	See Appendix E.
Raytheon Company	QKS1840	Forward-Wave	Platinum	Cathode-driven CFA See Appendix F.

SECTION IV

ASSUMPTIONS AND APPROXIMATIONS

The following are the main assumptions and approximations of the model.

1. The magnetic field is axial, uniform, and constant in time.
2. Motion in the magnetic-field direction is zero; this is a two-dimensional model only, using rods of charge to represent the beam.
3. The electric field is treated as an average value over the width of the tube in the magnetic-field direction. (Actual beams show maximum anode bombardment and sole emission in the center of the transverse plane.)
4. The beam velocity and fundamental circuit phase velocity are much less than the velocity of light ($v^2/c^2 \ll 1$) such that motion is nonrelativistic, forces due to RF magnetic fields are negligible and Poisson's equation replaces the wave equation for the electric field. (The self-magnetic field due to the rotating beam can be included as a small correction in future simulations.)
5. For computing the electric field, the electrode surfaces are treated as smooth and perfectly conducting. However, the RF network accounts for measured skin losses.
6. The cathode is a cylinder concentric with the anode. An "off-center cathode" will be treated in future versions of the program.
7. The slow-wave structure is replaced by a low-frequency RF network. Each node of this network represents one of the active vanes of the CFA.

8. The total voltage seen by the beam at any vane is the sum of the modulator voltage and an RF voltage. The modulator voltage is assumed to vary more slowly in time than the RF voltage, in order that the RF network equations can be solved independently of the modulator.

9. At any instant the average RF voltage over all the vanes is much less than the modulator voltage, so that the modulator circuit can be treated independently of the RF network.

10. The cold RF network is perfectly matched at each end.

11. The anode vane segments are identical and equally spaced. However, a "tapered-pitch" circuit will be included in future versions of the program.

12. Between the anode vanes the electric field is uniform around the circumference. (This field would be insufficiently accurate for a cathode circuit but is a good approximation where electrons move rapidly.)

13. There are no neutral or ionized gas atoms present.

14. The electron-electron collision time is large compared with the transit time through the amplifier. Nearest neighbor electron forces are small compared with the effects of the average field due to many electrons, and the collisionless particle-in-cell model²³ is applicable to treat collective space-charge interaction.

15. The relative change of the local electric field during one time step of the calculations is small. The effects of this approximation have been checked by running with a reduced time step and verifying that the results are consistent.

16. The computed results are insensitive to the number of simulation rods used. This approximation has been tested separately for each tube under simulation. About 7,000 rods suffice.

17. Electrons, primary or secondary, are emitted over several sites covering the cathode. The total emission current is uniform over each site. Sufficient sites should be chosen to give at least six per spoke of charge (per RF wavelength around the circumference). Usually 120 sites suffice.

18. If sufficient charge is available at any of the cathode emission sites to produce a local potential minimum, the potential minimum is treated as coincident with the cathode and its depth is neglected.

19. The time interval between successive electron emissions is an integer multiple of the time step.

20. The electron thermal velocities are negligible in the RF interaction; however, the user may select a single initial energy for primary or secondary electrons emitted from the sole.

21. The modulator acts as a constant voltage source in series with a resistance, an inductance, and the parallel combination of a capacitance and the CFA.

22. The modulator inductance and capacitance are chosen so that transient circuit voltages and currents decay over a few RF periods, in order to accelerate the development of a steady state in the simulation.

SECTION V

CATHODE EMISSION

A. Introduction

The operation of any CFA depends critically on the ability of the cathode to supply sufficient current. A realistic model enables the tube designer to predict the emission limits and backbombardment heating with thermionic or secondary-emitting surfaces of various types. The macroscopic model used here and in the injected-beam CFA study (Part II of this report) appears to reproduce the observed behavior well.

The user may simulate either thermionic or secondary emission or both. For thermionic emission a fixed number of charge rods is made available for emission at each time step. These rods are distributed uniformly around the cathode. However, the actual number emitted is controlled by the local electric field and charge density in a manner described below. These primary charges may be used throughout the run. Alternatively they can be used for the first NTINJ time steps only, to develop a beam hub before the secondary-emission model takes over.

The thermionic charges may be combined with or replaced by secondary charges produced by backbombarding electrons. The switch NSECSW controls the inclusion or exclusion of secondary emission.

B. Secondary Emission

A full description of the secondary-emission process as modeled by Harris SAI is presented here.

The computations of impact energy, backbombardment current, and the summation of secondary charge are performed in the "predictor" section of the trajectory subroutines (Section VI).

A separate subroutine allocates the secondary charge to new simulation particles (rods) at the start of the following time step.

When a particle is computed to intercept the sole (cathode), its last time step is repeated in several subintervals (typically 1/15 the normal time step). The angular electric field is linearly interpolated, as a function of radial distance from the sole, between a zero value at the sole and the value at the start of the time step. The radial space-charge and RF fields are not changed for the subintervals, but the exact direct radial field between the cylindrical anode and sole is evaluated for each subinterval. The reduced time interval gives a more accurate sole bombardment energy.

The angular region of the sole where the interception occurred is determined as the position for secondary emission. The cylindrical surface may be divided into one to 256 such regions.

According to a user option, secondary emission may be set to zero and the primary charge treated as if it had not been emitted in the case where its radial position at the start of the time step was less than 1.0002 times the sole radius. That procedure suppresses the emission of secondary charge due to primary particles emitted and collected in the same time step. The amount of such primary charge is recorded and is printed at each step.

The secondary-emission coefficient is supplied as a tabulated function of primary impact energy, for incidence normal to the cathode surface. For each intercepted particle, the program interpolates the table linearly using the computed impact energy.

The angle of primary incidence, θ , is used to correct the secondary-emission coefficient²⁴ to a value S_θ using the equation:

$$\delta_{\theta} = \delta_{\underline{1}} e^{p(1-\cos\theta)} \quad , \quad (1)$$

where $\delta_{\underline{1}}$ is the value determined for normal incidence, and the input parameter p is typically 0.55. An incident charge q then results in the production of secondary charge $\delta_{\theta}q$ at the same angular site. As all the trajectories are followed in a given time step, the total secondary charge to be emitted is summed for each of the emission sites around the cathode.

Next, program options of time smoothing and spatial smoothing of the charge to be emitted may be invoked for each emission site. Firstly, the time-smoothing option (subroutine TSMSEC) combines the charge with that from previous steps in the manner described by McDowell¹¹ with a smoothing parameter, TIMSEC, between zero and unity. A value TIMSEC of 0.15 causes about 73 percent of the secondary charge from a given step to be emitted over the eight succeeding steps. Secondly, the space-smoothing option (subroutine SMSEC) distributes the charge determined for a given emission site over seven adjacent sites in the proportions

$$s:s^2:s^3:s^4:s^3:s^2:s \quad ,$$

where S is a user-chosen parameter. This option has not been used in major runs.

At this point the total thermionic or secondary charge available for emission in each cathode site in the next time step is known. Next the local electric field and the charge already at the cathode are used to control the actual emission.

C. Control of Emitted Charge

The cathode is divided into between 120 and 256 angular regions for computation of the emitted charge. It is assumed that in each region at a given time step one of two conditions

exists:

(a) Space-charge limitation, defined here as the condition in which the charge available for emission during the time step is at least sufficient to create a potential minimum within the first mesh interval normal to the surface.

(b) Emission limitation, in which the normal electric field is directed towards the cathode throughout the first mesh interval.

In case (b) all the available charge is emitted; in case (a) sufficient charge is emitted to reduce the local electric field to zero on the cathode surface.

Hence the instantaneous local electric field normal to the cathode, including direct, RF and space-charge fields, controls the emission, while the magnetic field is ignored. When a region of the cathode is space-charge limited (with the definition above) the implicit assumption is that a sheath of charge covers the surface there and creates a "virtual cathode" at the potential minimum.

The time-dependent feature of this model allows the emitted charge to fluctuate with the instantaneous RF and space-charge fields.

D. Approximations of the Emission Model

Three approximations made here are:

(1) the time required to form the potential minimum (of the order of the local plasma oscillation period) is much less than the time step of the simulation,

(2) the distance from the cathode to the potential minimum is much less than the mesh interval normal to the surface and

(3) the depth of the potential minimum is much less than the potential difference over the first mesh interval.

Strictly, approximation (1) is violated in the model, where

a time step of, typically, 1/10 the cyclotron period is also 1/10 of the plasma oscillation period in a Brillouin stream. However, the error is probably unimportant for small fractional changes per step in the emitted charge.

To justify approximations (2) and (3) consider the plane-parallel diode with no magnetic field. Langmuir's solution²⁵ shows that the distance of the potential minimum from the cathode is approximately equal to the Debye shielding distance^{23,25} λ_D . This distance decreases as the local charge density increases and varies as the mean normal velocity of electron emission from the cathode.

The depth V_m of the potential minimum is given by

$$V_m = V_e \ln \left(\frac{\text{net emitted current}}{\text{available secondary current}} \right) \text{ Volts} \quad (2)$$

where V_e is the mean energy of available secondaries about 2 electron volts. Published estimates²⁶ of the potential minimum and its position in a crossed-field diode have the same order of magnitude. An upper estimate of λ_D can be obtained using the Brillouin charge density in the applied magnetic field and an initial secondary electron energy of 2eV. In the tubes studied here, these estimates range between 1/103 and 1/163 times the cathode-anode spacing. The radial mesh interval used in the model is 1/32 times the cathode-anode spacing. For a saturated emitter current of ten times the net emitted current (with an effective secondary-emission coefficient of 1.11) the potential minimum is only -4.6 V, while the anode voltage is 10 kV or more.

It should be mentioned in passing that Fischer²² has made a quite different approximation, namely that the potential minimum equals the mean ballistic impact energy (eV) due to the RF field, i.e. over 100 volts. However, with the resulting high space-charge field the ballistic equations are probably not valid. Moreover the steady potential assumed by Fischer is

inconsistent with the time-varying RF field at each cathode point.

E. Algorithm for Control of Emission

The steps followed by the program are

- (1) calculation of space-charge and RF electric fields at each emission site (subroutines ESCCAT and RFCAT),
- (2) counting of the charge already present above each site (subroutine CCGCAT),
- (3) limiting of the available charge where necessary (subroutines SECCAT and NOEMIT),
- (4) printing of diagnostic information (subroutine PRTCAT), and
- (5) initialization of new particles at the cathode surface (subroutine INSECS).

For solution of Poisson's equation the anode-cathode region is covered by a computational mesh of chosen radial interval Δr and angular mesh interval $\Delta\theta$, which may be equal to or less than the angular interval DTHSEC of each emission site. Figure 2 shows the configuration at the cathode with $\Delta\theta = 0.5$ DTHSEC in this example.

The region of angle DTHSEC between r_c and $r_c + \Delta r$, where r_c is the cathode radius, is used to count the charge already present. Applying Gauss's Law and setting the radial electric field E_r to zero at $r = r_c$ gives

(charge allowed for emission)

+ (charge already in the region)

$$= \epsilon_0 E_r h \Delta r \text{ DTHSEC} \quad (3)$$

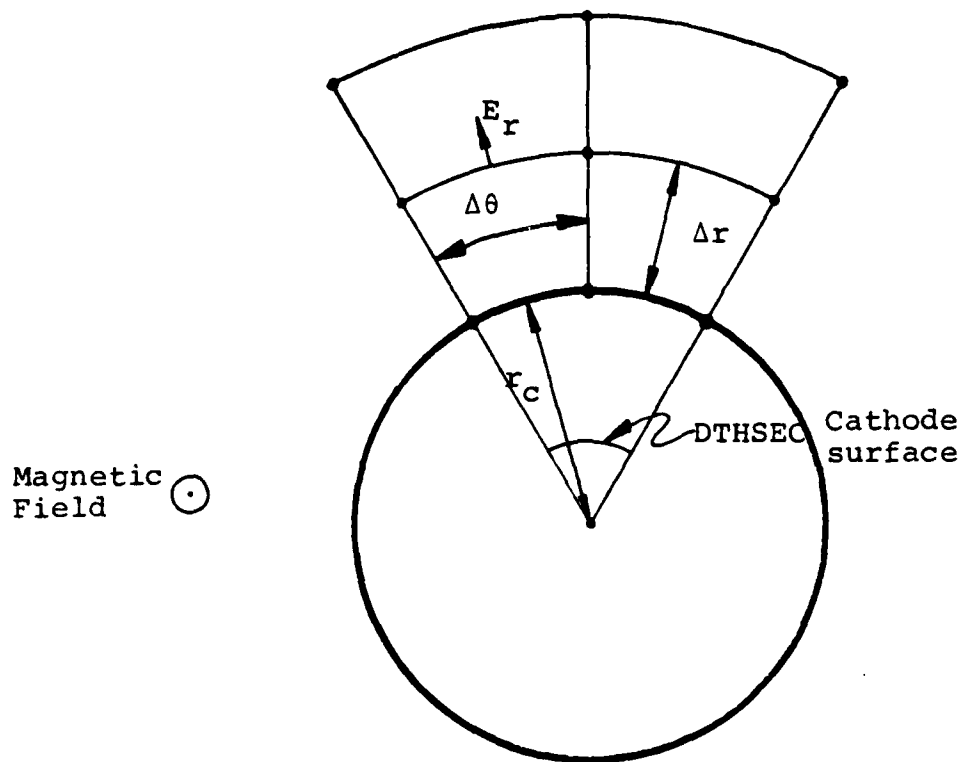


Figure 2. Mesh elements at the cathode in the DECFA simulation.

where ϵ_0 is the permittivity of free space, E_r is the total radial electric field evaluated at $r_c + \Delta r$ and h is the width of the cathode in the magnetic-field direction.

The RF electric field is computed at the midpoint of the angular segment DTHSEC. The space-charge fields are already stored at the Poisson mesh points. Their values are averaged over the mesh points at radius Δr above each emission site using an area-weighting procedure.

The charge in the region $r_c \leq r \leq r_c + 1.5\Delta r$ is assigned to the angular emission segments by the same area-weighting procedure. A fraction RFRAC of each particle is considered to lie within a distance Δr of the cathode, given by

$$\text{RFRAC} = 1 - \left| r - \frac{\Delta r}{2} \right| / \Delta r \quad (4)$$

for a particle at radius r .

If the charge allowed for emission exceeds the available charge stored for emission at any site, that site is treated as emission limited and only the available charge is emitted.

F. Test Results

1. Child's Law

Here the magnetic field is set to zero and a thermionic emission current is chosen sufficient to give space-charge-limited operation. With the present emission limitation and the predictor-corrector trajectory calculation the anode currents from the model are two percent greater than those predicted by Child's Law for the cylindrical geometry.²⁷ They follow the three-halves power law as the voltage is varied.

2. Secondary Emission

Before the present cathode model was implemented, runs with no limit imposed on secondary emission accumulated too many

charge rods and showed excess backbombardment power at the cathode. Apparently the model had insufficient resolution to return excess charge to the cathode, at which the radial mesh interval is larger than the distance to the actual potential minimum. Similar instabilities have been computed by Varian⁹ without smoothing.

Four runs were performed to test the effects of varying degrees of smoothing at the cathode. The results of Figures 3 and 4 and Table 3 show the computed anode current and RF output power in forward-wave CFA as the simulation progresses over 50 RF periods. These results were obtained without the modulator and show a runaway effect of current and RF power. Notice that the computed anode current and output power are higher than the measured 22 A and 1.65 P_0 , but decrease as the degree of smoothing in the model increases. The thermionic-emission model gives the closest agreement, for the anode current is within 10 percent of the measured value.

All the secondary-emission runs (runs 5, 6, 7 and 8) used a Child's Law limiting procedure, which produces similar effects to the more refined emission limitation described above. Runs 5, 6, and 7 used 120 equiangular regions subdividing the cathode for computing the local secondary emission. In run 5, no additional smoothing was performed. Runs 6 and 7 used a time-smoothing method, following that of Varian, but in a fixed, not a moving, reference frame. Complete spatial smoothing was applied in run 8 by distributing the total secondary charge evenly around the cathode in each step. The "thermionic cathode" of run 10 was simulated by placing 300 primary charge rods at equal intervals around the circumference at each time step and suppressing secondary emission. The corresponding total emitted current of 204 A compares with the 177 A used by Varian and is enough to maintain a retarding average electric field around the cathode for about 75 percent

Run No.

Secondary Emission with no Smoothing

5

Time-Smoothing Parameter = 0.15

6

Time-Smoothing Parameter = 0.075

7

Space-Averaging Around Tube; no Time Smoothing

8

Thermionic Cathode; no Secondary Emission

10

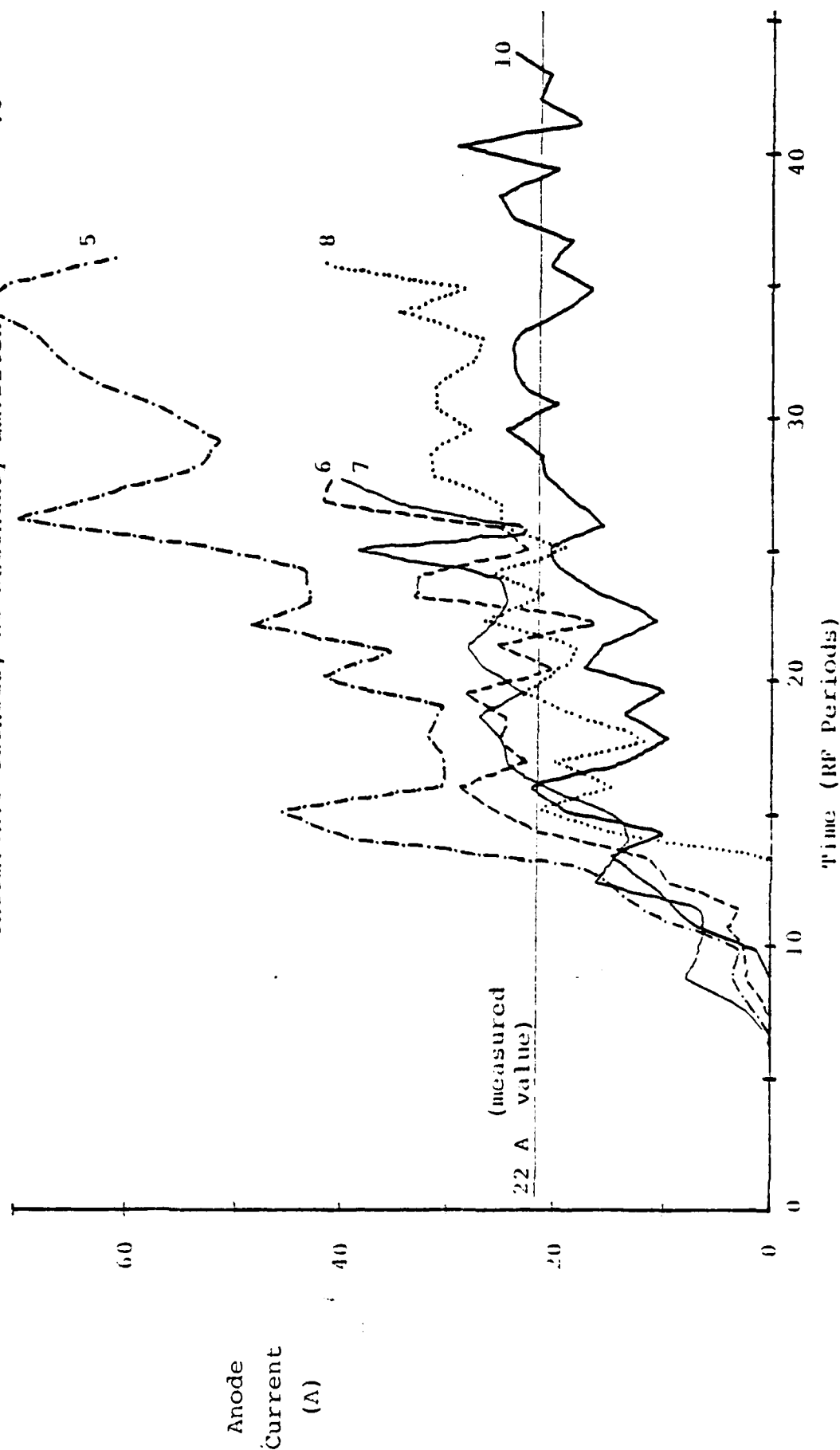


Figure 3. Anode current computed for Varian forward-wave DECFA for varying degrees of smoothing at cathode. Modulator not yet included.

Run No.

- 5 Secondary emission with no smoothing
- 6 Time-smoothing parameter = 0.15
- 7 Time-smoothing parameter = 0.075
- 8 Space-averaging around tube; no time smoothing
- 10 Thermionic cathode; no secondary emission

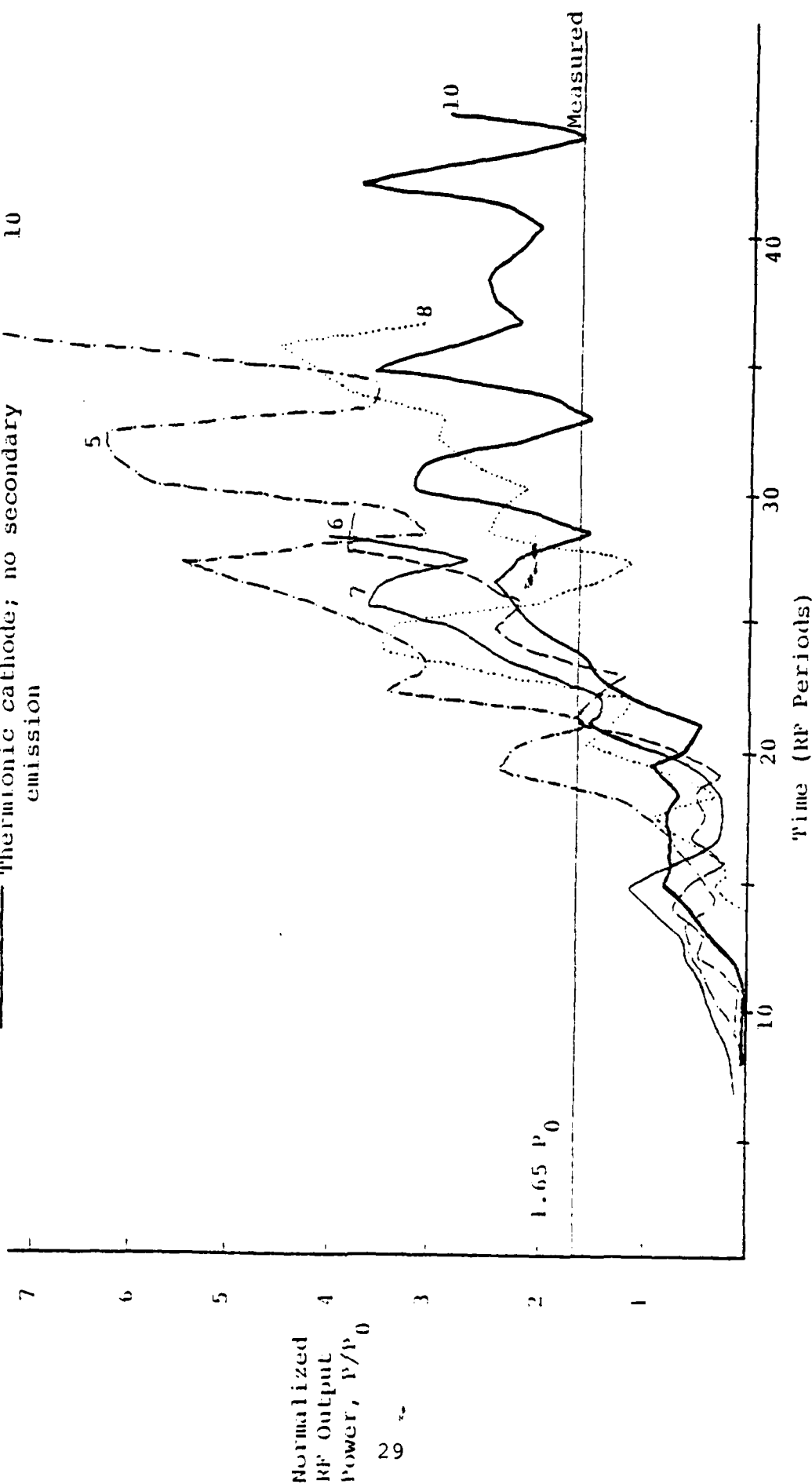


Figure 4. RF output power computed for Varian forward-wave CFA for varying degrees of smoothing at cathode. Modulator not yet included.

TABLE 3

COMPUTED RESULTS FOR VARIAN FORWARD-WAVE CFA WITH VARIED
SMOOTHING OF CATHODE EMISSION; AVERAGES OVER 18 RF PERIODS

Run No.	First and Last RF Periods of Averaging Interval	Smoothing Method	Anode Current (A)	Cathode Current (A)	Impact Current (A)	Emission Current (A)	Mean Secondary- Emission Coefficient	Mean Impact Energy (eV) on Cathode	RF Output Power/P ₀
5	19 to 36	None	55.1	56.8	116.8	174.0	1.49	347	4.27
6	14 to 31	Time- Smoothing Parameter 0.15	28.4	28.0	90.7	118.7	1.31	131	1.567*
7	14 to 31	Time- Smoothing Parameter 0.075	27.6	27.5	93.1	121.6	1.31	113	1.794*
8	23 to 40	Space Averaging Over Entire Cathode	30.9	30.7	108.4	139.1	1.28	82	2.934

TABLE 3 (CONTD.)

COMPUTED RESULTS FOR VARIAN FORWARD-WAVE CFA WITH VARIED
SMOOTHING OF CATHODE EMISSION; AVERAGES OVER 18 RF PERIODS

Run No.	First and Last RF Periods of Averaging Interval	Smoothing Method	Anode Current (A)	Cathode Current (A)	Impact Current (A)	Emission Current (A)	Mean Secondary- Emission Coefficient	Mean Impact Energy (eV) on Cathode	RF Output Power/ P_0
10	32 to 49	Uniform Thermionic Emission Only	24.8	23.9	180.5	204.1	1.13	49	2.815

Anode Voltage = 1.3 V_i Magnetic Field = 0.253 T

Measured Values: Anode Current - 22 A
 Backbombardment Power - About 5% of Direct Input Power
 RF Output Power - 1.65 P₀

*These runs were stopped after 31 periods since the computed power was rising too rapidly.

of the time. The net cathode current is the emission current minus the current of electrons returned to the cathode.

The details of the behavior of these test runs are not fully understood. Apparently time smoothing significantly reduces the noise in the discrete particle model. The angular distribution of secondary charge around the cathode is important in ballistic theory where the RF field produces phase focusing^{14,21} but the corresponding effects under space-charge-limited conditions in an actual tube are not so clearly defined.

SECTION VI

PARTICLE TRAJECTORIES

In each time step, the radial and angular components of position and velocity of the simulation particles must be advanced, with the vane voltages given at the start of the step. The rapid angular variation of the RF electric field and the cylindrical geometry present special problems of resolution. Initial trials at Harris SAI used a simple one-step trajectory calculation in local rectangular coordinates. The predictor-corrector calculation now used is less efficient but more accurate than the simple one-step algorithm. It includes two electric field computations per time step.

At the start of the time step, at time t , the following quantities are known for each particle:

1. Radius,
2. Angle,
3. Velocity,
4. Local electric field \bar{E}_1 (as radial and angular components), and
5. Charge.

The calculation of the position and velocity at time $t + \Delta t$ proceeds by using a basic algorithm twice for each particle.

A. Basic Algorithm

The equation of motion of a particle of charge q and mass m in an electric field \bar{E} and magnetic field \bar{B} is

$$\frac{d\bar{v}}{dt} = \frac{q}{m} (\bar{E} + \bar{v} \times \bar{B}) \quad . \quad (1)$$

A transformation from cylindrical coordinates (r, θ) to a local rectangular system is performed. At the start of the time step, define local coordinates as

$$x_p = 0 \quad , \quad (2)$$

and

$$y_p = r \quad , \quad (3)$$

and the velocity as

$$v_{xp} = r\dot{\theta} \quad , \quad (4)$$

and

$$v_{yp} = \dot{r} \quad , \quad (5)$$

with the local electric field components

$$E_x = E_\theta \quad (6)$$

and

$$E_y = E_r \quad . \quad (7)$$

Next, the particle equation of motion Equation 1 is solved for the new position (x_n, y_n) and velocity (v_{xn}, v_{yn}) . The scheme described by Vaughan¹⁴ is used to give cycloidal trajectories which would be exact in a uniform electric and magnetic field.

Finally, the new cylindrical coordinates are computed using the equations

$$r_n = \sqrt{x_n^2 + y_n^2} \quad (8)$$

and

$$\theta_n = \tan^{-1}(x_n/y_n) + \theta_p, \quad (9)$$

where θ_p is the previous angular position, and the new velocity $(\dot{r}_n, \dot{\theta}_n)$ is given by

$$\dot{r}_n = v_{yn} \frac{y_n}{r_n} + v_{xn} \frac{x_n}{r_n}, \quad (10)$$

and

$$\dot{\theta}_n = -v_{yn} \frac{x_n}{r_n} + v_{xn} \frac{y_n}{r_n}, \quad (11)$$

a rotation of the coordinate system through the angle $\tan^{-1}(x_n/y_n)$.

The direct electric field is radial and equal to $-V_a/(r \ln(r_a/r_s))$ at radius r , where V_a is the anode-sole voltage, r_a is the anode radius and r_s is the sole radius. The electric field changes with position both because of the cylindrical anode and sole and because of the RF field. The refinement of this calculation accounts for this change.

B. Predictor

For each particle, the stages of the calculations are as follows:

1. Store the initial position and velocity in separate arrays for use by the corrector.

2. Advance the trajectory using the basic cylindrical algorithm and the field \bar{E}_1 , check for electrode interception, and store the predicted positions and velocity for time $t + \Delta t$.

3. Use the predicted position to evaluate the local charge density at time $t + \Delta t$.

Solve Poisson's equation for the space-charge potential at time $t + \Delta t$, derive the space-charge field, and advance the network voltage solution from time t to time $t + \Delta t$.

At this stage the integrals are incremented for the Fourier components of the induced currents and vane voltages. These components are used for output information only at intervals of one RF period.

C. Corrector

For each particle:

1. Compute the local electric field \bar{E}_2 at the predicted position, using the space-charge field and the resultant RF field from all the vane voltages.

2. Repeat the trajectory advance from time t to time $t + \Delta t$, but now using the arithmetic mean of the electric fields \bar{E}_1 and \bar{E}_2 , to derive the corrected position.

3. Recompute the electric field \bar{E}_3 at the corrected position, increment the induced current on each vane (at time $t + \Delta t$), and store the local electric field \bar{E}_3 for use as the field \bar{E}_1 of the next time step.

The time-consuming element of this procedure is the summation of the RF electric field on all particles due to the separate vanes of the tube. This summation is performed

twice for each time step. However, trials have shown that an accurate resolution of the spatially varying electric field is essential for realistic RF interaction to appear in the overall solution.

D. Test Results

The program has been tested using ballistic motion of a single particle in the direct field only for one RF period. Results have been compared as the time step is successively reduced. In the absence of RF fields, the simple "predictor-only" calculation gives errors of 4.04, 2.07, 0.839, 0.420, 0.204 and 0.09 percent in total energy for time steps of respectively 1/20, 1/40, 1/100, 1/200, 1/400, and 1/800 the cyclotron period, whereas including the corrector reduces the error to only 0.04 percent for a step of 1/20 the cyclotron period.

The charge distributions of Figures 5 and 6 have been obtained for the QKS1300 amplatron. With only one field evaluation per step, prior to the corrector calculation, little interaction appears (Figure 5), but with the local field recalculated at the end of the step, the charge spokes develop (Figure 6).

When the time step is halved, the induced vane currents and sole backbombardment power agree to within a few percent and the plotted beam profiles appear consistent.

E. Proposed Development

The present procedure has two disadvantages, namely

(1) the "corrected" particle position is consistent with the derived RF fields, but not with the space-charge field unless a second Poisson solution is performed after the corrector step, and

CHARGE DISTRIBUTION AFTER STEP 992

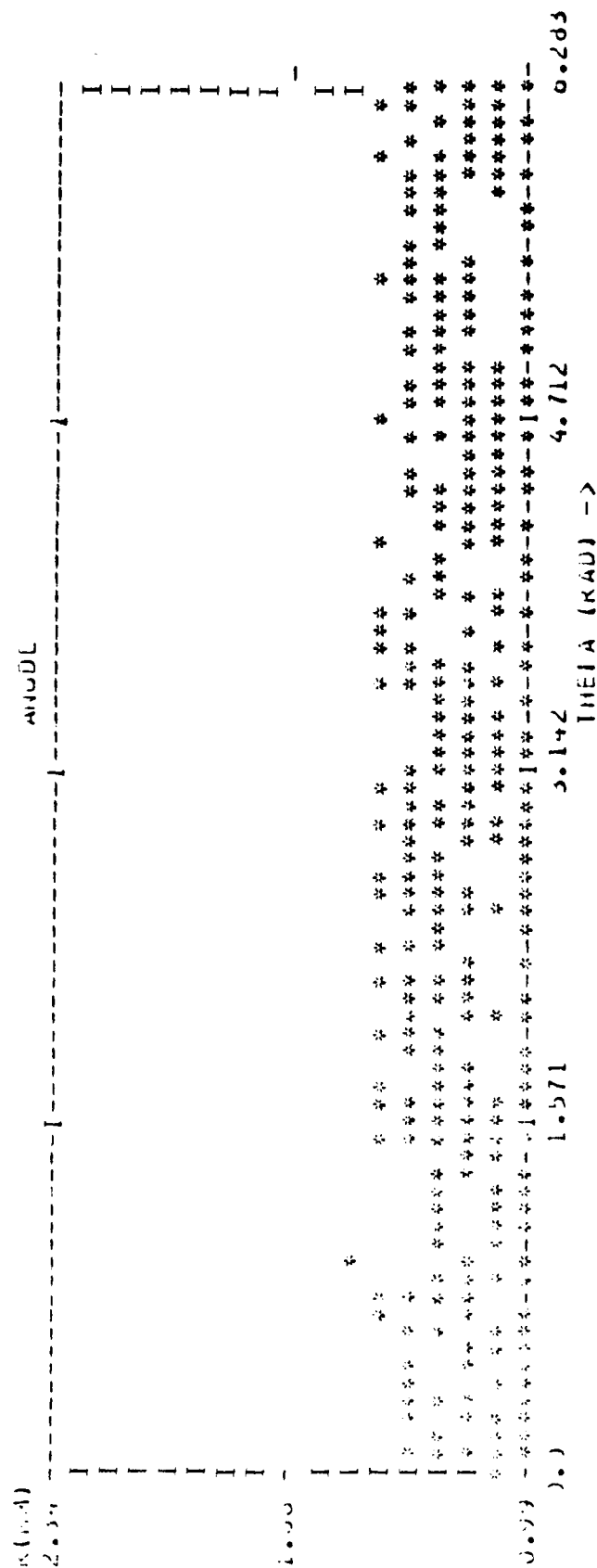


Figure 5. Charge distribution computed with one electric field evaluation per time step.

(2) the RF field is time-consuming to evaluate twice per step.

In further development of this program it is planned to test an alternative time-centered trajectory calculation, which may prove more efficient by eliminating one of the RF-field calculations per time step. If this proves successful an alternative RF field calculation will then be tested for a further increase of efficiency.

1. Time-Centered Trajectory Calculation

The steps of the time-centered trajectory procedure are as follows for each active particle:

(1) Start with the particle velocity \bar{v} at time $t - \Delta t/2$ and its position \bar{r} at time t .

(2) Evaluate the local electric field $\bar{E}(r,t)$, separating the space-charge field and the r and z components due to the voltage on each vane. Store these components in two work arrays of dimension NVANES.

(3) Advance the velocity \bar{v} to time $t + \Delta t/2$ as in the present cylindrical model.

(4) For each vane increment the induced current by the amount due to the particle (See Appendix H). The stored field components at (\bar{r},t) are used here, and the velocity $v(t)$ is approximated as

$$\bar{v}(t) = \frac{1}{2} \left(\bar{v}(t - \frac{\Delta t}{2}) + \bar{v}(t + \frac{\Delta t}{2}) \right) \quad (12)$$

The work arrays are then free to be reused for the next particle.

(5) Advance the position $\bar{r}(t)$ to $\bar{r}(t + \Delta t)$ and test for interception on the anode and cathode.

(6) Store the charge density at time $t + \Delta t$ for the next solution of Poisson's equation.

2. RF Field Calculation

Because the details of the circuit (which is generally three-dimensional) are modeled with an equivalent network, it is necessary to separate the space-charge field from the field due to the vane voltages in order to compute the induced current on each vane. The form of network used for the backward-wave device requires also that the RF voltages be defined separately from the direct voltage due to the modulator.

At present, the program computes the RF field at each particle by summing the components from all the vanes within a certain angular interval centered at the particle. For each vane the RF voltage is multiplied by the Green's functions for the radial and angular components. The induced current is computed simultaneously. This procedure requires only two 41×41 RF field arrays, but is time-consuming.

It may be practicable to replace the direct summation of the RF field on each particle with a solution of Laplace's equation. Then the induced charge and current on each vane will be obtained from the normal component of the space-charge field as in Appendix H. However, this modification must be carefully tested to ensure that it can reproduce the RF field with sufficient resolution with the available machine storage.

SECTION VII

SPACE-CHARGE FIELDS

The electrostatic field is obtained by solving Poisson's equation in finite-difference form at each time step. The axial self-magnetic field is now neglected. It is estimated below as less than one percent of the external magnetic field.

A. Solution of Poisson's Equation

In this two-dimensional model each particle is treated as a rod of charge, of arbitrary length in the magnetic-field direction. The charge density and electric fields are functions of the cylindrical coordinates (r, θ) only.

The cylindrical interaction region is subdivided with a mesh of points for the finite-difference solution of Poisson's equation. Charge from the simulation particles is assigned to the mesh by an "area-weighting" or "cloud-in-cell" procedure.²³ Poisson's equation is solved by standard numerical methods²⁸ for the cylindrical geometry with the anode and cathode voltages specified. Only the natural reentrancy boundary condition is imposed in the angular direction.

The radial and angular electric fields are computed and stored in separate arrays prior to the calculation of the trajectories. The area-weighting method is again used to interpolate the space-charge field to the position of a given electron. For greater accuracy, the space-charge field is derived for zero anode voltage and the exact external electric field is added at the particle position.

In order to avoid machine overflow during the Poisson solution, the charge density actually is stored in normalized form, as

(the number of units of initial charge
assigned to the mesh point)

x (radius at the mesh point)/(cathode radius)

This number is of the order of unity. A factor, VSCCON, multiplies the normalized potential solution to give the actual ratio of voltage to external magnetic field. (The magnetic field is included in this term only for greater efficiency in the trajectory calculations.)

Most of the simulations described here use a mesh with 256 angular intervals around the tube (for up to 18 RF wavelengths, or 18 charge spokes). There are 32 radial intervals between the anode and the cathode.

A useful check of the space-charge calculation is obtained by allowing a hub of charge to develop with uniform cathode emission and without the RF field, the solution for the "smooth-bore magnetron." The analysis and test results are given in Appendix J.

B. Charge Per Rod

The initial charge per rod is determined from the input variable NBRILL. This is the number of rods required to fill the cylindrical interaction region with a Brillouin charge density of $\epsilon_0 \omega_c^2 / n$, where $\omega_c / 2\pi$ is the cyclotron frequency and n the electron charge-to-mass ratio. Usually NBRILL is taken as 10,000 or 20,000: the smaller value where the anode voltage is further below cutoff. Section XII shows consistent test results with NBRILL as high as 45,000.

C. Self-Magnetic Field

Because of the sensitivity of the anode current (computed or measured) to the magnetic field it is useful to estimate the correction that would be added by including the axial field due to the rotating beam. The estimates of Table 4 are obtained from Ampere's Law as

$$|B_{\text{self}}| = \mu_0 I_{\text{circ}}/h \quad (1)$$

for a circulating current I_{circ} over a tube width h in the magnetic-field direction. The values of I_{circ} are computed as in Appendix J. The self-magnetic field opposes the applied field, but the correction is less than one percent. With the approximation of Equation 1 it can readily be included in the computation.

TABLE 4
AXIAL SELF-MAGNETIC FIELD

Tube	Circulating Current (A)	Tube Width (mm)	Self-Magnetic Field (T)	Applied Field (T)	Field Ratio
QKS1842 (high-power mode)	44.7	14.8	0.0038	0.395	.0095
QKS1842 (low-power mode)	38.2	14.8	0.0032	0.377	.0085
SFD-261	0.0216/D ₁ (normalized)	400D ₁	0.0011	0.253	.0043
QKS1319	8.79	35.56	0.0003	0.115	.0026

SECTION VIII

THE EQUIVALENT NETWORK FOR THE RF CIRCUIT

A. Introduction

The slow-wave vane structure of the DECFA is represented by an equivalent low-frequency network for which electrostatic node voltages are derived at each time step. With approximations discussed with the detailed equations in Appendix H, the RF and direct fields are treated independently and the vane-to-cathode capacitances are included as parts of the network. The network capacitances, inductances and resistances are computed from the measured cold-test values of phase delay, interaction impedance and attenuation at the drive frequency.

B. Comparison with Other Models

The present formulation has definite advantages over the continuous-transmission-line RF interaction model used by previous workers (e.g., Refs. 11 and 16).

1. By treating the total field due to all the vanes, the model automatically includes all space harmonics. In fact, the spatial Fourier components of the RF field have angular periodicity, so the space harmonics appropriate to an infinite linear structure are not required for computing the total RF field.

2. The fully transient network equations automatically include RF signals generated at frequencies other than the drive frequency. The behavior of these signals depends, of course, on the values of the network elements and the resulting dispersion and impedance characteristics. Only a single-frequency RF drive signal is applied at present.

3. Since the entire cylindrical tube is treated throughout the calculation, only the natural reentrancy boundary condition is imposed on the charge distribution. Moreover, for a given anode voltage and magnetic field, the charges are free to move into any spoke configuration or interaction mode.

4. Power may flow in either direction along the network and reflected waves due to "hot" mismatch at the input and output are automatically included. Hence the program can predict RF oscillation.

In a third model, a full time-varying solution of Maxwell's equations is obtained for the electric and magnetic fields in a magnetron using the actual "toothed" vane shape as the anode boundary. No cold-test dispersion or impedance data are used. However, that model may be difficult to adapt to the complex forward-wave and backward-wave circuits of crossed-field amplifiers, such as the strapped vane line of the QKS1842 and the stub-supported helix of the SFD-261 tube.

C. Forms of Network

The general form of the low-frequency equivalent network is shown in Figure 7. Nodes 1, 2, 3, 4 ..., represent the vanes of the CFA circuit and their voltages produce quasistatic RF fields seen by the electrons. Only the driving current is given a sinusoidal variation in time; all other currents and voltages may have arbitrary time dependence, periodic or non-periodic. Appendix I gives the general equations and the calculations used for the network elements.

The network used in the present calculations is a simple case of the general structure of Figure 7. This network, shown for the forward-wave tube in Figure 8, uses only one driving current source, and the admittance Y_c between alternate nodes is zero. The three elements G_a (conductance), C_a (capacitance) and $1/\Gamma_b$ (inductance) are chosen automatically in the program,

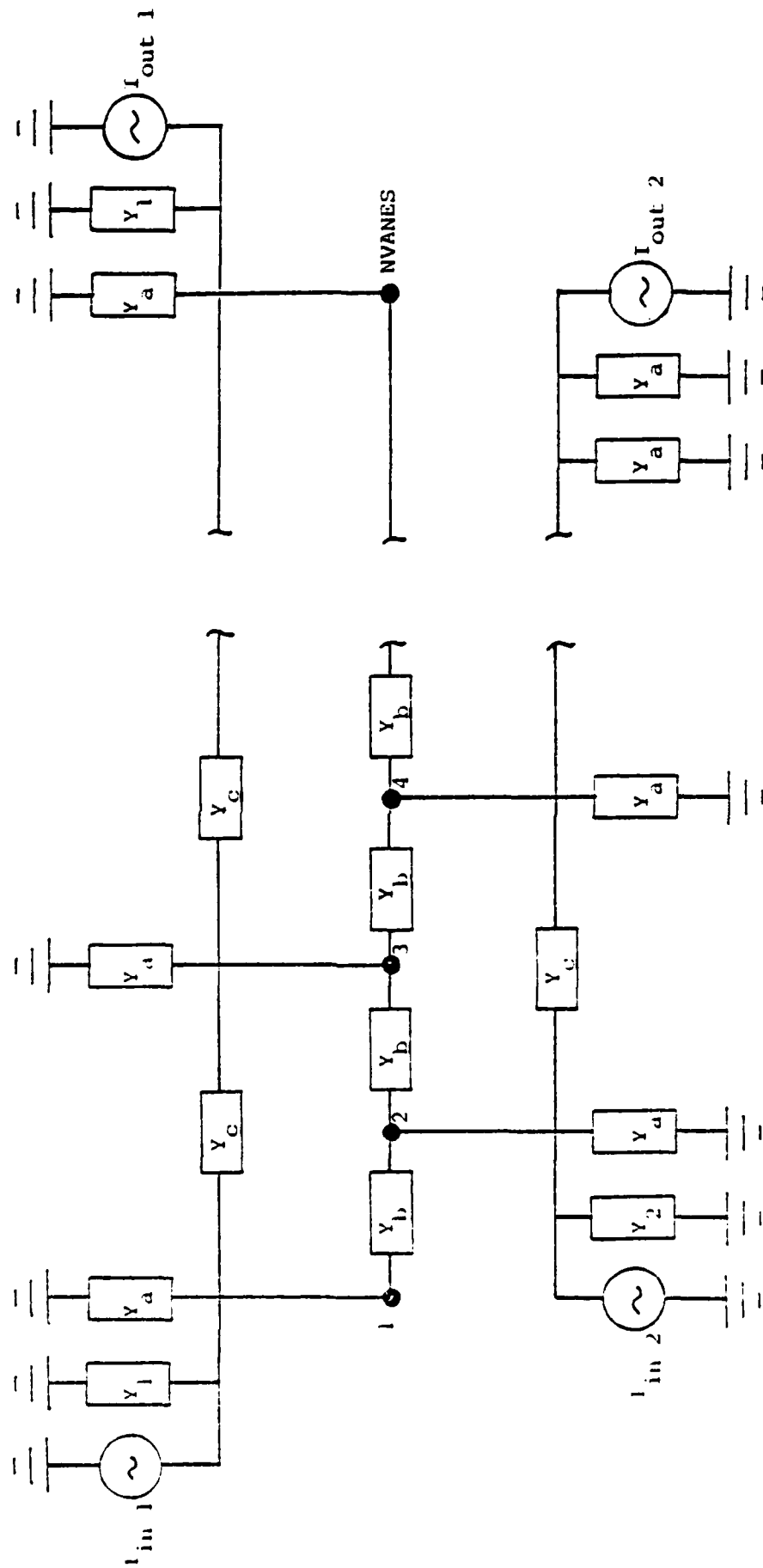


Figure 7. General equivalent network for DECFA slow-wave circuit.

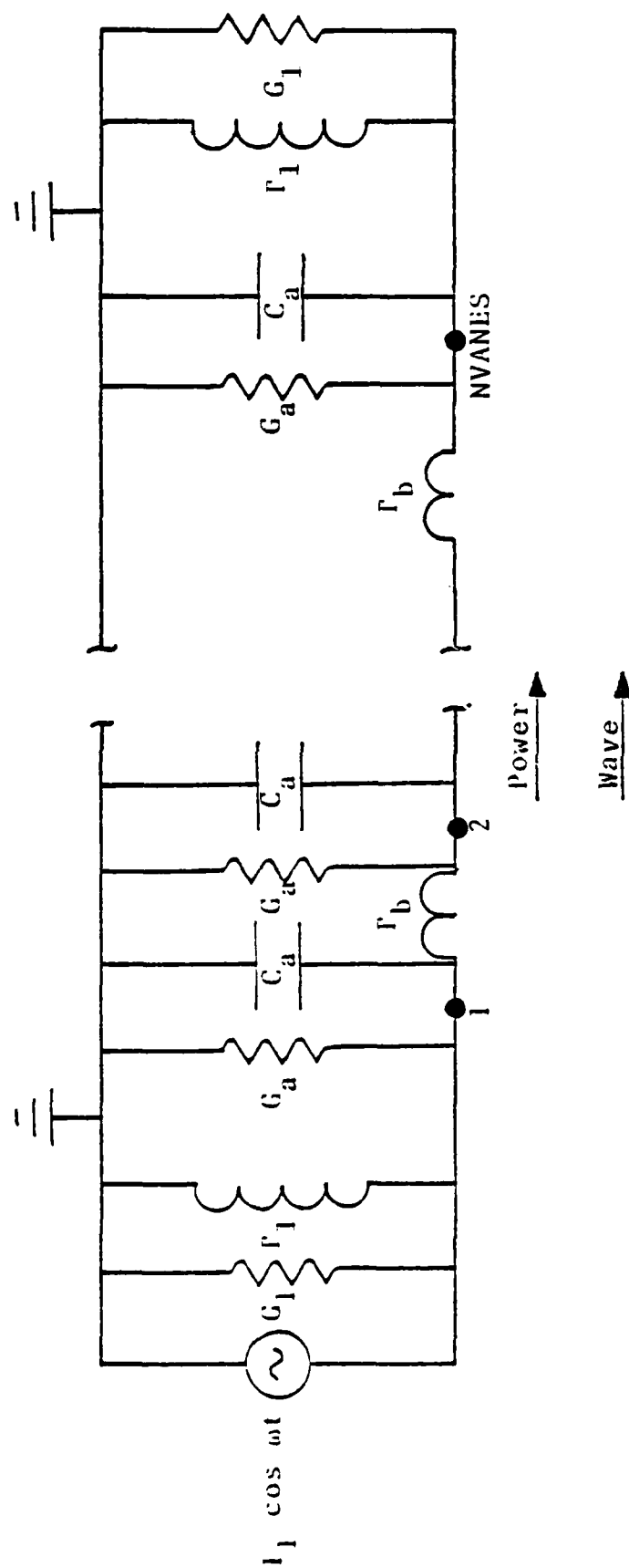


Figure 8. Simple equivalent network.

using the values of delay per section (pitch), characteristic impedance $V_1^2/(2 \times \text{power flow})$, and attenuation (dB) per pitch for a given frequency. The program also computes the matching load elements G_1 and Γ_1 , and the driving current I_1 to give a particular RF drive power.

In a backward-wave tube, the direction of beam motion is still defined as from vane 1 to vane NVANES, while the RF power flow and measured external phase delay are in the reverse direction. The form of network used is the same as in Figure 8, but three modifications are made:

1. The driving current is applied at the last vane (number NVANES in Figure 8).
2. The voltage seen by the network at the even-numbered vanes is defined as (-1) times the voltage acting on the beam. For this transformation it is necessary to separate the RF vane voltages from the modulator voltage.
3. The current induced in the even vanes, as seen by the network, is defined as (-1) times the value computed from the beam motion.

With this transformation applied to the instantaneous voltages and currents, the phase delay per pitch of each Fourier component of the wave seen by the beam equals π minus the delay seen by the network, and the directions of the waves seen by the beam and network are opposite, as required. However, the network time delay remains equal to the externally measured value, and the transient response time of the numerical solution is correct, at least at the drive frequency.

The simple network of Figure 8 has the advantage of eliminating spurious reflected signals. These appeared during trial computation with non-zero values of the admittance Y_c between alternate vanes. Harris SAI has attempted to use the general

network of Figure 7 to fit experimental values of phase delay or impedance at more than one frequency, or to fit a given value of the cutoff frequency. However, this has not proved straightforward, as there is in general no physical solution for the network elements for an arbitrary dispersion or impedance variation. At present, instead, the network of Figure 8 is used, and its elements are changed by the program as the drive frequency is changed.

D. Oscillation Conditions

The network of Figure 8 is sufficiently general to include the backward traveling wave due to reflection at the output or to the induced currents from the beam. This wave, identical to the interacting wave apart from its direction, causes feedback of power to the RF input. If the resultant power flow at the first node is in the backward direction, the value of RF drive power printed by the program is negative (Appendix I) and the network is producing an oscillation. This is not a numerical effect: the network voltages are stable and well-defined throughout the calculation. This oscillation condition occurs only when the induced RF current exceeds a threshold value, determined in turn by the RF voltage driving the charge to the anode and hence by the tube output power. Computed and measured threshold powers for oscillation are compared in Section XI, with order-of-magnitude agreement for two tubes. In the actual CFA the oscillation shows as a mode boundary and may induce spurious output signals at other frequencies.

SECTION IX

THE MODULATOR

A. Line Type and Hard Tube Modulators

Most practical distributed-emission crossed-field amplifiers are operated in pulses each covering several thousand RF periods. Two types of modulator, "line-type" or "hard-tube", are used to supply the anode-cathode voltage and the direct current during the pulse.^{1,29}

In the SFD-261 and QKS1319 forward-wave CFAs a hard-tube modulator supplies an open-circuit voltage between the pulses, and the tube is started in each pulse by applying the RF drive power. The anode-cathode voltage falls to the operating value as the anode current rises. A quench electrode removes the charge from the CFA at the end of each pulse. In the QKS1842 backward-wave CFA the anode-cathode voltage is pulsed by discharging a line-type modulator while the RF drive power is being fed through the circuit.

One purpose of the present simulations is to reproduce the anode current and RF output power under the dynamic steady-state operating conditions during a single pulse. A simple equivalent circuit is used to represent the modulator.

B. Equivalent Circuits

In Figure 9, V_{OPEN} is a constant open-circuit voltage, L and R are series inductance and resistance, and C is the CFA capacitance together with external leakage capacitance. The induced current $I_{CFA}(t)$ is obtained from the charge motion in the CFA (Appendix H). The following ordinary differential equations are solved for the voltage $V_{CFA}(t)$ seen by the

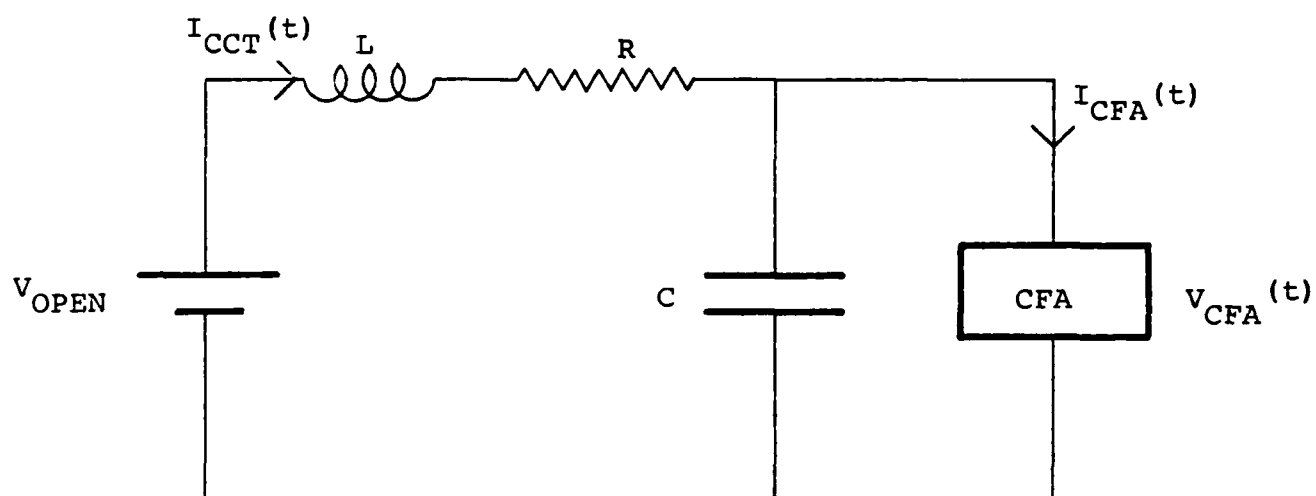


Figure 9. Equivalent circuit for the DECFA modulator.

electrons and for the current I supplied by the modulator:

$$C \frac{d V_{CFA}}{dt} = I_{CCT} - I_{CFA} \quad (1)$$

$$L \frac{d I_{CCT}}{dt} = V_{OPEN} - V_{CFA} - R I_{CCT} \quad (2)$$

Here the direct voltage V_{CFA} is treated as independent of the RF voltages on the vanes by neglecting the sum of the RF voltages at each instant (Appendix H).

C. Typical Parameters

For a hard-tube modulator, V_{OPEN} is typically about 1.1 times the mean operating voltage V_{CFA} . For a line-type modulator it is about twice the operating voltage. This value and the circuit elements L , R and C are supplied to the present program. In practice only the CFA voltage V_{CFA} and current I_{CCT} are accurately measured, as average values over the steady-state portion of a pulse.

To run a simulation the user must first estimate the desired operating voltage V_{CFA} and current I_{CCT} (given the magnetic field). Next the open-circuit voltage V_{OPEN} is chosen for the modulator type. The resistance R is then derived for a steady state using Equation 2 with $d I_{CCT}/dt = 0$. Table 5 shows the values used in present runs.

Using typical tube values (e.g. $L = 1.0 \times 10^{-4}$ H, $R = 1421 \Omega$, and $C = 1.0 \times 10^{-10}$ F on the QKS1842) give characteristic times, L/R and RC , for decay of transients that are unacceptably long for the computer simulation. (These times are about 1400 RF periods, a fraction 0.08 of the pulse length of 1.7 ns in the QKS1842 and fourteen times the length of a typical run.)

TABLE 5

MODULATOR DATA USED FOR DECFA SIMULATION

Tube	Type of Modulator	Voltage (V) (Measured values)	Current (A) (Measured values)	Open-Circuit voltage (V)	Resistance (Ω) (Values supplied to model)		Capacitance (F)	Inductance (H)	Voltage (V) (Computed results)	Current (A) (Computed results)
QEC1842 High-power mode	Line	21,800	49.0	44,000	458		3.65×10^{-12}	0.0	27,900	35.2
	Line	24,300	17.1	48,600	1421		3.65×10^{-12}	0.0	23,100	17.9
SFD-261	Hard Tube	$1.3V_1$ (normalized)	22.0	$1.45V_1$	$6.8 \times 10^{-1} V_1$		$1.93 \times 10^{-7} D_1$	0.0	$1.26V_1$	27.0
QEC1119	Hard Tube	10,200	20.0	11,000	40		1.52×10^{-11}	0.0	9,520	37.0

Therefore the inductance and capacitance must be chosen arbitrarily by the user. Present simulations use zero inductance and use for C the capacitance of the cylinders that form the anode and cathode of the CFA (ignoring the detailed structure of the vanes).

With the line-type modulator in the QKS1842 the CFA voltage starts at its full open-circuit value instead of at zero as in the actual tube. Hence transient values of the current and power appear on the computed curves for the first 50 RF periods. The alternative procedure is to choose a small but nonzero inductance, and to start V_{CFA} at or near zero. This should give an accelerated simulation of the starting phenomena.

D. Stabilizing Effect of the Load Line

Both the measured and the computed values of current and voltage in Table 5 satisfy the constraint of Equation 2 with $d I_{CCT}/dt = 0$. This constraint serves to stabilize the calculation. In earlier simulations without the modulator the current and RF power could rise indefinitely at a fixed anode voltage. However, the modulator reacts by reducing the voltage if the current exceeds the mean operating value.

The present modulator model is applicable also to studies over a frequency band, when the modulator setting is fixed and only the drive frequency varies. The computed current and voltage should adjust automatically for best synchronism. Of course, the correct RF-circuit phase velocity and impedance must be provided for each frequency used.

SECTION X

DESCRIPTION OF THE NUMERICAL SOLUTION

The major elements of the calculation are shown in the flow diagram, Figure 10. The following are the principal steps in advancing the particle coordinates and the RF and direct voltages by one time step, Δt . Auxiliary computations not listed here provide output information such as the Fourier components of the vane voltages and currents, and the time-averaged anode current, cathode emission, electron bombardment power on the electrodes, and the RF output power.

1. Compute the cathode emission at each secondary-emitting site using the available charge, the local electric field, and the coordinates of the charge in the anode-sole region (see Section V).

2. Place the emitted charge on the cathode surface with a user-chosen initial energy (normally 2eV).

3. For each particle in the anode-cathode region:

- (a) Store the coordinates (r, θ) in arrays RP and THP. The velocity $(dr/dt, d\theta/dt)$ is already in arrays VRP and VTP. Advance the position by one time step. Use the local electric field from arrays ERDBP and ETDBP which contain the components $(E_r/B, E_\theta/B)$, where B is the magnetic field.
- (b) Test for interception on the anode and cathode. If the particle has intercepted the cathode, recompute its final velocity using a smaller time step to obtain an accurate impact energy. Evaluate the local secondary charge produced.

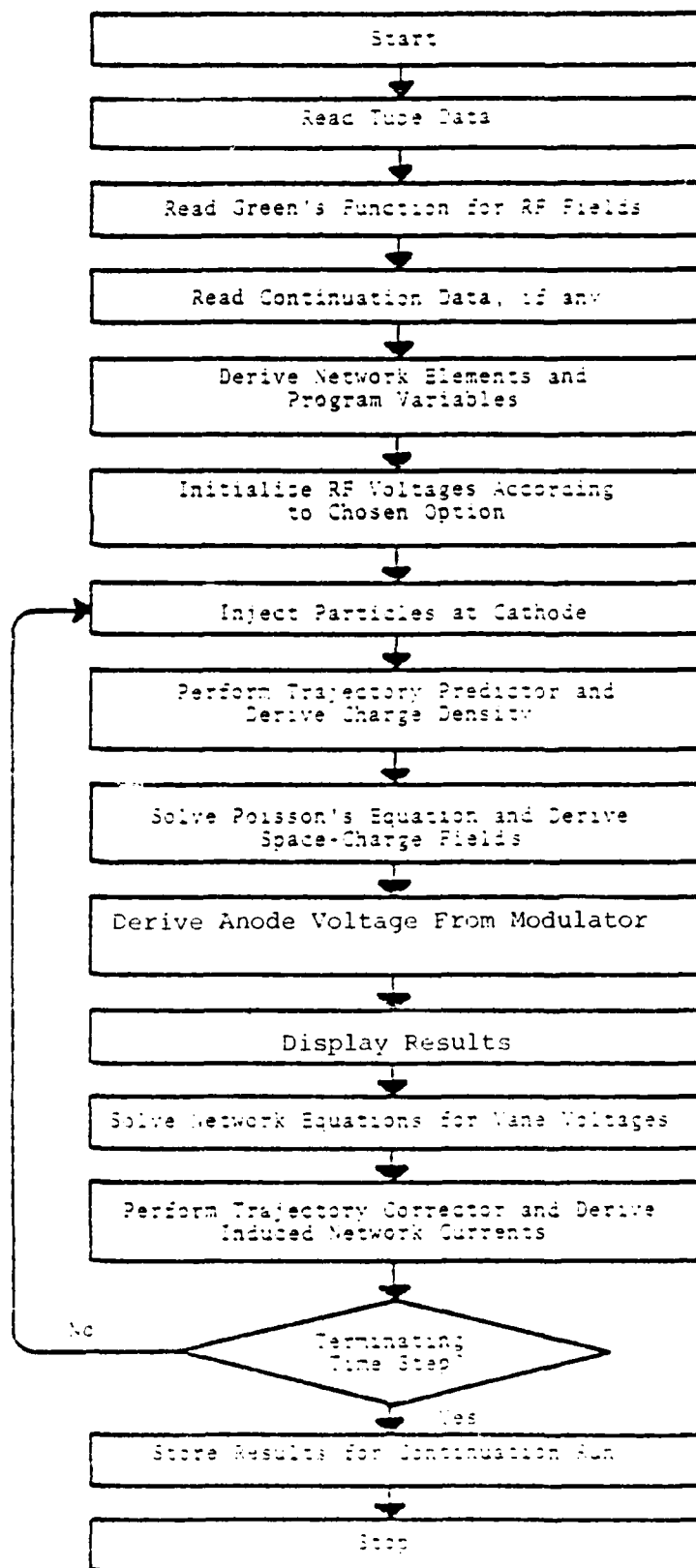


Figure 10. General flow chart for DECFA analysis program.

(c) For charges not intercepted, store the predicted position (r, θ) for time $t + \Delta t$ in arrays R and TH, and increment the induced direct current. Also assign the local space-charge density to array WVSC.

4. Solve Poisson's equation for the space-charge potential in the same array WVSC (actually normalized to avoid machine overflow).

5. Derive the electric-field components over the space-charge mesh in arrays ERSC and ETSC, which contain the components $(E_r/B, E_\theta/B)$.

6. Store the radial space-charge electric field at the cathode and one mesh interval above the cathode to control the emission in the next step, using array SCCAT. This array, but not the full space-charge-field array, is included in the continuation data file used to run a simulation in several stages.

7. Derive the convection currents and electrode impact powers. Store the induced direct current at time $t + \Delta t$ in the scalar CURCCT.

8. Advance the anode voltage VAVARY and the modulator current DCTOT from time t to time $t + \Delta t$ using the induced current CURCCT in a predictor-corrector computation.

9. The RF network equations are advanced in NCSTEP time steps subdividing the main time step Δt . The following steps are performed to advance the vane voltages V_n ($1 \leq n \leq NVANES$) and their derivatives dV_n/dt (arrays VVRF and DVRF) by one such intermediate step.

(a) Advance the voltage V_n and its derivative dV_n/dt in the predictor step.

- (b) For the network currents, obtain the derivatives dI_n/dt at vane n using the stored values for I_n at times t , $t - \Delta t$, $t - 2\Delta t$, and $t - 3\Delta t$ (arrays CURIND, CURP, CURPP and CURPPP). Here the value of dI_n/dt at time $t + (NC/NCSTEP)\Delta t$ ($1 \leq NC \leq NCSTEP$) is obtained by polynomial extrapolation.
- (c) Obtain the second derivative d^2V_n/dt^2 from the network matrix equation (Appendix I). Apply the corrector to obtain dV_n/dt and V_n .

10. For a backward-wave amplifier, change the sign of the RF voltage on the even-numbered vanes to obtain the voltage seen by the beam (in array VVBMD as V_n/B).

11. For each particle in the anode-cathode region:

- (a) Evaluate the local electric field (direct, RF, and space-charge components) in temporary scalars ERDBA and ETDBA, using the predicted position (r, θ) at time $t + \Delta t$.
- (b) Average this field with the field stored in arrays ERDBP and ETDBP from time t (before the predictor step).
- (c) Advance the trajectory again using arrays RP, THP, VRP and VTP, repeating the predictor step but with the newly averaged electric field. No test for interception is necessary since most intercepted particles have already been eliminated. Any further interception is computed in the succeeding time step.
- (d) Recompute the local electric field at the "corrected" position and simultaneously compute the induced current I_n on each vane (array CURINB). Store the final position, velocity and electric field in

arrays R, TH, VR, VT, ERDBP and ETDBP for
time $t + \Delta t$.

12. For the backward-wave tube, change the signs of
the RF induced current on the even vanes to obtain the current
(array CURIND) seen by the network.

13. If more time steps are required, return to stage 1
for the next step.

SECTION XI

RESULTS OF THE SIMULATIONS

The distributed-emission CFA program has been applied to study three existing tubes, and the results are described here. The corresponding experimental data are in Appendices B-D for the Raytheon QKS1842 backward-wave tube and for the Varian SFD-261 and the Raytheon QKS1319 forward-wave tubes. There is reasonable agreement between the computations and the measurements. The numerical results are summarized in Table 6 and more details are given below.

A. QKS1842 Backward-Wave CFA

Typical charge distributions in the QKS1842 backward-wave amplifier are shown in Figures 11 and 12. The cylindrical anode-cathode region is displayed for convenience as two rectangular plots, from angle 0 to π radians and π to 2π radians around the tube. The RF output is at an angular position of 0 radians and the sever region at the input end, near 2π radians. In the actual calculation the charge distribution is of course continuous. The electron stream moves from left to right, close to synchronism with the interacting space harmonic of the RF wave, but in the opposite direction to the power flow in this backward-wave amplifier.

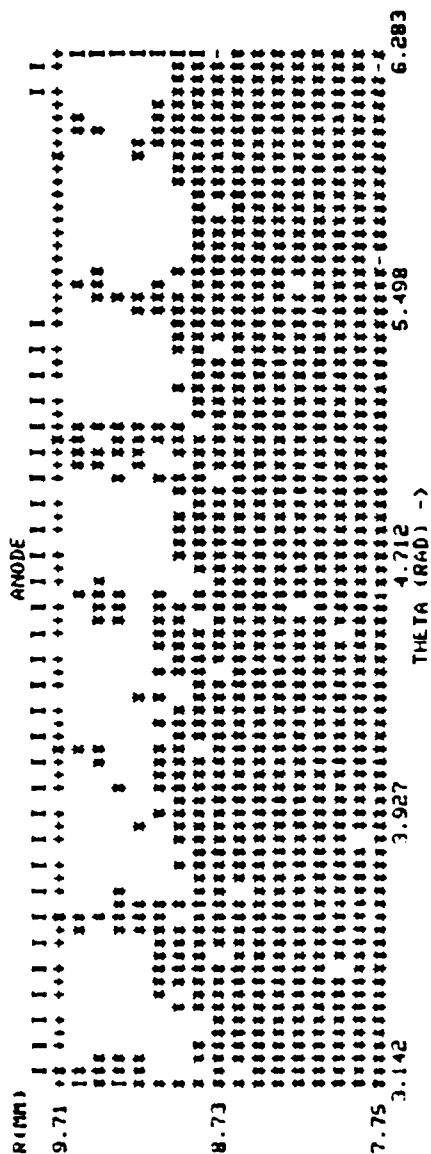
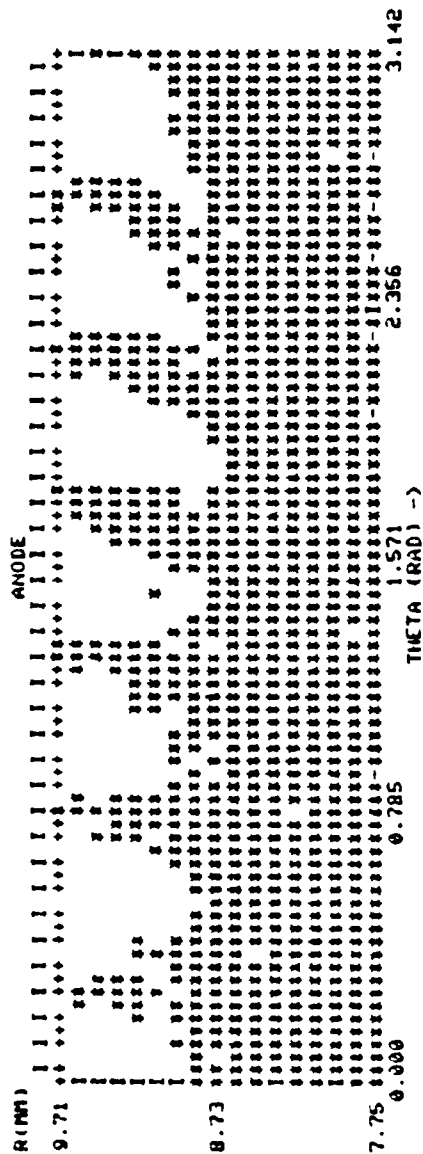
There are two distinct modes of operation. The charge hub covering most of the cathode and the distinct charge spokes near the anode (Figure 11) form as expected in the high-power mode. However, at power levels of about 168 kW, as in normal tube operation, the beam develops an irregular lumped charge distribution (Figure 12). The high-power mode was achieved in practice with a more highly emitting cathode (gold and

TABLE 6
COMPUTED AND MEASURED RESULTS FOR THREE
DISTRIBUTED-EMISSION CROSSED-FIELD AMPLIFIERS

Tube	Magnetic Field (P)		Voltage (V)		Current (A)		RF Output Power (W)		Note
	Mode	Measured	Computed	Measured	Computed	Measured	Computed	Measured	
OKS1842 (backward-wave; high power mode)	.377	.377	27,900	21,300	35.2	35.2	398,000	400,000	1
QKS1342 (backward-wave; low power mode)	.395	.378 .411	23,100	22,200 25,500	17.9	15.0 17.1	126,000	124,000 175,000	
5FD-261 (forward-wave)	.253	.253	1.088V ₁ (normalized)	1.16V ₁ 1.20V ₁	8.4	5.2 8.4	0.65P ₀	0.4P ₀ 0.69P ₀	1
	.2606	.253	1.29V ₁	1.30V ₁	23.5	22.0	2.33P ₀	1.65P ₀	2
QKS1319 (forward-wave)	.1150	.1150	9,520	10,200	37.0	20.0	286,000	111,000	
	.1300		10,100		22.4		111,000		2

Notes: 1. Measured values interpolated to fit computed current.
2. Magnetic field set above measured value.

CHARGE DISTRIBUTION AFTER STEP 1440



These two linear sections depict the continuous cylindrical anode and cathode of the model.

Figure 11. Beam profile computed in QKS1842 high-power mode.

CHARGE DISTRIBUTION AFTER STEP 1584

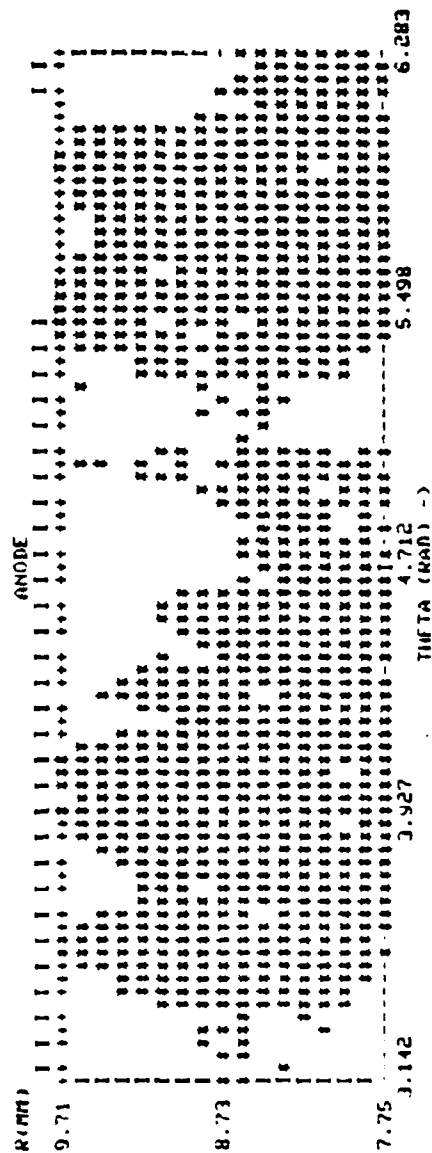
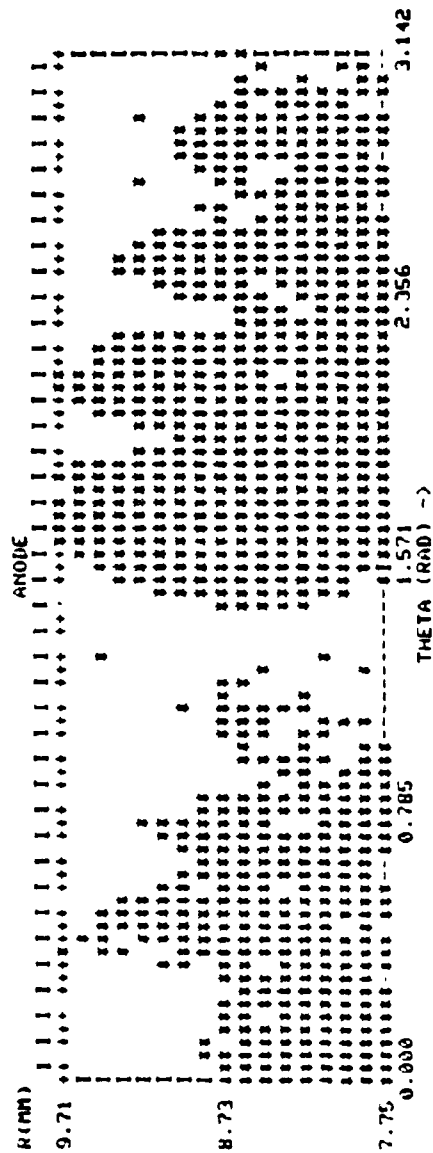


Figure 12(a). Beam profiles computed in QKS1842 low-power mode.

CHARGE DISTRIBUTION AFTER STEP 4000

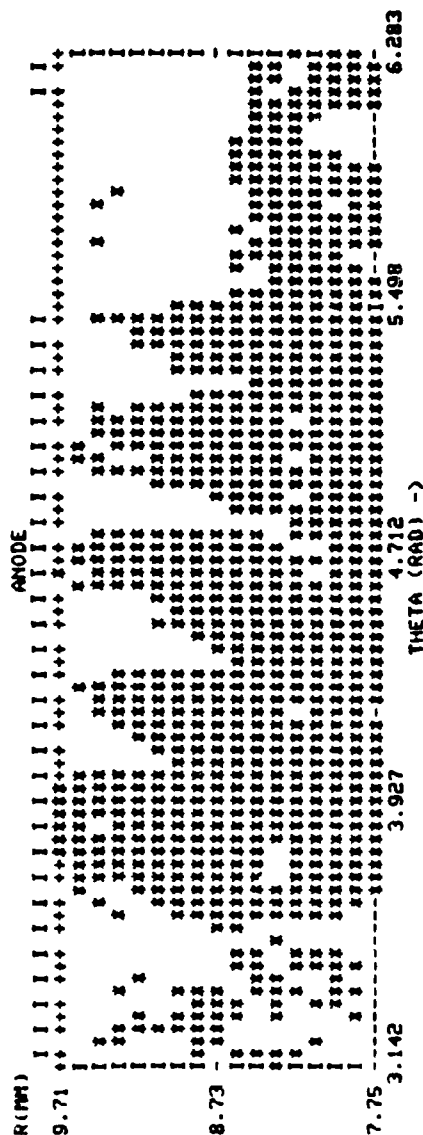
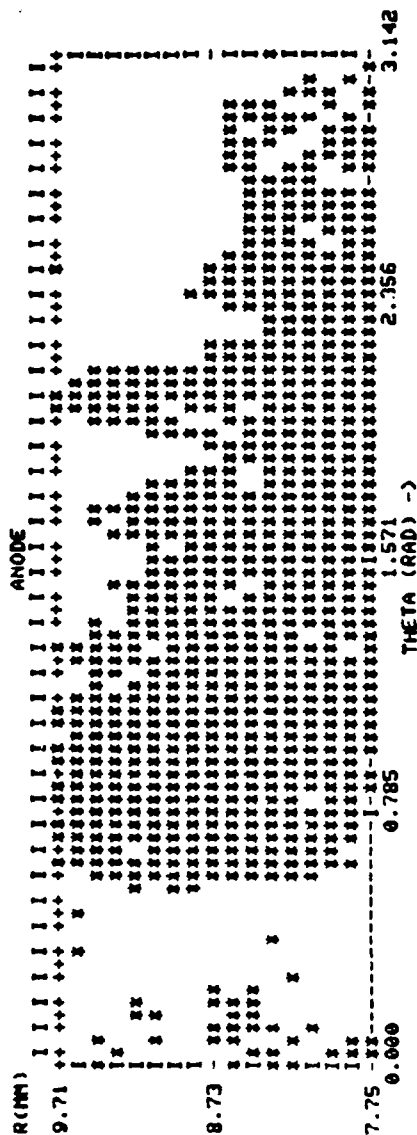


Figure 12(b). Beam profiles computed in QKS1842 low-power mode.

magnesium oxide) than the cermet or platinum surface normally used. The RF drive power was raised from 5.5 kW to 19 kW to suppress oscillations and the magnetic field lowered. RF powers up to 500 kW were obtained at about 50 percent efficiency, compared with only 168 kW at 39 percent efficiency in the low-power mode. The existence of these two modes was unexpected before these simulations were performed. They provide an explanation for design problems encountered in the QKS1842 tube, such as delayed starting and high cathode heating.

Previous simulations without the modulator have consistently shown these two types of mode. When the spokes of charge develop they transfer to the RF field a high instantaneous power ranging between 168 kW and 770 kW. The irregular groups of charge deliver only about 150 kW or less. Figure 13 is a further example, where the beam is transferring only 44 kW to the wave. These groups show a tendency to break into spokes near to the anode, suggesting that the same cold RF-network wave is being amplified in both cases.

Apparently in the low-power mode the spokes of charge develop intermittently and then coalesce at irregular intervals.

1. High-Power Mode

Numerical results for the high-power mode are summarized in Figure 14 and Table 7.

The modulator open-circuit voltage of 44,000 V and short resistance of 458 Ω are chosen so that the load line passes through the operating point of 48 A at 22,000 V. In fact in all three cases a higher voltage (e.g. 27,900 V) and lower current (e.g. 35 A) develop in the simulation. The measured magnetic field of 0.377 T was obtained using a solenoid calibration

CHARGE DISTRIBUTION AFTER STEP 400

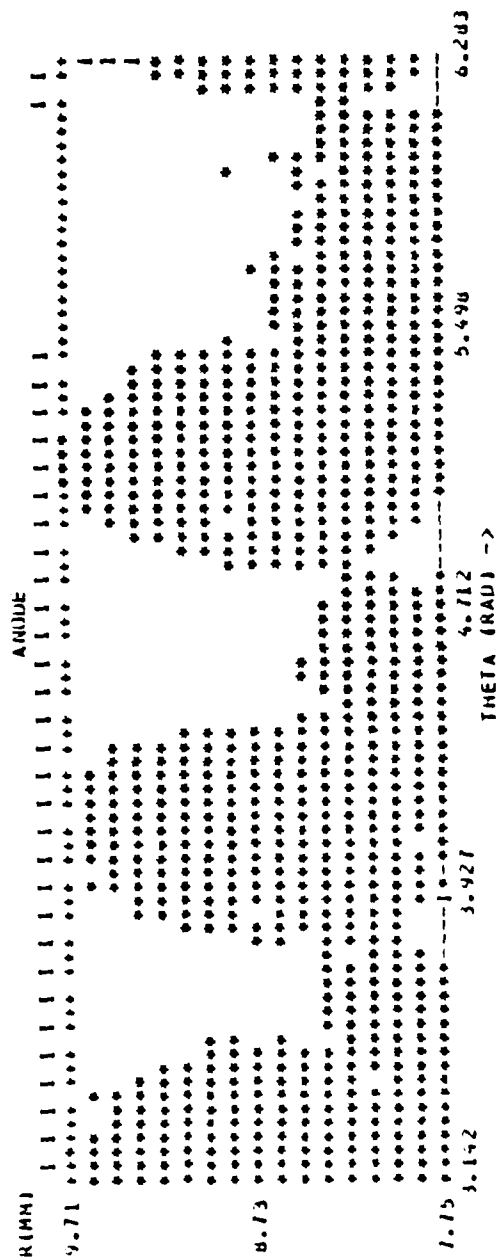
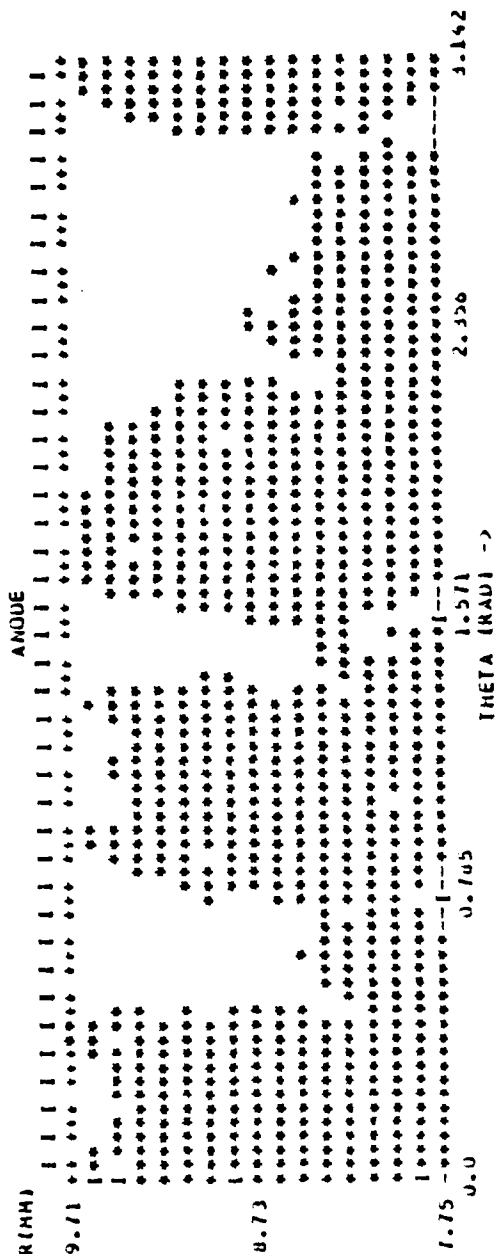


Figure 13. Irregular charge distribution computed in QKS1842 with unsmoothed secondary emission and 9,576 interacting particles.

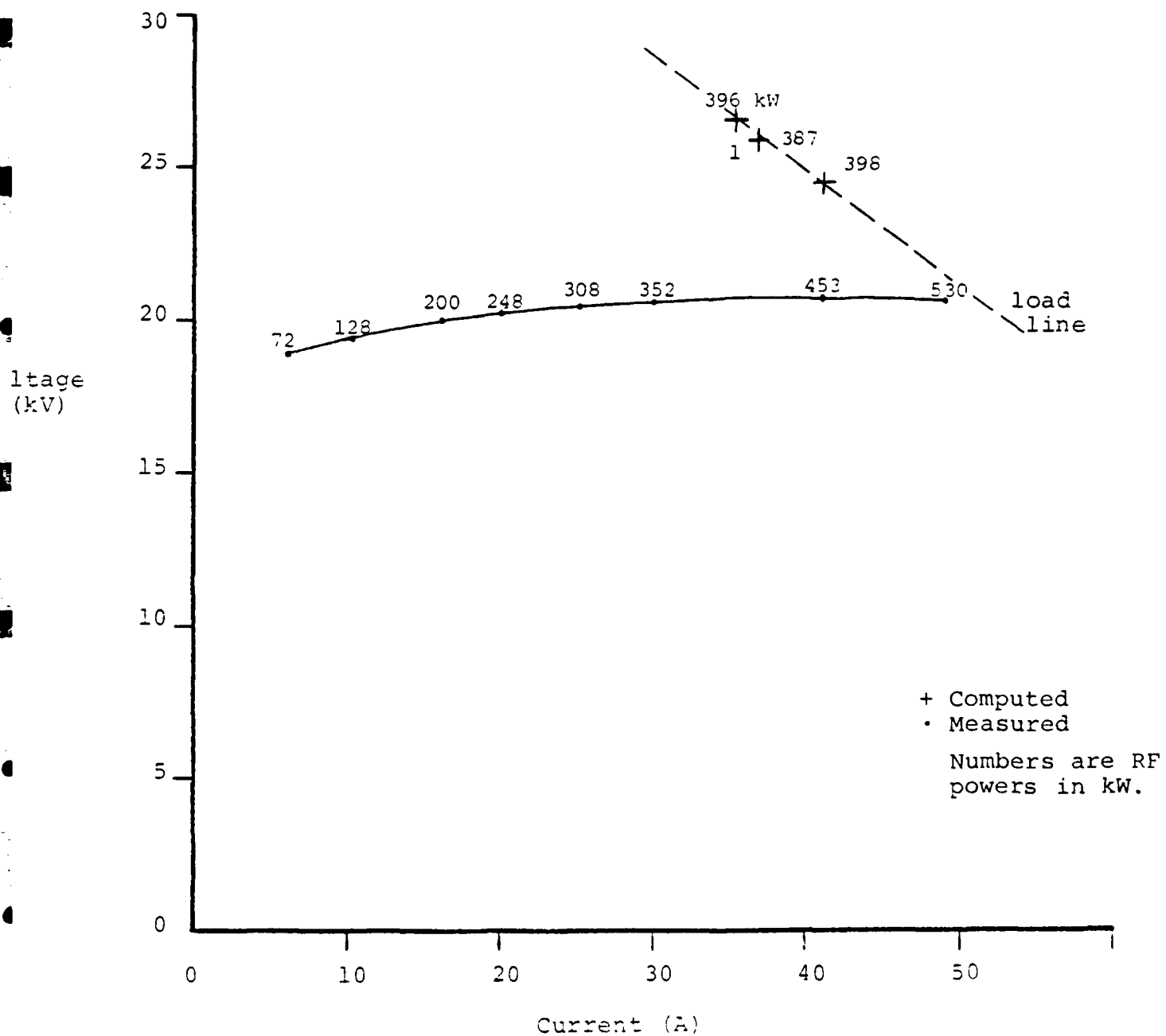


Figure 14. Computed and measured results for QKS1842 backward-wave amplifier in high-power mode.

TABLE 7

COMPUTED AND MEASURED RESULTS FOR
QKS1842 BACKWARD-WAVE AMPLIFIER IN HIGH-POWER MODE

Points on Figure	Measured or Computed	Magnetic Field (G)	Voltage (V)	Current (A)	RF Drive Power (W)	RF Output Power (W)	Anode Dissipation (W)	Cathode			Error in Power Balance (% increase)	Notes
								Back bombard- ment Power (W)	Average Secondary Emission Coefficient	Average Cathode Impact Energy (eV)		
Curve	Measured values	0.375 throughout	18,000	6	19,000	72,000						Gold and
			19,000	10	19,000	128,000						Magnesium
			20,200	16	19,000	200,000						Oxide Cathode
			20,600	20	19,000	248,000						(high emission)
			21,000	25	19,000	308,000						
			21,200	30	19,000	352,000						
1	Run 42078; Per loads 45-50	.377	21,700	41	19,000	453,000						Gold and
			21,800	40	19,000	530,000						Magnesium Oxide Cathode
			27,900	35.2	19,000	396,000	422,000	44,700	1.16	203	-12.2	Gold and Magnesium Oxide Cathode
2	Run 52080; Per loads 61-75	.377	25,192	41.1	19,000	398,000	485,000	131,300	1.17	533	0.2	Cermet cathode (lower emission)
3	Run 12079; Per loads 63-92	.3625	27,180	36.7	19,000	387,000	525,000	50,200	1.17	237	-3.52	Magnetic field set 4% below measured value. Gold and Magnesium Oxide Cathode.

made without the CFA and is believed to be correct. Reducing the magnetic field by four percent (point 3) reduces the voltage by only 2.6 percent to 27,180 V.

The RF output power is displayed as a function of time in Figure 15. The "1-period mean" is the fundamental Fourier component from a single RF period. The "15-period" mean is the moving average covering one transit time around the tube for the cold-circuit backward wave. The high transient power at the start is due to the open-circuit modulator voltage. After this power has been dissipated in the external load terminating the network, a dynamic equilibrium develops. The fluctuations are apparently due to the reverse-directed circuit wave. They appear in both forward-wave and backward-wave tubes.

The corresponding current delivered by the modulator (Figure 16) is almost constant. This external current has been smoothed by the shunt capacitance of the CFA. Counting the actual charges emitted and collected by the cathode gives a net current that fluctuates between 26 A and 44 A. However, over 15 RF periods the average values from these two alternative current calculations agree to within 1.3 percent.

The upper lineprinter plots of Figure 17 show the RF power at each of the 35 active vanes, averaged over the preceding 15 RF periods. The standing-wave pattern towards the output (vanes 1-18) is due to the reflected wave. With a higher output power or a lower RF drive power the tube would approach oscillation.

The lower plot of Figure 17 shows the phase lag of the induced current from the peak voltage on each vane, again averaged over 15 periods. At vane 1 (RF output) the induced circuit current and the RF voltage are 117° out of phase because the beam contains spokes of charge recirculating after passing the drift region (beyond vane 35). Clearly the modulation fed through on the beam is appreciable (see also Figure 11).

RUN NO. 42079

○ 1-PERIOD MEAN

△ 15-PERIOD MEAN

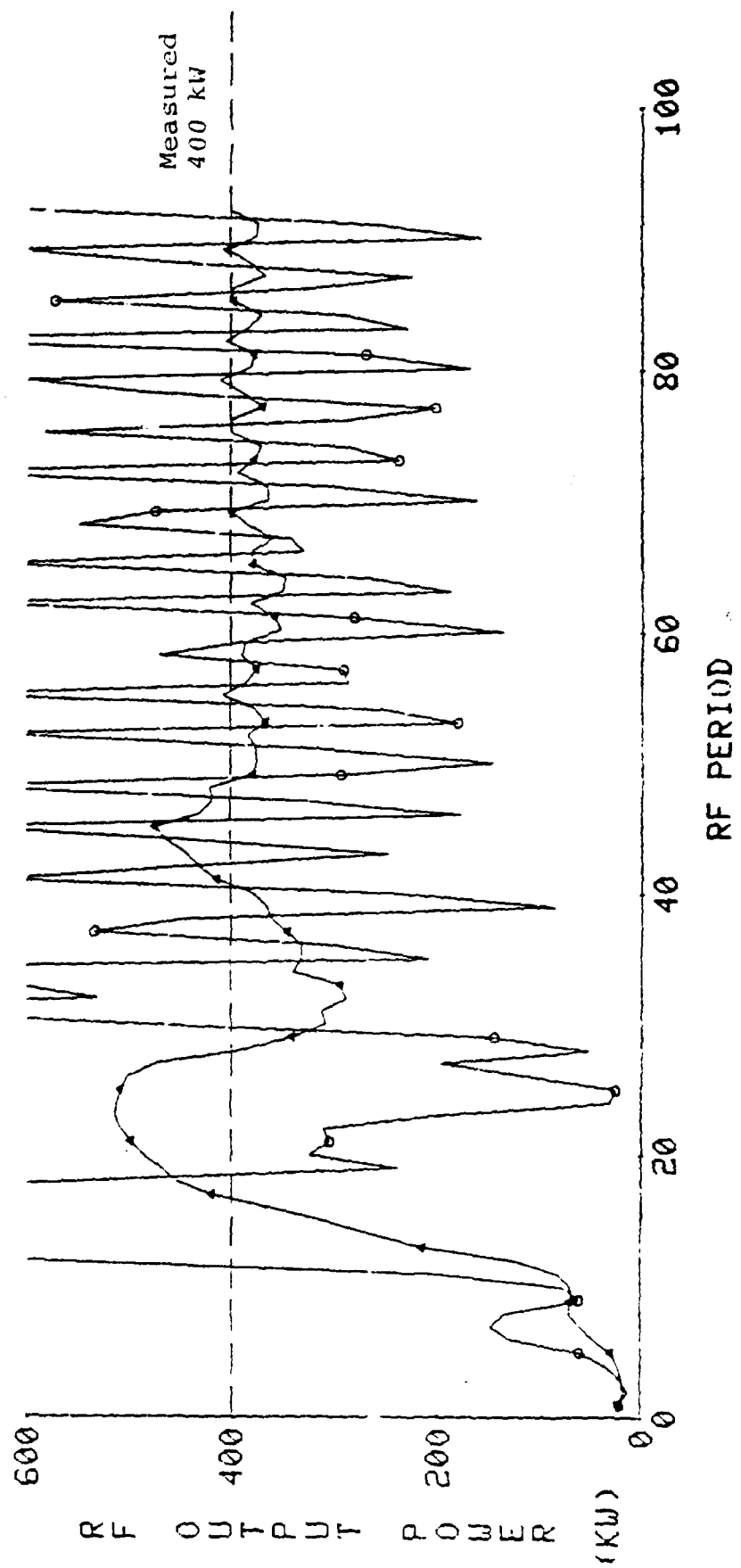


Figure 15. RF output power computed over 91 RF periods in OKS1842 high-power mode

READY

RUN NO. 42079

○ 1-PERIOD MEAN

△ 15-PERIOD MEAN

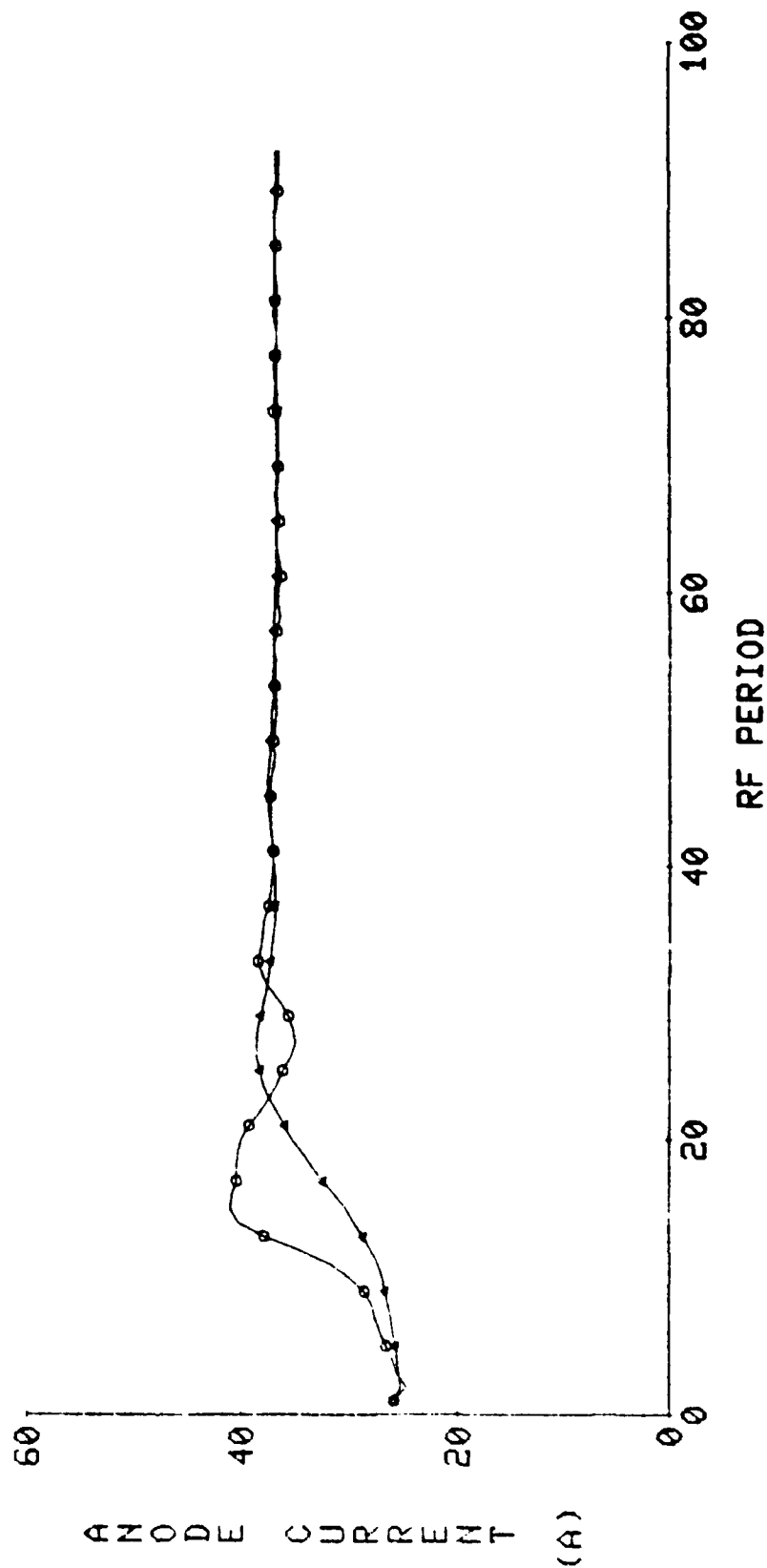
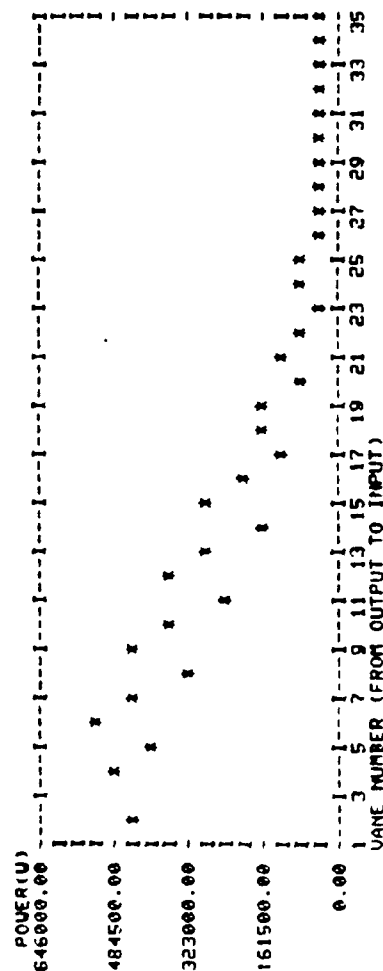


Figure 16. Anode current computed over 92 RF periods in the QKS1842 high-power mode.

RF POWER DISTRIBUTION AFTER 90.0 RF PERIODS



RF CURRENT PHASE LAG FROM CIRCUIT VOLTAGE AT DRIVE FREQUENCY AFTER 90.0 RF PERIODS

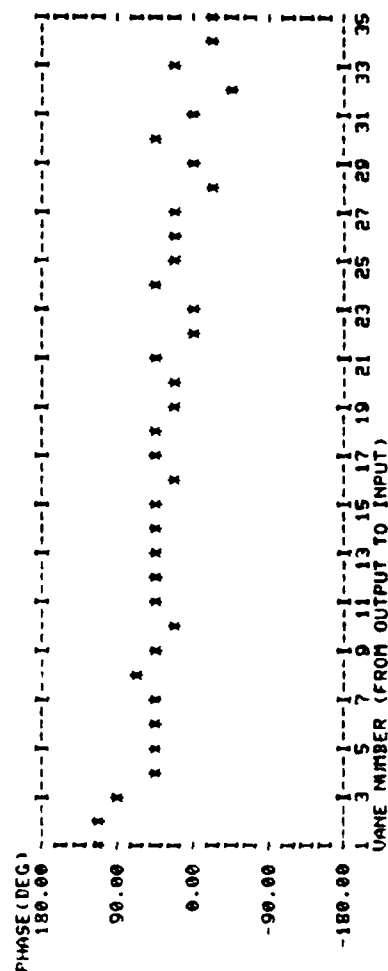


Figure 17. RF power and phase computed around the QKS1842 in the high-power mode.

In this cylindrical model the anode-cathode region seen by the beam is continuous. In the rectangular model,¹¹ the recirculating rods must be shifted in phase to make the transit time of the interaction region an integer multiple of the RF period. No such correction is needed here because the entire RF network is viewed at every time step.

2. Low-Power Mode

In this mode the RF output power fluctuates because of the irregular beam shape (Figure 18), while the anode current is almost constant (Figure 19). The numerical results (Table 8 and Figure 20) are well within the range of the measurements especially as the magnetic field is known only within about 5 percent.

The peaks of the RF power, such as at period 138, correspond to formation of the spoke mode of charge distribution. The spokes appear only intermittently in the charge distributions displayed by the program. For most of the run the particles form an irregular pattern such as in Figure 12.

3. Results at Constant Voltage

Before the modulator circuit was included in the model the anode voltage was fixed and the anode current was unconstrained. The plotted power and current of Figures 21 and 22 demonstrate clearly the "runaway" effect that can be caused by even a small numerical error. Excess charge driven to the anode leads in turn to higher RF fields. The modulator, however, acts by reducing the direct voltage to oppose growth of the current.

B. SFD-261 Forward-Wave CFA

This tube was selected for study because of the experimental data available for instrumented tubes, and for comparison of

RUN NO. 42077

○ 1-PERIOD MEAN

△ 15-PERIOD MEAN

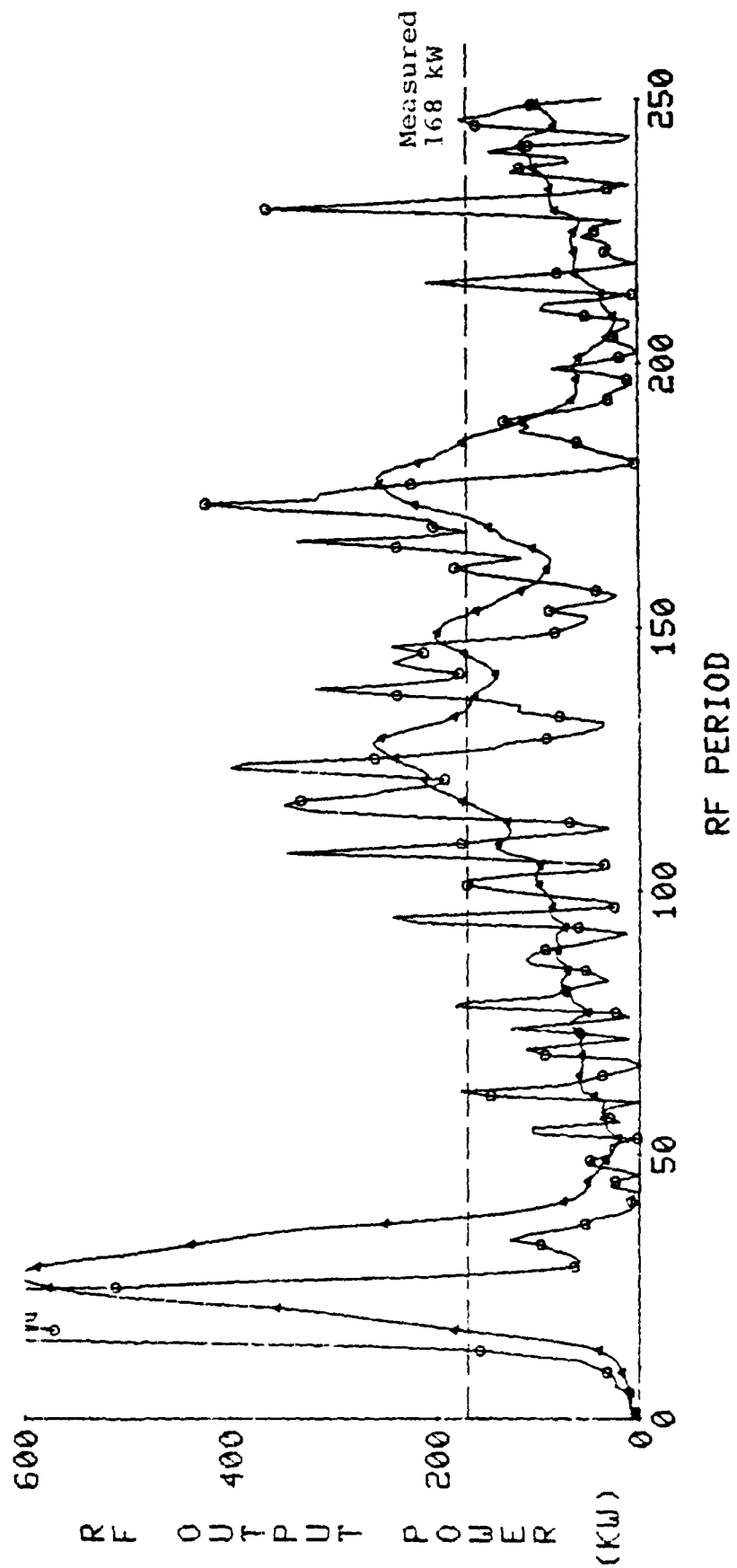


Figure 18. RF output power computed over 250 periods in QKS1842 low-power mode.

READY

RUN NO. 42077

○ 1-PERIOD MEAN

△ 15-PERIOD MEAN

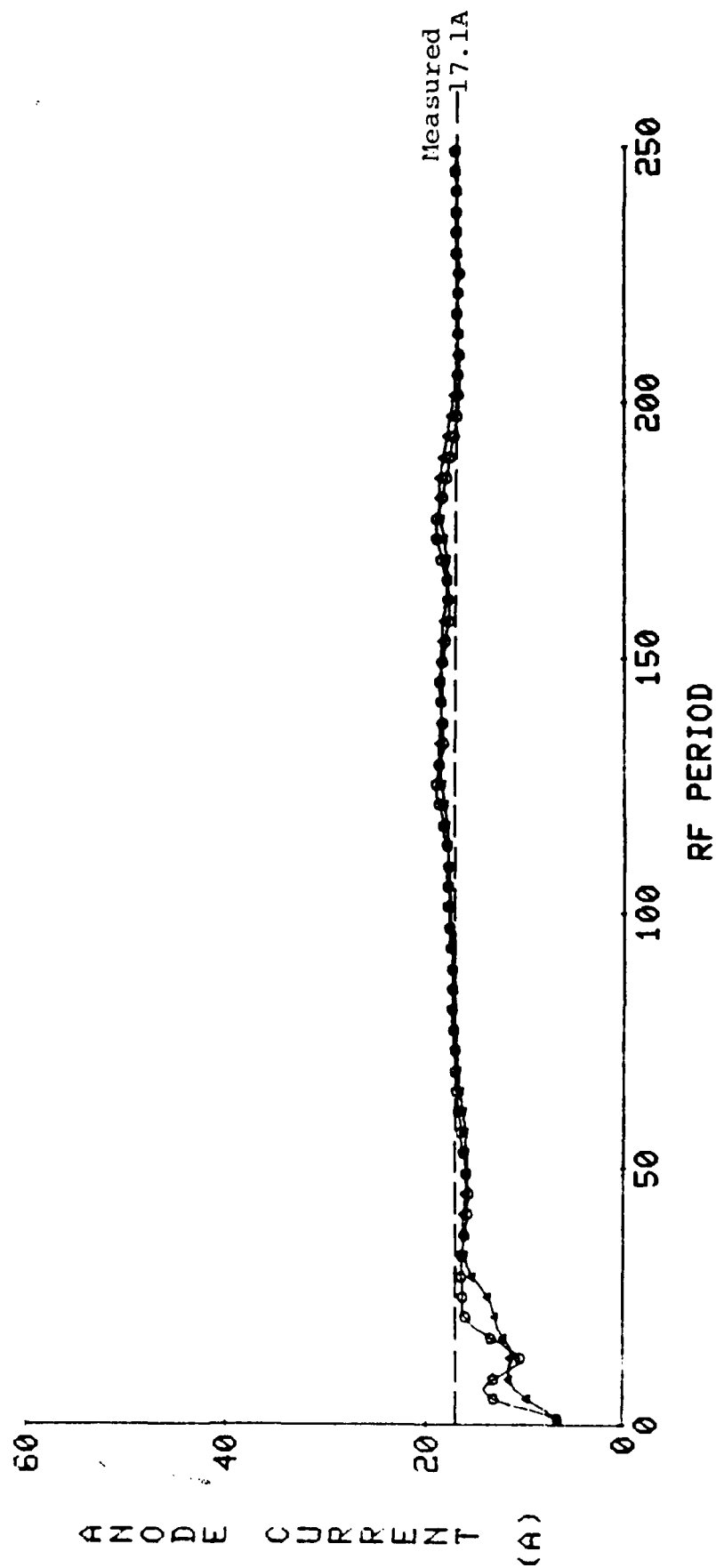


Figure 19. Anode current computed over 250 periods in QKS1842 low-power mode.

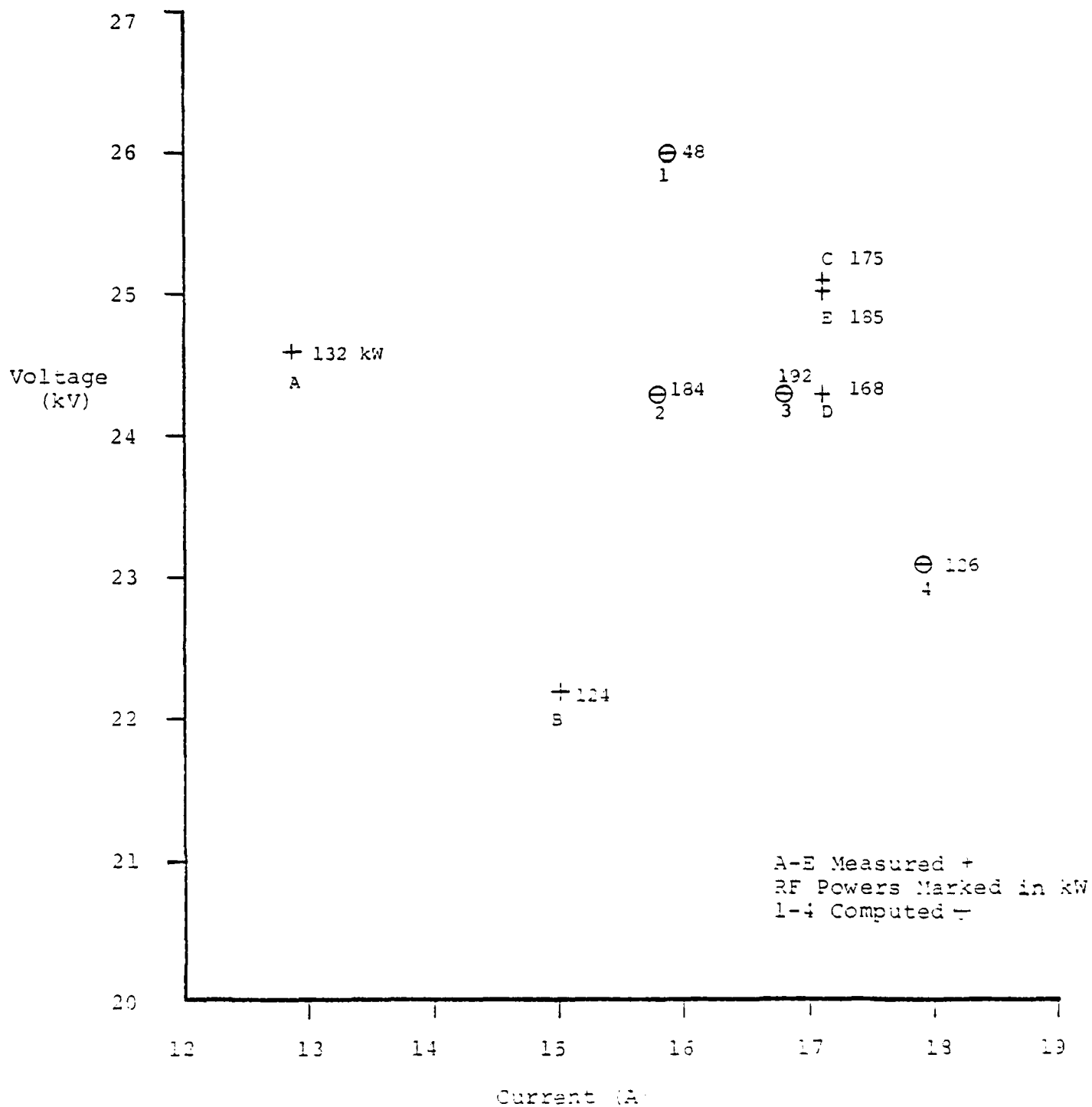


Figure 20. Computed and measured results for QKS1842 backward-wave amplifier in low-power mode.

RUN NO. 42053

○ 1-PERIOD MEAN

△ 15-PERIOD MEAN

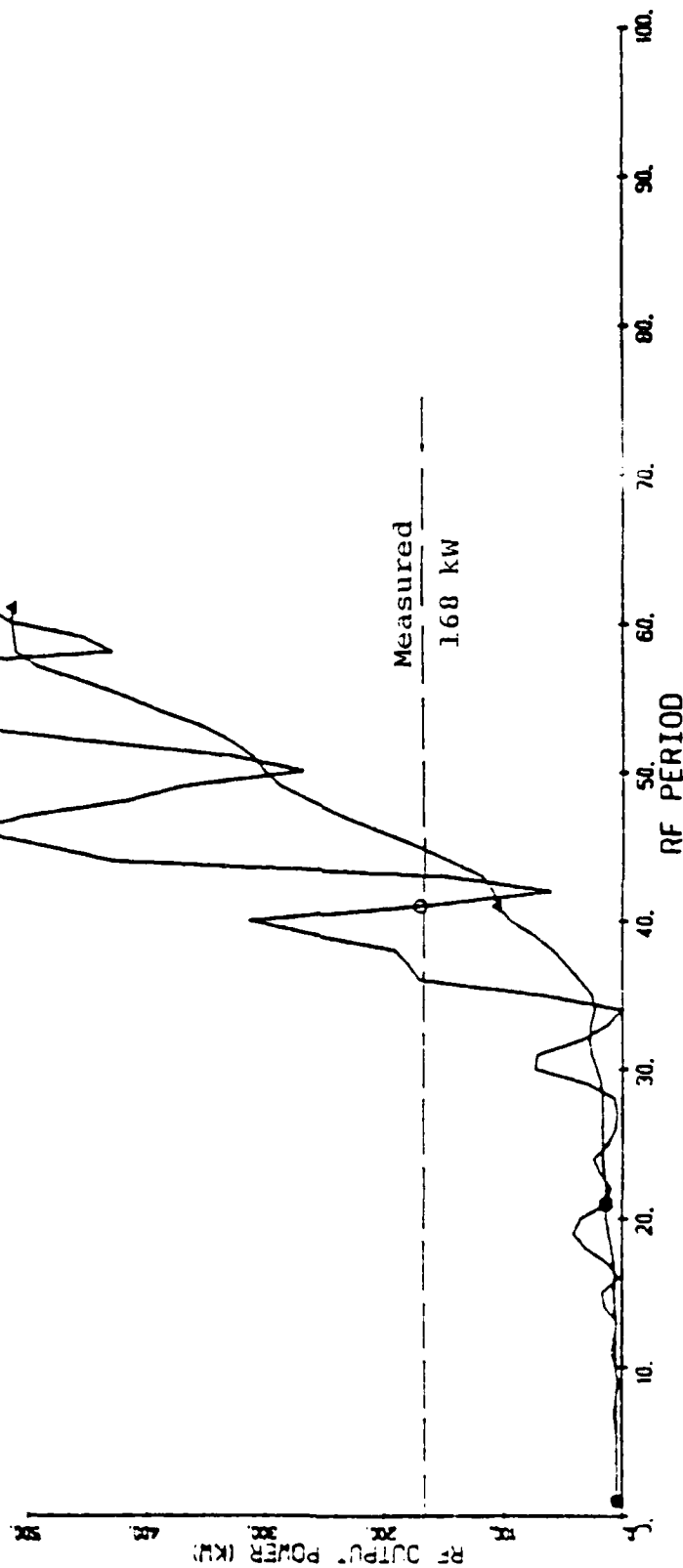


Figure 21. RF output power computed in the QKS1842 CFA at 24.3 kV and 0.4114 T with 10,000-rod model and full secondary emission. Demonstrate runaway effect in absence of modulator.

RUN NO. 42053

○ 1-PERIOD MEAN
 ▲ 15-PERIOD MEAN

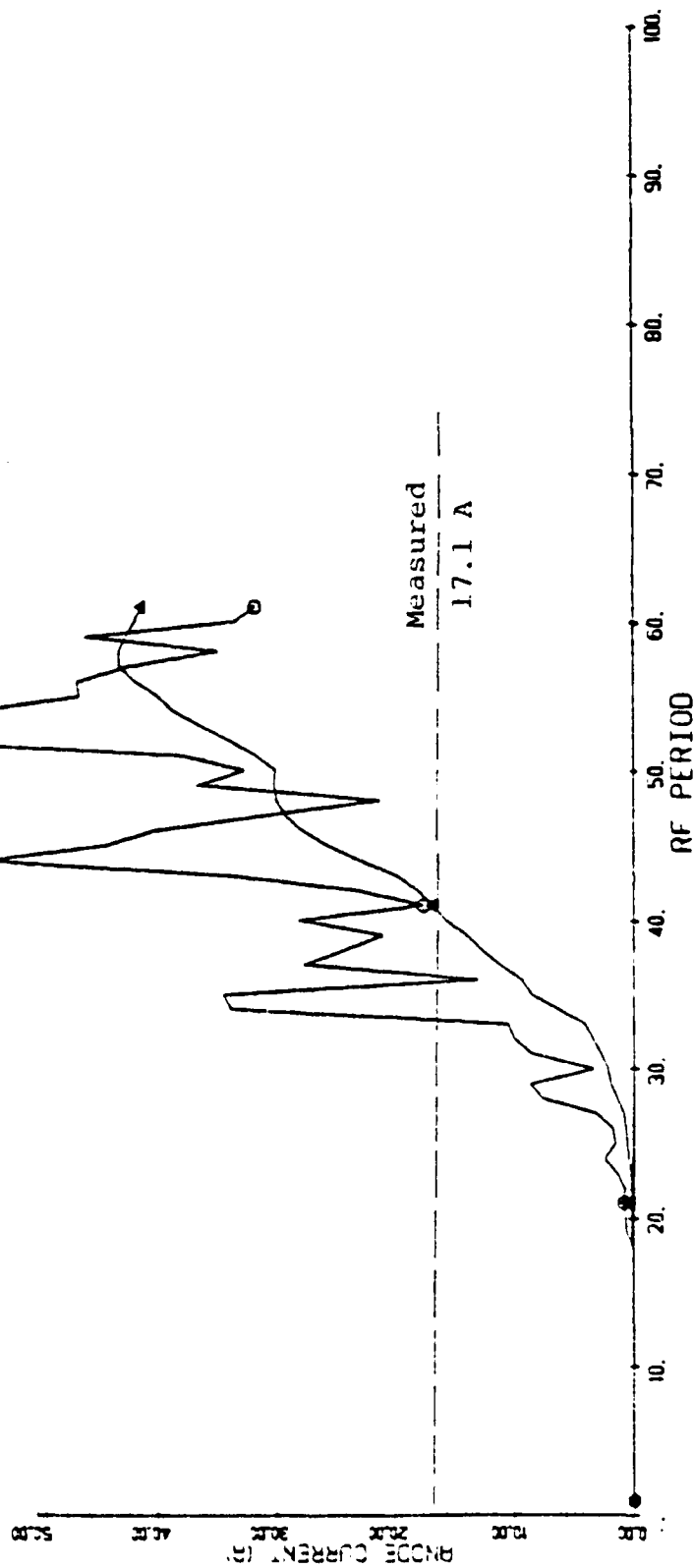


Figure 22. Anode current computed in the QKS1842 CFA at 24.3 kV and 0.4114 T with 10,000-rod model and full secondary emission. Demonstrate runaway effect in absence of modulator.

TABLE 8

COMPUTED AND MEASURED RESULTS FOR
QKS1842 BACKWARD-WAVE AMPLIFIER IN LOW-POWER MODE

Points on Figure	Measured or Computed	Magnetic Field (T)	Voltage (V)	Current (A)	RF Drive Power (W)	RF Output Power (W)	Anode Dissipation (W)	Cathode Back- bombard- ment Power (W)	Average Secondary Emission Coefficient	Average Cathode Impact Energy (eV)	Error in Power Balance (% increase)	Notes
Between												
A	Measured	.398 and .44	24,600	12.9	5,500	132,000						Tube A10; Platinum cathode (lower emission)
B	Measured	.3778	22,200	15.0	5,500	124,000						Tube 3C; Cermet cathode (higher emission)
C	Measured	.4115	25,500	17.1	5,500	175,000	about 195,000	about 60,300				Cermet cathode Tube 8A; Cermet cathode
D	Measured	.4114	24,300	17.1	5,500	168,000						Tube 3C; cathode not known
E	Measured	0.4 to 0.444	25,000	17.1	5,500	185,000						Cermet cathode; Variable anode voltage
1	Run 42076; Periods 106 to 150	.4114	25,950	15.9	5,500	48,000	197,000	143,000	1.07	607	-7.0	Cermet cathode
2	Run 42045; Periods 121-150	0.444	24,600	15.8	5,500	184,000	125,800	75,500	1.055	287	-2.3	Cermet cathode
3	Run 42044; Periods 120-149	0.444	24,600	16.8	5,500	192,000	134,800	78,300	1.087	430	-3.3	Platinum cathode
4	Run 42077; Periods 116 to 250	.395	23,800	22.0	5,500	117,000	249,000	162,000	1.09	409	-0.2	Cermet cathode; Variable anode voltage

the present computed results with those of Varian Associates.¹¹

The computed currents and powers are higher than measured, as Figure 23 and Table 9 show. The Varian computer program has predicted an output power of $1.4 P_0$ at an anode current of 17.7 A, compared with the measured $1.65 P_0$ at 22 A (Point C, on Figure 23). These values are averaged over five passes around the CFA. The Varian results for a single pass vary between $1.33 P_0$ at 16.3 A to $1.53 P_0$ at 19.1 A. They lie above the measured V-I curve while the present results lie below it. Increasing the magnetic field by 3 percent (the limit of experimental error) reduces the computed current from 27.0 A to 23.5 A but the output power of $2.33 P_0$ is still above the measured $1.65 P_0$.

As in the QKS1842 simulations, the modulator constrains a dynamic steady state. Figures 24 and 25 show the evolution of a simulation over time. The transit time per pass around the tube with the cold RF phase velocity is about 18 RF periods, so that $5\frac{1}{2}$ passes are covered here.

The instantaneous charge distribution (Figure 26) shows that the spokes of charge formed in the RF field are passed through the drift space and cause anode bombardment even in the region of low RF power, the first 20 vanes. In experimental tubes the anode vane temperature is observed to peak near vane 40 (3.5 radians from the input) when the cathode is mechanically centered. Moving the cathode closer to the anode at the RF input shifts the peak temperature back to vane 27 of the instrumented tube. Future simulations will display both the RF power and the anode heating on each vane.

Varian Associates have concluded that amplification in the SFD-261 is due first to collection of recirculated charge near

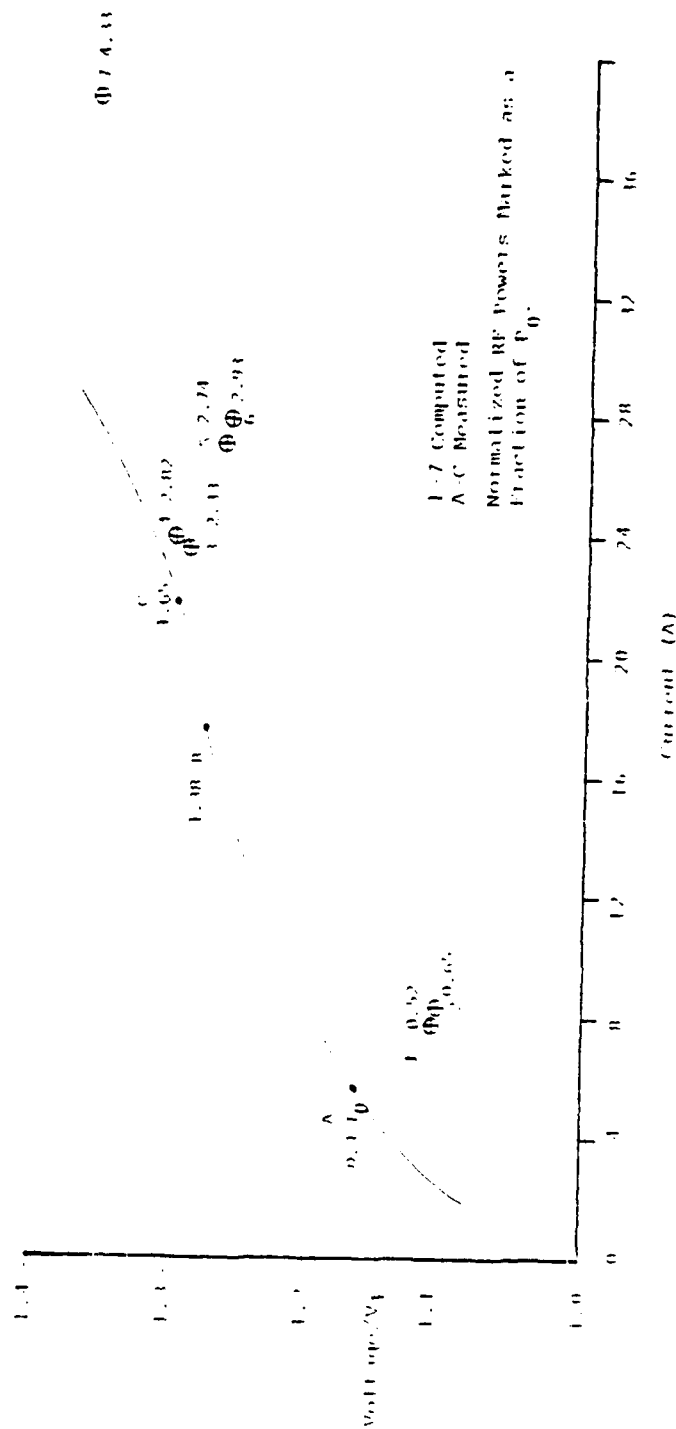


Figure 23. Computed and measured results for SFD-261 forward-wave amplifier. Modulator included in model.

RUN NO. 23029

○ 1-PERIOD MEAN

△ 18-PERIOD MEAN

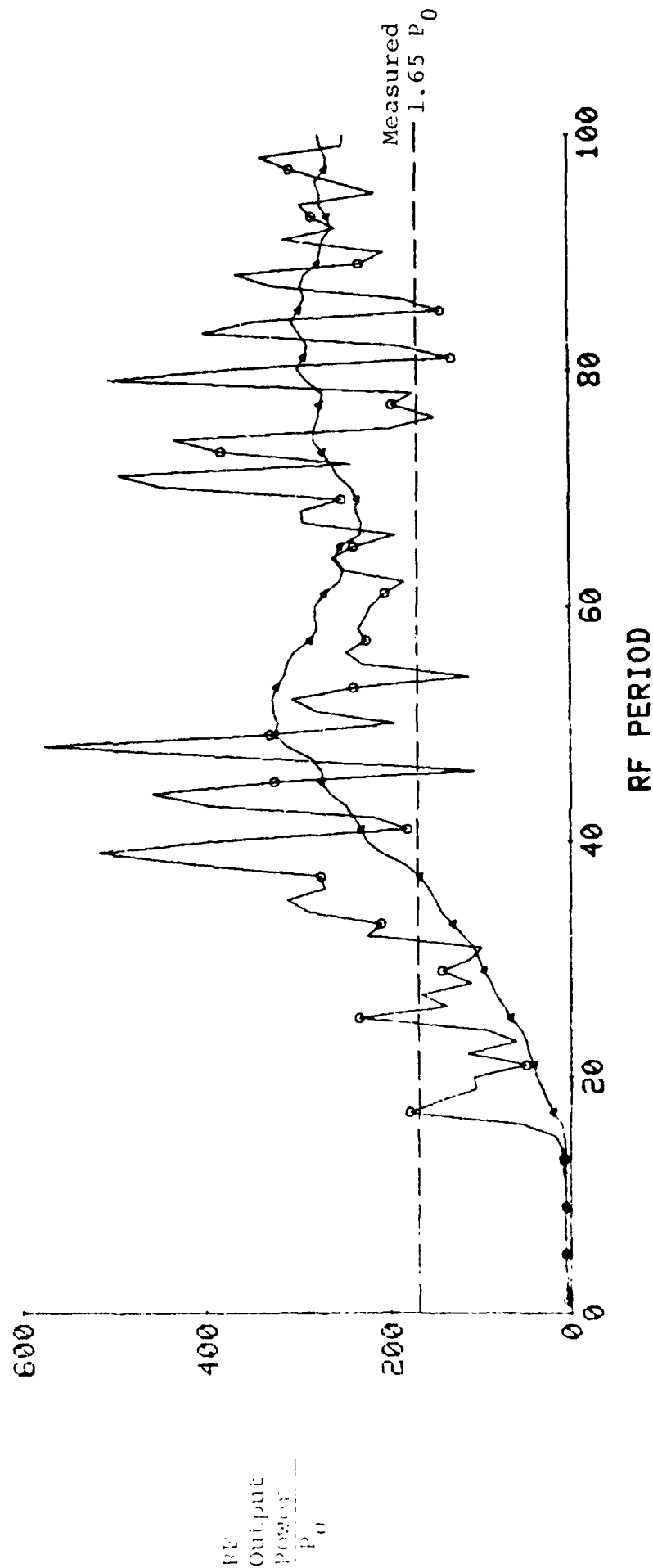


Figure 2A. RF output power computed in SFD-261 forward-wave CFA. Modulator included in mode 1.

RUN NO. 23029

○ 1-PERIOD MEAN

△ 18-PERIOD MEAN

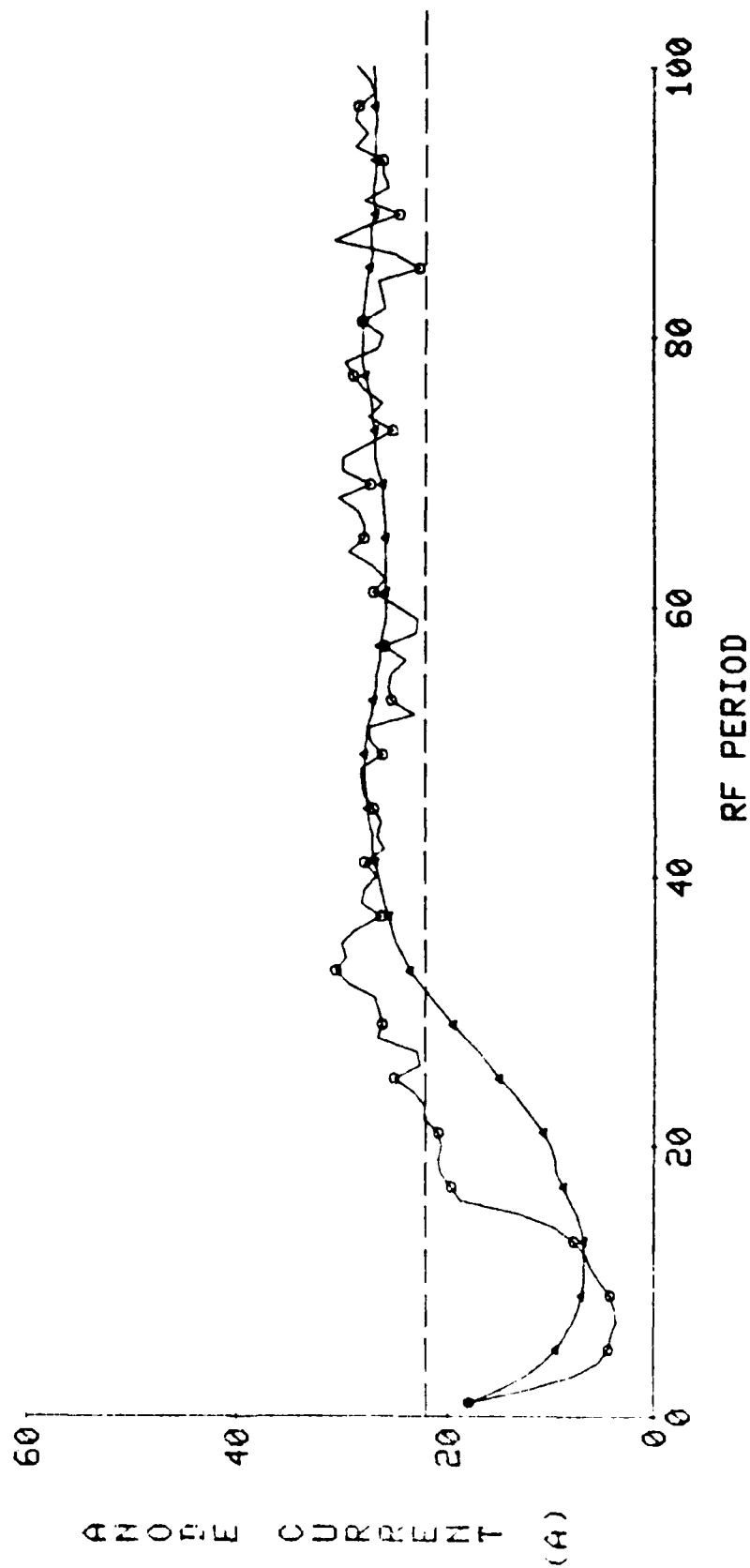


Figure 25. Anode current computed in SFD-261 forward-wave CFA. Modulator included in model.

AD-A125 340

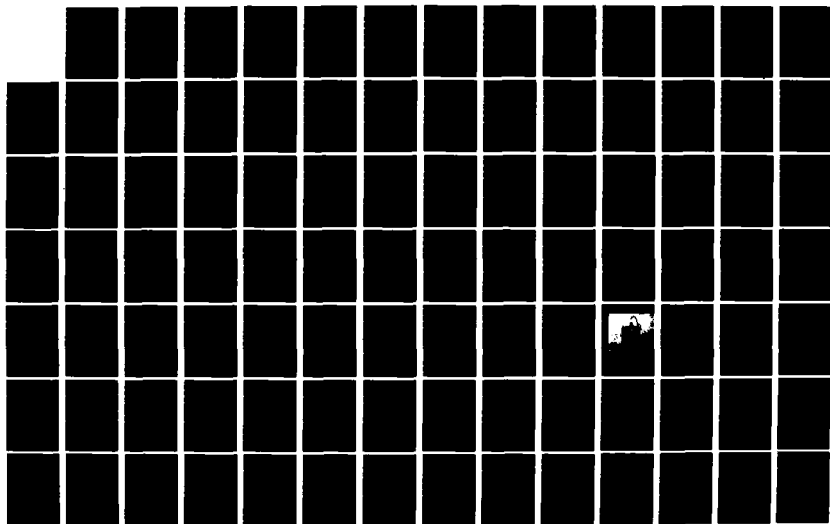
SIMULATION OF DISTRIBUTED-EMISSION AND INJECTED-BEAM
CROSSED-FIELD AMPLIF. (U) HARRIS SAI INC ANN ARBOR MI
D M MACGREGOR ET AL. APR 80 AFOSR-TR-80-0554
F49620-77-C-0091

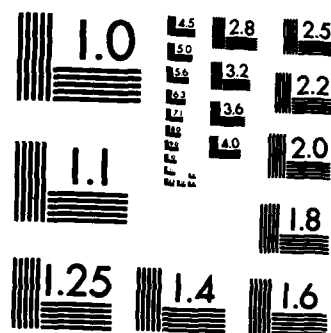
2/3

UNCLASSIFIED

.F/G 9/1

NL





MICROCOPY RESOLUTION TEST CHART
NATIONAL BUREAU OF STANDARDS-1963-A

CHARGE DISTRIBUTION AFTER STEP 1600

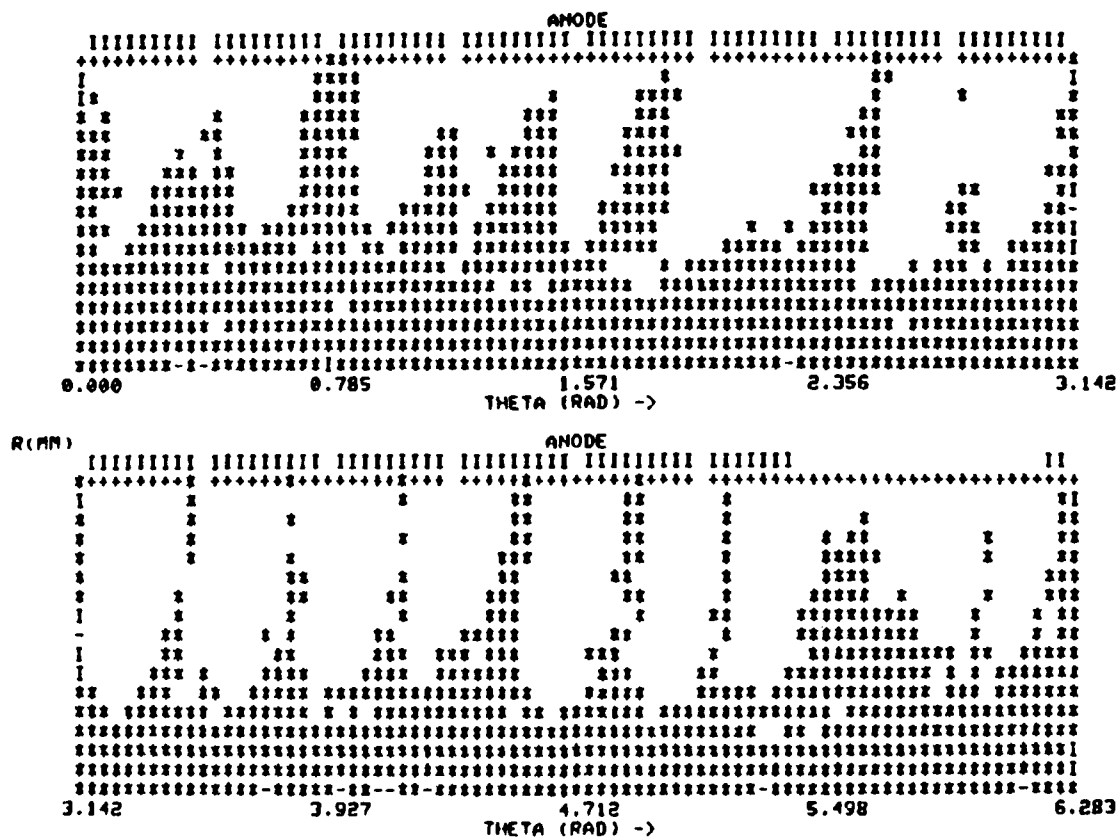


Figure 26. Beam profile computed in SFD-261 forward-wave DECFA.

TABLE 9

COMPUTED AND MEASURED RESULTS FOR
SFD-261 FORWARD-WAVE AMPLIFIER

Points on Figure	Measured or Computed	Magnetic Field (T)	Voltage V_L	Current (A)	RF		Anode Dissipation P_0	Cathode Back bombard- ment Power P_0		Average Secondary Emission Coefficient	Average Cathode Impact Energy (eV)	Error in Power Balance (% increase)	Notes
					Drive Power P_0	Output Power P_0							
A	Measured	.253	1.16	5.2	0.08	0.4							
B	Measured	.253	1.28	18.0	0.08	1.38							
C	Measured	.253	1.30	22.0	0.08	1.65							
1	Run #23031; Periods 57-74	.2606	1.102	7.76	0.08	0.52							Magnetic field set 3 percent above measured value
2	Run #23030; Periods 45-62	.253	1.088	8.4	0.08	0.65	0.47	0.06	1.14	107	19.0		Low-power point
3	Run #23028; Periods 83-100	.2606	1.29	23.51	0.08	2.33	1.65	0.123	1.28	137	32.0		Magnetic field set 3 percent above measured value
4	Run #20010; Periods 32-48	.2530	1.3	23.9	0.08	2.82	1.19	0.083			28.0		Fixed anode voltage; thermionic cathode
5	Run #23029; Periods 47-100	.2530	1.264	27.0	0.08	2.74	1.82	0.116	1.35	139	34.0		Medium-power point
6	Run #23033; Periods 33-50	.2530	1.260	27.9	0.08	2.93							11,400 rods and 513 x 33 space- charge array to double resolution of run #23029
7	Run #23032; Periods 52-87	.2606	1.359	38.6	0.08	4.33	3.08	0.154	1.45	165	42.0		High-power point; closest to emission limit.

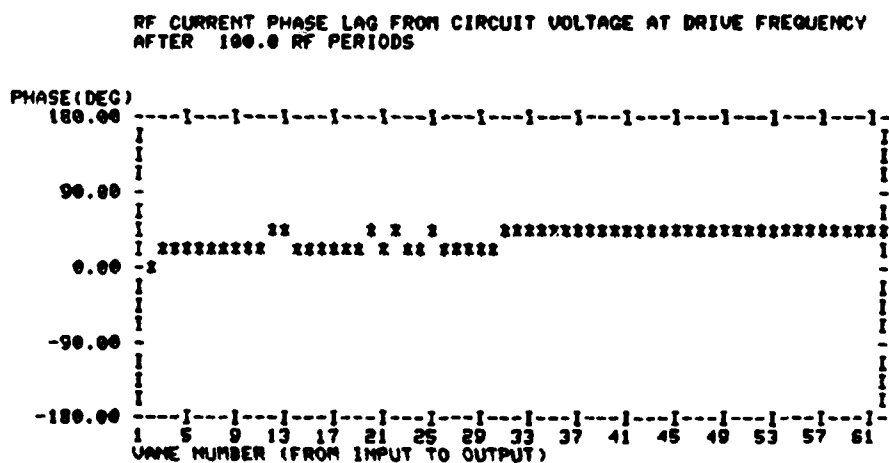
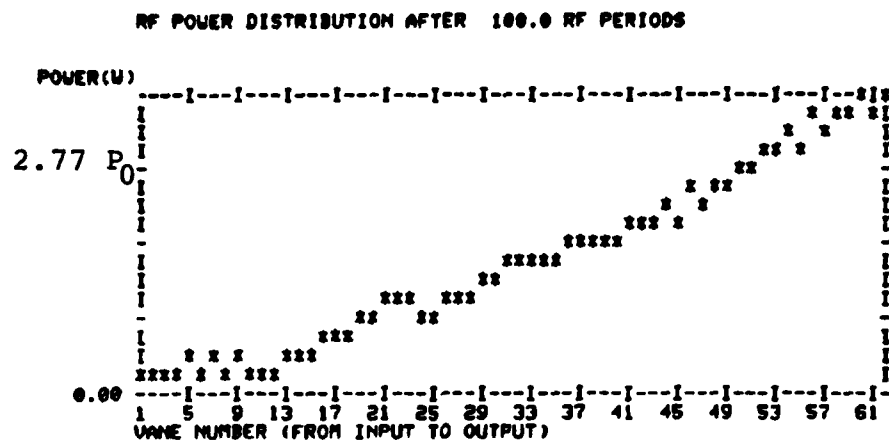
the RF input and then to the current extracted directly from the hub.¹¹ However, it is difficult to distinguish these two regions in the present calculations, perhaps because of the limits of the numerical accuracy. In fact Figure 27, which shows the RF power and phase distributions over the 62 vanes, predicts a more rapid rise over the first half of the circuit than measured (see Figure 18, p. 58 of ref. 10).

As the output power is raised, the measured V-I curve bends upwards and the tube becomes more noisy. Point 7 on the extreme right of Figure 23 was obtained in an attempt to reproduce this behavior. Here the cathode is believed to be emission-limited, and unable to supply sufficient current by secondary emission. The actual limit of current measured can be as high as 40 A at the low end of the frequency band, but depends on the cathode in the particular tube under study. The most significant feature here (see Table 9) is the computed mean impact energy and effective secondary-emission coefficient, both of which are higher than at the lower currents in the other runs. Apparently there is a reduced charge density near the cathode as more of the emitted charge is pulled towards the anode, and hence less charge is available to produce secondaries and maintain the beam.

C. QKS1319 Forward-Wave CFA

This tube, which has not previously been simulated by computer, has, of all the tubes studied, the highest ratio of RF voltage to anode voltage (a range of 0.12 to 0.65) and the lowest ratio of anode voltage to cutoff voltage (only 0.33). A typical beam profile (Figure 28) shows distinct but uneven charge spokes and a narrow hub of charge.

The cathode does not emit secondary charge for the final 1/9th of its circumference, but sufficient charge is generated



***** RESULTS ARE SAVED TO CONTINUE RUN 23029 AFTER STEP 1600 *****

Figure 27. RF power and phase computed around the SFD-261 DECFA.

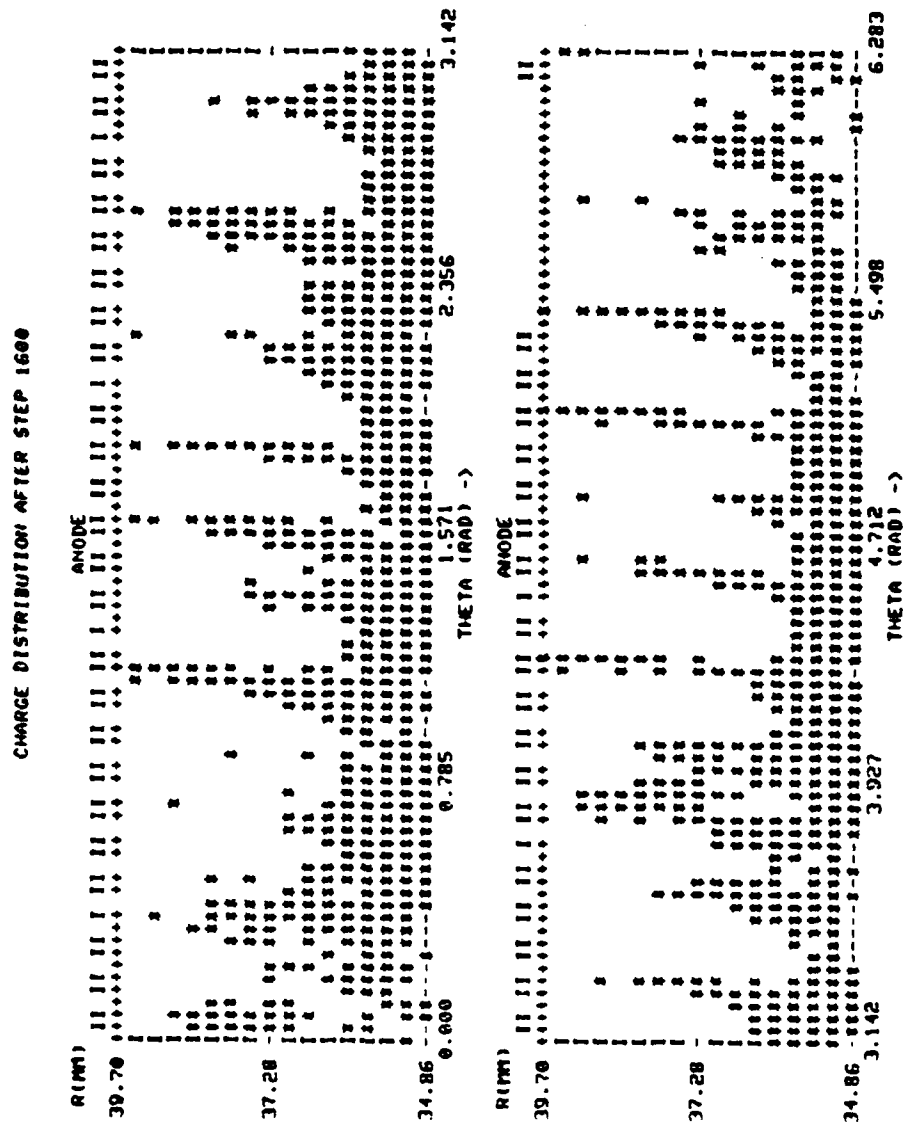


Figure 28. Beam profile computed in forward-wave QKS1319 DECFA close to emission limit.

before this region to cross the gap. The beam feeds significant RF current through to the input, as in the other tubes studied.

The numerical results are summarized in Figure 29 and Table 10. Computed points 1, 3 and 4 lie on the same load line as the measured point A but the computed currents and powers are high. This tube clearly provides a severe but useful test of the accuracy of the computations. At present an increase of the magnetic field from the actual 0.1150 T to 0.1300 T (point 1 on Figure 29) is necessary for close agreement. However, the anode voltage of 10,100 V is then only 0.99 times the Hartree voltage, and the large fluctuations of computed output power (Figure 30) are probably unrealistic. The computation should be repeated after adjustments have been made to the model.

D. Cathode Phenomena

The QKS1842 is normally operated in the lower power mode. Here as much as 14 percent of the input power appears as cathode heating due to backbombardment, whereas 5 percent is typical of other CFAs. The simulation provides, for the first time, an explanation of this observed anomaly. Notice in Table 11 that the QKS1842 low-power mode gives the highest cathode impact energies and the highest relative values of backbombardment power. Apparently two factors are involved.

First, the normal effect of space charge is to reduce the distance of penetration of electrons into the RF field and hence reduce the impact energy from the ballistic value.²¹ In the QKS1842 low-power mode, however, the reduced space charge at the voids near the cathode, increases the impact energy of returning electrons by allowing them to experience the higher RF field closer to the anode circuit. Second, the angular space-charge field near the cathode varies more than in the

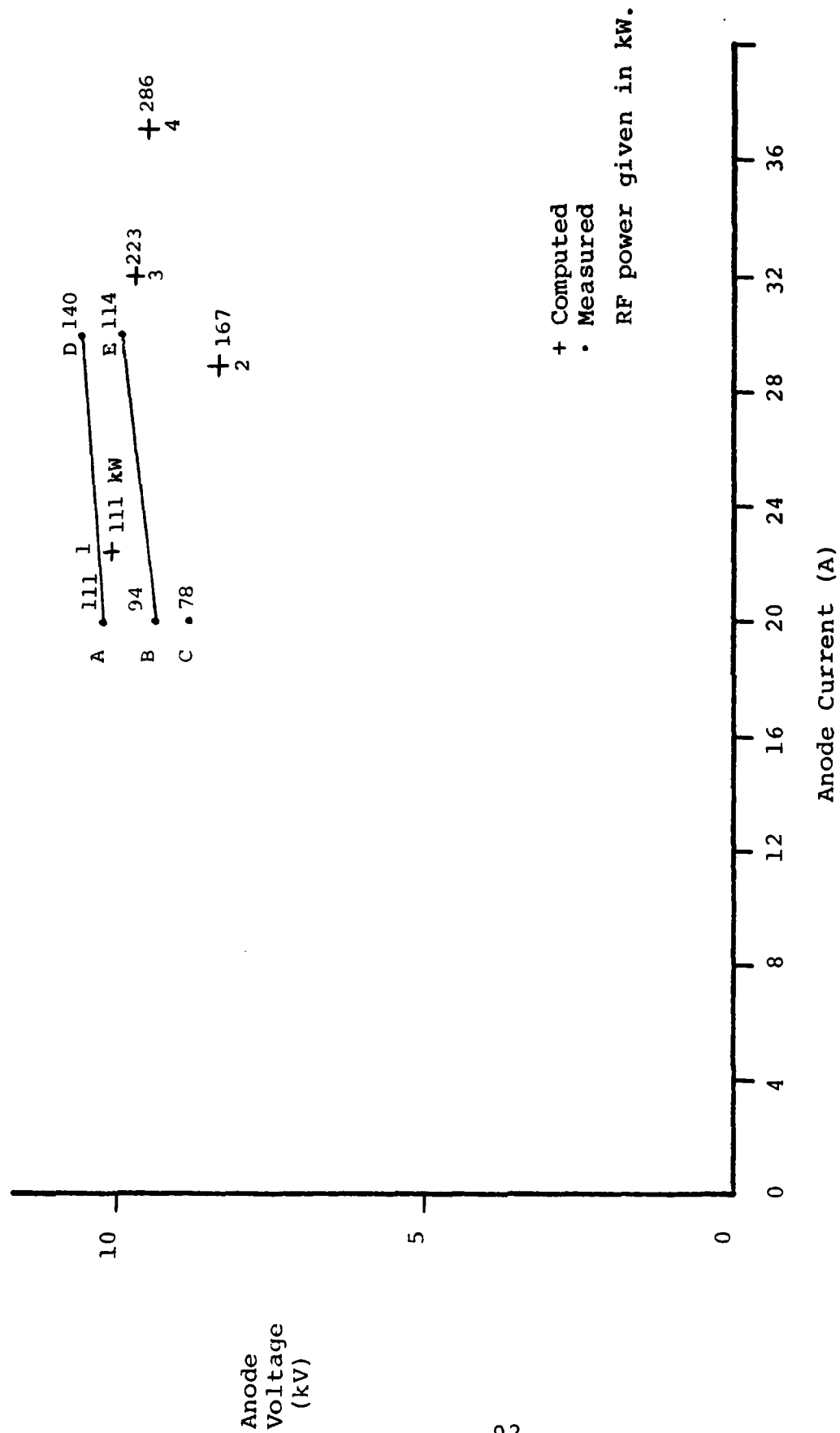


Figure 29. Computed and measured results for QKS1319 forward-wave amplifier.

RUN NO. 19006

○ 1-PERIOD MEAN

△ 17-PERIOD MEAN

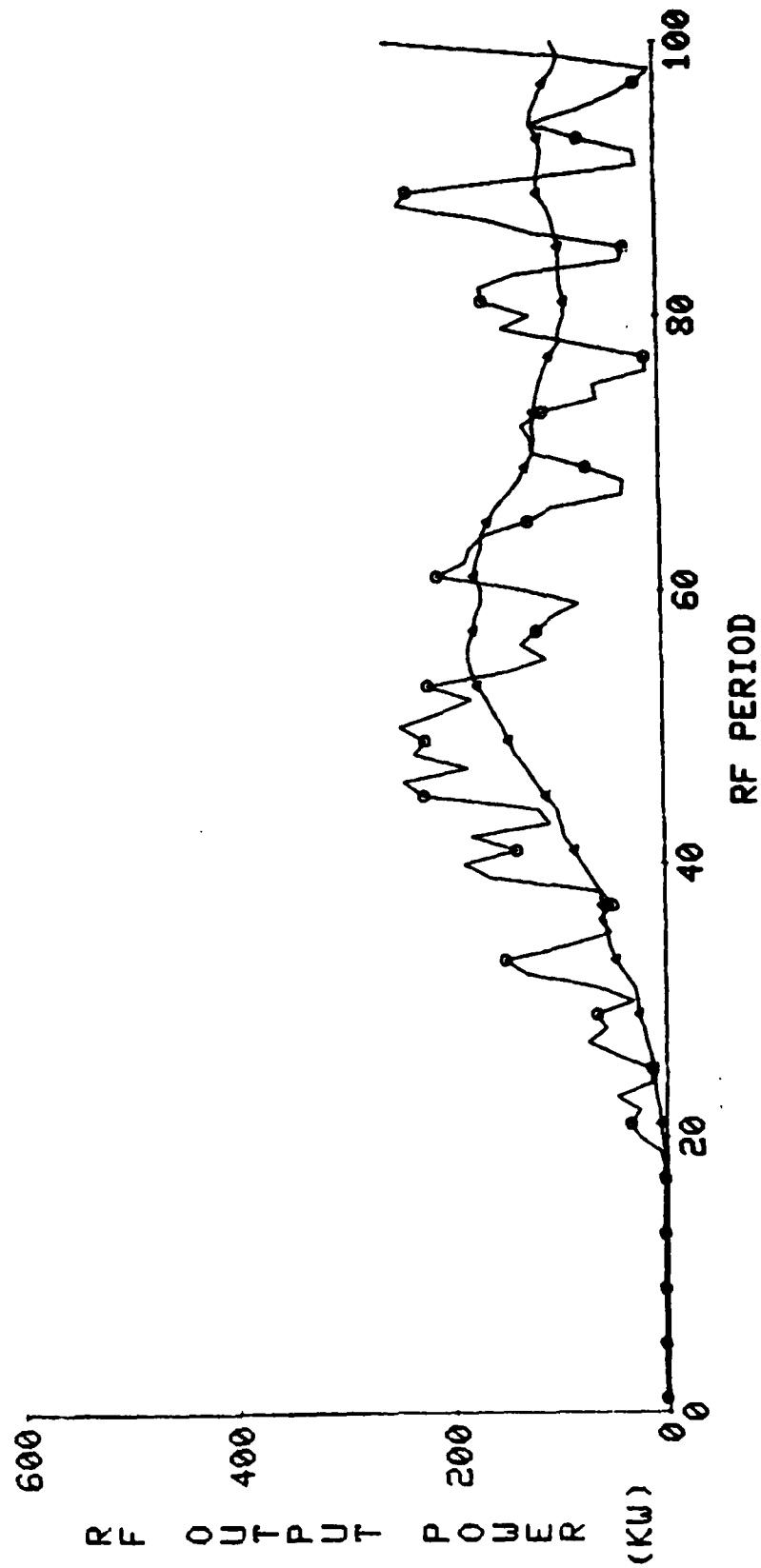


Figure 30. RF output power computed in QKS1319 DECFA with magnetic field raised to 0.13 T.

TABLE 10
COMPUTED AND MEASURED RESULTS FOR
QKS1319 FORWARD-WAVE AMPLIFIER

Points on Figure	Measured or Computed	Magnetic Field (T)	Voltage (V)	Current (A)	RF		Anode Dissipation (W)	Cathode Back- bombard- ment Power (W)	Average Secondary Emission Coefficient	Average Electron Impact Energy (eV)	Error in Power Balance (% increase)	Notes
					Drive Power (W)	Output Power (W)						
A	Measured	0.1150	10,200	20.0	3,500	111,000	123,000	8,700			17.0	
B	Measured	0.1050	9,430	20.0	3,500	94,000	117,700	8,800			15.0	Measured anode dissipation is inaccurate
C	Measured	0.950	8,820	20.0	3,500	78,000	112,300	8,700			10.0	
D	Measured	0.1150	10,600	30.0	3,500	140,000	192,600	13,000			7.0	
E	Measured	0.1050	9,900	30.0	3,500	111,000	203,300	10,400			9.0	
1	Run #19006; Periods 51-100	.1300	10,100	22.4	3,500	111,000	173,000	8,160	1.3	102	27.0	Close to oscillation Magnetic field set above measured value
2	Run #19007; Periods 51-100	.1074	8,430	28.8	3,500	167,000	193,000	7,870	1.6	140	49.0	Oscillating at Period 73
3	Run #19005; Periods 51-100	.1200	9,710	32.0	3,500	223,000	236,000	9,800	1.52	140	49.0	Oscillating at Period 90. Magnetic field set above measured value Complete results not available
4	Run #19004; Periods 41-57	.1150	9,520	37.0	3,500	286,000						

TABLE 11

CATHODE CHARACTERISTICS COMPUTED IN
DISTRIBUTED-EMISSION CROSSED-FIELD AMPLIFIERS

Tube	Cathode Material	Cathode Back -bombardment Power		Computed Average Secondary Emission Coefficient	Computed Average Cathode Impact Energy (eV)	Ballistic Impact Energy (eV) in RF field
		Input	Measured			
QKS1842 (high- power mode)	Gold and magnesium oxide (high emission)	0.05	—	1.14	232	261 to 2320
QKS1842 (high power mode)	Cermet (tungsten- thoria)	0.10	—	1.18	460	261 to 2320
QKS1842 (low- power mode)	Cermet or platinum	0.35	about 0.14	1.12	588	141 to 708
SFD-261	Beryllium Oxide	0.03	about 0.05	1.46	137	324 to 1470
QKS1319	Beryllium Oxide	0.03	0.04	1.36	108	183 to 1030

more uniform stream of the high-power mode.

The effect of changing the cathode emitter is demonstrated in a second simulation with the same modulator, magnetic field and RF drive but a lower emitting cermet cathode. This causes twice as much backbombardment power as the more highly emitting gold and magnesium oxide surface and the computed efficiency (lower than measured) falls from 39% to 36%. A similar effect is observed in a magnetron with a thermionic cathode, in which the backbombardment energy rises as the available cathode current is reduced by lowering the cathode temperature. Here too, it is hypothesized that lower space charge density permits cycloiding electrons to gain more energy from the RF circuit by moving closer to the anode.

The program provides an estimate of the maximum current available from the cathode at the emission boundary.

The effective secondary-emission coefficient shown in Table 11 increases as the emission boundary is approached. This coefficient is actually computed by counting the electrons that escape from a partially space-charge-limited cathode. Hence it is less than that from the emission table supplied for the cathode material. As the current drawn to the anode is increased, this effective coefficient, α , increases and a smaller fraction, $1/\alpha$, of the emitted charge returns to the surface. Thus a value of α close to unity implies that ample charge exists to maintain the electron stream, whereas a larger value indicates that the cathode is close to emission limitation.

The highest values of α are computed in the two forward-wave tubes (the SFD-261 and QKS1319 tubes). These tubes also have the highest ratios of RF voltage to direct anode voltage (0.34 and 0.65 compared with about 0.14 in the QKS1842) so that a larger fraction $(1-1/\alpha)$ of the emitted charge is drawn to the anode. In practice the QKS1319 shows an emission boundary at an anode current of about 30 A; the SFD-261 can provide up

to 40 A at the low end of its frequency band but less at higher frequencies.

A further example of the cathode modelling is the comparison (Table 12) between runs for the QKS1842 low-power mode with cermet and platinum cathodes. Here the anode voltage is a constant 24.3 kV and cathode emission is limited by applying Child's Law over the first mesh interval normal to the surface. Replacing the platinum cathode normally used in production tubes by the higher-yield cermet cathode reduces the mean impact energy from 430 eV to 287 eV. The anode current falls (at constant voltage) from 16 A to 14.4 A as more current returns to the cathode, keeping the net backbombardment power relatively unchanged. In practice, however, with the modulator to regulate the current, no significant differences in tube performance have been observed.

E. RF Oscillation and Mode Boundary

Competing oscillations limit the output power, gain and operating bandwidth of practical CFA's. The situation is certainly more complex in the tube than in the model, which now reproduces the RF circuit dispersion and impedance only at the drive frequency. However, the model includes both forward and reverse-directed power flow, and can produce standing waves as a result. Figure 31 shows such a standing wave between vanes 26 and 45 in the QKS1319 where the computed output power is 167 kW with an anode current of 28.8A. The RF output power shows corresponding fluctuations over time and approaches zero in certain RF periods (Figure 30).

The RF network elements are chosen so that the cold circuit is matched by the equivalent of an infinite line at each end. Therefore these standing waves must arise from power transferred

TABLE 12

COMPUTED RESULTS FOR QKS1842 DECFA
WITH PLATINUM AND CERMET CATHODES COMPARED
OVER 30 RF PERIODS

ANODE VOLTAGE 24.6 KV; MAGNETIC FIELD 0.444 T

Run Number	Cathode Material	Net Anode Current (A)	Net Cathode Current (A)	Emission Current (A)	Impact Current (A)	Back- bombard- ment power (W)	Mean Secondary Emission Coefficient	Mean Impact Energy (eV)	Mean RF Output Power (kW)
42044	Platinum (lower- yield)	16.8	16.0	199.0	183.0	78,300	1.087	430	192,300
42045	Cermet (higher- yield)	15.8	14.4	277.4	263.0	75,500	1.055	287.0	184,000

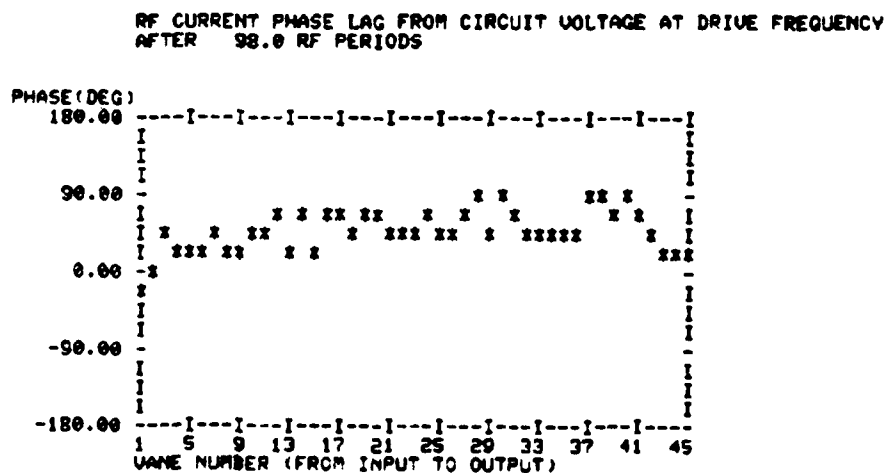
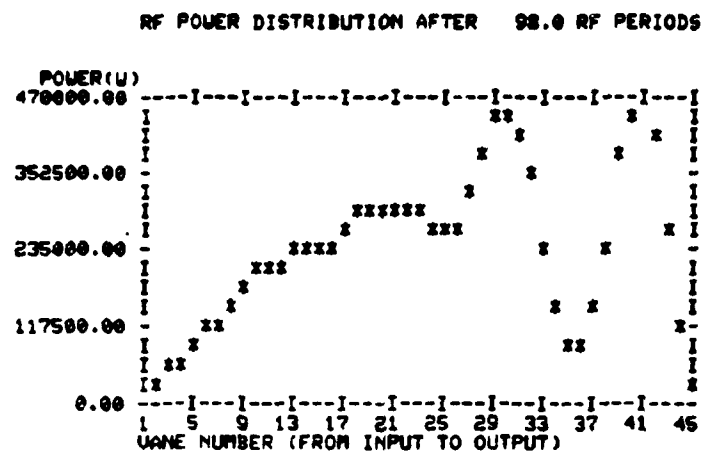


Figure 31. RF power and phase distributions computed in QKS1319 DECFA as averages over 14 periods.

to the network from the beam. A wave flows in both directions from each node as a result, but normally only the forward wave is in synchronism with the beam. The wave returning to the input is attenuated. If more power is returning to the RF input than is being supplied by the network driving current, the computed net power delivered to the network is negative (Appendix I). This condition is interpreted as an oscillation at the drive frequency. The difference between the cold-circuit drive power and the net power delivered to the circuit in the presence of the beam is an estimate of the minimum drive power required for stability.

The numerical results (Table 13) show good qualitative agreement with the available measurement data, but quantitative estimates of the mode boundaries require a more accurate calculation of the actual operating current and voltage.

Both in laboratory tests and in these simulations the QKS1842 high-power mode was stable with an RF drive power of 19 kW. Notice however, that Figure 15 shows significant oscillations of the RF output power over time. Figure 17 shows the corresponding standing waves on vanes 1-23 (towards the RF output of this backward-wave circuit). The maximum power of 8,500 W returning to the RF input during the simulation is above the 5,500 W drive level that is available for practical operation. In the QKS1842 low-power mode, however, (run 42077, Figure 18) the backward power at the input is only about 500 W with an RF drive of 5,500 W. This result implies that the tube will not oscillate, at least at the drive frequency.

At the two highest-power points computed for the SFD-261 about half the RF drive power is returning to the input vane. The low-power point ($0.65 P_0$ output) has a corresponding reverse-directed power of less than one percent of the drive. These numbers agree only qualitatively with the measurements.

TABLE 13

COMPUTED AND MEASURED OSCILLATION CONDITIONS

Tube	Run Number	Magnetic Field (T)	Voltage (V)	Current (A)	RF Drive Power (W)	RF Output Power (W)	Maximum Returning RF Power (W)		Measured Results
							at Input	at Input	
QKS1842 High-power mode	42078	0.377	27,900	35.2	19,000	396,000	8,500		Tube not stable at 5.5 kW drive.
	42077	0.395	23,100	17.9	5,500	126,000	1,900		Measurements of mode boundary not available for low-power mode.
SFD-261	23029	0.2530	1.26V ₁ (normalized)	27.0	0.08 P ₀	2.74 P ₀	0.058 P ₀		Oscillation thresholds: At 0.08 P ₀ drive: 20 A 1.47 P ₀ output
	23030	0.2606	1.09V ₁	8.4	0.08 P ₀	0.60 P ₀	0.002 P ₀		At 0.06 P ₀ drive: 14.5 A 1.38 P ₀ output
	23012	0.2606	1.36V ₁	38.6	0.08 P ₀	4.33 P ₀	0.038 P ₀		At 0.04 P ₀ drive: 11.7 A 0.83 P ₀ output
QKS1319	19005	0.1200	9,710	32.0	3,500	223,000	4,000*		Mode boundary 30 A, 140 kW, at .1150T; lower at reduced magnetic field
	19007	0.1074	8,430	28.8	3,500	167,000	4,000*		
	19008 ^f	0.1300	9,730	32.0	3,500	33,000	8,700*		

*Oscillation.

^fFrequency reduced to 1.25 GHz, but magnetic field too high for synchronism.

They predict stability with currents up to 39 A, whereas the instrumented Varian tube can produce only 20 A without oscillation. At the rated 22 A an oscillation signal develops about 1 GHz from the band center. Since the tube is stabilized at 22 A by using a non-circular cathode (as in production models) it appears that the recirculating charge is responsible. The barely visible standing wave on vanes 4-9 in Figure 27 may be a warning of trouble. It would be interesting to repeat the simulation using the actual cathode shape for the production version of the SFD-261.¹¹

In the QKS1319 the measured upper mode boundary limits the measured current to about 30 A with 140 kW RF output power. In the simulation, oscillations actually appear for anode currents above 28 A, at which the returning RF power may be as high as 8,700 W for 3,500 W drive. Probably one cause is the high interaction impedance of 84 Ω at 1.3 GHz and 146 Ω at 1.25 GHz. With incorrect beam-wave synchronism (run 19008) the oscillation is computed with an RF output power of only 33 kW. It is, however, still necessary to verify, with a more accurate numerical model, that the measured operating points are stable.

The Harris SAI model is significantly better than other CFA models which neglect the reverse-directed power entirely. However, it predicts only oscillations at the drive frequency, while practical tubes produce spurious out-of-band signals at power thresholds below those now computed. A more accurate correlation of theoretical and measured output power must next be obtained, particularly for the forward-wave tubes. Then the computed standing-wave pattern on the vanes near the RF input may be useful as an additional indication of mode problems in a design.

F. Sources of Computational Error

The preceding results have shown two areas, probably related, where the quantitative results can be improved. Firstly, the anode current and RF output power computed for a given voltage are above the measured values for the forward-wave tubes, and below the measured values for the backward-wave tube. Secondly, the power balance is unsatisfactory at present.

Consider the input and output powers averaged over several RF periods. One or more transit times around the tube are used in the computations. In a steady state, the conservation equation is:

$$\begin{aligned} \text{Direct input power from modulator} + \text{RF drive power} \\ = \text{RF output power} + \text{anode dissipation power} \\ \text{due to circuit loss} + \text{anode bombardment power} \\ + \text{cathode backbombardment power.} \end{aligned} \quad (1)$$

The measured powers satisfy this relation within the limits of experimental error.

The computed results of Tables 7-10 show a 3 to 12 percent deficit of total output power in the backward-wave tube and up to 49 percent excess total output power in the 2 forward-tubes, averaged over several RF periods that show an approximate steady state.

There are several possible sources of these computational errors.

(1) The anode bombardment power is over-estimated by about 3 percent of the total power in the backward-wave simulations and by about 13 percent in the forward-wave tubes.

At the cathode the trajectories of intercepted electrons are recomputed with a reduced time step so that the backbombardment power is accurate. However, the present program makes no such correction at the anode. Future versions of the program will compute the impact energy accurately at both the cathode and the anode.

(2) It was suspected earlier in the study that the model may be using insufficient simulation particles. However, tests have been performed with as many as 26,000 particles (Section XII) and the results imply that the normal 7,000 particles are sufficient in all three tubes.

(3) The predictor-corrector trajectory calculation, which is not time-centered, may introduce small but cumulative errors into the space-charge forces. In Section VI a modified trajectory calculation is proposed.

(4) The induced RF current on each vane includes terms both from the charge in the interaction region and from the charge collected on the vane. It is now believed that the collected current should be omitted. This correction will not affect the observation of two modes in the beam of the QKS1842, since the "groups of charge" such as in Figure 13 develop at the start of a run before significant charge is collected on the vanes. However, it could have an important effect on the quantitative results.

(5) The time step is now $1/15$, less than $1/10$, and $1/6$ cyclotron period in the QKS1842, SFD-261 and QKS1319 respectively. Varian's SFD-261 simulations use $1/10$ cyclotron period. Initial trials have shown that the QKS1842 time step is sufficiently small. For the two forward-wave tubes further tests should be made with a smaller step.

G. Comparison of QKS1842 With Other Distributed-Emission Crossed-Field Amplifiers

The QKS1842 was designed using parametric equations to scale down in size a similar backward-wave CFA, the QKS1705 which operates over the same 9.5-10 GHz frequency band. The smaller anode circumference and smaller vane spacing of the QKS1842 give it a reduced RF phase velocity and a reduced interaction impedance. Consequently, the QKS1842 requires a lower operating voltage and a higher magnetic field to provide the beam drift speed for synchronism. It now supplied 175 kW peak power at 17.1 A over a reduced bandwidth, with a 5.5 kW RF drive at about 39% efficiency. This is the low-power mode demonstrated in the simulations. The tube shows anomalously high cathode backbombardment and has also given difficulties with starting.

The parameters of the QKS1842 and QKS1705 are compared in Table 14, together with those of the QKS1319 and Varian SFD-261 tubes. Clearly the QKS1705 and QKS1842 have the lowest interaction impedances and also the lowest ratios of RF voltage to direct voltage. In addition, the QKS1842 is operating closest to the Hartree threshold voltage^{1,11} (even below this if the measured 0.4114 T magnetic field is accurate). These two observations may account for the irregular beam bunches that develop in the low-power mode in the QKS1842 and hence for the high backbombardment and starting delay. Detailed studies on the SFD-261¹¹ have in fact shown that for a given RF field there is a minimum ratio of anode voltage to Hartree voltage allowing spokes of charge to form. In the high-power mode of the QKS1842 the RF field is sufficient to produce the expected behavior, and the efficiency is increased to 50%. However, this mode is unsuitable for practical use because of the high RF drive power (19 kW) needed to suppress oscillation. The 5.5 kW

TABLE 14

PARAMETERS FOR FOUR DISTRIBUTED-EMISSION
CROSSED-FIELD AMPLIFIERS

	QKS1842 (High-power mode) (Backward-wave)	QKS1842 (Low-power mode) (Backward-wave)	QKS1705 (Backward-wave)	SFD-261 (Forward-wave)	QKS1319 (Forward-wave)
Frequency (GHz)	9.6	9.75	9.75	$f_o + 0.3$ (normalized)	1.3
Magnetic Field (T)	0.377	0.395	0.36	0.253	0.13
Anode Current (A)	49	17.1	34	22	20
Anode Voltage (V)	21,800	24,300	33,000	$1.3V_1$	10,200
Anode Voltage Cutoff Voltage	0.56	0.57	0.75	0.49	0.33
Anode Voltage Barrier Voltage	1.019	1.039	1.193	1.137	1.146
Number of Charge Spokes	14-15	14-15	15	18	17
RF Drive Power (W)	19,000	5,500	30,000	$0.08P_1$	3,500
RF Output Power (W)	530,000	175,000	513,000	$1.65P_1$	111,000
Interaction Impedance (Ω)	7.2	7.5	8.8	45.0	84.17
RF Voltage Anode Voltage	0.030	0.013	0.022	0.075	0.12
RF Input	0.16	0.076	0.091	0.34	0.65
RF Output					
(Width in Magnetic- Field Direction)/(Free- Space RF Wavelength)	0.47	0.48	0.48	less than 0.4	0.15

actually used is necessitated by the required gain and by the available driver tubes.

SECTION XII

PROGRAM REQUIREMENTS

The computing resources required are controlled primarily by the number of particles (rods), the time step, and the length of the run.

A. Number of Simulation Particles

Table 15 summarizes the particle requirements for these runs. The charge per rod and the number of rods used are controlled by the input parameter NBRILL, the number of rods required to fill the cylindrical anode-cathode region with a density such that the electron plasma frequency equals the cyclotron frequency. This is the Brillouin-flow condition for a crossed-field tube.

In trials with varied resolution and both with and without the modulator the number of simulation rods has been increased and the space-charge array size changed from 257 (angular) by 33 (radial) to 513 by 33. Both in this tube and in the QKS1842 and QKS1319 tubes the results are not sensitive to the changes. Figures 32 and 33 are good examples showing that 6,000 rods are sufficient, although up to 27,900 are tested. (The modulator is absent here.)

These curves show that the mean currents and powers over 18 periods agree within 6 percent, although the finer details of the interaction are more sensitive to the model. The power balance shows an excess output power between 23 and 25 percent in both cases. In the QKS1319 corresponding figures are 53.5 A and 392 kW with 4,100 rods compared with 58.4 A and 402 kW with 15,800 rods, the mean current and power over periods 36 to 52. The results are high compared with the measured values because

TABLE 15
PARTICLE NUMBERS REQUIRED IN
CFA SIMULATIONS

Run Number	Tube	Number (NBRILL) of Rods to Fill Tube at Brillouin Density	Maximum Rods Used
42079	QKS1842 (high-power mode)	10,000	7,603
42077	QKS1842 (low-power mode)	10,000	7,027
42073	QKS1842 (low-power mode)	45,000	23,471
23029	SFD-261	20,000	7,330
23024	SFD-261	90,000	27,886
19006	QKS1319	20,000	5,602

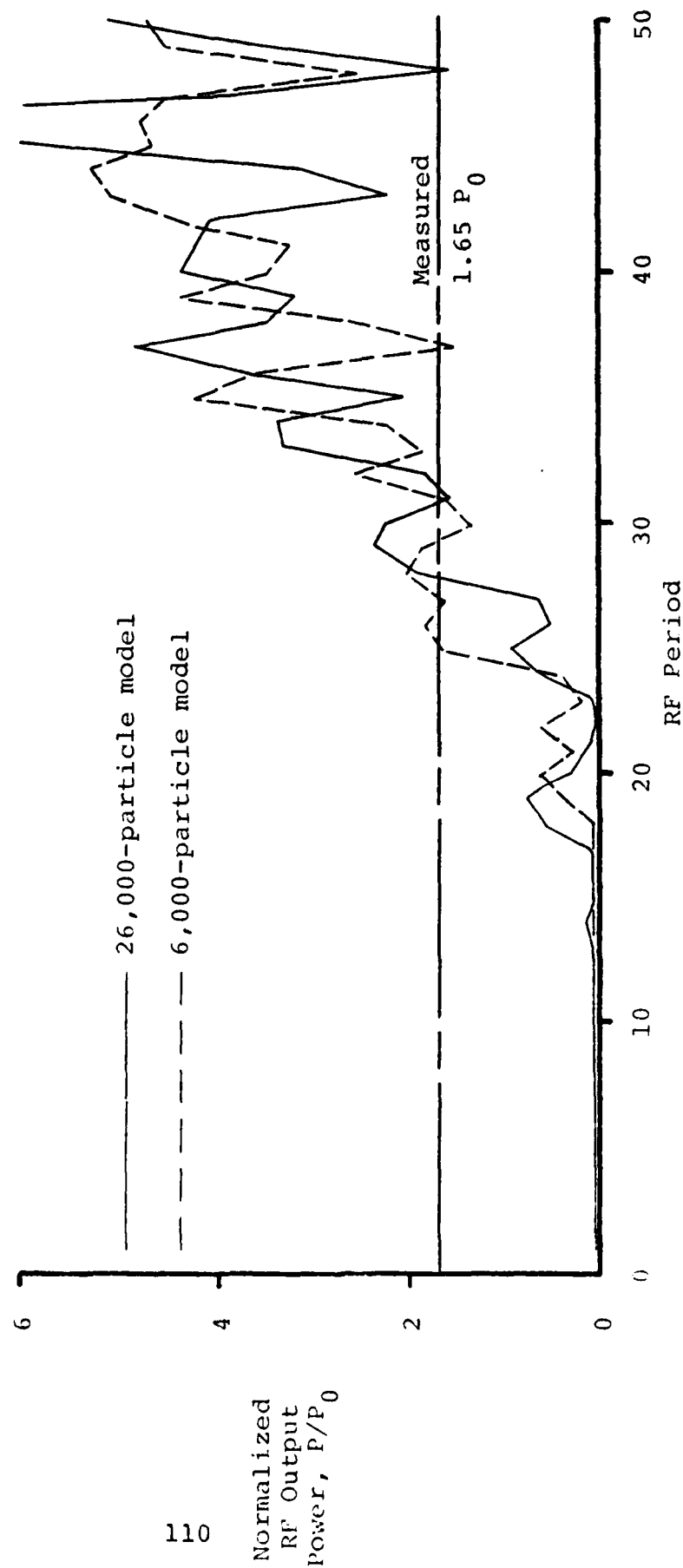


Figure 32. RF output power computed for Varian forward-wave DECFA. Modulator not included in model.

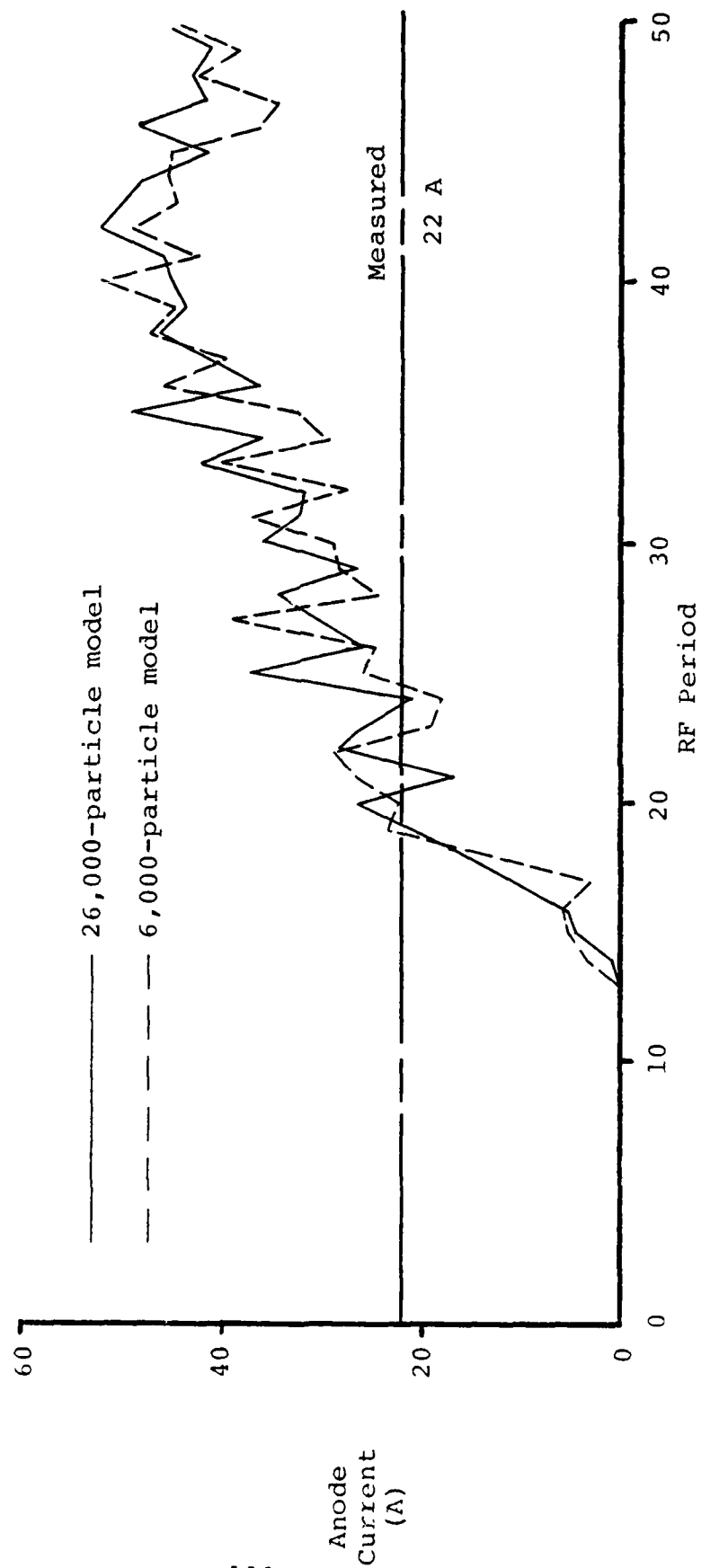


Figure 33. Anode current computed for Varian forward-wave DECFA. Modulator not in model.

the modulator model was not implemented for these runs. To attain here the resolution of the Varian single-wavelength model would require about 60,000 rods and a 2049 x 49 space-charge array. Such detail appears not to be necessary in the present model.

B. Time Step

The three criteria used to estimate the largest allowable step size are

- (1) At least 16 steps per RF period
- (2) At least 8 steps per electron cyclotron period
- (3) Not more than one mesh interval to be crossed by a typical particle in one step.

The user actually supplies the number of steps per RF period. It is recommended that consistency tests be performed with a given step and then one half that step whenever a new CFA is simulated.

The values used for the simulations are shown in Table 16. Criterion (3) is satisfied for angular velocities in the charge hub and for radial velocities less than 1/6 the RF phase velocity. It is not generally satisfied in the spokes where charge approaches the anode.

The QKS1842 interaction has been computed over six RF periods with 32 time steps per period in place of the usual 16, and the powers transferred to the RF wave agree within 9 percent. This power transferred from the beam to the RF circuit in one period is a conveniently sensitive measure of the accuracy. Similar tests should be performed for the QKS1319 and SFD-261 tubes.

TABLE 16

TIME STEPS USED IN DECFA SIMULATIONS

Tube	Step Length (s)	Time Steps per RF Period	Time Steps Per Cyclotron Period	Mesh Intervals Crossed Per Step with RF Phase Velocity	
				Radial	Angular
QKS1842	6.51×10^{-12}	16	14	4	0.7
SFD-261	Not Shown	16	less than 10	3	0.5
QKS1319	4.81×10^{-11}	16	6.5	6	0.9

C. Length of Run

In the results described in Section XI, between 50 and 100 RF periods suffice to attain a dynamic steady state in the two forward-wave tubes. The RF circuit in the backward-wave tube has a longer response time to initial transients because of the feedback of power from the RF input once the beam is fully bunched there. The QKS1842 high-power mode requires 100 RF periods and the lower-power mode has been run for 250 periods because of the larger fluctuations in the charge distribution.

D. Computing Time and Storage

The computing times required for simulations of the three tubes are summarized in Table 17. These figures are for the Harris 550 computer. Relative values for other machines are estimated below:

<u>Computer</u>	<u>CPU Time (sec)</u>
Harris 550	1
IBM 360/67	1.16
IBM 370/148	0.51
CDC 6500	2.28
Amdahl 470V/6	0.124
Amdahl 470V/7	0.083

The CPU time per particle (rod) per time step is a useful figure of merit for computer programs of this type. It decreases as more particles are introduced. It is almost independent of the number of vanes that produce the RF field in the CFA. A figure of 6.4×10^{-3} sec. is typical for the 550 computer.

From Table 17 it can be seen that a typical 100-period run with 16 time steps per RF period and 7,000 rods of

TABLE 17
COMPUTING TIME FOR DECFA SIMULATION ON
HARRIS 550 COMPUTER

Tube	Number of Active Vanes In Tube	Number of Rods in Simulation	CPU Seconds Per Particle Per Time Step	CPU Time (hours) for 100 RF Periods
QKS1842	35	7,050	6.62×10^{-3}	20.7
QKS1842	35	5,600	7.57×10^{-3}	18.8
SFD-261	62	5,740	7.24×10^{-3}	18.5
SFD-261	62	25,500	5.52×10^{-3}	62.6
QKS1319	45	3,610	8.31×10^{-3}	13.3
QKS1319	45	12,300	6.40×10^{-3}	35.0

charge requires about 20 hours of computing. However, more efficient trajectory and RF field calculations are planned (Section VI) which should halve this time.

With a maximum of 20,000 rods the program now requires 505,000 24-bit words (252,500 48-bit floating-point numbers) on the Harris 550 machine. The requirements on other machines are similar, as most of the storage is for particle and field arrays.

SECTION XIII

CONCLUSIONS AND RECOMMENDATIONS FOR FUTURE WORK

The capabilities of the Harris SAI distributed-emission CFA simulation program are summarized in Table 18, which shows the important features of the tube that a useful simulation should reproduce.

This AFOSR-sponsored study has advanced the understanding the operation of the DECFA, demonstrating particularly the following results:

- The modulator controls the anode current and voltage even over the small time scale of a few RF periods, during which small fluctuations of voltage and current occur. A rise of current causes a fall in the voltage, maintaining stability.
- The circulating charge carries significant RF current across the drift region in both the forward-wave and backward-wave tubes.
- The SFD-261 and QKS1319 forward-wave tubes operate with the characteristic spoked beam expected from analytic theory.
- The QKS1842 shows two types of operating mode, with efficiencies of 39% and 56%. The lower efficiency is obtained in normal operation, where the charge distribution is irregular.
- Anomalously high backbombardment power results from sparse charge density in the QKS1842 low-power mode.

TABLE 18

CAPABILITIES OF THE HARRIS SAI DECFA MODEL

<u>Feature</u>	<u>Result</u>
Anode current at given voltage and given magnetic field.	Less than measured value in backward-wave CFA; above measured value in forward-wave CFA; in actual runs the voltage is allowed to vary.
RF output power.	About 25% below measured value in backward-wave CFA; 50%-100% above measured value in forward-wave CFA.
Anode heating.	Now overestimated by up to 30 percent but an improved computation of electron energy at the vanes will be straightforward. Power distribution over vanes is computed and can readily be displayed.
Backbombardment and cathode heating.	Good order-of-magnitude agreement with measurements, including the anomalously high value of 15% beam power in QKS1842 low-power mode.
Steady-state power balance balance in model.	After correction of the anode heating a 7%-15% deficit of output power is computed in the backward-wave tube and a 9%-38% excess in the forward-wave tubes.
Secondary emission.	The beam hub forms stably. Cathode emission model reproduces different cathodes. A lower-yield surface results in higher backbombardment as the charge density falls. The emission-free drift region is reproduced in the QKS1319.

TABLE 18 (cont.)

<u>Feature</u>	<u>Result</u>
Cathode emission limit.	Approached but not reached in simulations.
Mode selection in beam.	Two types of mode (lumps of charge and spokes of charge) distinguished in QKS1842 tube. One mode (spokes) in each of SFD-261 and QKS1319 with the normal operating voltage and magnetic field.
Oscillation and upper current mode boundary.	RF network can allow oscillation at drive frequency. Order-of-magnitude agreement with measured RF output power limit in QKS1319 and with minimum RF drive in QKS1842 high-power mode, but SFD-261 oscillations not reproduced by present model.
Spurious RF signals away from operating band.	Not included but may be induced by oscillation due to reverse-directed RF power.
Upper power limit due to loss of synchronism.	Not yet simulated but should be predicted by model.
Lower mode boundary due to oscillation at lower cutoff frequency of backward-wave circuit.	Not included with present RF network.
Modulator.	Both hard-tube and line-type modulators are treated, but with reduced inductance and capacitance for rapid decay of transient voltages. A run requires a prior

TABLE 18 (cont.)

<u>Feature</u>	<u>Result</u>
	estimate of current and voltage in the steady state.
Starting a tube pulse.	Starting can be simulated on an accelerated time scale. (About 1/1000 of a pulse is treated in a typical run). Rise of line-type modulator voltage is not now reproduced but is straightforward to include.
Turn-off at the end of a pulse when RF drive is removed in forward-wave tubes.	Straightforward to reproduce but not yet studied.
Transverse effects (in the magnetic-field direction).	All motion in the magnetic-field direction is neglected, but the measured interaction impedance is an average over the width of the device and accounts for the RF field variation across the vanes.

- Increasing the secondary-emission yield at the cathode reduces the backbombardment power and raises the efficiency at a fixed RF output power.
- Reverse-directed RF power along the vane circuit creates standing waves and may produce oscillation corresponding to a measured mode boundary.

Consistency tests have shown that 7000 simulation rods give sufficient resolution. Although the steady-state power balance is not yet satisfactory in the forward-wave tubes, adjustments to the RF network and trajectory calculations are proposed to improve this. It should be possible also to halve the present computing time of 20 CPU hours per run on the Harris 550 minicomputer (equivalent to about 23 hours on an IBM 360/67).

The following are the priorities recommended for a continuation of this study:

1. Improve the trajectory and RF network models (as described in detail in this report) in order to obtain results that show a better power balance, particularly in the two forward-wave tubes. Verify the program using the measured values for the QKS1842, SFD-261 and QKS1319 tubes.

2. Test alternative calculations of RF field and induced current to eliminate the RF Green's function and give a more efficient computation.

3. Simulate the QKS1842 and SFD-261 tubes at band-edge frequencies.

4. Simulate the QKS1705 backward-wave CFA to obtain additional verification for the program.

5. Study the starting conditions in the QKS1842 on an accelerated time scale. Choose the modulator inductance to allow the anode voltage to rise from zero over about one RF transit time around the tube.

6. Reduce the RF drive to simulate the oscillation thresholds in the SFD-261.

7. Model the production SFD-261 forward-wave CFA with a noncylindrical cathode. It will suffice to include only the effect of the variable spacing on the applied (direct) field; for the space-charge and RF fields the cathode will be treated as circular.

8. Incorporate an option of a tapered pitch for the vane circuit. The RF network will be unchanged if it is assumed that the phase delay between vanes and the characteristic impedance are unaltered.

9. Test a more general form of RF network with a dispersion characteristic that includes a cutoff frequency. The general equations for such a network have already been included in the model.

10. Develop a model for the cathode-driven CFA. An accurate solution of Poisson's equation is required including the vane shape on the cathode as a boundary. A suitable technique has been used at the Naval Research Laboratory for magnetron simulations and could be applied to the CFA.

The basic elements of the model have been established and thoroughly tested in the present study.

It is expected that the above additional effort will produce a reliable simulation program that can be used to improve or scale existing crossed-field amplifiers.

REFERENCES

1. J. F. Skowron, "The Continuous Cathode (Emitting-Sole) Crossed-Field Amplifier," Proc. IEEE, vol. 61, No. 3, pp. 330-356; March 1973.
2. J. Skowron, "Crossed-Field Amplifiers and Magnetrons," Raytheon Company Report AV-1460, Presented at 1977 Microwave Power Tube Conference, Monterey, CA; Raytheon Company, Microwave and Power Tube Division, Waltham, MA; April 1977.
3. G. E. Dombrowski, "Theory of the Amplitron," IRE Trans. Electron Devices, vol. ED-6, No. 4, pp. 419-428; October 1959.
4. J. R. M. Vaughan, "A Model for Calculation of Magnetron Performance," IEEE Trans. Electron Devices, vol. ED-20, No. 9, pp. 818-826; Sept. 1973.
5. S. P. Yu, G. P. Kooyers, and O. Buneman, "Time-Dependent Computer Analysis of Electron-Wave Interaction in Crossed Fields," J. Appl. Phys., vol. 36, No. 8, pp. 2550-2559; August 1965.
6. D. M. MacGregor and J. E. Rowe, "Manual for Crossed-Field Amplifier Analysis Program," Prepared for Naval Electronics Laboratory Center by Shared Applications, Inc., Ann Arbor, MI; August 1976.
7. D. M. MacGregor and J. E. Rowe, "Computer Program for Crossed-Field Amplifier Analysis," Final Report, Task Order 75-382, Project Period 30 June 1975-15 August 1976, Prepared for Battelle Columbus Laboratories and Naval Electronics Laboratory Center by Shared Applications, Inc., Ann Arbor, MI; August 1976.
8. "CFA Design Improvement Program," Semi-Annual Report, July 1, 1975-December 31, 1975, Contract No. N00123-75-C-1294, Varian Associates, Beverly, MA; March 1976.
9. "CFA Design Improvement Program," Second Semi-Annual Report, January 1, 1976-June 30, 1976, Contract No. N00123-75-C-1294, Varian Associates, Beverly, MA; October 1976.

10. G. K. Farney, "CFA Design Improvement Program, Volume I-Instrumented CFA Studies," Final Report, Contract No. N00123-75-C-1294, Prepared for U. S. Navy Ocean Systems Center, San Diego, CA, by Varian Associates, Inc., Beverly, MA; June 2, 1978.
11. H. L. McDowell, "CFA Design Improvement Program, Volume II-Computer Modeling Studies," Final Report, Contract No. N00123-75-C-1294, Prepared for U. S. Navy Ocean Systems Center, San Diego, CA, by Varian Associates, Inc., Beverly, MA; June 2, 1978.
12. D. M. MacGregor and J. E. Rowe, "Computer Modeling and Simulation of Crossed-Field Amplifiers," Final Report, MIT Lincoln Laboratory, Purchase Order CX-1109, Shared Applications, Inc., Ann Arbor, MI; November 1976.
13. D. M. MacGregor and J. E. Rowe, "Analysis of Distributed-Emission Crossed-Field Amplifiers," Final Report, No. ESD-TR-77-268, Prepared for MIT Lincoln Laboratory, Under Purchase Order CX-1256, by Shared Applications, Inc., Ann Arbor, MI; August 1977.
14. J. R. M. Vaughan, "Beam Buildup in a DEMATRON Amplifier," IEEE Trans. Electron Devices, vol. ED-18, No. 6, pp. 365-373; June 1971.
15. J. R. M. Vaughan and G. R. Good, "Source Program and User's Manual for Cathode-Driven CFA," Technical Report No. L-69342-1, Prepared by Litton Industries, San Carlos, CA, Under Contract No. DAAB07-76-C-1359 to USAECOM, Fort Monmouth, NJ; February 1977.
16. J. R. M. Vaughan, "Computer Analysis of the Cathode-Driven Crossed-Field Amplifier," Final Report No. L-69342-2, Prepared by Litton Industries, San Carlos, CA, Under Contract No. DAAB07-76-C-1359 to USAECOM, Fort Monmouth, NJ; May 1977.
17. J. R. M. Vaughan, "Application of CADAVA to the Design of a Cathode-Driven CFA," Technical Report No. L-69342-3, Prepared by Litton Industries, San Carlos, CA, Under Contract No. DAAB07-76-C-1359 to USAECOM, Fort Monmouth, NJ; February 1977.
18. G. E. Dombrowski and W. C. Price, "Analytic and Experimental Study of Reentrant Stream Crossed-Field Amplifiers," NASA CR-72442, University of Connecticut, Storrs, CT; 1968.

19. A. T. Drobot, "Simulation Techniques for Self-Consistent Treatment of Electron Dynamics in High Power Microwave Tubes," Technical Digest, 1979 IEEE International Electronics Devices Meeting, Washington DC, pp. 633-665; December 1979.
20. G. MacMaster and L. Nichols, "High-Gain Crossed-Field Amplifier Tube," (abstract only) Technical Digest, 1977 IEEE International Electron Devices Meeting, Washington DC, p. 245B; December 1977.
21. E. K. Shaw, "Starting in the Cold Cathode Distributed-Emission Crossed-Field Amplifier," IEEE Trans. Electron Devices, vol. ED-24, No. 1, pp. 22-26; January 1977.
22. P. Fischer, "Space-Charge Flow Starting Conditions in RF-Keyed Crossed-Field Amplifiers," Tech. Digest, 1977 IEEE Int. Elect. Dev. Meeting, Wash., DC, pp. 252-A - 252-E; December 1977.
23. D. Potter, Computational Physics, John Wiley & Sons, New York; 1973.
24. H. Bruining, Physics and Applications of Secondary Electron Emission, Pergamon Press Ltd, London; 1954.
25. C. K. Birdsall and W. B. Bridges, Electron Dynamics of Diode Regions, Academic Press, New York; 1966.
26. R. Y. C. Ho and T. Van Duzer, "Approximate Formulas for Crossed-Field Potential-Minimum Parameters," IEEE Trans. Electron Devices, vol. ED-15, No. 2, pp. 70-74; February 1968.
27. M. Chodorow and C. Susskind, Fundamentals of Microwave Electronics, McGraw-Hill, New York; 1964.
28. P. Swartztrauber and R. Sweet, "Efficient FORTRAN Subprograms for the Solution of Elliptic Partial Differential Equations," NCAR Tech. Note NCAR-TN/IA-109, National Center for Atmospheric Research; July 1975.
29. G. N. Glasoe and J. V. Lebacqz, Eds., "Pulse Generators," MIT Radiation Laboratory Series vol. 5, Dover Publications Inc., New York; 1965.
30. J. C. Walling, "Interdigital and Other Slow Wave Structures," J. of Electronics and Control, vol. 3, pp. 239-258; September 1957.

31. W. C. Brown, "The Platinotron: Amplitron and Stabilotron," Crossed-Field Microwave Devices, E. Okress (Ed.), vol. 2, pp. 165-209, Academic Press, New York; 1961.
32. J. C. Slater, Microwave Electronics, Van Nostrand, Inc., New York; 1950.
33. J. M. Osepchuk, "Magnetron Diode Oscillations," Crossed-Field Microwave Devices, E. Okress (Ed.), vol. 1, pp. 275-317, Academic Press, New York; 1961.
34. W. A. Smith, "A Wave Treatment of the Continuous Cathode Crossed-Field Amplifier," IRE Trans. Electron Devices, vol. ED-9, No. 5, pp. 379-387; September 1962.

APPENDIX A

DATA FOR THE RAYTHEON QKS1300 AMPLITRON

The parameters tabulated below were used in initial development of the DECFA program. Some of the operating values were supplied by the Raytheon Company;* the remainder are taken from Dombrowski and Price.¹⁸ A few of the numbers have been changed for testing purposes. For example, the high RF drive of 43 W was used to provide strong RF fields and ensure good beam-wave synchronism with reduced computing time.

<u>Quantity</u>	<u>Operating Value</u>	<u>Value Used in Test Runs</u>
Number of vanes	11	11
Number of active vanes	11	11
Magnetic field (T)	.21	.21
Beam width (mm) in the magnetic-field direction	5.334	5.334
Anode radius (mm)	2.337	2.337
Cathode radius (mm)	0.991	0.991
Drive frequency (GHz)	2.2825	2.2825
Anode-sole voltage (V)	1800.0	1800.0
RF drive power (W)	0.4	43.0
Cold Phase delay (rad) per pitch of network as measured in forward-wave direction	$3\pi/11$	$3\pi/11$
Direction of wave seen by beam	Backward	Backward

* Telephone communication, Dr. J. Skowron to Dr. D. MacGregor, October 28, 1977.

<u>Quantity</u>	<u>Operating Value</u>	<u>Value Used in Test Runs</u>
Interaction impedance (Ω)	Not known	120
Characteristic impedance (Ω)	120 estimated	202.3
Attenuation (dB) per pitch	Not known	0.00312
Ratio of vane spacing to pitch (period) on the anode surface	0.392	0.392
Cathode emission	Thermal	Thermal
Maximum current density at cathode (A/m^2)	Not known	1.068×10^6
Anode current (A)	0.018	No values have been obtained from present calculations.
RF output power	25 W	
Time step		1/64 RF period
Pitch of circuit (mm)	1.335	1.335

APPENDIX B

DATA FOR THE RAYTHEON QKS1842 CFA

I.	<u>Basic Tube Data</u>	
1.	Manufacturer.	<u>Raytheon</u>
2.	Tube identification number.	<u>QKS1842</u>
3.	Forward-wave or backward-wave amplifier (see note 1).	<u>Backward-wave</u>
4.	Total number of anode vanes.	<u>40</u>
5.	Number of active anode vanes.	<u>35</u>
6.	Transverse magnetic field (T), treated as uniform.	<u>0.4115</u>
7.	Beam width (mm) in the magnetic-field direction, treated as constant.	<u>14.8</u>
8.	Cathode radius (mm).	<u>7.748</u>
9.	Anode radius (mm), measured from the axis to the vane tips.	<u>9.708</u>
10.	Displacement, if any, of cathode axis from geometrical center (mm).	<u>None</u>
11.	Distance (mm) around the anode from RF input to RF output.	<u>52.4</u>
12.	Length (mm) around the anode of the RF circuit sever between the RF output and RF input. (Items 11 and 12 should add to equal the anode circumference.)	<u>8.6</u>
13.	Pitch (period) of the RF circuit measured around the anode surface (mm).	<u>1.52</u>
14.	Ratio of vane spacing to pitch (period) on the anode surface.	<u>0.328</u>
15.	Drive frequency (GHz).	
	a. Lower end of operating band.	<u>9.5</u>
	b. Midband.	<u>9.75</u>
	c. Upper end of operating band.	<u>10.0</u>
	(These frequencies are used in following items.)	

16. Anode-cathode voltage, as a function of frequency:

Frequency (GHz)	a.	<u>9.5</u>
	b.	<u>9.75</u>
	c.	<u>10.0</u>
Anode-cathode voltage.	a.	<u>24,300</u>
	b.	<u>25,500</u>
	c.	<u>26,850</u>

17. RF drive power (W) for peak output, tabulated as a function of frequency:

Frequency (GHz)	a.	<u>9.5</u>
	b.	<u>9.75</u>
	c.	<u>10.0</u>
RF drive (W).	a.	<u>5,500</u>
	b.	<u>5,500</u>
	c.	<u>5,500</u>

Notice that a separate run must be made for each frequency specified.

18. Cold-circuit phase delay (degrees) per vane in the direction of power flow:

Frequency (GHz)	a.	<u>9.5</u>	d.	<u>9.8</u>
	b.	<u>9.6</u>	e.	<u>9.9</u>
	c.	<u>9.7</u>	f.	<u>10.0</u>
Phase delay (degrees).	a.	<u>41.0</u>	d.	<u>48.5</u>
	b.	<u>43.5</u>	e.	<u>51.0</u>
	c.	<u>46.0</u>	f.	<u>53.5</u>

19. Interaction impedance (Ω) as a function of frequency (use the definition in note 3 or supply an alternative definition in Part III):

Frequency (GHz)

a. <u>9.5</u>	d. <u>9.8</u>
b. <u>9.6</u>	e. <u>9.9</u>
c. <u>9.7</u>	f. <u>10.0</u>

Impedance (Ω).

a. <u>6.0</u>	d. <u>7.8</u>
b. <u>6.6</u>	e. <u>8.5</u>
c. <u>7.2</u>	f. <u>9.2</u>

20. Cold-circuit RF power attenuation (dB) per anode pitch as a function of frequency:

Frequency (GHz)

a. <u>9.5</u>	d. <u>9.8</u>
b. <u>9.6</u>	e. <u>9.9</u>
c. <u>9.7</u>	f. <u>10.0</u>

Attenuation (dB).

a. <u>.0187</u>	d. <u>.0187</u>
b. <u>.0187</u>	e. <u>.0187</u>
c. <u>.0187</u>	f. <u>.0187</u>

21. Type of cathode emitter surface:

a. Thermal emitter (yes/no). _____

b. Secondary emitter (yes/no). _____

c. Both thermal and secondary emitter (yes/no). _____

Yes

For thermally emitting cathode (a):

- (1) Current density that would exist under temperature-limited conditions and with no transverse magnetic field (A/m^2).

Estimated as less than 10% of operating value.

- (2) Average energy (eV) of thermal electrons on emission.

Not known.

For secondary emitter (b):

- (1) Secondary-emission coefficient (may be fractional) as a function of primary impact energy (eV). A single constant value will suffice if the detailed variation is not known.

Primary Impact Energy	Secondary-Emission Coefficient
200	1.86
400	2.36
600	2.58
800	2.63
900	2.63
1,000	2.63
1,200	2.58
1,400	2.53

- (2) Average energy (eV) of secondary electrons on emission.

Not known.

II. Performance Data for Comparison of Computation and Measurement

Please indicate whether the value supplied is a result of measurement or an analytical estimate. If no value is available, please write "not known."

- | | | |
|---|----------------------|-------------------|
| 1. Drive frequency (GHz). | a. <u>9.5</u> | d. <u>9.8</u> |
| | b. <u>9.6</u> | e. <u>9.9</u> |
| | c. <u>9.7</u> | f. <u>10.0</u> |
| 2. Anode current (A). | a. <u>15.3</u> | d. <u>17.1</u> |
| | b. <u>16.7</u> | e. <u>17.1</u> |
| | c. <u>17.1</u> | f. <u>17.1</u> |
| 3. RF output power (W). | a. <u>159,000</u> | d. <u>169,000</u> |
| | b. <u>184,000</u> | e. <u>158,000</u> |
| | c. <u>181,000</u> | f. <u>153,000</u> |
| 4. Efficiency (see note 4). | a. <u>40.9</u> | d. <u>36.6</u> |
| | b. <u>42.5</u> | e. <u>33.1</u> |
| | c. <u>40.4</u> | f. <u>31.7</u> |
| 5. Measured hot phase delay
(degrees) per cavity in
direction of power flow. | a. <u>Not known.</u> | |
| | b. _____ | |
| | c. _____ | |
| 6. Hot RF phase delay (degrees)
between input and output. | a. <u>Not known.</u> | |
| | b. _____ | |
| | c. _____ | |
| 7. Total anode power dissipation
(W), from both RF attenuation
and beam interception. | a. <u>158,000</u> | d. <u>195,000</u> |
| | b. <u>173,000</u> | e. <u>205,000</u> |
| | c. <u>178,000</u> | f. <u>218,000</u> |

8. Total cathode power dissipation
(W) due to backbombardment.

a. 58,000 d. 62,600

b. 58,000 e. 65,800

c. 58,000 f. 68,100

III. Space for Additional Comments

The above values were supplied in September, 1976. The following additional data were supplied by Raytheon.

(1) The low frequency cutoff of the vane circuit occurs at 7.88 GHz.

(2) The following power measurements at 9.75 GHz were supplied.

Date Supplied	Tube Number	Anode Voltage (V)	Magnetic Field (T)	Anode Current (A)	RF Output (W)
1/13/77	8A	24,300	0.4114	17.1	168,000
1/13/77	8A	22,000	0.3788	15.0	124,000
4/10/78	3C	25,000	Between 0.4 and 0.44	17.1	185,000
4/10/78	A10 (platinum cathode)	24,600	Between 0.3982 and 0.444	12.9	132,000

(3) Modulator.

The QKS1842 uses a line-type pulser with an open-circuit voltage approximately 2.2 times the operating voltage, a series resistance, a series inductance of about 100 μ H, and in parallel with the CFA a leakage capacitance of about 100 pF. The CFA itself has a capacitance of 3.65 pF. The pulse length is 1.7 μ s.

(4) The following data were supplied for operation of a tube in the high-power mode

Tube: QKS1842 X-Band Test Vehicle No. 1.

Date: Feb. 21, 1978.

Duty factor	0.001
Electromagnet current	0.64 A
Magnetic field	0.3775 T
Frequency	9.6 GHz
RF Drive Power	19.0 kW

Cathode: gold with magnesium oxide, as a cold secondary emitter.

Measured results:

Anode Current (A)	Anode voltage (kV)	RF Output Power (kW)
6.0	18.0	72.0
10.0	19.0	128.0
16.0	20.2	200.0
20.0	20.6	248.0
25.0	21.0	308.0
30.0	21.2	352.0
41.0	21.7	453.0
49.0	21.8	530.0

The high RF drive power is necessary to suppress oscillation.

Notes

1. In a forward-wave amplifier, the beam and the RF power flow in the same direction; in a backward-wave amplifier, the beam moves around the tube from output to input in the opposite direction to the power flow. In both tubes, the average beam velocity and the phase velocity of the interacting space harmonic are in synchronism when maximum RF interaction occurs.
2. The cold RF phase velocity v_p is given by

$$v_p = \frac{2\pi f}{\beta_0} \text{ m/s} ,$$

where f (Hz) is the drive frequency and β_0 (m^{-1}) is the phase constant for the interacting space harmonic, such that the phase delay per pitch is $(\beta_0 * \text{pitch length})$ radians.

3. The RF interaction impedance Z_0 is defined as the expression

$$Z_0 = \frac{|E_{RF}|^2}{2\beta_0 P} ,$$

where $|E_{RF}|$ is the peak RF electric field (V/m) parallel to the anode surface, evaluated at the anode surface for the interacting space harmonic, β_0 (m^{-1}) is the cold-circuit phase constant for the same space harmonic and P (W) is the total power flow parallel to the anode (in all space harmonics and integrated over the entire cross section of the interaction region).

4. The efficiency is defined as the expression

$$\frac{(\text{RF Output} - \text{RF Drive})}{(\text{Anode Current}) * (\text{Anode-Sole Voltage})} * 100\% .$$

5. The phase velocity is given by one of the following expressions:

$$v_p = \frac{\omega p}{\beta}$$

for the forward-wave circuit or

$$v_p = \frac{\omega p}{\beta - \beta_0}$$

for the backward-wave strapped circuit, where $\omega = 2\pi f$, p = the pitch (period) and ϕ (radians) = the measured phase shift per cavity in the direction of power flow.

APPENDIX C

DATA FOR THE VARIAN SFD-261 CFA

Data for two versions of the SFD-261 are given: one instrumented tube with a uniform anode-cathode spacing, and the production tube which has a non-circular cathode.

Normalizing parameters P_0 , f_0 , D_1 , D_2 , V_1 are used to allow an UNCLASSIFIED publication. The values are classified CONFIDENTIAL.

I.	<u>Basic Tube Data</u>	
1.	Manufacturer.	<u>Varian</u>
2.	Tube identification number.	<u>SFD-261</u>
3.	Forward-wave or backward-wave amplifier (see note 1).	<u>Forward-wave</u>
4.	Total number of anode vanes.	<u>Not known.</u>
5.	Number of active anode vanes.	<u>62</u>
6.	Transverse magnetic field (T), treated as uniform.	<u>.2530</u>
7.	Beam width (mm) in the magnetic-field direction, treated as constant.	<u>400 D₁</u>
8.	Cathode radius (mm).	<u>735 D₁</u>
9.	Anode radius (mm), measured from the axis to the vane tips.	<u>825 D₁</u>
10.	Displacement, if any, of cathode axis from geometrical center (mm).	<u>Zero (instrumented tube only)</u>
11.	Distance (mm) around the anode from RF input to RF output.	<u>4.52 D₂</u>
12.	Length (mm) around the anode of the RF circuit sever between the RF output and RF input.	<u>0.66 D₂</u>
13.	Pitch (period) of the RF circuit measured around the anode surface (mm).	<u>0.072 D₂</u>
14.	Ratio of vane spacing to pitch (period) on the anode surface.	<u>0.5</u>
15.	Drive frequency (GHz).	
	a. Lower end of operating band.	<u>$f_0 + 0.1$</u>
	b. Midband.	<u>$f_0 + 0.3$</u>
	c. Upper end of operating band.	<u>$f_0 + 0.5$</u>
	(These frequencies are used in following items.)	

16. Anode-cathode voltage, as a function of frequency:		Instrumented Tube	Production Tube
Frequency (GHz)	a.	_____	_____
	b.	_____	_____
	c.	_____	_____
Anode-cathode voltage.	a.	<u>1.325 V₁</u>	<u>1.33 V₁</u>
	b.	<u>1.3 V₁</u>	<u>1.304 V₁</u>
	c.	<u>1.18 V₁</u>	<u>1.27 V₁</u>
17. RF drive power (W) for peak output, tabulated as a function of frequency:		Instrumented Tube	Production Tube
Frequency (GHz)	a.	_____	_____
	b.	_____	_____
	c.	_____	_____
RF drive (W).	a.	<u>0.08 P₀</u>	_____
	b.	<u>0.08 P₀</u>	_____
	c.	<u>0.08 P₀</u>	_____
Notice that a separate run must be made for each frequency specified.			
18. Cold-circuit phase delay (degrees) per vane in the direction of power flow:		Instrumented Tube	Production Tube
Frequency (GHz)	a.	_____	_____
	b.	_____	_____
	c.	_____	_____
Phase delay (degrees).	a.	<u>77.99</u>	_____
	b.	<u>90.99</u>	_____
	c.	<u>104.49</u>	_____

19. Interaction impedance (2) as a function of frequency (use the definition in note 3 or supply an alternative definition in Part III):

Frequency (GHz)

	Instrumented Tube	Production Tube
a.	_____	_____
b.	_____	_____
c.	_____	_____
a.	68	_____
b.	45	_____
c.	30	_____

Impedance (2).

20. Cold-circuit RF power attenuation (dB) per pitch as a function of frequency:

Frequency (GHz)

	Instrumented Tube	Production Tube
a.	_____	_____
b.	_____	_____
c.	_____	_____
a.	.036	.0252
b.	.036	.0252
c.	.036	.0252

Attenuation (dB).

21. Type of cathode emitter surface:

a. Thermal emitter (yes/no).

No

b. Secondary emitter (yes/no).

Yes (Beryllium oxide)

c. Both thermal and secondary emitter (yes/no).

No

For thermally emitting cathode (a):

- (1) Current density that would exist under temperature-limited conditions and with no transverse magnetic field (A/m²).

Not known.

- (2) Average energy (eV) of thermal electrons on emission.

Not known.

For secondary emitter (b):

- (1) Secondary-emission coefficient (may be fractional) as a function of primary impact energy (eV). A single constant value will suffice if the detailed variation is not known.

Primary Impact Energy	Secondary-Emission Coefficient
0	0
50	1.1
100	2.06
200	2.47
300	2.71
400	2.80
500	2.78
1000	1.93
1600	1.38

- (2) Average energy (eV) of secondary electrons on emission.

About 2.0

22. Name, mailing address and telephone number of engineer who may be contacted should questions arise concerning the data provided here.

II. Performance Data for Comparison of Computation and Measurement

Please indicate whether the value supplied is a result of measurement or an analytical estimate. If no value is available, please write "not known."

	Uniform Instrumented	Off-Center Cathode
1. Drive frequency (GHz).	a. $f_0+0.1$	
	b. $f_0+0.3$	
	c. $f_0+0.5$	
2. Anode current (A).	a. 21.4	22
Measured	b. 22	22
	c. 8.4	22
3. RF output power (W).	a. $1.6 P_1$	$1.2 P_1$
Measured	b. $1.65 P_1$	$1.51 P_1$
	c. $0.62 P_1$	$1.57 P_1$
4. Measured hot phase delay (degrees) per cavity in direction of power flow.	a. Not known.	
	b. _____	
	c. _____	
5. Hot RF phase delay (degrees) between input and output.	a. Not known.	
	b. _____	
	c. _____	
6. Total anode power dissipation (W), from both RF attenuation and beam interception.	a. Not known.	
	b. _____	
	c. _____	

7.	Total cathode power dissipation (W) due to backbombardment.	Estimated as 0.05xdirect input power.
	a.	d. _____
	b.	e. _____
	c.	f. _____

III. Space for Additional Comments

All the data summarized above are taken from the report of Varian Associates, Inc.*

The variation of anode-cathode spacing in the production tube is tabulated on p. 154 of that report.

Experimental Accuracy

Magnetic field: $\pm 3\%$

Anode voltage: $\pm 1\%$

Phase delay per pitch: $\pm 2\%$

Modulator

The SFD-261 uses a hard-tube modulator with an open-circuit voltage about 1.12 times the operating voltage, and a series resistance. The pulse length is between 8 μ s and 12 μ s. Except for the starting behavior, the tube operation is observed to be insensitive to the modulator, and open-circuit voltages up to 1.38 times the operating voltage have been used.

The CFA capacitance is 4.88 pF; any additional stray capacitance has not been measured.

* H.L. McDowell, "CFA Design Improvement Program, Volume II--Computer Modeling Studies," Final Report, Contract No. N00123-75-C-1294. Prepared for U.S. Navy Ocean Systems Center, San Diego, California, by Varian Associates, Inc., Beverly, Massachusetts; 2 June 1978.

APPENDIX D

DATA FOR THE RAYTHEON QKS1319 CFA

The data presented here were measured by Raytheon Company under Subcontract No. 009439 from Harris SAI, Inc. (then Shared Applications, Inc.). The report provided by Raytheon is included here.

RAYTHEON COMPANY
Microwave and Power Tube Division
Waltham, Mass. 02154

FINAL REPORT

CFA DATA PROGRAM
FOR
COMPUTER MODELING

Prepared For

Subcontract No. 009439
of
Shared Applications, Inc.
Ann Harbor, Michigan

PT-5263
6 October 1978

TABLE OF CONTENTS

<u>Section</u>	<u>Title</u>	<u>Page</u>
1.0	PURPOSE	1
2.0	WORK STATEMENT	1
2.1	Work Performed-General	1
2.1.1	SAI Data Transmittal Form	3
2.1.2	RF Circuit Interaction Impedance Characteristics	3
2.1.3	Dispersion Curve	3
2.1.4	Full Power Operation	5
2.2	Conference at Raytheon, June 29, 1978	8
APPENDIX I		
APPENDIX II		
APPENDIX III		
APPENDIX IV		

LIST OF ILLUSTRATIONS

<u>Figure No.</u>	<u>Title</u>	<u>Page</u>
1	QKS1319 Crossed Field Amplifier	2
2	QKS1319 Dispersion Curve (Cold RF Circuit).	4
3	QKS1319 Performance at 20 amperes (Peak) (0.01 du)	6
4	Performance above 20 amperes (Peak) (0.01 du)	7

1.0 PURPOSE

A computer model and program for distributed emission crossed field amplifiers (DECFA) that is now under development at Shared Applications, Inc. (SAI) is expected to improve the techniques for designing these devices. Evaluations of this program would be enhanced by using design and performance data from an existing CFA. The purpose of this task was to provide to SAI certain technical information about one of Raytheon Company's CFAs, said information to be used solely for the evaluation of the computer model.

2.0 WORK STATEMENT

The CFA information requirements of SAI were described in the Work Statement delivered to Raytheon as part of this subcontract and they are listed as Appendix I to this final report. Data on one tube type, the QKS1319, was provided. The QKS1319 is a forward-wave device whose development was completed a few years ago and which is now being used in a production version of a radar system.

A photograph of the distributed emission crossed field amplifier, QKS1319, is depicted in Figure 1.

2.1 Work Performed - General

The following paragraphs describe the work performed in fulfillment of each item in the work statement.

Some of the information requested already existed and a simple compilation was all that was necessary. Other data items required engineering analysis and computations. The balance of the information was obtained through both low level microwave measurements and full power operation.

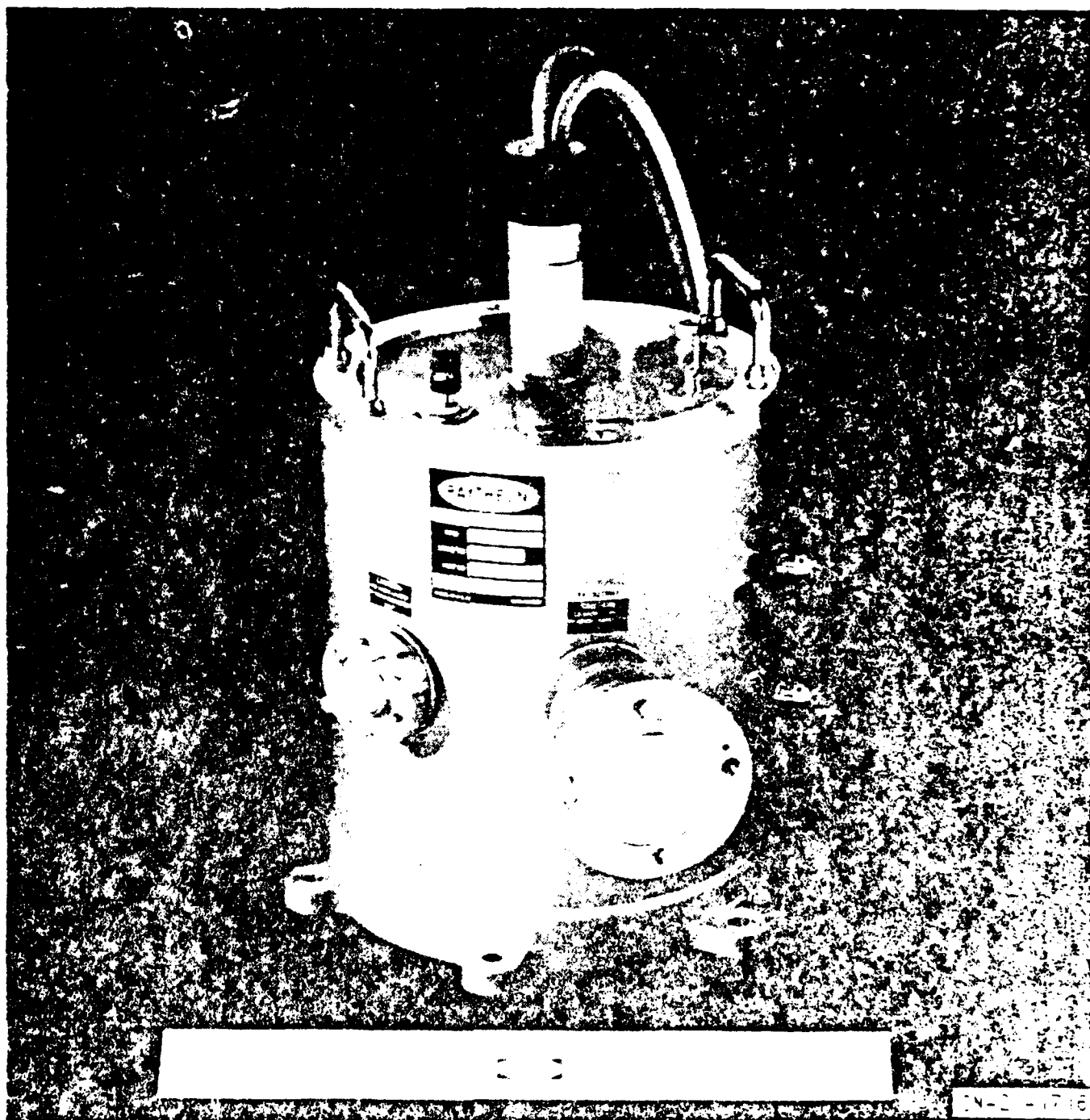


Figure 1. QMS 131P Crossed Flow Amplifier

2.1.1 SAI Data Transmittal Form

The Data Transmittal Form provided by SAI was completed to the extent possible using existing information on dimensions, cathode properties, circuit rf properties, and operating parameters and data under standard conditions.

The form, as completed, is included as Appendix II to this report.

2.1.2 RF Circuit Interaction Impedance Characteristics

Low level microwave measurements were made with an existing, typical, circuit and computations were made to determine the circuit impedance characteristics. These appear as part of the Data Transmittal Form, Appendix II.

2.1.3 Dispersion Curve

Low level microwave measurements were made on the cold rf circuit and computations were made to determine the phase shift per cavity as a function of frequency.

The dispersion curve, showing lower and upper cutoff frequencies, is presented as Figure 2.

A tabulation of numerical values of the measured points is included as Appendix III of this report.

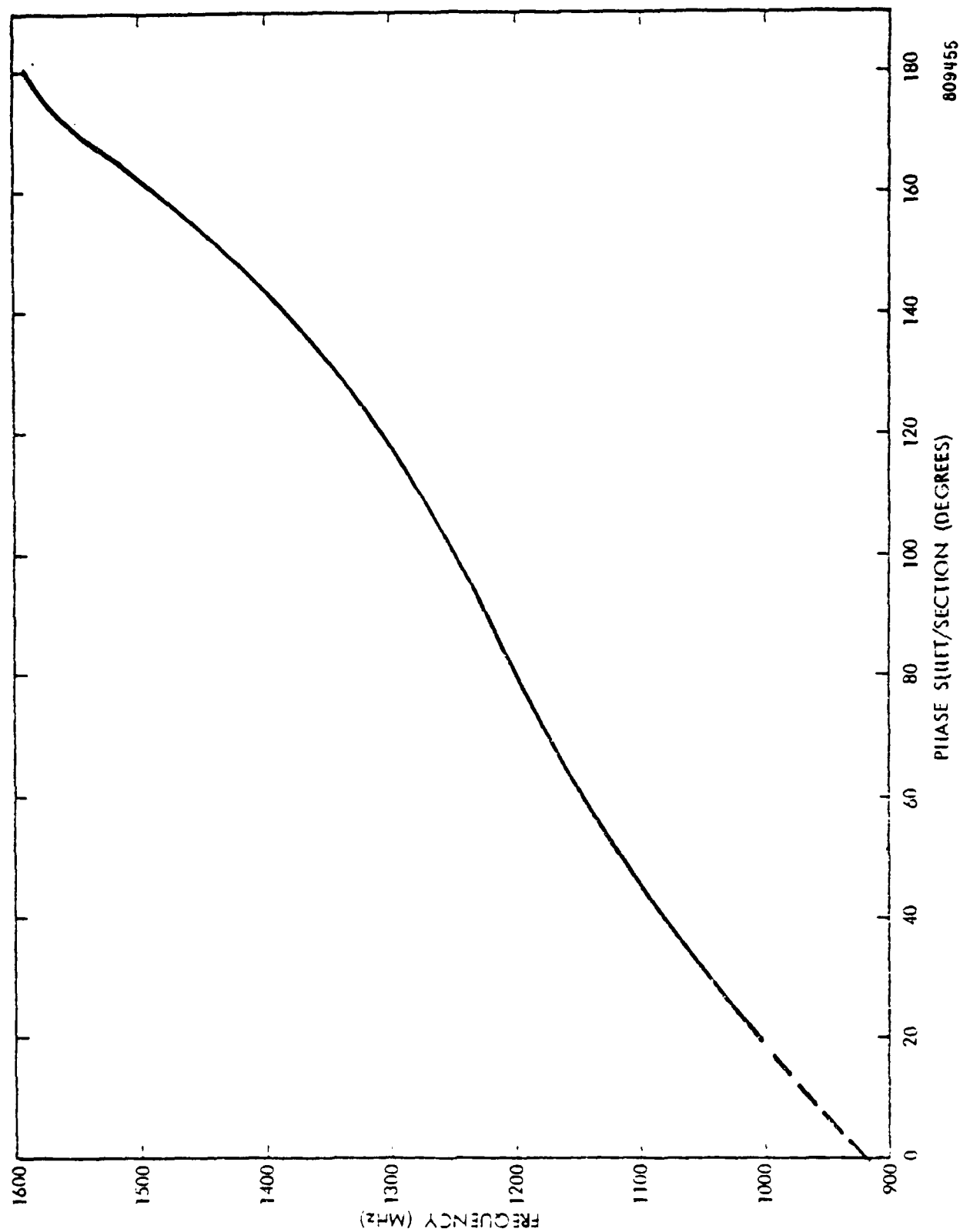


Figure 2. QK51319 Dispersion Curve (Cold RF Circuit).

2.1.4 Full Power Operation

QKS1319, Serial No. 24, was installed in the high-power test equipment with an electromagnet and measurements were made of:

- The minimum rf drive power for starting
 - The upper current mode boundary
 - The power dissipated on the anode and sole (cathode)
- a. Minimum drive power for starting was measured by setting tube input conditions for normal operation and then reducing the input drive power to the level where the tube failed to amplify. As required, this test was performed at three rf frequencies and three values of magnetic field.

These data are presented graphically in Figure 3 and a tabulation of the numerical values for the measured points appear in Appendix IV.

- b. The upper current mode boundary was measured by setting tube input conditions for normal operation and then raising the supply voltage to the current level where the tube failed to amplify.

As required, this test was performed at three rf frequencies and three values of magnetic field.

These data are presented graphically in Figure 4 and a tabulation of the numerical values for the measured points appear in Appendix IV.

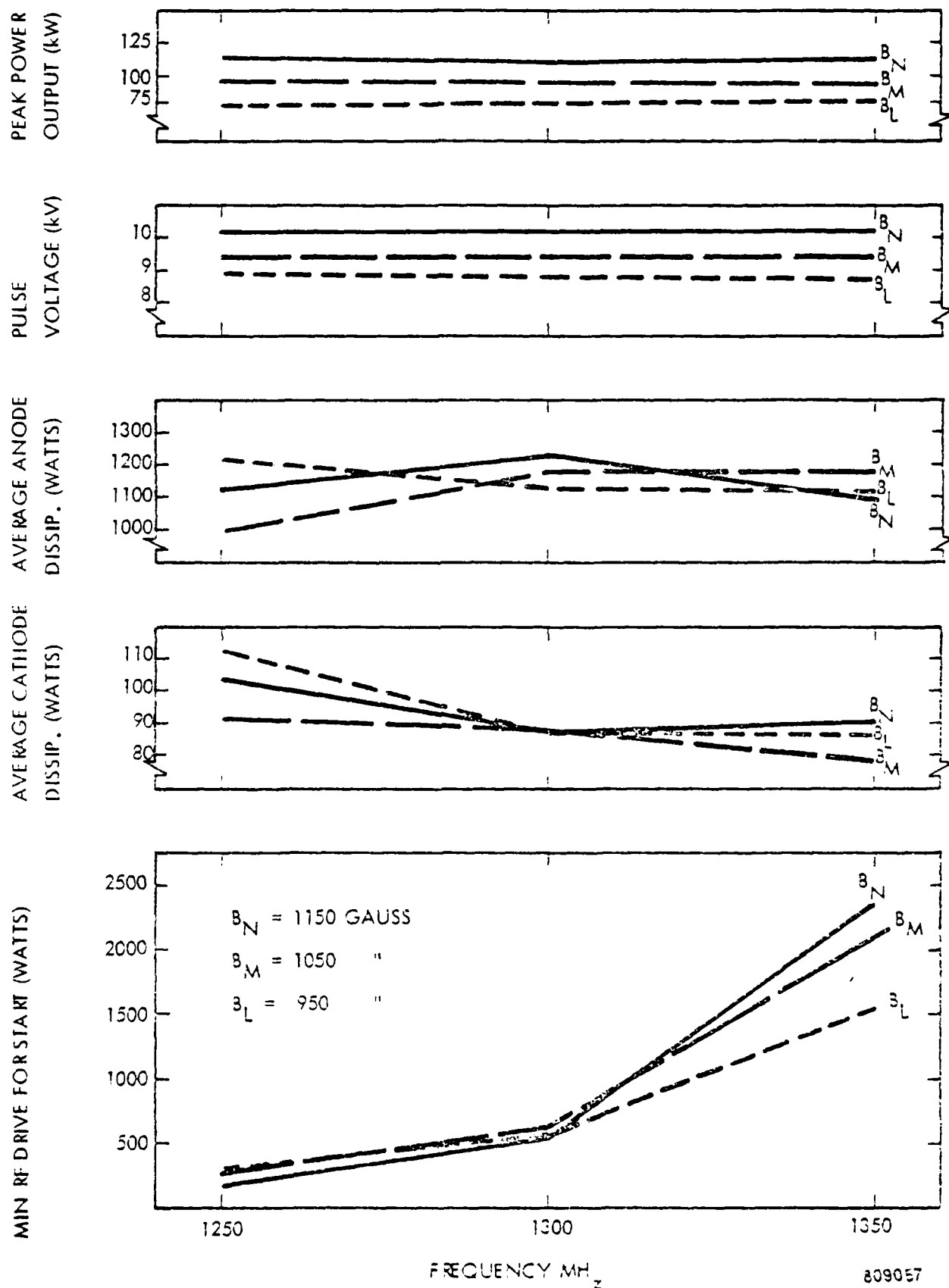


Figure 3. QKS1319 Performance at 20 amperes (Peak) (0.01 du)

PT-5263

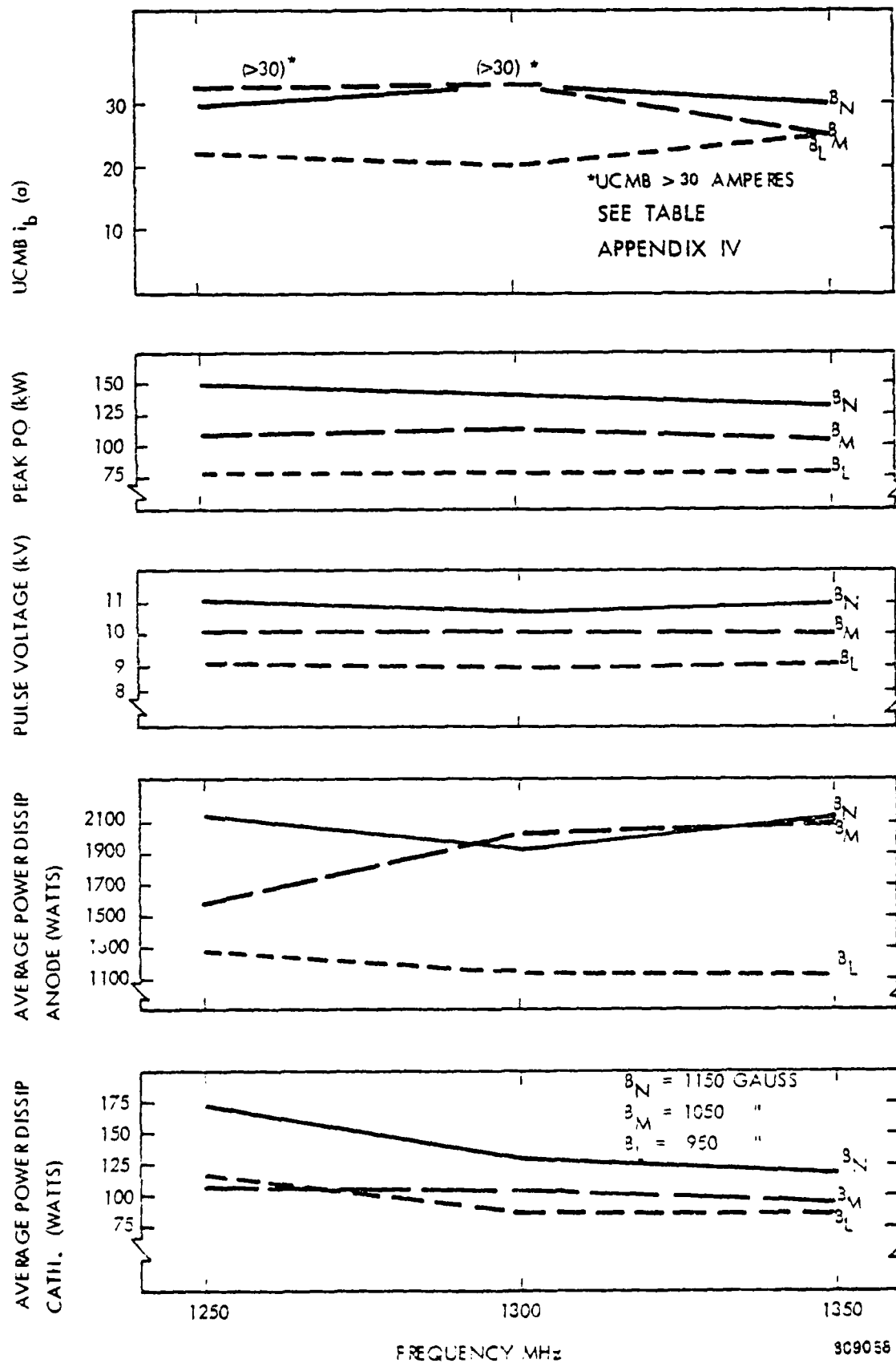


Figure 4. QKS1319 Performance Above 20 Amperes (Peak) (0.01 du).

- c. The power dissipated in the anode and in the sole (cathode) was measured calorimetrically using a thermocouple in each of the two cooling circuits.

These data are taken at each of the test points previously described except during test for minimum rf drive for starting, and are presented graphically in Figure 3 and 4. A tabulation of the numerical values for the measured points appears in Appendix IV.

2.2 Conference at Raytheon, June 29, 1978

After the above design and data information was completed, a representative of SAI met with engineers at Raytheon for the purpose of discussion and analysis of measured and computed results.

The data was judged to be satisfactory and in compliance with the requirements. No additional action is required.

APPENDIX I

CFA DATA PROGRAM FOR COMPUTER MODELING

Subcontract No. 009439

Terms and Conditions

II. Statement of Work

Raytheon shall provide SAI design and performance data on one type of forward-wave distributed-emission crossed-field amplifier, the QKS1319, as follows:

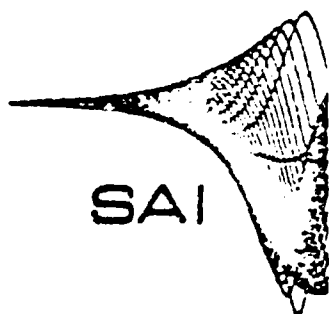
1. Basic tube data as requested in Section I of the attached SAI Data Transmittal Form. This includes information on tube dimensions, cathode properties, RF circuit properties and standard operating parameters.
2. RF circuit interaction impedance characteristics, as requested on page 5 of the SAI Data Transmittal Form. If necessary, experimental measurements will be made to determine the circuit impedance.
3. Measurements of the minimum RF drive power for starting the QKS1319 at three RF frequencies and three values of magnetic field (nine measurements total). It should be stated whether the tube operates with constant RF drive and pulsed anode voltage, with a constant anode voltage applied and pulsed RF drive or under other conditions to be described.
4. Measurements of the upper current mode boundary at three RF frequencies and three values of magnetic field (nine measurements total).

5. Measurement of the power dissipated on the anode and sole (cathode) at the highest RF output power level at each of three frequencies.
6. The data requested by tasks 3, 4, and 5 is to be presented graphically.
7. A dispersion curve for the cold RF circuit showing frequency plotted against phase shift per cavity. The curve should show the lower and upper cutoff frequencies, if any. Numerical values of measured points should be included so that SAI may derive suitable equivalent network parameters.

One conference at Raytheon is to be held between SAI and Raytheon engineers to discuss and clarify the data presented and the measurement techniques used.

DATA TRANSMITTAL FORM FOR COMPUTER ANALYSIS OF
THE DISTRIBUTED-EMISSION CROSSED-FIELD AMPLIFIER

JULY 1977



SHARED APPLICATIONS, INC.
ANN ARBOR, MICHIGAN 48104

I. Basic Tube Data

1. Manufacturer	<u>Raytheon</u>
2. Tube identification number	<u>QKS1319</u>
3. Forward-wave or backward-wave amplifier (see note 1)	<u>Forward Wave</u>
4. Total number of anode vanes	<u>52</u>
5. Number of active anode vanes	<u>45</u>
6. Transverse magnetic field (T), treated as uniform	<u>1150 Gauss</u>
7. Beam width (mm) in the magnetic field direction, treated as constant	<u>35.56 mm</u>
8. Cathode radius (mm)	<u>34.86 mm</u>
9. Anode radius (mm), measured from the axis to the vane tips	<u>39.70 mm</u>
10. Displacement, if any, of cathode axis from geometrical center (mm)	<u>Zero</u>
11. Distance (mm) around the anode from RF input to RF output	<u>210.96 mm</u>
12. Length (mm) around the anode of the RF circuit sever between the RF output and RF input (Items 11 and 12 should add to equal the anode circumference)	<u>38.25 mm</u>
13. Pitch (period) of the RF circuit mea- sured around the anode surface (mm)	<u>4.79 mm</u>
14. Ratio of vane spacing to pitch (period) on the anode surface	<u>0.424</u>
15. Drive frequency (GHz)	
a. Lower end of operating band	<u>1.250</u>
b. Midband	<u>1.300</u>
c. Upper end of operating band	<u>1.350</u>

(These frequencies are used in follow-
ing items)

16. Anode-cathode voltage, as a function of frequency:

Frequency (GHz)

a. 1.250

b. 1.300

c. 1.350

Anode-cathode voltage

a. 10,200

b. 10,200

c. 10,200

17. RF drive power (W) for peak output, tabulated as a function of frequency:

Frequency (GHz)

a. 1.250

b. 1.300

c. 1.350

RF drive (W)

a. 3500

b. 3500

c. 3500

Notice that a separate run must be made for each frequency specified.

18. Cold-circuit phase delay (degrees) per vane in the direction of power flow:

Frequency (GHz)

a. 1.250

b. 1.300

c. 1.350

Phase delay (degrees)

a. 100°

b. 118°

c. 132°

19. Interaction impedance (Ω) as a function of frequency (use the definition in note 3 or supply an alternative definition in Part III):

Frequency (GHz)

a. 1.250

b. 1.300

c. 1.350

Impedance (Ω)

a. 146.00

b. 84.17

c. 55.91

20. Cold-circuit RF power attenuation (dB) per vane as a function of frequency:

Frequency (GHz)

a. 1.250

b. 1.300

c. 1.350

Attenuation (dB)

a. .044

b. .038

c. .035

21. Type of cathode emitter surface:

a. Thermal emitter (yes/no)

no

b. Secondary emitter (yes/no)

yes (beryllium)

c. Both thermal and secondary emitter (yes/no)

no

For thermally emitting cathode (a):

(1) current density that would exist under temperature-limited conditions and with no transverse magnetic field (A/m^2)

X

(2) average energy (eV) of thermal electrons on emission

X

For secondary emitter (b):

- (1) Secondary-emission coefficient (may be fractional) as a function of primary impact energy (eV). A single constant value will suffice if the detailed variation is not known

Primary Impact Energy	Secondary-Emission Coefficient
50 eV	1.2
100	1.9
200	2.6
300	2.95
400	3.10
500	3.05
600	2.8
700	2.7
800	2.6
900	2.4

- (2) Average energy (eV) of secondary electrons on emission

Not known

APPENDIX III

DISPERSION DATA - QKS1319

$$\left(\text{PHASE SHIFT/SECTION} = \frac{(N \times \pi)}{44} \right)$$

<u>N</u>	<u>Frequency (MHz)</u>	<u>N</u>	<u>Frequency (MHz)</u>
5	1005	25	1255
6	1021	26	1266
7	1038	27	1277
8	1054	28	1289
9	1070	29	1301
10	1085	30	1314
11	1099	31	1329
12	1113	32	1343
13	1126	33	1360
14	1139	34	1377
15	1150	35	1396
16	1162	36	1416
17	1172	37	1437
18	1183	38	1460
19	1193	39	1483
20	1203	40	1505
21	1213	41	1530
22	1223	42	1552
23	1235	43	1573
24	1244	44	1583

APPENDIX IV

FULL POWER OPERATION DATA QKS1319

A. Performance @ 20 amps (peak) @ .01 du

	<u>F1</u>	<u>F2</u>	<u>F3</u>	*
Power Output	115	111	113	B Normal
kW (peak)	95	94	93	B Medium
	78	78	80	B Low
Pulse Voltage	10.2	10.2	10.2	B Normal
(kV)	9.43	9.43	9.43	B Medium
	8.98	8.82	8.68	B Low *
Anode Dissipation	1125	1230	1100	B Normal
(watts)	995	1177	1177	B Medium
	1220	1123	1123	B Low
Cathode Dissipation	104	87	90	B Normal
(watts)	92	88	78	B Medium
	112	87	87	B Low
Min RF Drive	175	525	2360	B Normal
for start	262	612	2100	B Medium
(watts)	280	577	1575	B Low

* B Normal = 1150 Gauss
 B Medium = 1050 Gauss
 B Low = 950 Gauss

FULL POWER OPERATION DATA QKS1319

B. Performance above 20 amps (peak) @ .01 du

	<u>F1</u>	<u>F2</u>	<u>F3</u>	*
UCMB	30 (emission)	>30	30 (emission)	B Normal
ib	>30	>30	25 (M.B.)	B Medium
	22 (M.B.)	20 (M.B.)	25 (emission)	B Low
Power Output	150	140	133	B Normal
kW(peak)	106	114	111	B Medium
	78	78	80	B Low
Pulse Voltage	11.0	10.6	10.9	B Normal
(kV)	10.0	9.9	10.0	B Medium
	9.0	8.3	9.0	B Low
Power				
Dissipation	2140	1926	2140	B Normal
(anode)	1584	2033	2097	B Medium
watts	1273	1123	1123	B Low
Cathode				
Dissipation	173	130	118	B Normal
(watts)	107	104	93	B Medium
	116	87	87	B Low

*B Normal = 1150 Gauss
 B Medium = 1050 Gauss
 B Low = 950 Gauss

In addition to the information given in the Raytheon report, the following additional tube data were supplied at the June 29, 1978 meeting at Raytheon.

Severed Cathode

The cathode is in two regions: an emitting region and a non-emitting region. The emitting region covers the angular segment $-4.065^\circ \leq \theta \leq 308.69^\circ$, where $\theta = 0$ is defined as the center of the input anode vane. The non-emitting region covers the segment $312.86^\circ \leq \theta \leq 351.78^\circ$. Two 4.17° gaps separate the emitting and non-emitting regions. The non-emitter is recessed with a radius of 33.7 mm, whereas the emitter radius is 34.86 mm.

The following information was supplied by telephone in January 1980.

Modulator

The QKS1319 uses a hard-tube modulator with an open-circuit voltage of 15 kV and a series regulator tube with a voltage drop of about 4 kV. The effective open-circuit voltage seen by the CFA without RF drive is between 10.5 and 11 kV depending on the actual equipment used. The pulse length is 40 μ s (52,000 RF periods) at 1% duty cycle.

Measured Power Balance

The measured power balance shows a discrepancy of about 17 percent. The errors are probably in the anode dissipation; 6 percent is a more typical experimental error.

Magnetic-Field Measurements

The magnetic field is measured with a gaussmeter in the absence of the tube both with an ALNICO permanent magnet and with an electromagnet using the same steel pole pieces. The electromagnet

current values are tabulated for the measured fields. These currents are then used to estimate the field when the tube is inserted in the magnet. The field values supplied are reproducible measurements and are believed to be accurate.

APPENDIX E

DATA FOR THE RAYTHEON QKS1705 CFA

I.	<u>Basic Tube Data</u>	
1.	Manufacturer.	<u>Raytheon</u>
2.	Tube identification number.	<u>QKS1705</u>
3.	Forward-wave or backward-wave amplifier (see note 1).	<u>Backward</u>
4.	Total number of anode vanes.	<u>Not known.</u>
5.	Number of active anode vanes.	<u>35</u>
6.	Transverse magnetic field (T), treated as uniform.	<u>0.36</u>
7.	Beam width (mm) in the magnetic-field direction, treated as constant.	<u>14.8</u>
8.	Cathode radius (mm).	<u>9.78</u>
9.	Anode radius (mm), measured from the axis to the vane tips.	<u>11.94</u>
10.	Displacement, if any, of cathode axis from geometrical center (mm).	<u>zero</u>
11.	Distance (mm) around the anode from RF input to RF output.	<u>65.5</u>
12.	Length (mm) around the anode of the RF circuit sever between the RF output and RF input. (Items 11 and 12 should add to equal the anode circumference.)	<u>9.5</u>
13.	Pitch (period) of the RF circuit measured around the anode surface (mm).	<u>1.829</u>
14.	Ratio of vane spacing to pitch (period) on the anode surface.	<u>0.404</u>
15.	Drive frequency (GHz).	
	a. Lower end of operating band.	<u>9.5</u>
	b. Midband.	<u>9.75</u>
	c. Upper end of operating band.	<u>10.0</u>
	(These frequencies are used in following items.)	

16. Anode-cathode voltage, as a function of frequency:

Frequency (GHz)	a.	<u>9.5</u>
	b.	<u>9.75</u>
	c.	<u>10.0</u>
Anode-cathode voltage.	a.	<u>31,800</u>
	b.	<u>33,000</u>
	c.	<u>34,000</u>

17. RF drive power (W) for peak output, tabulated as a function of frequency:

Frequency (GHz)	a.	<u>9.5</u>	d.	<u>9.8</u>
	b.	<u>9.6</u>	e.	<u>9.9</u>
	c.	<u>9.7</u>	f.	<u>10.0</u>
RF drive (W).	a.	<u>30,000</u>	d.	<u>30,000</u>
	b.	<u>30,000</u>	e.	<u>30,000</u>
	c.	<u>30,000</u>	f.	<u>30,000</u>

Notice that a separate run must be made for each frequency specified.

18. Cold-circuit phase delay (degrees) per vane in the direction of power flow:

Frequency (GHz)	a.	<u>9.5</u>	d.	<u>9.8</u>
	b.	<u>9.6</u>	e.	<u>9.9</u>
	c.	<u>9.7</u>	f.	<u>10.0</u>
Phase delay (degrees).	a.	<u>43</u>	d.	<u>49</u>
	b.	<u>45</u>	e.	<u>51</u>
	c.	<u>47</u>	f.	<u>53</u>

19. Interaction impedance (Ω) as a function of frequency (use the definition in note 3 or supply an alternative definition in Part III):

Frequency (GHz)

a. 9.5 d. 9.8

b. 9.6 e. 9.9

c. 9.7 f. 10.0

Impedance (Ω).

a. 7.4 d. 9.2

b. 8.0 e. 9.8

c. 8.6 f. 10.4

20. Cold-circuit RF power attenuation (dB) per anode pitch as a function of frequency:

Frequency (GHz)

a. 9.5 d. 9.8

b. 9.6 e. 9.9

c. 9.7 f. 10.0

Attenuation (dB).

a. 0.018 d. 0.018

b. 0.018 e. 0.018

c. 0.018 f. 0.018

21. Type of cathode emitter surface:

a. Thermal emitter (yes/no).

b. Secondary emitter (yes/no).

c. Both thermal and secondary emitter (yes/no).

Yes

For thermally emitting cathode (a):

- (1) Current density that would exist under temperature-limited conditions and with no transverse magnetic field (A/m^2).

Not known.

- (2) Average energy (eV) of thermal electrons on emission.

Not known.

For secondary emitter (b):

- (1) Secondary-emission coefficient (may be fractional) as a function of primary impact energy (eV). A single constant value will suffice if the detailed variation is not known.

Primary Impact Energy	Secondary-Emission Coefficient
200	1.52
400	1.93
600	2.11
800	2.15
900	2.15
1000	2.15
1200	2.11
1400	2.07

- (2) Average energy (eV) of secondary electrons on emission.

Not known.

II. Performance Data for Comparison of Computation and Measurement

Please indicate whether the value supplied is a result of measurement or an analytical estimate. If no value is available, please write "not known."

- | | | |
|---|--------------------------------|-------------------|
| 1. Drive frequency (GHz). | a. <u>9.5</u> | d. <u>9.8</u> |
| | b. <u>9.6</u> | e. <u>9.9</u> |
| | c. <u>9.7</u> | f. <u>10.0</u> |
| 2. Anode current (A). | a. <u>34</u> | d. <u>34</u> |
| Measured | b. <u>34</u> | e. <u>34</u> |
| | c. <u>34</u> | f. <u>34</u> |
| 3. RF output power (W). | a. <u>546,000</u> | d. <u>521,000</u> |
| Measured | b. <u>502,000</u> | e. <u>519,000</u> |
| | c. <u>504,000</u> | f. <u>504,000</u> |
| 4. Efficiency (see note 4). | a. <u>45.6</u> | d. <u>41.7</u> |
| Measured | b. <u>40.4</u> | e. <u>40.7</u> |
| | c. <u>40.5</u> | f. <u>39.3</u> |
| 5. Measured hot phase delay
(degrees) per cavity in
direction of power flow. | a. <u>Not known.</u> | |
| | b. <u> </u> | |
| | c. <u> </u> | |
| 6. Hot RF phase delay (degrees)
between input and output. | a. <u>Not known.</u> | |
| | b. <u> </u> | |
| | c. <u> </u> | |
| 7. Total anode power dissipation
(W), from both RF attenuation
and beam interception. | a. <u>488,000</u> | d. <u>552,000</u> |
| Estimated | b. <u>562,000</u> | e. <u>577,000</u> |
| | c. <u>552,000</u> | f. <u>594,000</u> |

8. Total cathode power dissipation
(W) due to backbombardment.

Estimated

a. 54,400 d. 56,450

b. 54,900 e. 57,300

c. 55,750 f. 57,800

III. Space for Additional Comments

Calibration of electromagnet:

Magnet current (A)	Magnetic field (T)
<u>.49</u>	<u>.3250</u>
<u>.52</u>	<u>.3375</u>
<u>.57</u>	<u>.3600</u>
<u>.59</u>	<u>.3700</u>
<u>.61</u>	<u>.3750</u>
<u>.65</u>	<u>.3900</u>

Duty factor 0.001

Operating pulse length 0.44 μ s

APPENDIX F

DATA FOR THE RAYTHEON QKS1840 CATHODE-CIRCUIT CFA

I. Basic Tube Data

1. Manufacturer.	<u>Raytheon</u>
2. Tube identification number.	<u>OKS1840</u>
3. Forward-wave or backward-wave amplifier (see note 1).	<u>Forward-wave</u>
4. Total number of anode vanes.	<u>48</u>
5. Number of active anode vanes.	<u>41</u>
6. Transverse magnetic field (T), treated as uniform.	<u>0.3 (approx.)</u>
7. Beam width (mm) in the magnetic-field direction, treated as constant.	<u>14.48</u>
8. Cathode radius (mm).	<u>20.89</u>
9. Anode radius (mm), measured from the axis to the vane tips.	<u>24.13</u>
10. Displacement, if any, of cathode axis from geometrical center (mm).	<u>0.0</u>
11. Distance (mm) around the anode from RF input to RF output.	<u>129.5</u>
12. Length (mm) around the anode of the RF circuit sever between the RF output and RF input. (Items 11 and 12 should add to equal the anode circumference.)	<u>22.11</u>
13. Pitch (period) of the RF circuit measured around the anode surface (mm).	<u>3.175</u>
14. Ratio of vane spacing to pitch (period) on the anode surface.	<u>0.304</u>
15. Drive frequency (GHz).	
a. Lower end of operating band.	<u>3.11</u>
b. Midband.	<u>3.292</u>
c. Upper end of operating band.	<u>3.54</u>

(These frequencies are used in following items.)

16. Anode-cathode voltage, as a function of frequency:

Frequency (GHz)

- a. 3.11
- b. 3.292
- c. 3.54

Anode-cathode voltage.

- a. 23,000
- b. 23,100
- c. 22,500

17. RF drive power (W) for peak output, tabulated as a function of frequency:

Frequency (GHz)

- a. 3.11
- b. 3.292
- c. 3.54

RF drive (W).

- a. 500
- b. 500
- c. 500

Notice that a separate run must be made for each frequency specified.

18. Cold-circuit phase delay (degrees) per vane in the direction of power flow:

Frequency (GHz)

- a. 3.1
- b. 3.3
- c. 3.5

Phase delay (degrees).

- a. 100.0
- b. 123.0
- c. 138.0

19. Interaction impedance (Ω) of anode circuit as a function of frequency (use the definition in note 3):

Frequency (GHz)

a. 3.1

b. 3.3

c. 3.5

Impedance (Ω).

a. 135

b. 75

c. 40

20. Cold-circuit RF power attenuation (dB) per vane as a function of frequency:

Frequency (GHz)

a. 3.1

b. 3.3

c. 3.5

Attenuation (dB).

a. 0.05

b. 0.05

c. 0.05

21. Cathode material.

Platinum (secondary emitter)

22. Forward-wave or backward-wave cathode circuit.

Forward-wave; wave is parallel to anode-circuit wave.

23. Total number of cathode vanes.

48

24. Number of active cathode vanes.

40

25. Pitch (period) of the cathode RF circuit (mm). 2.743
26. Ratio of vane spacing to pitch on cathode surface. 0.417
- (The vane centers on the cathode and anode have no angular separation.)
27. Cold-circuit phase delay (degrees) per pitch of cathode circuit in the direction of cathode power flow:
- Frequency (GHz) a. 3,100
- b. 3,300
- c. 3,500
- Phase delay (degrees) per pitch. a. 98
- b. 129
- c. 147
28. Interaction impedance (Ω) for cathode circuit as a function of frequency (see definition in note 3):
- Frequency (GHz) a. 3,100
- b. 3,300
- c. 3,500
- Impedance (Ω). a. 136
- b. 75
- c. 43

29. Cold-circuit RF power attenuation (dB)
per cathode pitch as a function of
frequency:

Frequency (GHz)

a. 3.1

b. 3.3

c. 3.5

Attenuation (dB).

(3.9 dB

a. 0.1 per pitch total)

(4.0 dB

b. 0.1 per pitch total)

(5 dB

c. 0.125 per pitch total)

30. Number of inactive vanes in
drift space.

8

a. Pitch (mm).

2.743

b. Ratio of spacing to pitch.

0.417

AD-A125 340

SIMULATION OF DISTRIBUTED-EMISSION AND INJECTED-BEAM
CROSSED-FIELD AMPLIF. (U) HARRIS SAI INC ANN ARBOR MI
D M MACGREGOR ET AL. APR 80 AFOSR-TR-80-0554

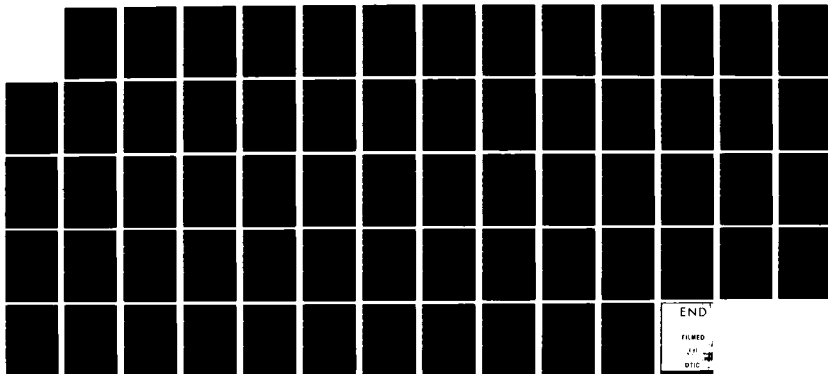
3/3

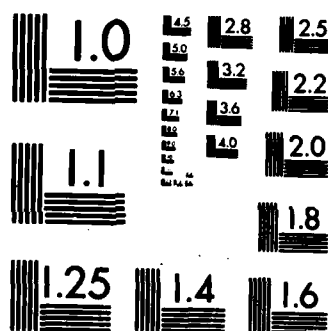
UNCLASSIFIED

F49620-77-C-0091

F/G 9/1

NL





MICROCOPY RESOLUTION TEST CHART
NATIONAL BUREAU OF STANDARDS-1963-A

II. Performance Data for Comparison of Computation and Measurement

Please indicate whether the value supplied is a result of measurement or an analytical estimate. If no value is available, please write "not known."

- | | |
|---|----------------------|
| 1. Drive frequency (GHz). | a. <u>3.110</u> |
| | b. <u>3.292</u> |
| | c. <u>3.540</u> |
| 2. Anode current (A). | a. <u>49</u> |
| | b. <u>50</u> |
| | c. <u>45</u> |
| 3. RF output power (W). | a. <u>312,000</u> |
| | b. <u>337,000</u> |
| | c. <u>250,000</u> |
| 4. Efficiency (%). | a. <u>27</u> |
| | b. <u>29</u> |
| | c. <u>27</u> |
| 5. Measured hot phase delay
(degrees) per cavity in
direction of power flow. | a. <u>Not known.</u> |
| | b. _____ |
| | c. _____ |
| 6. Hot RF phase delay (degrees)
between input and output. | a. <u>Not known.</u> |
| | b. _____ |
| | c. _____ |
| 7. Total anode power dissipation
(W), from both RF attenuation
and beam interception. | a. <u>Not known.</u> |
| | b. _____ |
| | c. _____ |

8. Total cathode power dissipation
(W) due to backbombardment.

a. Not known.

b. _____

c. _____

III. Space for Additional Comments

APPENDIX G

MEASURED SECONDARY-EMISSION CHARACTERISTICS OF CATHODE SURFACES

The data here show the secondary-emission coefficient as a function of primary impact energy for normal incidence for (1) platinum, (2) cermet (tungsten-thoria), (3) beryllium oxide, and (4) gold and magnesium oxide surfaces.

I. Platinum

Source: Raytheon Company.

The values are plotted in Fig. G.1 and tabulated below.

<u>Primary Impact Energy (eV)</u>	<u>Secondary-Emission Coefficient</u>
0	0
200	1.2
400	1.55
600	1.75
800	1.80
1,000	1.78
1,200	1.75
1,400	1.70
1,600	1.65
1,800	1.60
2,000	1.55

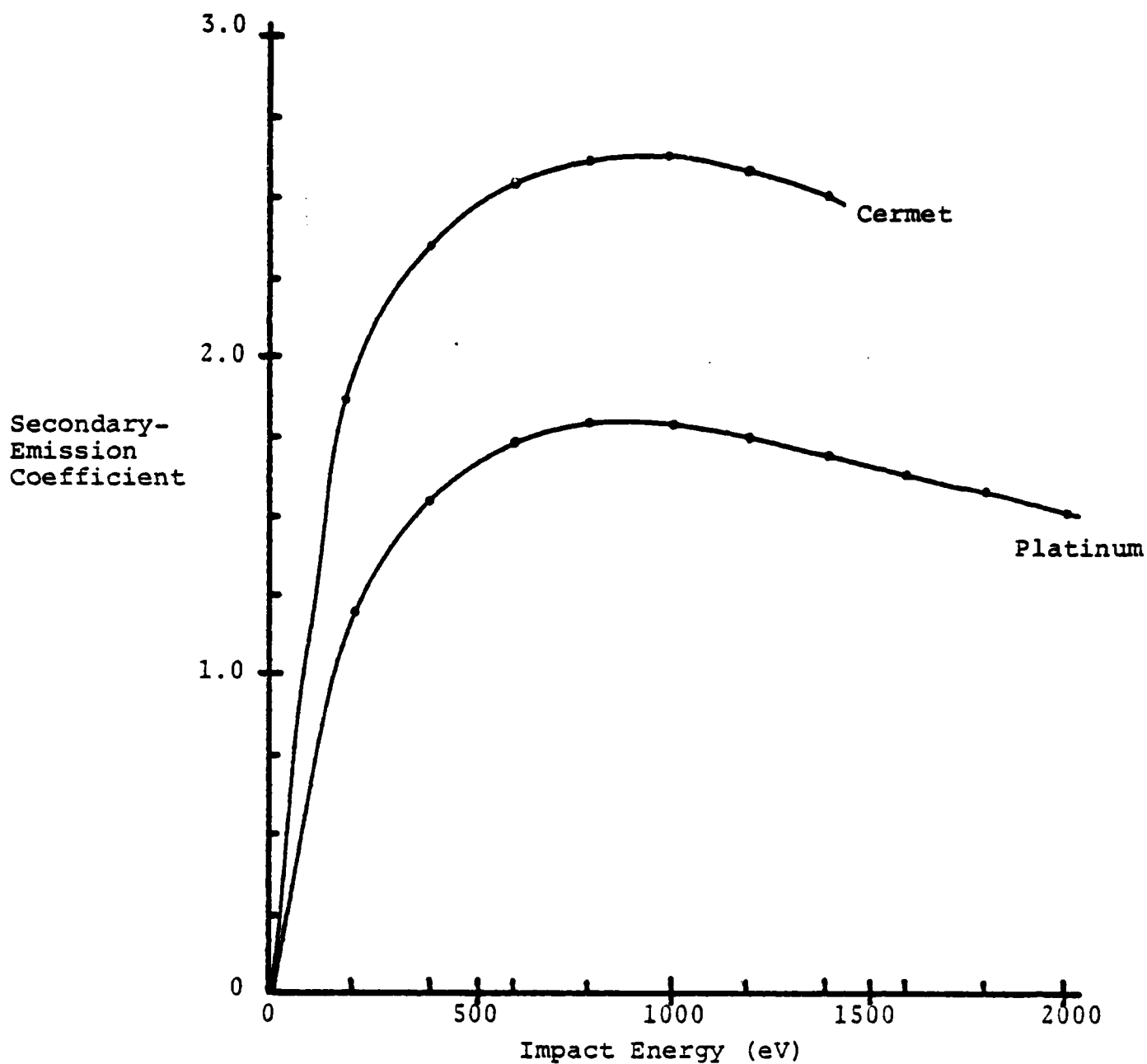


Figure G.1 Measured secondary-emission coefficient versus primary impact energy for platinum and cermet cathodes.

II. Cermet (Tungsten-Thoria)

Source: Raytheon Company.

See Fig. G.1.

<u>Primary Impact Energy (eV)</u>	<u>Secondary-Emission Coefficient</u>
200	1.86
400	2.36
600	2.58
800	2.63
900	2.63
1,000	2.63
1,200	2.58
1,400	2.53

III. Beryllium Oxide

Source: Mr. Richard Thomas, Naval Research Laboratory,
Washington, D.C.

Fig. G.2 shows the experimental values obtained at NRL.
The following compares the experimental values with those
originally used in the Varian and Harris SAI computer simulations
of the SFD-261 CFA.

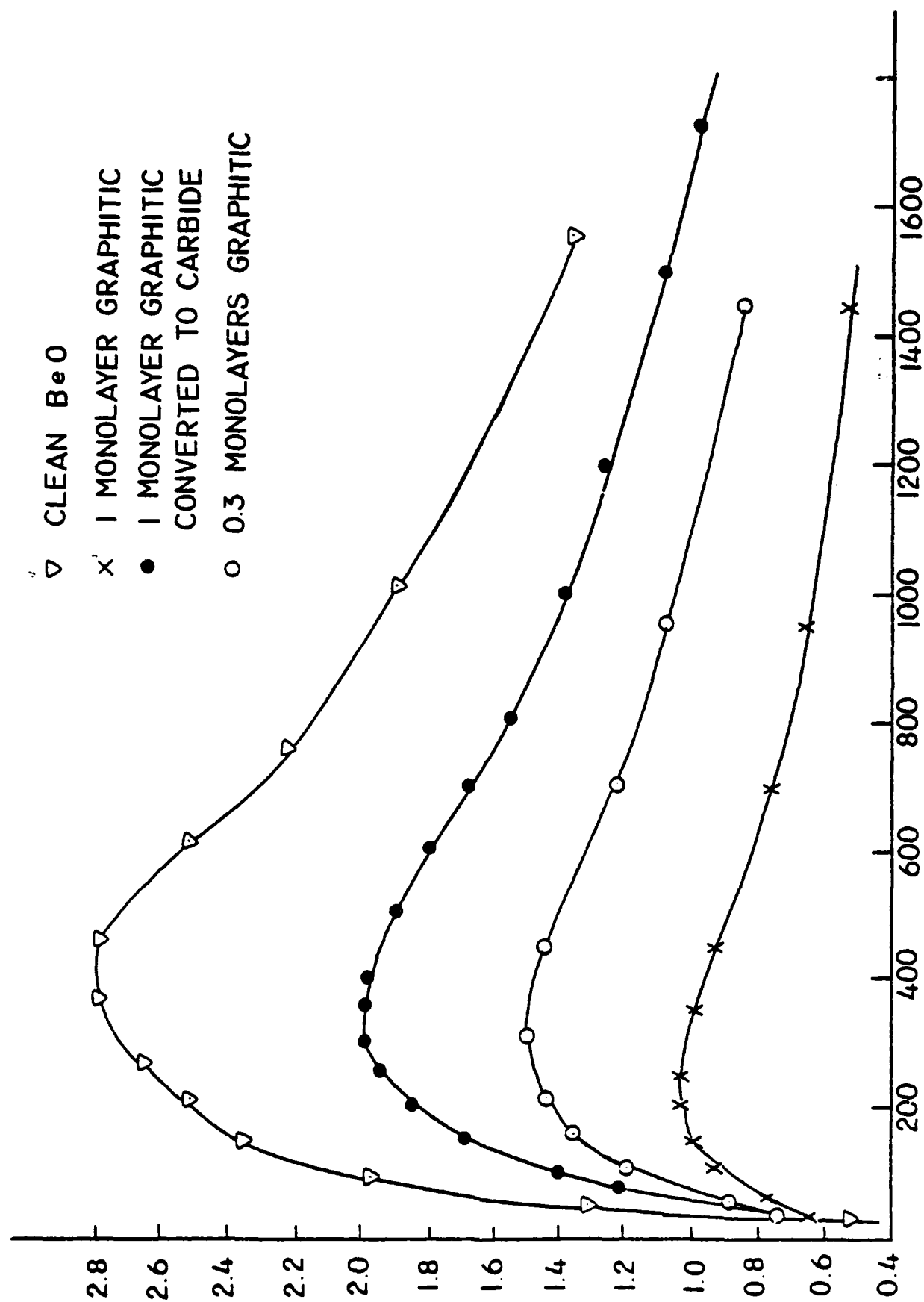


Figure G.2 Secondary-emission measurements for beryllium oxide.

Secondary-Emission Coefficient

<u>Primary Impact Energy (eV)</u>	<u>Used in 1978 Varian Simulations</u>	<u>Measured in 1978 at NRL (for Clean Surface)</u>
0.0	0.0	0.0
50.0	1.1	1.10
100.0	2.2	2.06
200.0	4.2	2.47
300.0	5.0	2.71
400.0	5.0	2.80
500.0	5.0	2.78
1,000.0	4.0	1.93
1,600.0	2.8	1.38
2,500.0	1.0	--

IV. Magnesium Oxide and Gold

Source: Raytheon Company (measured at Naval Research Laboratory).

The high secondary yield of this material has been used in the QKS1842 to produce up to 48 A anode current and 530 kW RF output power at 0.3775 T and 22 kV with 19 kW RF drive at 9.6 GHz.

The characteristic is plotted in Fig. G.3 and tabulated as follows.

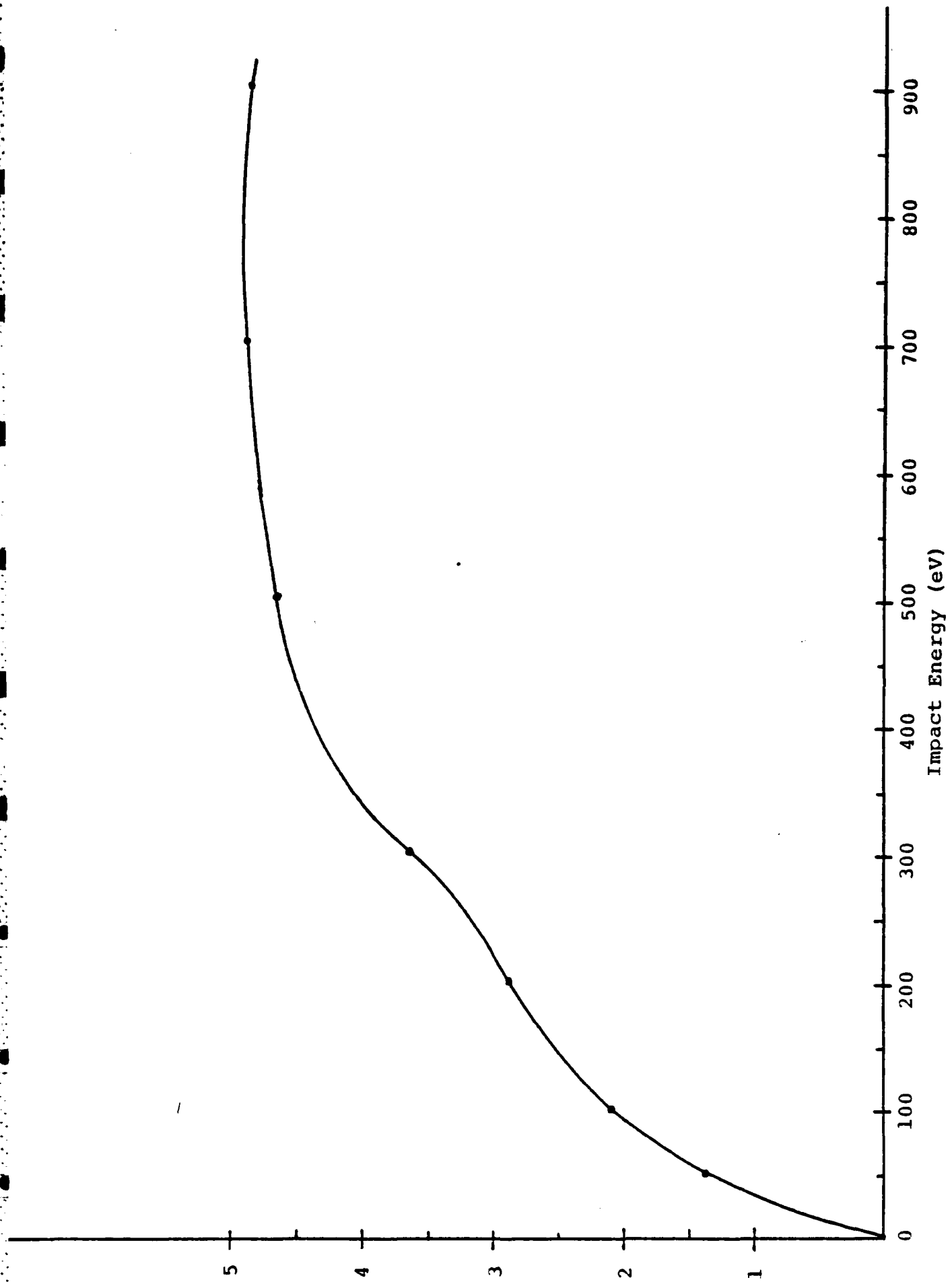


Figure G.3 Secondary-emission coefficient of magnesium oxide and gold surface.

<u>Primary Impact Energy (eV)</u>	<u>Secondary-Emission Coefficient</u>
50	1.35
100	2.15
200	2.85
300	3.65
500	4.65
700	4.85
900	4.8

APPENDIX H

CIRCUIT THEORY FOR THE DECFA

This appendix derives the equivalent networks for the RF circuit and modulator, and gives the details of the calculation of the applied electric field and the induced currents.

The three basic approximations are that

- (1) the electric fields are static,
- (2) the modulator voltage varies slowly over one RF period, and
- (3) the instantaneous average of the vane voltages is equal to the modulator voltage.

These approximations enable the vane and modulator networks to be solved independently. A further approximation of uniform azimuthal field between the vane tips allows a cylindrical solution of Poisson's equation to be used, with the corresponding analytic solution of Laplace's equation for the applied field.

A. Separation of Electric Fields due to Applied Voltages and Space Charge

With the electrostatic approximation, the total field at any point is separable into an external part due to applied direct and RF voltages and a space-charge part. Each field is derived from an electrostatic potential. The space charge potential, ϕ_{sc} , satisfies the two-dimensional Poisson's equation and is zero on the cylindrical surface of the cathode and on the vane tips. It is also approximated as zero between the vane tips. The external potential V satisfies Laplace's equation and the boundary conditions of applied voltages on the vanes. The total potential, $\phi_{sc} + V$, satisfies both Poisson's equation and the boundary conditions and is therefore the unique solution to the static problem.

B. Green's Function

Suppose that vane n of the CFA has potential V_n and that all other vanes have potential zero, relative to the cathode. The potential at point (r, θ) in the anode-cathode region is then

$$\phi = V_n G(r, \theta - \theta_n) \quad (\text{H.1})$$

where θ_n is the angular coordinate at the center of the vane, and G is a Green's function. Make the approximation that the angular electric field is uniform around the circumference in the gap between the vanes. This is a useful approximation at the anode, but it would not be sufficiently accurate for an emitting cathode circuit where electrons move more slowly.

Define the following notations:

θ_B = one-half the angle subtended at the axis by the gap between adjacent vanes.

θ_G = one-half the pitch angle subtended by one vane and its adjacent gap,

r_a = anode radius,

r_c = cathode (sole) radius.

Then the Green's function is given by the following solution of Laplace's equation

$$G(r, \theta) = a_0 \ln \left(\frac{r}{r_c} \right) + \sum_{k=1}^{\infty} a_k \left[\left(\frac{r}{r_a} \right)^k - \left(\frac{r_c}{r_a} \right)^{2k} \left(\frac{r}{r_a} \right)^{-k} \right] \cos k\theta \quad (\text{H.2})$$

with

$$a_0 = \frac{\theta_B + \theta_G}{\pi \ln(r_a/r_c)} \quad (\text{H.3})$$

and

$$a_k = \frac{2 \sin k\theta_B \sin k\theta_G}{\pi k^2 \theta_G \left[1 - \left(\frac{r_c}{r_a} \right)^{2k} \right]} \quad (\text{H.4})$$

for $k \geq 1$.

The coefficients a_0 and a_k are derived by Fourier analysis of the voltage around the period $0 \leq \theta \leq 2\pi$, with $G(r_a, \theta) = 1$ on one vane and $G(r_a, \theta)$ decreasing linearly to zero in the gap on each side.

The corresponding electric field Green's functions are

$$G_r(r, \theta) = - \frac{\partial}{\partial r} G(r, \theta) \quad (\text{H.5})$$

and

$$G_\theta(r, \theta) = - \frac{1}{r} \frac{\partial G(r, \theta)}{\partial \theta} , \quad (\text{H.6})$$

or

$$G_r(r, \theta) = - f_0/r$$

$$- \sum_{k=1}^{\infty} f_k \left[\left(\frac{r}{r_a} \right)^{k-1} + \left(\frac{r_c}{r_a} \right)^{2k} \left(\frac{r}{r_a} \right)^{-(k+1)} \right] \cos k\theta \quad (\text{H.7})$$

$$G_{\theta}(r, \theta) = \sum_{k=1}^{\infty} f_k \left[\left(\frac{r}{r_a} \right)^{k-1} - \left(\frac{r_c}{r_a} \right)^{2k} \left(\frac{r}{r_a} \right)^{-(k+1)} \right] \sin k\theta, \quad (H.8)$$

where

$$f_0 = \frac{(\theta_B + \theta_G)}{\pi \ln(r_a/r_c)} \quad (H.9)$$

and

$$f_k = \frac{2 \sin k\theta_B \sin k\theta_G}{\pi k \theta_G r_a \left[1 - (r_c/r_a)^{2k} \right]} \quad (H.10)$$

The field (G_r, G_{θ}) has zero divergence and curl to satisfy Maxwell's equations for a quasistatic field.

In the model, 100 terms of the anode suffice up to half way from the sole to the anode. At greater radii, 500 terms are used. The fields are evaluated on a 41 x 41 mesh. Because of the symmetry in θ , only the fields for positive θ need to be stored. The mesh covers values of θ up to 2.5 vanes distant from the reference vanes, as trials show that the field components are less than six percent of their maximum values outside this range. On the anode, the radial field is extrapolated linearly from the two nearest mesh points and the angular field is known exactly. The local field at position (r, θ) is calculated for a given particle by area-weighting the contributions from the four nearest mesh points, treating the mesh as locally rectangular.

C. Applied Voltage

It is convenient to separate the charge-free potential into a slowly varying applied part $V_{CFA}(t)$ due to the modulator and

the RF part $V_{RFn}(t)$ on each vane. With this approximation of slow time variation, $V_{CFA}(t)$ is the time average, over 1 RF period, of the voltage on any of the vanes.

The potential V_n on vane n is

$$V_n = V_{CFA} + V_{RFn} \quad (H.11)$$

The term V_{RFn} is obtained from a solution of the network equations, and is the voltage across the admittance Y_a in the equivalent network, Figure H.1.

Summing over all the vanes gives the total potential

$$V(r, \theta) = V_{CFA} \sum_{n=1}^{NVANES} G(r, \theta - \theta_n) + \sum_{n=1}^{NVANES} V_{RFn} G(r, \theta - \theta_n) \quad (H.12)$$

Using the actual expression for G , Equation H.2, gives

$$V(r, \theta) = \frac{V_{CFA} \ln(r/r_d)}{\ln(r_a/r_c)} + \sum_{n=1}^{NVANES} V_{RFn} G(r, \theta - \theta_n) \quad (H.13)$$

showing the separation into direct and RF fields. In the program the two terms of Equation H.13 are computed separately.

D. Electrode Current

The current flowing from an electrode (cathode, a vane, or the drift section electrode) into an external circuit is

$$I_n = - \frac{dQ_n}{dt} \quad (H.14)$$

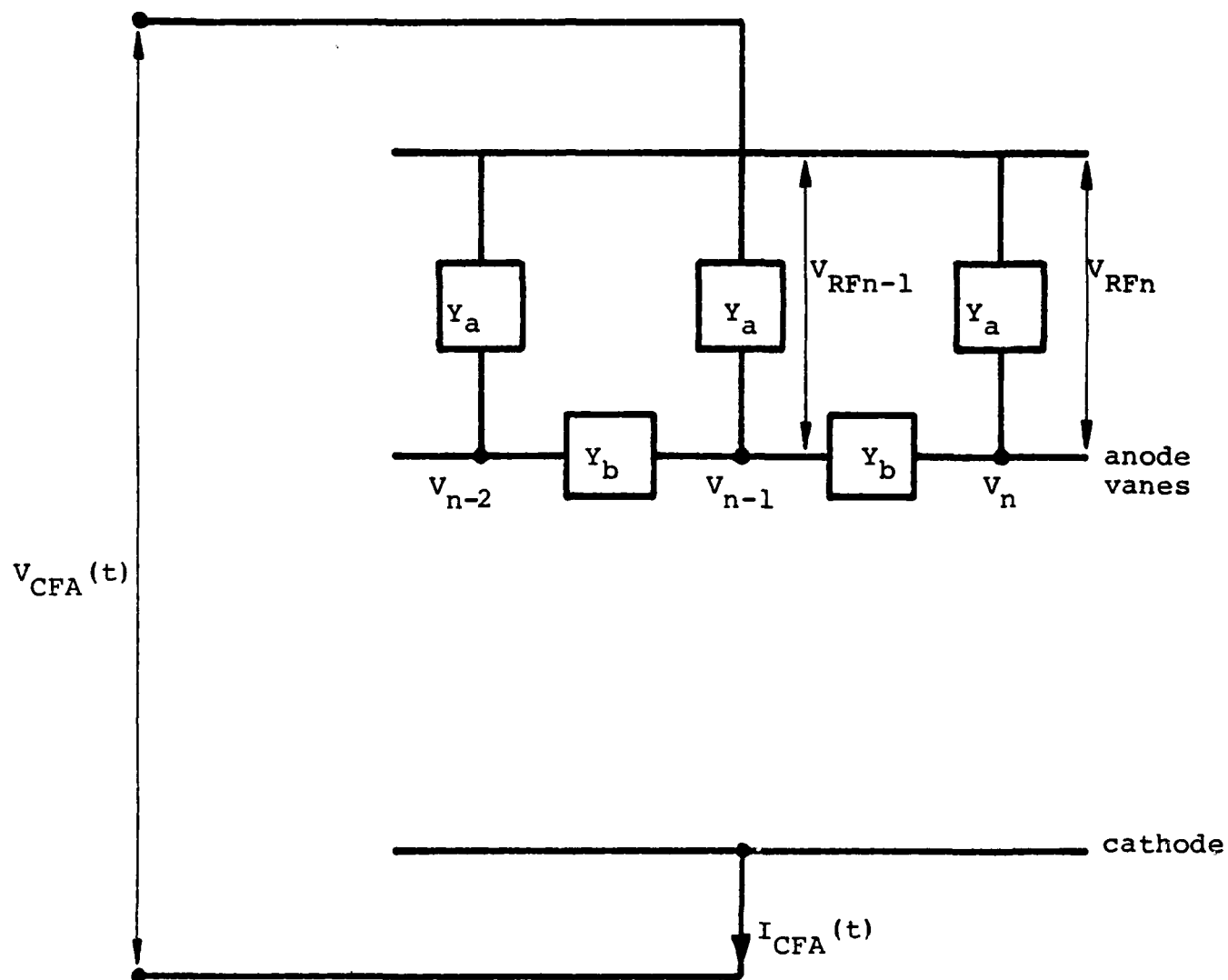


Figure H1. Portion of CFA equivalent network.

where Q_n is the total charge on the surface of the electrode. (Note that the current I_n does not include the surface "skin" current that is produced by the magnetic field tangential to the surface.)

Using Gauss's theorem, an equivalent expression for this current is

$$I_n = - \frac{d}{dt} \int_S \epsilon_0 \bar{E} \cdot d\bar{S} \quad (H.15)$$

in terms of the outward normal component of the electric field \bar{E} (all parts: space charge, direct and RF) on the surface S of the electrode. Equation H.15 can be used in the present model to calculate the total cathode current but not for the RF current on an individual vane, since the detailed configuration of the slow-wave circuit is not included in the calculation of the field \bar{E} . In general a three-dimensional solution of the wave equation would be needed. Separating \bar{E} into its applied component and space-charge component gives two parts of the current: that due to the electrode static potential V_n relative to the cathode, and the induced current due to space charge in the device.

The current can therefore be written

$$I_n = \text{induced current} - \sum_{j=1}^N C_{nj} dv_j/dt \quad (H.16)$$

where N is the total number of electrodes, and C_{nj} is the coefficient of capacitance between electrodes n and j .

Expressions for the induced current are given in Section F of this appendix.

E. Approximate Equivalent Circuits

The present program computes the induced current directly and incorporates the capacitances in an external equivalent circuit.

1. RF network

For the RF network, Equation H.16 gives for vane n

$$I_n = \text{induced current} - \frac{d}{dt} V_{CFA}(t) \sum_{j=1}^N C_{nj} - \sum_{j=1}^N C_{nj} \frac{d}{dt} V_{RFj} \quad (H.17)$$

The intervane capacitances C_{nj} for $n \neq j$ are not calculated directly, but are included in the admittance Y_b of Figure H1. Here the capacitances between non-adjacent vanes are neglected. The capacitance C_{nn} between vane n and the cathode is included in the admittance Y_a .

The network admittances are combinations of inductance, capacitance, and resistance, which cannot be computed from a purely electrostatic field. Instead they are chosen to fit the experimental phase velocity, interaction impedance and attenuation that are obtained in cold tests.

Finally the approximation of slowly varying modulator voltage allows the term including $\frac{d}{dt} V_{CFA}(t)$ to be neglected in Equation H.17. The RF network (Section VIII) is then treated as independent of the modulator.

2. Modulator circuit

For the modulator current, the last term of Equation H.17 is neglected, with the approximation that the RF voltages cancel

when they are summed at any instant. (With Equation H.15 this approximation would be unnecessary, however.) Hence Equation H.17 becomes, summing over n ,

$$I_{CCT}(t) = \text{induced current} - C \frac{d}{dt} V_{CFA}(t) \quad (H.18)$$

as in the equivalent circuit of Section IX.

The capacitance C is calculated by treating the anode and cathode as concentric cylinders, and is then added to any external leakage capacitance that is to be included.

F. Derivation of Induced Current

1. Computation from charges

The total charge-free potential at position (r, θ) is

$$V(r, \theta) = \sum_{n=1}^{NVANES} V_n G(r, \theta - \theta_n) \quad , \quad (H.19)$$

by linear superposition of the contributions of the NVANES vanes.

Then a charge q at (r, θ) induces a charge Q_n on vane n given by ^{25,27}

$$Q_n = -q G(r, \theta - \theta_n) \quad . \quad (H.20)$$

Let the charge q have velocity \bar{v} . Then the induced current on vane n is ^{25,27}

$$I_n = \frac{dQ_n}{dt} = -q \bar{v} \cdot \nabla G(r, \theta - \theta_n) \quad (H.21)$$

Notice that the actual rate of charge collection on any vane, or net emission from the cathode averaged over a finite time interval, should not be included in Equation H.21. The long-term averages of the anode convection current and the induced current summed over any set of vanes are equal. For each vane the instantaneous current is given by summing Equation H.21 for all the charges q between the anode and the cathode.

The local electric field $\bar{E}_n(r, \theta)$ due to vane n without space charge is given by

$$\bar{E}_n = -V_n \nabla G(r, \theta) \quad . \quad (H.22)$$

Hence combining Equations H.21 and H.22 gives

$$I_n = -q \frac{\bar{v} \cdot \bar{E}_n}{V_n} \quad (H.23)$$

and also

$$V_n I_n = -q \bar{v} \cdot \bar{E}_n \quad . \quad (H.24)$$

Equation H.24 shows that the induced current on vane n due to charge q gives the rate of working on the charge of the field \bar{E}_n , where the field \bar{E}_n due to vane n is computed as if the charge q were absent.²⁵

For example, the induced current leaving the cathode, due to a single charge q at radius r , is

$$I_{CFA}(t) = -q \left(\frac{dr}{dt} \right) \frac{1}{r \ln(r_a/r_c)} \quad (H.25)$$

where the anode and cathode are treated as concentric cylinders of radii r_a and r_c .

2. Computation from fields

Applying the divergence theorem to the volume τ bounded by the anode vanes, the gaps between the vanes, and the cathode (surfaces) and of unit width in the magnetic-field direction, gives

$$\int_{\tau} \nabla \phi_{SC} \cdot \nabla V \, d\tau = \int_S \phi_{SC} \frac{\partial V}{\partial n} \, dS - \int_{\tau} \phi_{SC} \nabla^2 V \, d\tau \quad (\text{H.26})$$

$$= \int_S V \frac{\partial \phi_{SC}}{\partial n} \, dS - \int_{\tau} V \nabla^2 \phi_{SC} \, d\tau \quad (\text{H.27})$$

where $\partial/\partial n$ represents the derivative along the outward normal. This is zero, because ϕ_{SC} is zero on S and V satisfies Laplace's equation.

Now use, in place of V , the Green's function $G(r, \theta - \theta_n)$ with unit potential on vane n only. Replace the volume integral in Equation H.27 by a sum over all charges q . Then the expression that results is

$$- \sum q G(r, \theta - \theta_n) = \epsilon_0 \int_{S_n} \frac{\partial \phi_{SC}}{\partial n} \, dS \quad (\text{H.28})$$

where S_n is now the surface of vane n . This is an alternative expression for the charge induced on vane n . The corresponding induced current due to all charges q is then

$$I_n = - \epsilon_0 \frac{d}{dt} \left[\int_{S_n} \frac{\partial \phi_{SC}}{\partial n} \, dS \right] \quad (\text{H.29})$$

If this expression can be computed with sufficient accuracy it will provide the induced current I_n on each vane more efficiently than direct summation of Equation H.21 over all the charges. Notice, however, that using Equation H.29 instead of the Green's function requires two solutions of Poisson's equation per time step in order to separate the space-charge field from the total field.

APPENDIX I

THEORY OF THE RF NETWORK

Throughout this section the approximation is made that the modulator voltage varies slowly relative to the RF drive voltage. Then the RF network can be treated independently of the modulator.

A general form of low-frequency equivalent network is shown in Figure 7 (Section VIII). Nodes 1, 2, 3, 4, ..., represent the vanes of the CFA circuit and their voltages produce quasistatic RF fields seen by the electrons.

The circuit calculations have three parts:

1. Derivation and solution of the network equations relating the vane voltages and the driving current,
2. Calculation of the induced current from the beam motion, and
3. Choice of the network parameters to represent an actual circuit.

A. General Network Equations. Number the nodes around the tube in the counterclockwise direction as 1 to NVANES, where NVANES is the total number of active vanes in the tube. For a forward-wave circuit, RF drive is applied at node 1; for a backward-wave circuit at node NVANES. Thus, in both cases, the RF wave and the synchronous electrons are defined to move in the counterclockwise direction (θ increasing).

Define the following notation:

C_a = capacitance (F) between node and ground,

Γ_a = reciprocal inductance (H^{-1}) between node and ground,

G_a = conductance (Ω^{-1}) between node and ground,

C_b = capacitance (F) between adjacent nodes,

Γ_b = reciprocal inductance (H^{-1}) between adjacent nodes,

G_b = conductance (Ω^{-1}) between adjacent nodes,

C_c = capacitance (F) between alternate nodes,

Γ_c = reciprocal inductance (H^{-1}) between alternate nodes.

G_c = conductance (Ω^{-1}) between alternate nodes,

C_1 = load capacitance at first and last nodes,

Γ_1 = reciprocal of load inductance at first and last nodes,

G_1 = load conductance at first and last nodes,

C_2 = load capacitance at second and penultimate nodes,

Γ_2 = reciprocal of load inductance at second and penultimate nodes,

G_2 = load conductance at second and penultimate nodes,

$I_{i1} \cos (\omega t - \gamma_1)$ = driving current at first node,

$I_{in2} \cos (\omega t - \gamma_2)$ = driving current at second node (normally zero),

$I_{inNV} \cos (\omega t - \gamma_{NV})$ = driving current at last node (used for a backward-wave circuit),

$I_{inNV1} \cos (\omega t - \gamma_{NV1})$ = driving current at penultimate node (normally zero)

$V_k(t)$ = instantaneous voltage at node k ($1 \leq k \leq \text{NVANES}$),

$I_k(t)$ = induced current at node k . (Appendix H).

Applying Kirchoff's Laws gives an expression for the voltage at an intermediate vane ($3 \leq k \leq \text{NVANES}-2$) as

$$\begin{aligned} C_a \frac{d^2 V_k}{dt^2} - C_b \frac{d^2}{dt^2} (V_{k+1} - 2V_k + V_{k-1}) - C_c \frac{d^2}{dt^2} (V_{k+2} - 2V_k + V_{k-2}) \\ + G_a \frac{dV_k}{dt} - G_b \frac{d}{dt} (V_{k+1} - 2V_k + V_{k-1}) - G_c \frac{d}{dt} (V_{k+2} - 2V_k + V_{k-2}) \\ + \Gamma_a V_k - \Gamma_b (V_{k+1} - 2V_k + V_{k-1}) - \Gamma_c (V_{k+2} - 2V_k + V_{k-2}) = \frac{dI_k}{dt} \end{aligned} \quad (I.1)$$

Similar equations apply at the end nodes with the appropriate admittance terms replaced by zero since the connecting network elements are absent there. In matrix form, these equations become

$$\underline{C} \frac{d^2 \bar{V}}{dt^2} + \underline{G} \frac{d\bar{V}}{dt} + \underline{\Gamma} \bar{V} = \frac{d\bar{I}}{dt} \quad (I.2)$$

where \bar{V} is the vector $(V_1, \dots, V_{\text{NVANES}})$, the vector \bar{I} is $(I_1 + I_{\text{in } 1}, I_2 + I_{\text{in } 2}, I_3, \dots, I_{\text{NVANES}-1} + I_{\text{out } 2}, I_{\text{NVANES}} + I_{\text{out } 1})$ and \underline{C} , \underline{G} and $\underline{\Gamma}$ are square matrices of size NVANES x NVANES.

B. Numerical Solution. At the start of the calculation, the capacitance matrix is inverted. With this rearrangement, the node equations become

$$\frac{d^2\bar{V}}{dt^2} = \underline{C}^{-1} \left(\frac{d\bar{I}}{dt} - \underline{G} \frac{d\bar{V}}{dt} - \underline{F}\bar{V} \right) . \quad (I.3)$$

This is a set of simultaneous second-order differential equations soluble in time steps by the predictor-corrector method. The initial conditons are

$$\bar{V} = 0 \quad (I.4)$$

and

$$\frac{d\bar{V}}{dt} = 0 . \quad (I.5)$$

The network equation Equation I.3 requires the time derivatives dI_k/dt for $1 \leq k \leq NVANES$. These are evaluated by extrapolating a third-degree polynomial fitted to the four previous values of current I_k computed. Trials have been made for a 35-vane tube with an ideal "spoke-of-charge" model. The results show that calculating the induced current at eight steps in the RF period gives a steady-state solution accurate only to within 30 percent, but with 16 such steps the error is reduced to four percent. To ensure numerical stability, the network equations are solved on a smaller time step (usually 1/500 the RF period) than that used for the beam motion.

C. Choice of the Network Elements. To relate the network parameters to the measured quantities, the analytical steps are as follows:

1. Specific forms of the admittances Y_a , Y_b and Y_c are chosen.

2. The dispersion equation is derived, giving the phase delay and attenuation per vane as a function of the network elements and the drive frequency.

3. The power flow for a single traveling wave is computed, giving the characteristic impedance.

4. The driving current I_1 representing a specified RF drive power is derived.

5. The vane geometry is used to relate the characteristic impedance to the measured interaction impedance for a given space harmonic of the electric field.

Step 3 also yields the load admittance required to match the cold circuit (i.e., with no reflected waves at the ends).

1. Simple Network. Figure 8 (Section VIII) shows a simple form of the general network. It is specified by only three parameters G_a , C_a , and Γ_b , which are chosen to give the measured values of phase delay per sectional pitch, interaction impedance and attenuation per section at a given frequency. The admittances of the generator and load are assumed to equal the cold network admittance in order to provide a match at both ends. The directions of power flow and wave motion are the same in both forward-wave and backward-wave tubes when viewed on the network, but in the backward-wave tube the driving current is applied at the right, at node NVANES.

2. Dispersion Equation. Define the following parameters for a signal at frequency $\omega/2\pi$:

- ϕ = cold-circuit phase delay between adjacent vanes,
- α = exponential voltage decay constant to account for attenuation,
- Z_{char} = characteristic impedance, $V_k^2/2P$ (real),
- P = power flow along the network for a single traveling wave,
- Y_0 = complex characteristic admittance of the network and admittance of matched load.

Consider a single traveling voltage so that the forward-wave voltages are

$$V_k = \text{Re}\{V_1 \exp j[\omega t - (k-1)\phi]\} \exp - (k-1)\alpha \quad (\text{I.6})$$

an a backward-wave tube has the voltages

$$V_k = \text{Re}\{V_1 \exp j[\omega t + (k - \text{NVANES})\phi]\} \exp(k - \text{NVANES})\alpha \quad (\text{I.7})$$

for $1 \leq k \leq \text{NVANES}$. Such a wave propagates with a matched 11 load and in the absence of driving currents from the beam.

Using the general network equation I.3 for a node away from the ends gives the dispersion equation as

$$1 - \cos \phi \cosh \alpha = \frac{\omega^2 C_a}{\omega^2 b} \quad (\text{I.8})$$

3. Characteristic Admittance and Load Admittance.

The load admittance Y_1 required for a reflectionless termination is given by

$$Y_1 = \frac{\Gamma_b \sin \phi e^{-\alpha}}{\omega} - \frac{j\Gamma_b(1 - \cos \phi e^{-\alpha})}{\omega} \quad (I.9)$$

This expression is the ratio of the current (in the direction of power flow) through the admittance Y_b to the voltage at vane k . Then, the characteristic impedance Z_{char} is given by

$$Z_{char} = \frac{|V_k|^2}{2P} \quad (I.10)$$

where P is the power flow along the line at node k or

$$Z_{char} = \frac{1}{\text{Re}(Y_1)} \quad (I.11)$$

Using Equations I.8 - I.11, it is seen that the values of the elements in Figure 8 are as follows:

$$G_a = 2\Gamma_b \sin \phi \sinh \alpha/\omega,$$

$$C_a = 2\Gamma_b(1 - \cos \phi \cosh \alpha)/\omega^2,$$

$$\Gamma_b = \omega e^{\alpha}/(\sin \phi Z_{char}),$$

$$G_1 = 1/Z_{char},$$

$$\Gamma_1 = \Gamma_b(1 - \cos \phi e^{-\alpha}).$$

The total admittance seen by the beam at a single vane is

$$Y = 2Y_1 + Y_a \quad (I.12)$$

For the lossless case ($\alpha=0$), this reduces to

$$Y = \frac{1}{Z_{\text{char}}} = \frac{1}{Z_0}$$

for both forward-wave and backward-wave tubes, where Z_0 is the impedance parameter used by Dombrowski.³ This identification enables the two models to be compared for the case of ideal spokes of current. Agreement is excellent, with less than 0.5 percent error for the synchronous case, thus verifying the numerical procedure used here. Of course, the present network equations are the more general of the two treatments.

The value of Z_{char} is related to an experimental measurement in Section F of this appendix.

4. Power and Driving Current. The driving current is $I_{\text{in } 1} \cos \omega t$ for the forward-wave tube (at node 1) and $I_{\text{in } NV} \cos \omega t$ for the backward-wave tube (at node NVANES). The amplitude is chosen so that the time-averaged RF power flowing into the input node in the absence of the beam equals the specified RF drive power excluding the power dissipated in the load conductance G_1 .

In the forward-wave tube, the condition that node 1, with voltage V_1 , "see" an infinite line is that the driving current is

$$I_{\text{in } 1} = V_1[Y_1 + Y_b(\exp j + \exp -j - 1)] \quad , \quad (\text{I.14})$$

in the absence of the beam.

The RF power leaving node 1 in the direction of propagation, towards node 2, is then

$$P_{\text{drive}} = \frac{1}{2} \operatorname{Re} (I_{\text{in } 1} - Y_1 V_1) V_1^* ; \quad (\text{I.15})$$

where P_{drive} is the drive power given as supplied to the CFA. Hence the voltage at node 1, again in the absence of the beam, is

$$V_1 = \sqrt{\{2P_{\text{drive}} / \operatorname{Re}[\exp j \phi \exp \alpha - 1]\}} . \quad (\text{I.16})$$

or

$$V_1 = \sqrt{2P_{\text{drive}} Z_{\text{char}}} \exp \alpha . \quad (\text{I.17})$$

(The general network of Figure 7 has been treated similarly, but requires two driving currents of different phase to represent the infinite line.) Equations I.14 and I.16 thus give the amplitude $I_{\text{in } 1}$ for a given RF drive power P_1 . In the backward-wave tube the same current is applied at node NVANES instead of node 1.

D. Oscillation

The driving current $I_{\text{in } 1}$ or $I_{\text{in } NV}$ is kept constant in the presence of the beam. Then Equation I.15 is used to define the effective RF drive power. In general this can be less than the cold RF drive power because of power traveling backwards towards the input. The difference between the computed value of P_{drive} and the cold RF drive power equals the reverse-directed power that is reaching the input node.

If this difference is zero or negative, the power returned to the load G_1 at the input exceeds the total RF power that is delivered by the driving current $I_{in 1}$, and the input power from Equation I.15 is printed as a zero or negative number. The interpretation is that the network is oscillating. However, the numerical solution is stable throughout. Notice, too, that this reverse-directed wave which produces oscillations has the same cold phase delay ϕ as the cold-circuit wave, while the directions of both the wave and the power flow are reversed. In the actual CFA such a condition shows as a mode boundary and may induce spurious signals at other frequencies.

The RF power at intermediate vanes is computed as $\overline{V_1^2}/Z_{char}$, and the RF output power is simply $G_1 \overline{V_{NVANES}^2}$ or $G_1 \overline{V_1^2}$ for forward- or backward-wave devices respectively. The bars denote averaging of the instantaneous values over one RF period.

E. Power Balance

A power-balance equation is used to check the accuracy of a steady state solution as seen by the network.

Thus, the input power from external drive and the beam is given by

$$\text{TOTAL INPUT} = \overline{V_1(t) I_{in 1} \cos \omega t} + \sum_{k=1}^{NVANES} \overline{I_k(t) V_k(t)} , \quad (I.18)$$

for the forward-wave tube, or

$$\begin{aligned} \text{TOTAL INPUT} = & \overline{V_{NVANES}(t) I_{in NV} \cos \omega t} \\ & + \sum_{k=1}^{NVANES} \overline{I_k(t) V_k(t)} , \quad (I.19) \end{aligned}$$

for the backward-wave tube.

The gross output power, including the power dissipated in the generator, is

$$\text{TOTAL OUTPUT} = G_1 \overline{V_1(t)^2} + \sum_{k=1}^{\text{NVANES}} G_a \overline{V_k(t)^2} + G_1 \overline{V_{\text{NVANES}}(t)^2} \quad (\text{I.2})$$

The program compares the two expressions and prints the difference as a percentage of the total input power.

This difference is the rate of change of stored energy in the network inductances and capacitances, or equivalently in the RF field between the vanes and the cathode. It is zero in a steady state but in general fluctuates between ± 80 percent of the total RF power.

F. Phase Delay, Interaction Impedance, and Characteristic Impedance

The vane RF voltage V_{RF} corresponding to RF power P is given by (Equation I.10)

$$V_{\text{RF}} = \sqrt{2Z_{\text{char}}P} \quad (\text{I.2})$$

The corresponding interaction impedance Z_{int} for the fundamental space harmonic is given by

$$Z_{\text{int}} = \frac{E_{\text{RF}}^2}{2\beta^2 p} \quad (\text{I.2})$$

where E_{RF} is the fundamental space harmonic amplitude of the electric field on the circuit and β is the corresponding wavenumber.

The wavenumber β is related to the vane period p and the phase shift ϕ_b per vane (as seen by the beam) by

$$\beta p = \phi_b \quad . \quad (I.23)$$

For the forward-wave circuit, the angles ϕ (Equation I.6) and ϕ_b are both equal to the total externally measured phase delay from the input to the output divided by the number (NVANES-1) of pitches along the vane circuit. For the backward-wave circuit, the angle ϕ_b equals $\pi - \phi$, as Section G of this appendix explains.

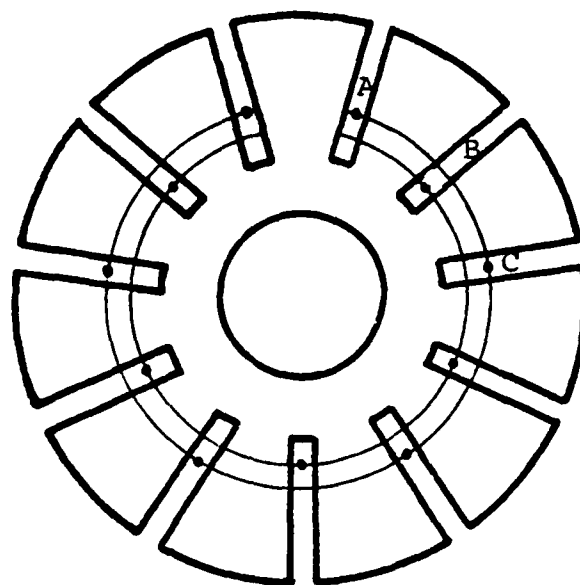
Neglect the reentrancy of the structure, assume that the total electric field is uniform between the vane tips and perform a spatial Fourier analysis to relate the terms E_{RF} and V_{RF} . The result is³⁰

$$\frac{Z_{int}}{Z_{char}} = \left(\frac{\sin \phi_b/2}{\phi_b/2} \frac{\sin \alpha \phi_b/2}{\alpha \phi_b/2} \right)^2, \quad (I.24)$$

where α is the ratio of the gap length between vanes and the vane period, and ϕ_b is the phase delay per pitch as seen by the beam. The interaction impedance is measurable by perturbing the fields in the beam region with a dielectric sheet. The computer program uses this measured value as an input parameter and derives the characteristic impedance Z_{char} using Equation I.24.

G. Backward Waves

The network equations used here make no distinction between forward-wave and backward-wave beam interaction. The network elements are chosen so that the power flow and phase delay from the RF input to the RF output match the measured values. A strapped vane line is treated as a parallel transmission line with adjacent vanes connected to alternate straps as in Figure I.1.³¹ Because the vanes are portions of



Phase delay from A to C = 2θ

Phase delay from A to B = $\theta - \pi$

Figure 11. Strapped vane line as a backward-wave RF circuit. (After Brown)

resonant cavities, the voltages between alternate vanes (at nodes A and C in Figure I.1) are in phase with the wave propagating along the line while the voltage at node B has a phase π radians out of phase with the average of the phases at A and C. In other words, the experimentally observed phase delay is 2ϕ along the line from A to C but the phase at node B is delayed by $\phi - \pi$ from that at A. Since ϕ is always less than π , the vane voltages produce a phase delay in the opposite direction, from C to B to A, of magnitude $\pi - \phi$ per pitch. Hence, the beam interacts with a wave traveling in the opposite direction to the power flow. In the model the voltages on the even-numbered vanes are reversed in sign when the beam RF fields are computed. This change is valid only for the time-harmonic fields; the time-averaged part of the vane voltage (the direct anode-cathode voltage) is not changed in sign.

Because the change in the sign of the vane voltage reverses the rate of working of the voltage on the electrons, the induced currents computed from the beam must also be reversed in sign on the even vanes before they are used in the network equations. Then spokes of charge traveling with the beam are seen by the network as a wave traveling in the opposite direction, from RF input to RF output.

H. Comparison of RF Field Calculations

Here the anode is treated as a set of segments (vanes) equally spaced around the interaction region. The RF voltage and phase are given for vane j as V_{RFj} and ϕ_j . Then the RF field (E_r, E_θ) at position (r, θ) at time t is given by

$$E_r(r, \theta) = \sum_{j=1}^{NVANES} V_{RFj} G_r[r, (\theta - \theta_j)] \cos(\omega t - \phi_j) \quad (I.25)$$

and

$$E_{\theta}(r, \theta) = \sum_{j=1}^{NVANES} V_{RFj} G_{\theta}[r, (\theta - \theta_j)] \cos(\omega t - \phi_j), \quad (I.26)$$

where θ_j is the angular position of vane j .

The terms G_r and G_{θ} in Equations I.25 and I.26 are given by Equations H.7-H.10 of Appendix H.

The θ -independent term of Equation H.7 is omitted throughout, in consistency with the approximation that the sum of the RF voltages over all the vanes equals zero at any instant. If the modulator voltage is included with the vane voltage V_n this term must be present.

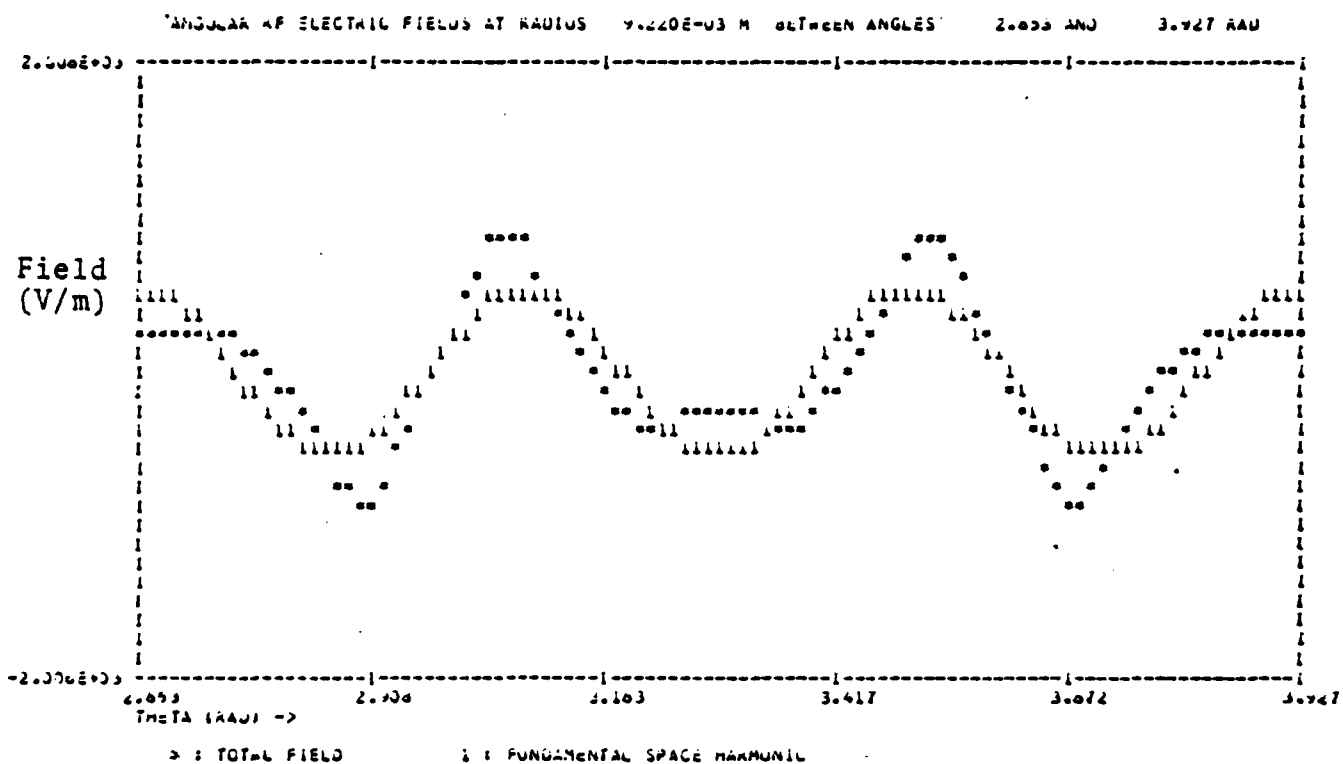
The fundamental RF space-harmonic amplitude V_s is given from Equations I.21-I.23 as

$$V_s = \left| \beta E_{RF} \right| \quad (I.27)$$

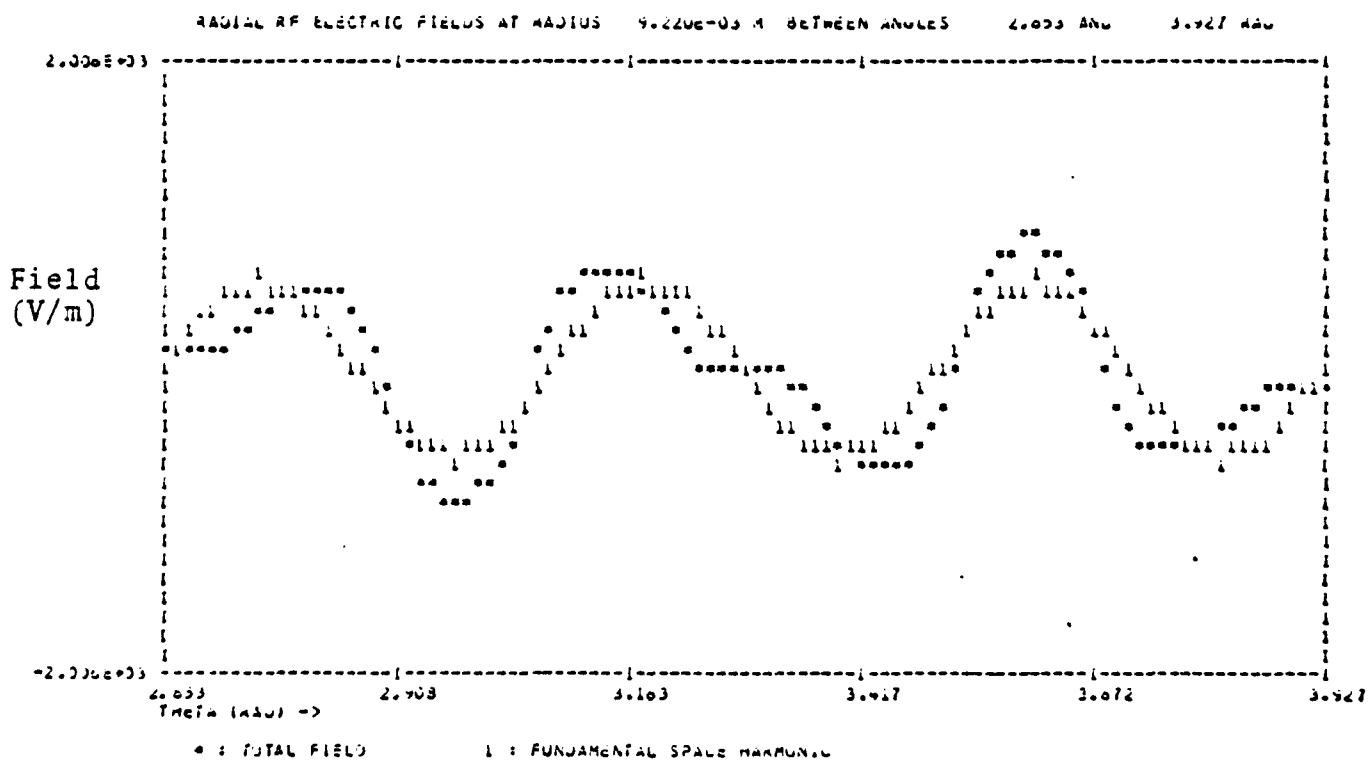
or

$$V_s = V_{RF} \sqrt{\frac{Z_{int}}{Z_{char}}} \quad (I.28)$$

In Figures I.2, I.3 and I.4, the total fields are compared with the analytical values for the fundamental space harmonic in rectangular coordinates. The numerical values correspond to the QKS1842 tube with an anode radius of 9.708 mm and a sole radius of 7.748 mm. All the vanes have the same voltage amplitude of 287 V (corresponding to an RF power of 5.5 kW). The voltage on successive vanes differs in phase by 133 degrees in the direction of wave motion as seen by the beam in the backward-wave tube. Equivalently, the phase shift in the input-output direction is 47 degrees since the voltages on alternate vanes have opposite signs because of the strap connections.

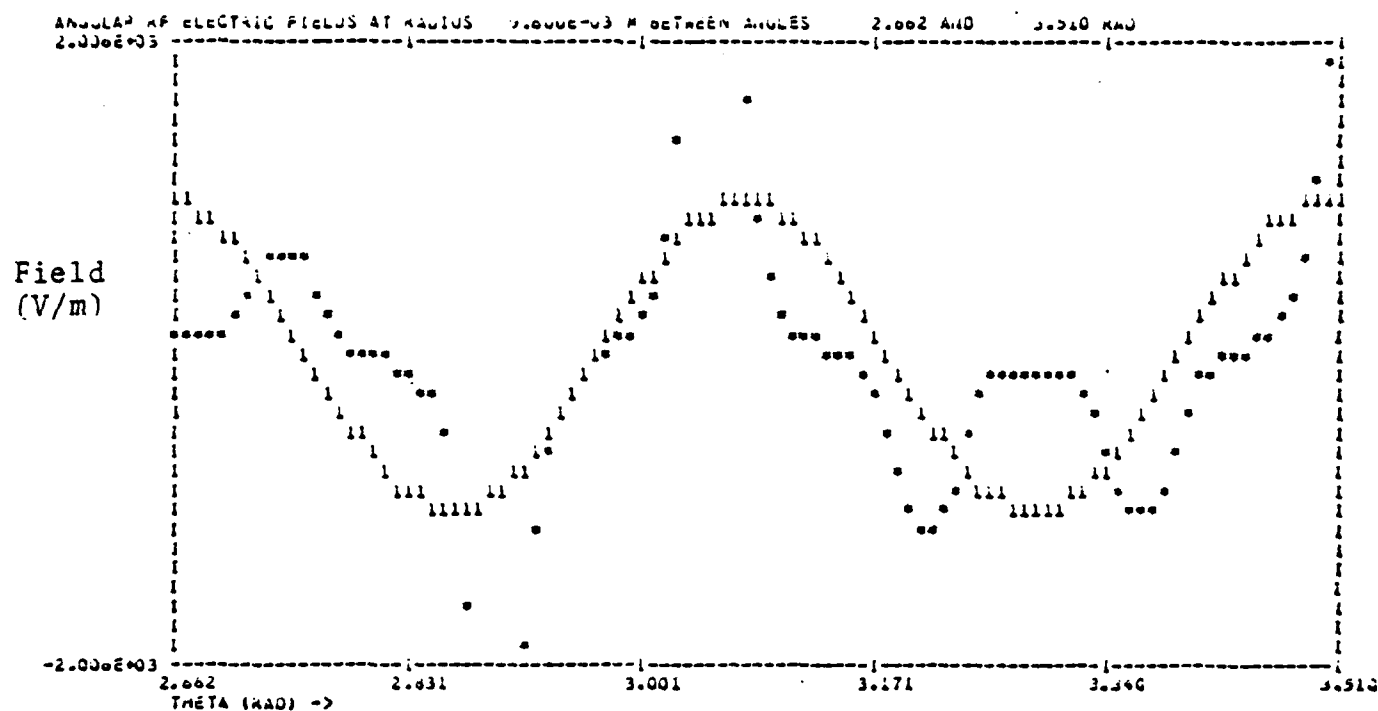


a. Angular Fields

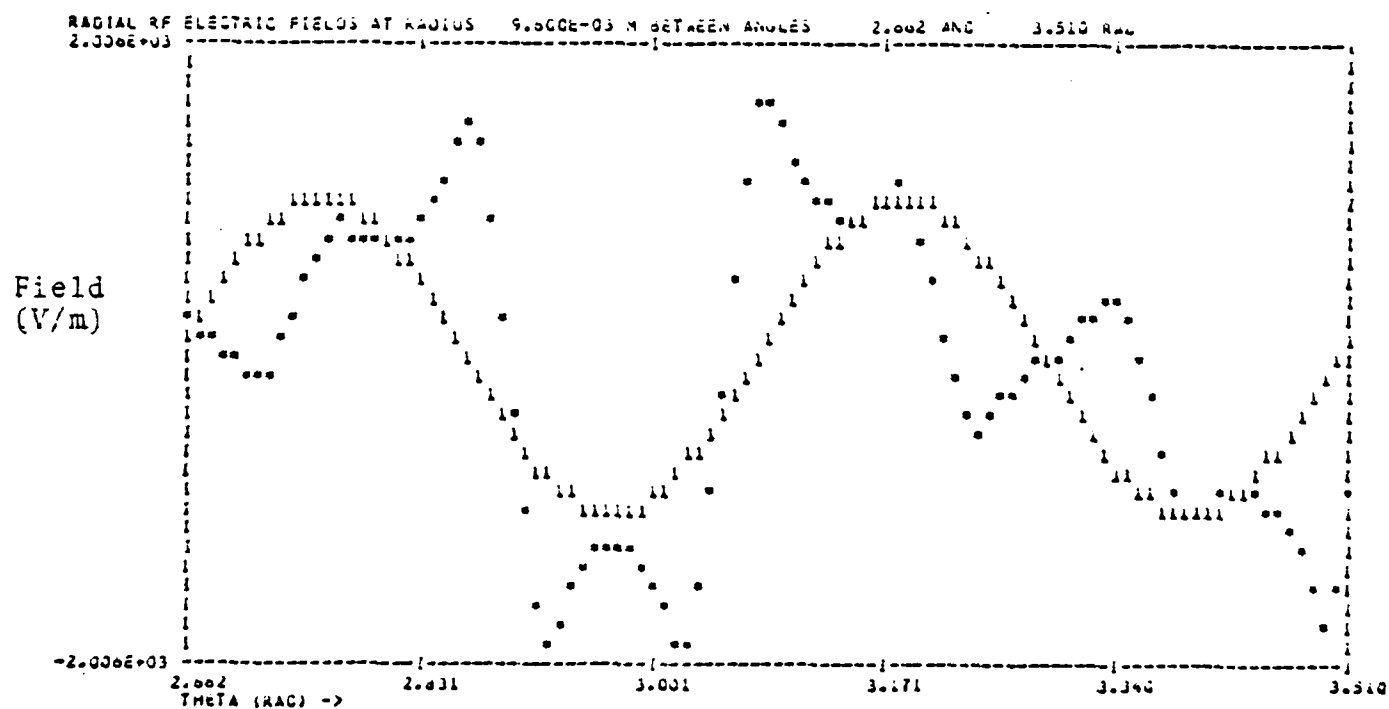


b. Radial Fields

Figure I.2 Comparison of exact values and single space harmonic of RF-circuit fields in QKS1842 at radius 9.2 mm.

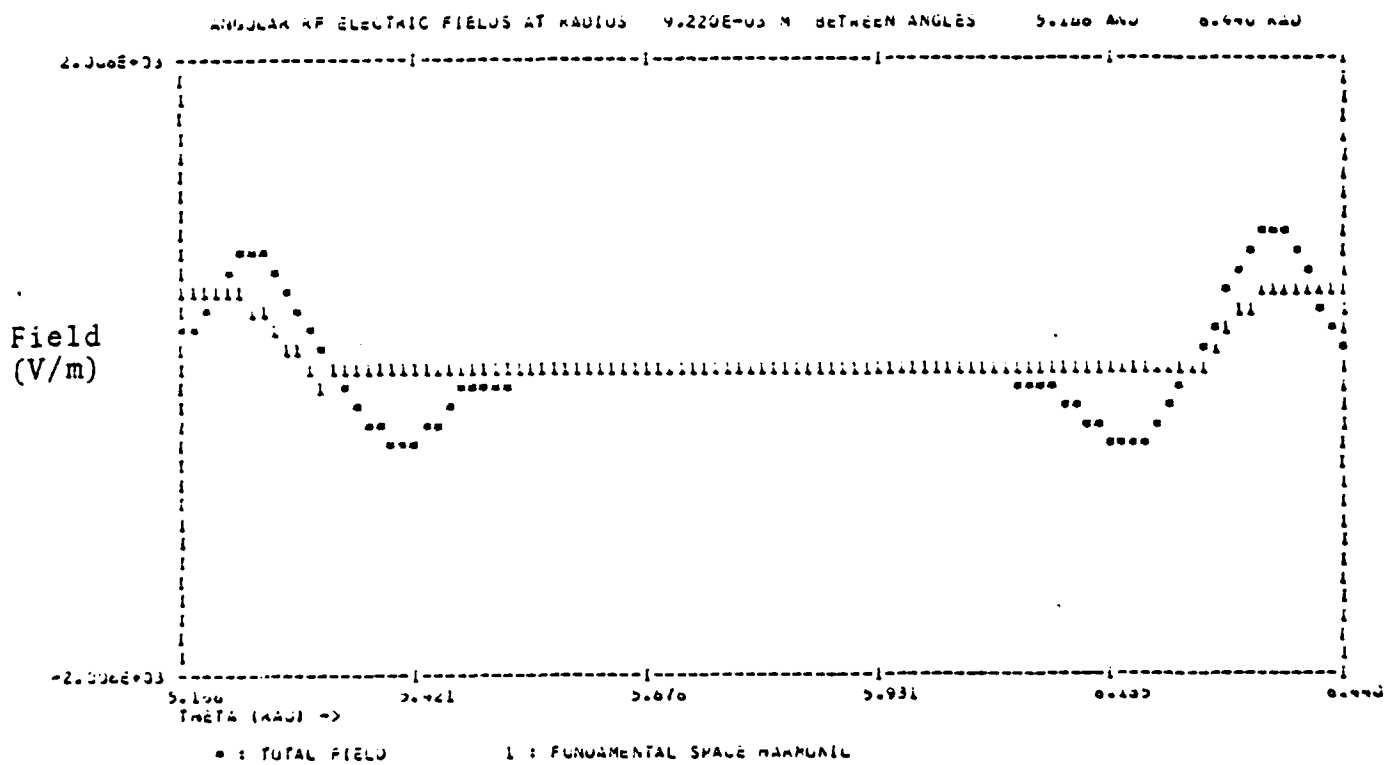


a. Angular Fields

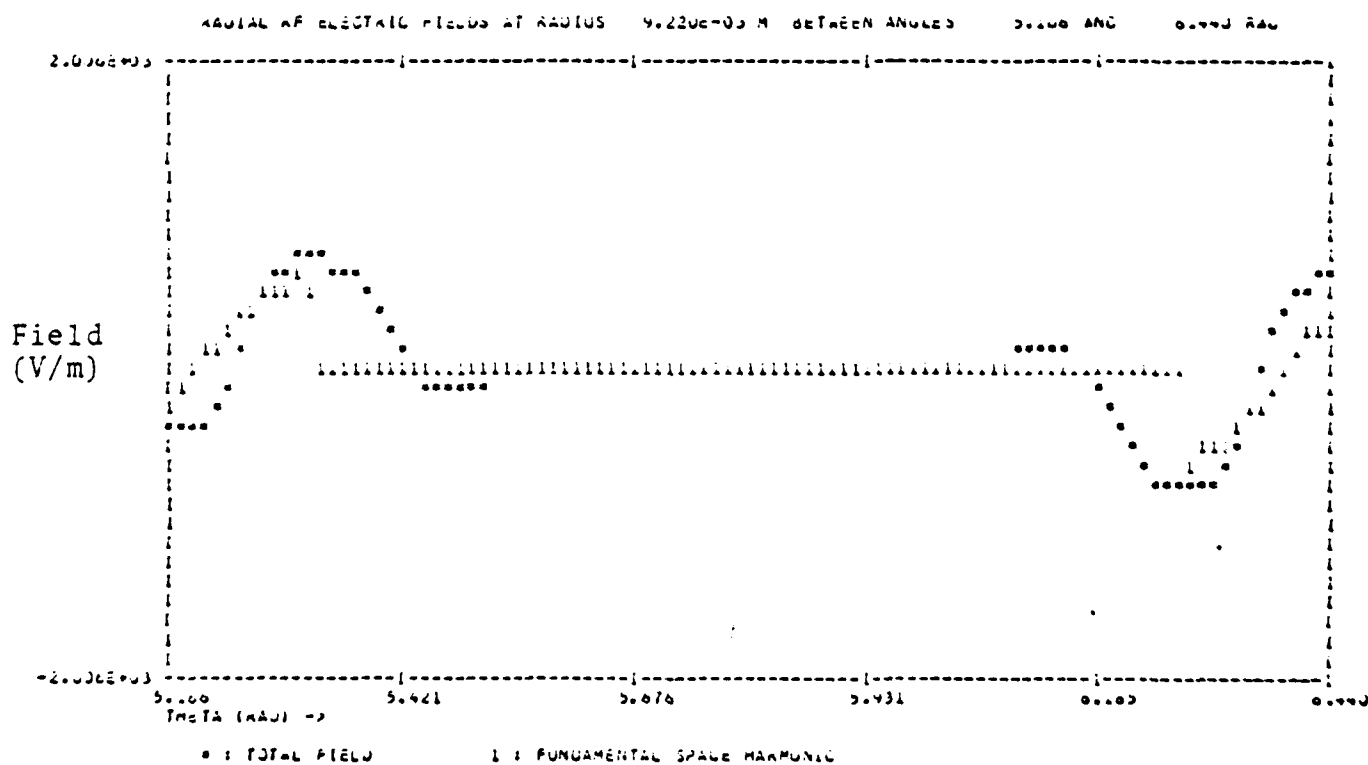


b. Radial Fields

Figure I.3 Comparison of exact values and single space harmonic of RF-circuit fields in QKS1842 at radius 9.6 mm.



a. Angular Fields



b. Radial Fields

Figure I.4 Comparison of exact values and single space harmonic of RF-circuit fields in sever region of QKS1842.

The single space harmonic is a good approximation at radii of 9.2 mm and less (Figure I.1). Closer to the anode, the exact field shows more rapid variations than the simple cosine curve (Figure I.2). Both fields are negligible throughout 70 percent of the sever region (Figure I.3).

Similar close agreement has been demonstrated to verify the RF-field calculations in the SFD-261 and QKS1319 tubes. Of course the Green's function method is more generally applicable to arbitrary sets of vane RF voltages, including standing waves of any wavelength or frequency.

APPENDIX J

THE CYLINDRICAL BRILLOUIN STREAM

Estimates of the circulating current and the size of the ~~hub of charge~~ around the cathode of a cutoff magnetron or distributed-emission CFA are readily obtained. Following, for example, Slater,³² Osepchuk,³³ and Smith,³⁴ assume that all electrons move in circles concentric with the cathode with constant angular velocities, and assume that the stream is in stable equilibrium.

Define the notation as follows, with MKS units throughout.

e	electron charge (in magnitude)
m	electron mass
η	e/m
r_c	cathode radius
r_a	anode radius
r_H	radius of outer edge of charge hub (in the absence of RF fields)
X	r_H/r_c
V_a	anode voltage
B	magnetic field

Using Busch's theorem and conservation of energy, and solving Poisson's equation gives the result

$$V_a = \frac{\eta B^2}{8} r_c^2 X^2 \left(1 - \frac{1}{X^2}\right)^2 + \frac{\eta B^2}{4} r_c^2 X^2 \left(1 - \frac{1}{X^2}\right) \ln(r_a/Xr_c) \quad (J.1)$$

This is quoted from Smith's article,³⁴ but with the correction of a typographical error. Osepchuk³³ gives the correct expression.

The computer program solves Equation J.1 using Newton's method with the initial estimate $r_H = 1/2(r_a + r_c)$. Convergence to within 0.1 percent is attained in three iterations.

The electron velocity v_θ at radius r then is given by³²

$$v_\theta = -\frac{\eta B}{2} r \left(1 - \frac{r_c^2}{r^2} \right), \quad (J.2)$$

the potential ϕ by

$$\phi = \frac{1}{8} \eta B^2 r^2 \left(1 - \frac{r_c^2}{r^2} \right)^2, \quad (J.3)$$

the local charge density ρ by

$$\frac{c}{\epsilon_0} = -\frac{1}{r} \frac{d}{dr} r \frac{d\phi}{dr}, \quad (J.4)$$

and the circulating current I by

$$I = -h \int_{r_c}^{r_H} \rho v_\theta dr, \quad (J.5)$$

where h is the width of the beam in the magnetic field direction.

The last integral evaluates as

$$I = \frac{\epsilon_0}{4} \eta^2 B^3 h r_c^2 \left(\frac{X^2}{2} - \frac{1}{2X^2} + \frac{1}{4X^2} - \ln X - \frac{1}{4} \right), \quad (J.6)$$

For the QKS1300 amplatron, the circulating current computed in this way is 0.606 A and the hub radius r_H is 1.36 mm. With 330 simulation particles, the DECFA model with a primary-emitting cathode and no angular space-charge field gives a circulating current varying between 0.598 and 0.619 A as particles are collected or emitted at the cathode. The computed hub radius is approximately 1.42 mm.

For the QKS1842, the circulating current in the particle model varies between 42.2 and 51.3 A over 1.18 cyclotron periods, with a mean of 47.0 A. The analytical value is 46.5 A for the same anode voltage (25.5 kV) and magnetic field (0.4114 T). The computed hub radius lies between 8.30 and 8.42 mm, and the analytical value is 8.36 mm. Thus the hub extends from the cathode a fraction of 0.31 of the anode-sole distance.

Of the three tubes shown in Table J.1, the QKS1319 has the smallest hub because its anode voltage is the least relative to the cutoff voltage (at which the hub would extend to the anode). The low ratio of operating current to circulating current in the QKS1842 is due to a low RF field.

TABLE J.1
CHARGE HUBS AND CIRCULATING CURRENTS

Tube	Anode Voltage/ Cutoff Voltage	Hub Thickness Anode-Cathode Distance	Circulating Current (A)	Operating Anode Current (A)
QKS1842	0.57	0.31	46.5	17.1
SFD-261	0.49	0.28	0.0216/D ₁ (normalized)	22.0
QKS1319	0.33	0.23	8.79	20.0

APPENDIX K

PROGRAM OUTPUT INFORMATION

Two programs are run: the primary DECFA program and the post-processing AVERAGE program to summarize the results. A third program, ERF, generates the RF field tables but its output is not shown. Appendix L gives examples of the output.

The following information is printed by DECFA. Much of it is self-explanatory.

- Data and initial conditions.
- At each time step:
 - Step number,
 - Total rods,
 - Number of active rods (NPCPRE),
 - Total charge units,
 - Induced current (IDCIND),
 - Modulator current (IDCTOT),
 - Anode voltage,
 - Mean radial electric field around cathode (ERSOL),
 - Collected charges (DQSOLE),
 - Maximum secondary charges (QNOLIM),
 - Emitted charges (DQSEC),
 - Charges collected in emission step and suppressed (DQSAME),
 - Anode and sole impact energies (eV),
 - Emission charges suppressed as rods of less than $\frac{1}{2}$ their initial charge (QSMALL)

At selected time steps:

- (Cathode electric fields)/(applied direct field) (%)
at each emission site, (charge density)/(Brillouin density)
(labeled as "(RHO/RHOB%)"), and numbers of emitted rods.

- Plotted charge distribution around the tube
- Currents and powers averaged over the preceding RF period
- Vane voltages and currents
- Power balance in network and in entire device (but for a single RF period the steady-state power balance does not hold)
- Averaged results over one transit around the tube' (periods 76 to 90 in the example)
- Plots of the RF power and phase distributions over the vanes (averaged over 1 transit around the tube)

The post-processor program, AVERAGE, summarizes the results for all the RF periods, prints the means over 1 transit around the tube, and prints the power balance from these mean values.

The columns P-ATTEN, P-ANODE, and P-CATH are the power losses due to RF attenuation and anode and cathode (sole) backbombardment. C-IMP and EV-IMP are the cathode impact current and mean backbombardment energy; ASEC is the effective secondary-emission coefficient after space-charge limitation.

APPENDIX L

EXAMPLE OF PROGRAM OUTPUT

A. Results of Program DECFA

HARRIS SAI, INC., ANN ARBOR, MICHIGAN
CYLINDRICAL DISTRIBUTED-EMISSION CROSSED-FIELD AMPLIFIER ANALYSIS PROGRAM
RUN NUMBER 42079

----- VERIFICATION OF DATA -----

QXS 1842 HIGH-POWER MODE WITH GOLD AND MAGNESIUM OXIDE CATHODE													
IDENT	42079	RTINET	0	NRPER	100	NOBER	0	NPVCVP	200	NRFP	16	MSIZE	20000
IPC	0	NETPRF	500	IRF	1	NDISPL	2	IPLDT	16	IOPT	1	ISAVE	16
MAXPCL	20000	NSC	1	ICDIN	41	JCDIN	41	IPCCT	1	ITRAJ	1		
JUAVE	-1	NPRRY	1200	ITIN	1	MTINJ	16	NSECSU	1	NESITE	120		
MUAVES	35	IPLTIC	5	INITRF	1	NBRILL	10000						
IUVSC	33	JUNSC	257	LSCPRI	0								
IFCOPY	2	LSCSEC	1	INTSEC	1								
IUPRNT	10	KATEAU	0	IUANEP	10	NOSAVE	0	JINDHS	0				
BRAG	0.3625	XBEAM	14.8000	RAMODE	9.7084	RSOLE	7.7484	UANODE	22000.0000	DURIN7	0.0000		
UAOPEN	4.400E+04	CRCTR	4.580E+02	CRCTL	0.000E+00	CRCTC	0.000E+00	DUR111	0.000E+00	DUR112	0.000E+00	DUR113	0.000E+00
PBAR5	1.5200	QDP	0.3280	THGCCT	22.4263	THRM	30.0000	THRAX	60.0000	DUR19	56.0000	DUR10	0.0000
FGH2	9.6000	PDRIVE	19000.0000	THCCT	43.5000	DPDF	25.0000	ZINT	6.6000	ATTEN	0.0182	F80T	7.8800
FGH2	9.6000	THCCT1	43.5000	ZINT1	6.6000	ATTEN1	0.0182						
FGH22	9.6000	THCCT2	43.5000	ZINT2	6.6000	ATTEN2	0.0182						
EUARI	2.0000	EUSEC	2.0000	ENANGL	30.0000	PSEC	0.5500	RFRD	9.0000	PINPOU	0.0000	OUTPOU	0.0000
CGNMIN	2.500E-01	SPSEC	0.000E+00	TINSEC	7.500E-02	THSUP1	0.000E+00	THSUP2	0.000E+00	DURINS	0.000E+00	DURING	0.000E+00

2.500E-01	0.000E+00	7.500E-02	0.000E+00	0.000E+00	0.000E+00	0.000E+00
CA	CB	CC	CA	CB	CC	
-1.000E+00	0.000E+00	0.000E+00	0.000E+00	0.000E+00	0.000E+00	0.000E+00
GAMA	GAMB	GAMC				
-1.000E+00	0.000E+00	0.000E+00				
G1	G2	G1	G2	GAML1	GAML2	
-1.000E+00	0.000E+00	0.000E+00	0.000E+00	0.000E+00	0.000E+00	
CIN1	CINMU	CIN2	CINU1			
-1.000E+00	0.000E+00	0.000E+00	0.000E+00			
CLAG11	CLAG01	CLAG12	CLAG02			
-1.000E+00	0.000E+00	0.000E+00	0.000E+00			
EUP	ASEC					
0.000	0.000					
50.000	1.350					
100.000	2.150					
200.000	2.850					
300.000	3.650					
500.000	4.650					
700.000	4.850					
900.000	4.800					
-1.000						

***** WITH SPACE CHARGE *****
 ***** WITH RF CIRCUIT *****
 ***** 1 TRANSIENT NETWORK EQUATIONS *****
 ***** ITRAJ - 1 PARTICLE MODEL WITH FULL TRAJECTORY EQUATIONS *****
 ***** 1200 PRIMARY PARTICLES EMITTED AT INTERVALS OF 1 STEPS UP TO STEP 16 *****
 SECONDARY EMISSION AT INTERVALS OF 1 STEPS

RF CIRCUIT FIELDS HAVE BEEN READ
 41 IN RADIAL DIRECTION
 ***** HARD-TUBE MODULATOR : INITIAL ANODE VOLTAGE 44000.00 V *****
 ***** SECONDARY-EMISSION MODEL *****
 SECONDARY-EMISSION COEFFICIENT FOR NORMAL INCIDENCE
 PRIMARY IMPACT ENERGY(EV)
 0.000
 50.000
 100.000
 200.000
 300.000
 500.000
 700.000
 900.000
 0.000
 1.350
 2.150
 2.850
 3.650
 4.650
 4.850
 4.800

FACTOR FOR ANGULAR IMPACT EXP(0.550*(1.-COS(ANGLE TO NORMAL))

SECONDARY EMISSION FROM 120 CATHODE EMISSION SITES

EMISSION AT ANGLE 0.524 RADIAN TO NORMAL WITH ENERGY 2.000 EU
 *** PARAMETERS FOR CYLINDRICAL BRILLOUIN STREAM ***
 ALL QUANTITIES IN MKS UNITS

MAGNETIC FIELD	0.3625	BEAM WIDTH	1.480E-02	ANODE RADIUS	9.708E-03	CATHODE RADIUS	7.748E-03	ANODE VOLTAGE	2.200E+04
ITERATIONS	3	HUB RADIUS	8.450E-03	HUB VELOCITY	4.286E+07	ENERGY (EV)	5.221E+03	CIRCULATING CURRENT	41.3915

WITH BRILLOUIN DENSITY TUBE IS FILLED BY 10000 PARTICLES
 INITIAL CHARGE PER PARTICLE -2.664E-11 COULOMBS

RF PERIODS 100.00
 TERMINATING TIME STEP 1600
 MAJOR STEPS PER RF PERIOD 16
 NETWORK STEPS PER RF PERIOD 512
 MAJOR STEPS PER CYCLOTRON PERIOD 15.14
 BEAM STEPS PER CYCLOTRON PERIOD AT SOLE 211.90
 BEAM STEPS PER MAJOR STEP AT SOLE 14
 NETWORK STEPS PER MAJOR STEP 32
 INITIAL RF PERIODS WITH NO BEAM 0
 INITIAL TIME STEPS WITH NO BEAM 0

PROGRAM VARIABLES (DIAGNOSTIC)

NRFP	16	NCSTEP	32	NSTORE	1	DEL	2.035E-13	MDL	1.017E-13
UC	6.3764E+10	MRFP	16	TCVC	DT		6.5104E-12		
BPHI	-2.0756E-01	BF1	BF2	BF3	BF4				
BPHI	-1.4826E-02	BF1INT	BF2INT	BF3INT	BF4INT				
THEA	4.1513E-01	BK1	BK2	BK3	BK4				
BK1INT	6.4966E-13	BK2INT	BK3INT	BK4INT	BK5INT				

*** TUBE PARAMETERS (MKS UNITS) ***

R-ANODE	- R-CATHODE	R-ANODE/R-CATHODE	CIRCUMFERENCE	INTERACTION LENGTH	SEVER LENGTH
1.9600E-03	1.2530E+00	6.1000E-02	5.3200E-02	7.7997E-03	
MAGNETIC FIELD	ANODE VOLTAGE	ANODE RADIUS	CATHODE RADIUS	CUTOFF VOLTAGE	U-ANODE/U-CUTOFF
3.6250E-01	2.2000E+04	9.7084E-03	7.7484E-03	3.5887E+04	6.1303E-01

ANGULAR FREQUENCY 6.0319E+10
 DRIVE FREQUENCY 9.6000E+09
 PHASE DELAY PER PITCH(DEG) (EXTERNAL) 4.3500E+01
 UP/C 1.2837E-01
 MODE NUMBER 1.5216E+01
 DRIVE POWER 1.9000E+04
 (BEAM) 1.3650E+02
 UC/U 1.0571E+00
 INTERACTION IMPEDANCE 4.2090E+03
 CHARACTERISTIC IMPEDANCE 1.2418E-01
 UANE GAP/PERIOD 3.2800E-01
 UANE PERIOD (ANODE) 1.5200E-03
 BETA-A 3.0720E+00
 U-ANODE/U-MARTREE 1.0790E+00
 U-RF/U-ANODE 2.0373E+04
 RF VOLTAGE 6.5891E+02
 RF WAVELENGTH (ANODE) 4.0088E-03
 RF WAVELENGTH (CATHODE) 3.1995E-03
 VELOCITY SLIP, B (CYLINDRICAL) 1.3063E-01

ANGULAR POSITIONS (RAD) OF UANE CENTERS
 0.000 0.157 0.313 0.470
 1.722 1.879 2.035 2.192
 3.444 3.601 3.758 3.914
 5.167 5.323 5.479 5.635
 COLD-CIRCUIT VOLTAGE PHASE LAG(DEG) RELATIVE TO UT=0.
 39.0 355.5 312.0 268.5
 280.5 237.0 193.5 150.0
 162.0 118.5 75.0 31.5
 43.5 0.0

*** MODULATOR CIRCUIT ***

OPEN-CIRCUIT VOLTAGE(U)	OPERATING VOLTAGE(U)	RESISTANCE (OHM)	INDUCTANCE (H)	CAPACITANCE (EXT) (F)	CAPACITANCE (CFA) (F)	CAPACITANCE (NET) (F)
0.00000E+00	2.20000E+04	4.58000E+02	0.00000E+00	0.00000E+00	3.64946E-12	3.64946E-12

INPUT UANES : 35 34
 OUTPUT UANES : 1 2

*** EQUIVALENT NETWORK PARAMETERS ***

CA	CB	CC	CD	CE	CF	CG	CH	CI	CJ	CK	CL	CM	CN	CO	CP	CQ	CR	CS	CT	CU	CV	CW	CX	CY	CZ	
1.160E-12	0.000E+00	0.000E+00	3.668E-04	0.000E+00	0.000E+00	0.000E+00	0.000E+00	0.000E+00	0.000E+00	0.000E+00	0.000E+00	0.000E+00	0.000E+00	0.000E+00	0.000E+00	0.000E+00	0.000E+00	0.000E+00	0.000E+00	0.000E+00	0.000E+00	0.000E+00	0.000E+00	0.000E+00	0.000E+00	0.000E+00
0.000E+00	7.686E+09	0.000E+00	0.000E+00	0.000E+00	0.000E+00	0.000E+00	0.000E+00	0.000E+00	0.000E+00	0.000E+00	0.000E+00	0.000E+00	0.000E+00	0.000E+00	0.000E+00	0.000E+00	0.000E+00	0.000E+00	0.000E+00	0.000E+00	0.000E+00	0.000E+00	0.000E+00	0.000E+00	0.000E+00	0.000E+00
8.753E-02	0.000E+00	0.000E+00	0.000E+00	0.000E+00	0.000E+00	0.000E+00	0.000E+00	0.000E+00	0.000E+00	0.000E+00	0.000E+00	0.000E+00	0.000E+00	0.000E+00	0.000E+00	0.000E+00	0.000E+00	0.000E+00	0.000E+00	0.000E+00	0.000E+00	0.000E+00	0.000E+00	0.000E+00	0.000E+00	0.000E+00
0.000E+00	1.153E+02	0.000E+00	0.000E+00	0.000E+00	0.000E+00	0.000E+00	0.000E+00	0.000E+00	0.000E+00	0.000E+00	0.000E+00	0.000E+00	0.000E+00	0.000E+00	0.000E+00	0.000E+00	0.000E+00	0.000E+00	0.000E+00	0.000E+00	0.000E+00	0.000E+00	0.000E+00	0.000E+00	0.000E+00	0.000E+00
0.000E+00	0.000E+00	0.000E+00	0.000E+00	0.000E+00	0.000E+00	0.000E+00	0.000E+00	0.000E+00	0.000E+00	0.000E+00	0.000E+00	0.000E+00	0.000E+00	0.000E+00	0.000E+00	0.000E+00	0.000E+00	0.000E+00	0.000E+00	0.000E+00	0.000E+00	0.000E+00	0.000E+00	0.000E+00	0.000E+00	0.000E+00

*** OPTION WITH INTRF - 1 ***

[illegible]

THETA (RAD) ->

[illegible]

4.712
THETA (RAD) ->

STEP	NTPCLS	NPCPRE	CHARGES	IDCIND(A)	IDCTOT(A)	UNODE(U)	ERSOL(U,N)	DOSOLE	QWOLIN	DOSOC	DOSAME	EU-ANODE	EU-SOLE	OSHALL
1440	7603	7058	5483.28	86.54	36.40	27327.19	-3.31E+05	54.23	127.24	49.30	0.00	13878.48	207.60	2.78

DISTRIBUTION OF CURRENT AND POWER OVER WAVES AFTER 90.0 RF PERIODS

0.000	0.546	1.032	1.627
0.273	0.669	1.050	2.571
0.000	0.564	0.000	0.192
0.602	0.361		

DIRECT ANODE CURRENT(A)

ANODE CURRENT IN SEVER REGION

0.000 A

0.467	0.449	1.483
1.651	1.242	0.000
0.180	0.161	0.590

IMPACT POWER(U)																	
0.00	7587.13	16522.24	26618.02	11708.61	14969.79	0.00	6893.93	7151.62	13218.37								
20089.92	8081.39	14315.44	35394.96	50896.63	27594.86	56633.74	21378.43	17059.29	17968.15								
0.00	7434.24	0.00	2264.32	1623.77	0.00	0.00	1594.33	7331.50	2213.80								
7481.14	4437.55	0.000 U															
IMPACT POWER IN SEVER REGION																	
POWER FLOW(U) ALONG CIRCUIT																	
265926.42	234750.84	342874.37	284925.33	271609.81	351685.83	373720.84	356832.73	441453.91	39543.55								
354084.48	38694.71	246242.42	259135.42	231834.01	114073.53	116394.24	118049.03	34430.00	35599.60								
5848.55	36724.51	19840.06	21090.41	54105.07	53423.12	32547.33	57419.57	53113.76	17459.61								
37327.75	11751.98																
POWER FLOW(U) FROM BEAM																	
-3363.6794	-7205.0569	-6524.8004	14787.0318	18932.5278	10121.5776	5432.3196	16365.0513	25557.9742	38182.2422								
25575.2023	32931.8200	30205.8536	36686.8566	22323.9009	22504.9873	15523.3728	18323.9186	7252.3730	6532.0467								
-1007.2590	-1594.4546	1790.8250	-226.1198	-925.0896	2656.4050	2710.8140	2623.9408	7081.9562	3871.2731								
3985.9138	579.1241																
AFTER STEP																	
1440	7603	6978	33.19	0.00	215.85	246.88	P-IMPACT ANODE(U)	AU EU-ANODE SOLE(U)	AU EU-SOLE (EU)								
							4.472E+05	5.018E+04	13476.17								
TOTAL OUT																	
								5.018E+04	8.925E+05								

*** BEAM POWERS (U) ***

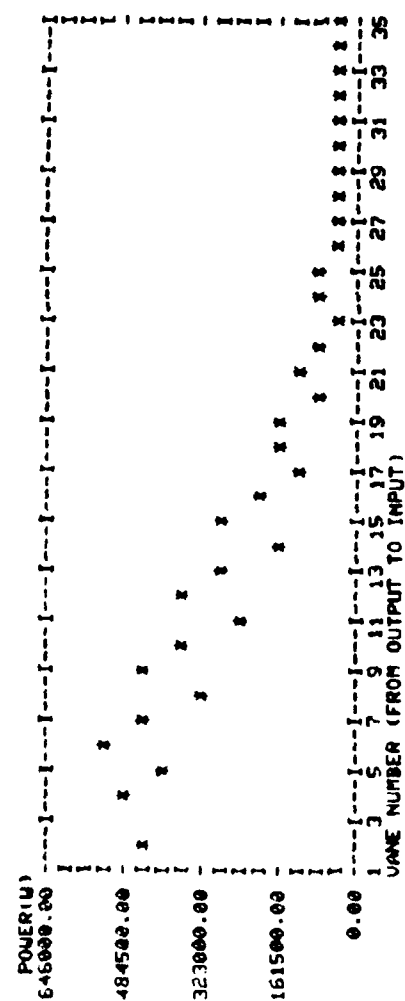
FOURIER COMPONENTS AFTER 90.0 RF PERIODS									
HOT-COLD									
U1	UPH1	UPH1-UPH1	UPH1	UPH1	UPH1	UPH1	UPH1	UPH1	UPH1
(U)	(U)	(U)	(U)	(U)	(U)	(U)	(U)	(U)	(U)
1	1908.78	-140.0	5.579	-179.0	1155.04	1155.04	1155.04	1155.04	1155.04
2	1300.44	155.4	13.122	107.5	159.9	159.9	159.9	159.9	159.9
3	1838.73	83.3	28.719	109.2	159.9	159.9	159.9	159.9	159.9
4	2060.43	19.4	19.363	66.5	110.9	110.9	110.9	110.9	110.9
5	2047.08	-43.6	20.698	45.4	91.4	91.4	91.4	91.4	91.4
6	2164.57	-110.5	10.322	64.8	68.0	68.0	68.0	68.0	68.0
7	2536.97	-168.6	11.844	87.3	53.4	53.4	53.4	53.4	53.4
8	2614.22	104.6	22.763	67.3	40.1	40.1	40.1	40.1	40.1
9	2751.98	75.6	31.530	68.6	24.6	24.6	24.6	24.6	24.6
10	2771.97	25.4	22.232	28.3	17.9	17.9	17.9	17.9	17.9
11	2626.79	-30.4	25.222	27.9	5.6	5.6	5.6	5.6	5.6
12	2568.72	-90.5	22.436	45.6	-11.0	-11.0	-11.0	-11.0	-11.0
13	2561.72	-141.4	22.492	33.9	-18.4	-18.4	-18.4	-18.4	-18.4
14	2238.85	164.3	24.740	17.8	-20.2	-20.2	-20.2	-20.2	-20.2
15	2110.03	105.9	34.575	36.4	-44.1	-44.1	-44.1	-44.1	-44.1
16	2081.48	52.8	19.383	3.4	-53.7	-53.7	-53.7	-53.7	-53.7
17	1470.39	2.1	25.481	2.4	-60.9	-60.9	-60.9	-60.9	-60.9
18	1368.48	-60.6	19.847	30.1	-80.1	-80.1	-80.1	-80.1	-80.1
19	1363.50	-112.2	20.477	20.7	-88.2	-88.2	-88.2	-88.2	-88.2
20	712.76	97.7	16.748	-31.3	-74.8	-74.8	-74.8	-74.8	-74.8
21	359.05	129.3	18.720	42.7	-151.3	-151.3	-151.3	-151.3	-151.3
22	459.57	-176.8	12.919	-3.3	-32.7	-32.7	-32.7	-32.7	-32.7
23	189.29	164.4	12.451	-127.8	-32.7	-32.7	-32.7	-32.7	-32.7
24	641.00	164.4	6.607	120.0	64.7	64.7	64.7	64.7	64.7
25	448.86	38.6	4.004	154.3	89.4	89.4	89.4	89.4	89.4
26	574.66	-15.8	9.811	118.2	27.8	27.8	27.8	27.8	27.8
27	907.23	-14.0	8.113	53.7	41.5	41.5	41.5	41.5	41.5
28	968.10	-100.8	8.113	55.9	-1.8	-1.8	-1.8	-1.8	-1.8
29	719.44								

43979.923 73052.708 63297.670 29516.934 54874.702 49105.896 26081.194 40211.140 39185.150 24737.546 30136.100
 28042.432 23263.114

RF POWER DISTRIBUTION AFTER 90.0 RF PERIODS

RF POWER DISTRIBUTION AFTER 90.0 RF PERIODS	RF POWER DISTRIBUTION AFTER 90.0 RF PERIODS	RF POWER DISTRIBUTION AFTER 90.0 RF PERIODS	RF POWER DISTRIBUTION AFTER 90.0 RF PERIODS	RF POWER DISTRIBUTION AFTER 90.0 RF PERIODS	RF POWER DISTRIBUTION AFTER 90.0 RF PERIODS	RF POWER DISTRIBUTION AFTER 90.0 RF PERIODS	RF POWER DISTRIBUTION AFTER 90.0 RF PERIODS	RF POWER DISTRIBUTION AFTER 90.0 RF PERIODS	RF POWER DISTRIBUTION AFTER 90.0 RF PERIODS	RF POWER DISTRIBUTION AFTER 90.0 RF PERIODS
117.121	109.706	82.739	40.208	41.153	38.738	47.736	61.643	51.206	25.672	39.842
42.055	35.917	42.857	41.458	18.677	34.771	39.170	24.933	22.637	48.213	3.761
-6.725	47.977	18.863	17.208	30.454	-28.041	3.641	50.659	-4.450	-38.228	15.680
-20.445	-11.898									

RF POWER DISTRIBUTION AFTER 90.0 RF PERIODS



RF CURRENT PHASE LAG FROM CIRCUIT VOLTAGE AT DRIVE FREQUENCY AFTER 90.0 RF PERIODS



2 JAN 30 7:01:12

STEP	NTPCLS	NP-CPRE	CHARGES	IDCIND(A)	IDCTOT(A)	VANODE(U)	ERSOL(U/M)	DOSOLE	GNOLIN	DOSSEC	DOSAVE	EU-ANODE	EU-ANODE	EU-SOLE	OSMALL
1441	7603	7664	5481.53	94.25	36.58	27245.17	-4.40E+05	54.75	126.36	66.59	0.00	13479.08	13479.08	229.25	1.59
1442	7603	7659	5491.53	94.07	37.19	27149.32	-3.62E+05	48.54	126.56	73.74	0.00	1417.47	1417.47	204.68	1.25
1443	7603	7673	5432.12	85.15	37.01	27047.16	-3.69E+05	54.49	126.35	63.95	0.00	1210.57	1210.57	210.99	1.54
1444	7603	7660	5482.69	86.36	37.22	26955.27	-3.42E+05	54.03	126.38	52.33	0.00	15418.87	15418.87	148.19	1.68
1445	7603	7651	5473.26	40.26	37.37	26884.44	-2.85E+05	41.70	122.58	49.68	0.00	14626.34	14626.34	196.43	1.98
1446	7603	7646	5471.44	15.83	37.43	26856.14	-2.63E+05	46.74	122.17	62.81	0.00	13131.76	13131.76	243.46	2.18
1447	7603	7655	5474.40	-3.25	37.40	26872.95	-3.11E+05	49.81	122.17	61.27	0.00	13125.95	13125.95	161.76	1.47
1448	7603	7660	5472.46	-10.18	37.27	26928.40	-2.88E+05	50.91	120.89	62.26	0.00	15173.78	15173.78	218.85	1.79
1449	7603	7662	5487.47	-12.48	37.10	27066.76	-2.28E+05	40.23	123.00	67.11	0.00	14982.98	14982.98	211.58	2.09
1450	7603	7669	5488.82	-16.37	36.91	27093.01	-2.02E+05	41.24	121.36	51.95	0.00	14594.55	14594.55	241.31	2.36
1451	7603	7667	5460.28	-15.85	36.72	27184.43	-2.84E+05	66.06	120.39	46.84	0.00	14956.39	14956.39	238.19	2.14
1452	7603	7346	5456.30	-4.52	36.51	27278.59	-2.73E+05	57.02	123.56	58.94	0.00	14503.18	14503.18	223.52	1.63
1453	7603	7652	5466.43	17.89	36.33	27361.62	-2.92E+05	48.17	124.49	69.71	0.00	13003.00	13003.00	250.71	1.85
1454	7603	7662	5470.62	46.98	36.21	27414.34	-3.74E+05	59.68	124.09	70.52	0.00	12109.11	12109.11	246.37	2.17
1455	7603	7663	5471.64	69.67	36.20	27421.77	-1.05E+05	65.00	126.60	70.20	0.00	12305.95	12305.95	253.99	1.61

[illegible]

CHARGE DISTRIBUTION AFTER STEP 1456

R (MM) ANODE
 9.71
 8.73

B. Results of Program AVERAGE

1000 AVERAGED RESULTS (IN MKS UNITS) FOR RUN NUMBER 42079 3333

PERIOD	I-ANOD	I-CATH	P-ATTN	P-ANODE	P-CATH	DBGAIN	RF DRIVE	RF OUTPUT	U-ANOD	C-IMP	EU-IMP	ASEC
1	25.9091	453.491	7.352E+03	1.257E+07	1.059E+06	0.87	1804.11	22037.01	32133.5	204.421	5181.623	8.110
2	24.777	47.205	6.877E+03	0.000E+00	8.014E+05	-1.50	1899.98	13448.17	32552.1	642.244	1247.802	1.214
3	25.539	93.439	5.697E+03	0.000E+00	4.018E+05	0.30	1899.98	20353.95	32303.4	436.455	920.591	1.096
4	25.948	42.103	8.284E+03	0.000E+00	4.790E+05	2.77	1899.98	35963.54	32115.9	439.474	1091.285	1.131
5	26.545	54.056	1.264E+04	0.000E+00	4.401E+05	5.25	18155.82	60779.70	31842.2	413.543	1064.198	1.124
6	27.204	44.621	1.349E+04	2.690E+04	3.374E+05	8.43	18699.66	130328.87	31540.6	360.239	936.484	1.123
7	27.533	38.898	1.038E+04	3.215E+04	2.601E+05	9.00	18990.75	150224.00	31390.0	314.972	825.572	1.141
8	27.874	42.895	7.547E+03	1.343E+05	1.991E+05	8.53	18785.32	133758.33	31233.8	304.974	653.547	1.116
9	28.578	33.531	1.452E+04	2.315E+05	1.702E+05	5.13	18781.54	61209.05	30911.8	289.490	589.543	1.105
10	29.994	30.960	3.060E+04	7.552E+05	1.697E+05	6.15	18995.85	78309.54	30262.9	294.421	576.461	1.157
11	31.781	41.617	4.559E+04	9.033E+05	1.474E+05	10.41	18970.29	208333.22	29444.5	277.488	531.177	1.130
12	34.556	43.280	5.947E+04	1.380E+06	1.208E+05	15.07	18998.08	610871.36	28173.4	274.876	439.415	1.216
13	37.790	32.794	7.81E+04	2.095E+06	8.605E+04	18.92	16307.48	1271688.11	26692.2	252.245	340.947	1.189
14	40.721	47.543	8.004E+04	1.880E+06	6.614E+04	16.78	18999.27	904198.24	25533.1	224.692	294.347	1.236
15	40.862	42.035	7.342E+04	1.050E+06	5.586E+04	17.36	17924.02	975331.42	25234.1	221.947	252.411	1.155
16	40.881	42.015	5.725E+04	7.001E+05	5.628E+04	16.89	16116.56	787877.47	25285.4	221.947	253.558	1.228
17	40.337	47.541	3.547E+04	4.923E+05	4.675E+04	16.78	18413.43	878823.73	25459.5	212.409	220.256	1.198
18	40.384	47.541	2.459E+04	4.509E+05	4.407E+04	14.59	18832.44	542340.44	25504.1	201.454	218.769	1.236
19	39.934	31.747	1.996E+04	5.245E+05	4.528E+04	12.73	12773.54	233694.26	25525.8	206.436	219.335	1.155
20	39.227	42.799	2.332E+04	4.732E+05	4.267E+04	12.95	16500.92	325571.87	25710.3	204.245	208.902	1.217
21	38.752	42.699	2.291E+04	1.419E+05	4.165E+04	13.16	14773.93	308033.28	26034.0	195.590	213.150	1.208
22	38.752	42.699	1.462E+04	4.478E+04	4.365E+04	12.22	18651.93	311090.22	26434.7	204.921	216.479	1.206
23	36.748	29.280	9.250E+03	8.817E+04	3.857E+04	10.48	18361.86	205006.09	26827.3	201.489	191.401	1.146
24	36.116	42.267	7.843E+03	6.805E+04	4.073E+04	2.67	17207.92	31792.70	27169.0	200.537	203.084	1.188
25	35.494	37.577	1.100E+04	1.743E+04	3.795E+04	1.38	18700.27	25666.42	27459.0	200.128	189.593	1.159
26	35.058	32.918	1.404E+04	5.288E+04	3.948E+04	7.74	18512.19	110959.43	27743.8	200.146	197.319	1.172
27	35.077	32.364	1.765E+04	2.324E+05	4.376E+04	10.38	18306.43	199700.58	27943.8	200.305	210.063	1.180
28	35.519	40.364	3.315E+04	5.882E+05	4.463E+04	4.59	18757.15	53929.62	27934.8	207.599	214.981	1.192
29	35.357	37.096	5.095E+04	1.138E+06	5.116E+04	9.01	18431.15	149002.62	27732.1	200.771	224.683	1.171
30	37.248	35.919	5.795E+04	9.534E+05	5.003E+04	14.19	18849.34	495109.50	27488.5	216.362	237.838	1.172
31	38.065	34.865	5.579E+04	9.527E+05	5.682E+04	16.46	18091.63	828047.05	26940.6	208.263	240.211	1.167
32	38.436	38.722	5.495E+04	9.343E+05	5.145E+04	15.73	16734.78	625700.76	26396.2	215.235	238.941	1.180
33	38.144	47.333	4.104E+04	4.976E+05	5.932E+04	16.84	15961.02	918156.71	26529.9	217.454	273.050	1.218
34	37.979	41.872	3.364E+04	3.458E+05	5.418E+04	11.48	14878.85	209369.98	26605.7	216.043	250.778	1.148
35	37.411	37.324	3.819E+04	3.404E+05	5.589E+04	13.09	14642.49	533965.97	26692.7	223.185	250.424	1.173
36	37.249	34.862	2.300E+04	3.019E+05	5.025E+04	16.15	10776.87	44508.56	26940.1	208.722	240.938	1.167
37	37.191	40.187	2.522E+04	3.365E+05	4.627E+04	6.75	18393.50	84332.10	26966.4	205.761	224.856	1.195
38	37.000	40.154	3.729E+04	4.925E+05	4.274E+04	12.82	12862.05	246345.71	27053.8	202.030	211.549	1.199
39	36.961	30.650	3.501E+04	5.263E+05	4.608E+04	15.24	18810.03	629553.62	27071.9	204.995	224.778	1.150
40	37.203	35.244	2.832E+04	5.281E+05	4.459E+04	14.38	16185.89	43983.24	26960.8	203.163	219.952	1.174
41	37.226	46.760	3.197E+04	5.274E+05	4.536E+04	11.38	18180.57	249582.30	26928.5	199.895	226.913	1.234
42	37.299	44.964	3.738E+04	6.265E+05	4.636E+04	14.29	16308.51	437523.43	26950.3	215.058	215.588	1.133
43	37.313	36.678	3.317E+04	5.837E+05	4.417E+04	15.89	17079.17	665981.68	26917.1	193.130	228.443	1.233
44	37.065	37.773	2.940E+04	5.304E+05	4.692E+04	9.90	18397.87	170853.04	26912.2	209.403	224.049	1.175
45	36.875	34.098	3.688E+04	3.649E+05	4.931E+04	13.81	13811.35	32356.14	27024.0	212.795	231.727	1.178
46	36.970	36.554	2.737E+04	5.246E+05	5.174E+04	15.60	18370.39	666391.12	27111.0	209.345	247.791	1.163
47	36.886	32.109	2.802E+04	4.814E+05	5.168E+04	13.36	17985.42	295709.88	27067.6	216.043	247.516	1.167
48	36.875	37.773	2.737E+04	5.246E+05	5.174E+04	15.60	18370.39	666391.12	27111.0	209.345	247.791	1.163
49	36.875	37.773	2.737E+04	5.246E+05	5.174E+04	15.60	18370.39	666391.12	27111.0	209.345	247.791	1.163
50	36.875	37.773	2.737E+04	5.246E+05	5.174E+04	15.60	18370.39	666391.12	27111.0	209.345	247.791	1.163
51	36.875	37.773	2.737E+04	5.246E+05	5.174E+04	15.60	18370.39	666391.12	27111.0	209.345	247.791	1.163
52	36.875	37.773	2.737E+04	5.246E+05	5.174E+04	15.60	18370.39	666391.12	27111.0	209.345	247.791	1.163
53	36.875	37.773	2.737E+04	5.246E+05	5.174E+04	15.60	18370.39	666391.12	27111.0	209.345	247.791	1.163
54	36.875	37.773	2.737E+04	5.246E+05	5.174E+04	15.60	18370.39	666391.12	27111.0	209.345	247.791	1.163
55	36.875	37.773	2.737E+04	5.246E+05	5.174E+04	15.60	18370.39	666391.12	27111.0	209.345	247.791	1.163
56	36.875	37.773	2.737E+04	5.246E+05	5.174E+04	15.60	18370.39	666391.12	27111.0	209.345	247.791	1.163
57	36.875	37.773	2.737E+04	5.246E+05	5.174E+04	15.60	18370.39	666391.12	27111.0	209.345	247.791	1.163

57	36.783	36.652	3.146E+04	4.695E+05	4.616E+04	11.98	18595.80	293549.40	27153.5	210.226	219.178	1.174
58	36.447	32.152	2.764E+04	3.801E+05	5.179E+04	14.38	17216.51	471617.57	27307.4	212.188	244.058	1.152
59	36.508	37.560	2.738E+04	3.870E+05	5.459E+04	14.13	15363.39	397191.81	27279.3	216.084	252.643	1.174
60	36.535	42.714	2.683E+04	4.473E+05	5.177E+04	8.67	18650.73	139059.79	27266.8	200.013	247.671	1.204
61	36.278	32.185	3.294E+04	4.552E+05	4.815E+04	13.06	13978.01	282727.35	27384.6	213.676	225.327	1.151
62	36.478	34.982	2.927E+04	5.551E+05	4.894E+04	15.51	18220.55	139310.12	27293.0	216.276	226.394	1.186
63	36.682	32.295	2.750E+04	6.512E+05	4.894E+04	10.41	17273.78	190112.31	27199.8	210.736	231.736	1.186
64	36.646	33.444	3.561E+04	4.959E+05	5.113E+04	11.88	17364.59	267880.25	27216.2	217.525	236.069	1.154
65	36.331	30.331	3.314E+04	4.340E+05	4.755E+04	15.28	18406.57	63479.27	27285.7	213.339	221.706	1.171
66	36.784	38.548	3.081E+04	5.896E+05	4.586E+04	13.02	16552.90	331508.12	27153.1	205.591	220.209	1.187
67	36.869	38.692	3.557E+04	6.955E+05	4.707E+04	12.66	18009.32	343632.10	27113.8	209.512	224.681	1.185
68	36.620	35.678	3.289E+04	3.709E+05	5.009E+04	15.62	18009.30	550026.20	27228.0	212.242	237.376	1.168
69	36.614	36.245	2.656E+04	4.893E+05	5.045E+04	14.43	17155.23	475602.52	27231.2	212.749	236.640	1.170
70	36.665	34.622	2.844E+04	4.776E+05	4.977E+04	9.53	18248.10	163825.15	27207.3	212.911	233.757	1.163
71	36.654	43.642	3.561E+04	4.926E+05	4.877E+04	12.82	18096.65	308127.61	27212.5	208.933	233.378	1.209
72	36.785	28.407	3.239E+04	5.462E+05	5.072E+04	15.74	18996.36	713006.67	27152.7	213.440	237.623	1.124
73	37.008	41.137	2.870E+04	5.015E+05	4.979E+04	11.68	16265.74	239470.80	27050.4	205.260	242.585	1.200
74	36.875	41.826	3.441E+04	4.550E+05	4.706E+04	12.13	17599.23	288732.26	27111.2	208.552	225.646	1.201
75	36.702	37.569	2.593E+04	4.840E+05	4.988E+04	15.21	17571.74	583637.70	27190.5	216.588	228.902	1.138
76	36.791	30.076	2.702E+04	5.374E+05	5.374E+04	12.97	14813.30	293553.68	27149.7	218.511	245.949	1.175
77	36.701	37.555	3.322E+04	4.346E+05	5.839E+04	10.36	18770.12	203802.63	27149.7	214.599	272.072	1.185
78	36.658	38.984	3.397E+04	4.015E+05	5.237E+04	14.97	15169.48	475559.90	27210.5	218.266	248.829	1.186
79	36.731	40.504	2.896E+04	5.307E+05	5.455E+04	15.58	16787.31	607252.31	27177.2	211.272	244.256	1.140
80	36.937	29.600	2.966E+04	5.444E+05	5.140E+04	9.68	18430.00	171066.18	27082.9	211.272	244.256	1.140
81	36.829	42.442	3.776E+04	5.082E+05	4.742E+04	12.97	13692.99	271037.51	27132.2	207.029	229.034	1.205
82	36.918	42.107	2.359E+04	6.647E+05	4.741E+04	16.08	18574.22	757229.00	27091.5	209.923	235.855	1.201
83	36.909	28.450	2.815E+04	4.691E+05	5.081E+04	11.62	15881.02	231797.48	27095.6	213.832	237.631	1.124
84	36.838	39.241	3.327E+04	4.709E+05	5.442E+04	12.29	17174.77	290940.32	27128.2	215.205	252.887	1.182
85	36.649	40.166	3.001E+04	4.081E+05	4.876E+04	15.34	16811.67	574486.69	27214.5	211.790	230.211	1.190
86	36.904	28.623	3.000E+04	5.591E+05	5.208E+04	13.65	14172.92	328612.48	27097.7	210.396	247.549	1.184
87	36.906	29.275	3.331E+04	5.141E+05	5.306E+04	10.77	18999.89	226641.20	27096.9	215.719	248.464	1.136
88	36.718	39.288	3.410E+04	5.266E+05	4.922E+04	15.39	13399.58	463290.07	27183.3	211.147	233.128	1.186
89	36.575	43.651	2.681E+04	4.160E+05	4.867E+04	15.23	18247.79	608525.50	27242.5	215.853	232.468	1.144
90	36.523	31.032	3.511E+04	4.472E+05	5.081E+04	9.50	17879.10	159447.83	27245.2	215.419	239.435	1.176
91	36.439	37.623	3.175E+04	5.361E+05	4.683E+04	12.12	16020.11	212125.83	27310.7	213.419	219.435	1.176
92	36.370	39.520	2.858E+04	4.959E+05	5.147E+04	15.07	18972.61	609320.58	27342.4	209.875	245.249	1.188
93	25.909	453.491	7.352E+03	1.257E+07	1.059E+06	0.87	18044.11	22037.01	32133.5	204.421	5181.623	8.110
94	25.343	750.348	7.114E+03	6.286E+06	9.303E+05	-0.19	18522.02	17742.59	32392.8	423.332	2197.594	2.772
95	25.408	531.378	6.642E+03	4.191E+06	7.51E+05	-0.02	18531.17	18613.04	32363.0	427.707	1763.230	2.242
96	25.543	409.059	7.052E+03	3.143E+06	6.855E+05	0.88	18760.40	22950.77	32301.2	430.648	1591.704	1.950
97	25.744	338.059	8.171E+03	2.515E+06	6.364E+05	2.14	18639.49	30516.55	32209.9	427.227	1489.654	1.791
98	25.987	289.153	9.058E+03	2.100E+06	5.866E+05	4.03	18649.52	47151.94	32097.9	416.063	1409.829	1.695
99	26.208	253.402	9.246E+03	1.805E+06	5.399E+05	5.20	18685.41	61876.52	31996.8	401.621	1344.383	1.631
100	26.416	227.089	9.034E+03	1.596E+06	4.944E+05	5.79	18697.90	70861.75	31901.4	389.540	1276.275	1.583
101	26.656	205.582	9.643E+03	1.444E+06	4.611E+05	5.76	18707.19	69789.23	31791.6	378.424	1218.361	1.543
102	26.990	188.120	1.174E+04	1.375E+06	4.319E+05	5.72	18736.06	70641.26	31638.6	370.023	1167.286	1.508
103	27.426	174.801	1.481E+04	1.332E+06	4.081E+05	8.31	18777.42	83158.71	31439.1	361.611	1122.911	1.463
104	28.020	163.841	1.853E+04	1.336E+06	3.823E+05	10.64	18777.42	127131.76	31167.0	354.383	1078.732	1.444
105	28.771	153.761	2.309E+04	1.395E+06	3.595E+05	10.64	18777.42	215177.33	30822.8	346.526	1037.420	1.444
106	29.506	146.174	2.716E+04	1.429E+06	3.375E+05	11.52	18616.83	311788.99	30044.9	337.824	1002.118	1.433
107	30.355	139.610	3.035E+04	1.405E+06	3.137E+05	12.25	18570.65	362845.03	29641.5	331.224	968.607	1.423
108	31.352	125.513	3.357E+04	6.126E+05	2.508E+05	12.94	18442.14	420403.38	29641.5	302.568	969.747	1.199
109	32.398	115.167	3.548E+04	6.454E+05	2.055E+05	13.59	18403.93	455282.48	28708.2	286.591	922.774	1.147
110	33.388	102.107	3.674E+04	6.755E+05	1.707E+05	13.94	18391.91	468784.50	28268.9	271.366	882.774	1.156
111	34.347	92.439	3.752E+04	7.104E+05	1.475E+05	14.16	17976.94	486437.31	27866.1	257.412	847.709	1.159
112	35.200	80.951	3.827E+04	7.420E+05	1.232E+05	14.35	17666.61	498150.93	27413.0	246.436	820.046	1.166
113	36.042	68.803	3.886E+04	7.495E+05	1.035E+05	14.52	17504.90	508875.35	27163.6	239.090	772.792	1.172
114	36.763	41.057	3.914E+04	7.505E+05	8.913E+04	14.61	17588.31	513625.20	26868.6	232.500	737.716	1.176
115	37.404	40.958	3.925E+04	7.744E+05	7.842E+04	14.66	17560.07	511664.11	26619.4	226.370	708.252	1.180
116	37.940	40.675	3.881E+04	7.365E+05	6.975E+04	14.67	17455.17					

MEAN	11	TO	25	38	357	41	435	3	750E+04	6	873E+05	6	897E+04	14	65	17435.46	508154.57	219.984	277.155	1.188
MEAN	12	TO	26	38	605	41	166	3	549E+04	6	397E+05	5	378E+04	14	65	17404.92	501605.65	214.028	250.322	1.192
MEAN	13	TO	27	38	638	40	475	3	237E+04	5	428E+05	4	864E+04	14	76	17358.81	47194.26	210.390	231.195	1.195
MEAN	14	TO	28	38	457	40	459	2	836E+04	4	18E+05	3	588E+04	13	51	17522.15	393010.39	206.418	221.214	1.194
MEAN	15	TO	29	38	137	40	010	3	523E+04	3	335E+05	4	462E+04	12	92	17484.28	345324.01	206.418	216.142	1.191
MEAN	16	TO	30	37	829	39	302	2	373E+04	3	384E+05	4	432E+04	12	48	17545.96	310509.22	206.089	215.064	1.191
MEAN	17	TO	31	37	588	38	894	2	375E+04	3	553E+05	4	391E+04	12	48	17677.62	31817.19	205.177	213.989	1.190
MEAN	18	TO	32	37	427	38	417	2	512E+04	3	886E+05	4	391E+04	12	14	17715.56	290660.88	204.953	213.236	1.187
MEAN	19	TO	33	37	297	37	829	2	714E+04	4	209E+05	4	440E+04	12	26	17757.72	295618.93	205.871	215.662	1.184
MEAN	20	TO	34	37	151	37	855	2	855E+04	4	191E+05	4	453E+04	12	77	17988.22	340715.53	206.605	219.444	1.183
MEAN	21	TO	35	36	325	37	767	2	925E+04	4	406E+05	4	461E+04	12	70	17880.08	332968.74	207.392	222.312	1.183
MEAN	22	TO	36	36	862	37	767	3	025E+04	4	208E+05	4	470E+04	12	70	17871.32	332370.11	207.392	224.882	1.181
MEAN	23	TO	37	36	862	37	767	3	182E+04	4	427E+05	4	476E+04	13	04	17261.96	347328.49	209.930	227.481	1.178
MEAN	24	TO	38	36	846	36	972	3	238E+04	4	458E+05	4	485E+04	13	36	16756.23	363295.22	210.412	230.674	1.179
MEAN	25	TO	39	36	876	37	699	3	353E+04	4	478E+05	4	491E+04	13	36	16835.33	36937.95	210.761	235.045	1.179
MEAN	26	TO	40	36	975	37	551	3	529E+04	4	505E+05	4	492E+04	13	68	16445.12	381649.00	210.887	233.422	1.178
MEAN	27	TO	41	37	032	37	089	3	665E+04	4	530E+05	4	493E+04	14	03	16465.97	416240.18	211.211	235.144	1.176
MEAN	28	TO	42	37	175	37	051	3	767E+04	4	597E+05	4	497E+04	14	23	16324.60	435225.09	211.868	235.820	1.177
MEAN	29	TO	43	37	436	38	148	3	837E+04	4	594E+05	4	497E+04	14	37	16286.14	44569.18	210.354	236.626	1.181
MEAN	30	TO	44	37	436	37	379	3	891E+04	4	591E+05	4	492E+04	14	59	16144.63	464943.90	210.707	236.987	1.177
MEAN	31	TO	45	37	498	37	904	3	725E+04	4	550E+05	4	492E+04	14	73	16026.62	476135.38	209.158	236.395	1.181
MEAN	32	TO	46	37	503	37	555	3	584E+04	4	568E+05	4	490E+04	14	31	16047.65	43222.45	209.234	234.831	1.181
MEAN	33	TO	47	37	332	38	169	3	437E+04	4	871E+05	4	491E+04	14	27	15702.30	419751.13	209.092	235.414	1.182
MEAN	34	TO	48	37	332	37	122	3	115E+04	4	509E+05	4	488E+04	13	92	15455.95	381100.70	209.199	233.651	1.177
MEAN	35	TO	49	37	176	37	914	3	075E+04	4	456E+05	4	487E+04	13	82	15663.06	377045.37	208.585	233.538	1.182
MEAN	36	TO	50	37	060	37	060	3	034E+04	4	474E+05	4	480E+04	13	82	16011.16	38769.38	208.148	232.135	1.177
MEAN	37	TO	51	37	103	37	316	3	015E+04	4	460E+05	4	482E+04	13	87	15544.16	368595.02	208.377	230.440	1.177
MEAN	38	TO	52	37	036	37	695	3	033E+04	4	487E+05	4	478E+04	13	48	16539.57	368595.02	208.280	229.915	1.181
MEAN	39	TO	53	37	036	37	786	3	093E+04	4	509E+05	4	481E+04	13	67	16326.83	37930.92	208.522	230.982	1.180
MEAN	40	TO	54	37	017	37	567	3	074E+04	4	568E+05	4	485E+04	13	88	16733.87	39598.09	209.422	231.978	1.176
MEAN	41	TO	55	37	012	36	891	3	074E+04	4	568E+05	4	485E+04	13	88	16733.87	39598.09	209.583	232.449	1.180
MEAN	42	TO	56	37	013	37	695	3	051E+04	4	513E+05	4	488E+04	13	52	16738.70	36531.09	210.061	232.389	1.180
MEAN	43	TO	57	36	985	37	786	3	022E+04	4	504E+05	4	492E+04	13	70	16674.43	391333.44	210.881	233.518	1.175
MEAN	44	TO	58	36	930	36	809	2	926E+04	4	481E+05	4	497E+04	13	69	16610.75	38844.67	210.949	236.043	1.177
MEAN	45	TO	59	36	882	37	411	2	884E+04	4	490E+05	4	490E+04	13	25	16370.12	35716.54	212.008	237.269	1.176
MEAN	46	TO	60	36	831	37	261	2	908E+04	4	470E+05	4	493E+04	13	41	16435.46	369574.63	212.293	237.337	1.174
MEAN	47	TO	61	36	762	36	961	2	875E+04	4	484E+05	4	493E+04	13	59	16776.08	383304.00	212.525	236.962	1.173
MEAN	48	TO	62	36	723	36	775	2	887E+04	4	484E+05	4	493E+04	13	59	16776.08	383304.00	212.525	236.962	1.175
MEAN	49	TO	63	36	710	37	122	2	887E+04	4	484E+05	4	493E+04	13	59	16776.08	383304.00	212.525	236.962	1.175
MEAN	50	TO	64	36	689	36	915	2	982E+04	4	507E+05	4	495E+04	13	51	16952.33	349697.67	212.929	235.051	1.174
MEAN	51	TO	65	36	667	36	419	2	982E+04	4	507E+05	4	495E+04	13	51	16952.33	349697.67	212.929	235.051	1.174
MEAN	52	TO	66	36	674	36	849	3	054E+04	4	515E+05	4	493E+04	13	45	17226.67	381533.10	212.219	232.538	1.174
MEAN	53	TO	67	36	680	36	680	3	054E+04	4	515E+05	4	493E+04	13	45	17226.67	381533.10	212.219	232.538	1.176
MEAN	54	TO	68	36	662	36	524	3	035E+04	4	516E+05	4	492E+04	13	18	17366.29	361566.04	211.930	232.493	1.172
MEAN	55	TO	69	36	643	36	480	3	035E+04	4	516E+05	4	492E+04	13	18	17366.29	361566.04	211.930	232.493	1.172
MEAN	56	TO	70	36	626	36	788	3	035E+04	4	516E+05	4	492E+04	13	18	17366.29	361566.04	211.930	232.493	1.172
MEAN	57	TO	71	36	604	36	849	3	045E+04	4	567E+05	4	497E+04	13	30	17822.50	36242.97	212.080	232.812	1.170
MEAN	58	TO	72	36	604	36	166	3	055E+04	4	518E+05	4	496E+04	13	61	17209.21	39206.79	212.288	234.015	1.174
MEAN	59	TO	73	36	641	36	765	3	063E+04	4	516E+05	4	495E+04	13	45	17145.82	381160.29	211.826	233.898	1.174
MEAN	60	TO	74	36	646	37	050	3	138E+04	4	521E+05	4	490E+04	13	33	17302.21	379730.34	211.324	232.077	1.175
MEAN	61	TO	75	36	677	36	733	3	158E+04	4	521E+05	4	490E+04	13	33	17302.21	379730.34	211.324	232.077	1.173
MEAN	62	TO	76	36	711	36	593	3	118E+04	4	531E+05	4	492E+04	13	68	17215.36	40138.23	211.820	230.835	1.172
MEAN	63	TO	77	36	732	36	764	3	188E+04	4	521E+05	4	490E+04	13	33	17261.34	39559.68	212.039	232.343	1.173
MEAN	64	TO	78	36	730	36	744	3	188E+04	4	521E+05	4	490E+04	13	33	17261.34	39559.68	212.039	232.343	1.173
MEAN	65	TO	79	36	736	37	214	3	145E+04	4	506E+05	4	491E+04	13	58	17082.16	39656.19	212.076	237.324	1.173
MEAN	66	TO	80	36	766	36	766	3	121E+04	4	501E+05	4	491E+04	13	51	17082.16	39656.19	212.076	237.324	1.173
MEAN	67	TO	81	36	769	37	025	3	121E+04	4	501E+05	4	491E+04	13	51	17082.16	39656.19	212.076	237.324	1.173
MEAN	68	TO	82	36	772	37	253	3	154E+04	4	506E+05	4	491E+04	13	51	16893.06	37928.88	212.076	237.324	1.175
MEAN	69	TO	83	36	772	36	638	3	123E+04	4	506E+05	4	491E+04	13	51	16893.06	37928.88	212.076	237.324	1.175
MEAN	70	TO	84	36	806	36	837	3	167E+04	4	507E+05	4	491E+04	13	43	16958.07	37335.96	212.160	239.460	1.173
MEAN	70	TO	84	36	806	36	837	3	167E+04	4	507E+05	4	491E+04	13	43	16958.07	37335.96	212.160	239.460	1.173

MEAN	71 TO	85	36.805	37.207	3.177E+04	5.038E+05	5.101E+04	13.76	16862.31	400713.38	27143.3	212.249	240.312	1.175
MEAN	72 TO	86	36.822	36.872	3.127E+04	5.143E+05	5.121E+04	13.81	16734.06	402079.04	27135.6	212.347	241.179	1.174
MEAN	73 TO	87	36.830	37.063	3.133E+04	5.125E+05	5.141E+04	13.44	16734.29	369554.67	27131.9	212.499	241.910	1.174
MEAN	74 TO	88	36.811	36.940	3.165E+04	5.075E+05	5.137E+04	13.66	16542.55	384575.96	27140.8	212.891	241.286	1.174
MEAN	75 TO	89	36.791	37.062	3.118E+04	5.046E+05	5.147E+04	13.89	16579.12	405895.51	27149.9	212.879	241.691	1.172
MEAN	76 TO	90	36.783	36.599	3.086E+04	5.023E+05	5.152E+04	13.57	16599.61	377616.18	27153.6	212.930	240.934	1.175
MEAN	77 TO	91	36.759	37.193	3.117E+04	5.021E+05	5.105E+04	13.52	16680.07	375461.65	27164.3	212.590	240.154	1.175
MEAN	78 TO	92	36.731	37.234	3.086E+04	5.061E+05	5.059E+04	13.82	16693.56	402496.18	27177.2	212.276	238.338	1.175

MEAN AFTER PERIOD	U-ANODE SI-ANODE	U-ANODE SI-SOLE	TOTAL POWER IN	TOTAL POWER OUT	ERROR(%)
-------------------	---------------------	--------------------	-------------------	--------------------	----------

1	8.326E+05	4.671E+07	8.506E+05	1.365E+07	1506.11
2	8.275E+05	2.431E+07	8.460E+05	7.242E+06	755.96
3	8.208E+05	1.720E+07	8.395E+05	4.970E+06	492.10
4	8.243E+05	1.721E+07	8.391E+05	3.859E+06	359.87
5	8.197E+05	1.089E+07	8.384E+05	3.190E+06	280.46
6	8.196E+05	9.281E+06	8.383E+05	2.743E+06	227.18
7	8.227E+05	8.108E+06	8.413E+05	2.416E+06	187.11
8	8.251E+05	7.244E+06	8.438E+05	2.173E+06	157.54
9	8.240E+05	6.526E+06	8.437E+05	1.985E+06	135.52
10	8.168E+05	5.952E+06	8.355E+05	1.890E+06	126.16
11	8.075E+05	5.496E+06	8.263E+05	1.836E+06	122.25
12	7.894E+05	5.106E+06	8.082E+05	1.864E+06	130.68
13	7.683E+05	4.730E+06	7.866E+05	1.993E+06	153.32
14	7.557E+05	4.450E+06	7.743E+05	2.059E+06	165.98
15	7.660E+05	4.202E+06	7.845E+05	2.066E+06	163.32
16	7.927E+05	1.349E+06	8.112E+05	1.262E+06	55.56
17	8.248E+05	1.317E+06	8.433E+05	1.304E+06	54.62
18	8.515E+05	1.209E+06	8.699E+05	1.365E+06	54.74
19	8.767E+05	1.200E+06	8.947E+05	1.366E+06	52.72
20	9.060E+05	1.141E+06	9.239E+05	1.390E+06	50.44
21	9.383E+05	1.125E+06	9.595E+05	1.390E+06	45.43
22	9.718E+05	1.115E+06	9.894E+05	1.388E+06	40.25
23	1.003E+06	1.100E+06	1.021E+06	1.379E+06	35.03
24	1.031E+06	1.083E+06	1.049E+06	1.357E+06	29.40
25	1.053E+06	1.095E+06	1.071E+06	1.294E+06	20.85
26	1.071E+06	1.083E+06	1.088E+06	1.221E+06	12.22
27	1.080E+06	1.065E+06	1.097E+06	1.098E+06	0.09
28	1.074E+06	1.068E+06	1.092E+06	8.859E+05	-18.86
29	1.059E+06	1.062E+06	1.075E+06	7.449E+05	-30.71
30	1.035E+06	1.048E+06	1.052E+06	7.170E+05	-31.86
31	1.011E+06	1.042E+06	1.030E+06	7.361E+05	-26.12
32	9.943E+05	1.032E+06	1.012E+06	7.477E+05	-28.55
33	9.845E+05	1.018E+06	1.002E+06	7.880E+05	-21.36
34	9.856E+05	1.021E+06	1.004E+06	8.377E+05	-16.93
35	9.850E+05	1.024E+06	1.003E+06	8.189E+05	-18.34
36	9.856E+05	1.023E+06	1.004E+06	8.336E+05	-16.93
37	9.903E+05	1.014E+06	1.008E+06	8.692E+05	-13.74
38	9.926E+05	1.003E+06	1.000E+06	9.011E+05	-10.72
39	9.942E+05	1.022E+06	1.011E+06	9.242E+05	-8.61
40	9.992E+05	1.017E+06	1.016E+06	9.727E+05	-4.23
41	1.003E+06	1.003E+06	1.019E+06	1.041E+06	2.12
42	1.002E+06	1.005E+06	1.019E+06	1.090E+06	6.97
43	1.005E+06	1.027E+06	1.021E+06	1.123E+06	9.99
44	1.005E+06	1.004E+06	1.025E+06	1.146E+06	11.75
45	1.005E+06	1.017E+06	1.025E+06	1.118E+06	9.04
46	1.005E+06	1.018E+06	1.025E+06	1.045E+06	1.88
47	1.012E+06	1.024E+06	1.027E+06	9.904E+05	-3.60
48	1.012E+06	1.018E+06	1.028E+06	9.532E+05	-7.27

49	1.008E+06	1.006E+06	1.02E+06	9.12E+05	-10.32
50	1.009E+06	1.02E+06	1.02E+06	9.11E+05	-11.07
51	1.009E+06	1.00E+06	1.02E+06	9.21E+05	-10.07
52	1.007E+06	9.92E+05	1.02E+06	9.39E+05	-8.17
53	1.004E+06	1.02E+06	1.02E+06	9.35E+05	-8.31
54	1.003E+06	1.01E+06	1.01E+06	9.66E+05	-5.24
55	1.003E+06	9.97E+05	1.01E+06	1.00E+06	-1.35
56	1.002E+06	1.02E+06	1.01E+06	9.84E+05	-3.35
57	1.004E+06	1.02E+06	1.02E+06	9.68E+05	-5.02
58	1.008E+06	9.90E+05	1.02E+06	9.74E+05	-4.00
59	1.006E+06	1.01E+06	1.02E+06	9.58E+05	-6.54
60	1.004E+06	1.01E+06	1.02E+06	9.11E+05	-10.69
61	1.007E+06	1.00E+06	1.02E+06	9.14E+05	-10.66
62	1.002E+06	9.95E+05	1.01E+06	9.47E+05	-7.07
63	9.98E+05	1.00E+06	1.01E+06	9.34E+05	-7.98
64	9.98E+05	1.00E+06	1.01E+06	9.31E+05	-8.30
65	1.000E+06	9.98E+05	1.01E+06	9.68E+05	-4.77
66	9.96E+05	1.00E+06	1.01E+06	9.76E+05	-3.64
67	9.94E+05	1.01E+06	1.02E+06	9.70E+05	-4.12
68	9.98E+05	9.98E+05	1.01E+06	9.85E+05	-2.91
69	9.97E+05	9.92E+05	1.01E+06	9.91E+05	-2.28
70	9.96E+05	1.00E+06	1.01E+06	9.45E+05	-6.69
71	9.96E+05	1.00E+06	1.01E+06	9.43E+05	-6.85
72	9.93E+05	9.86E+05	1.01E+06	9.77E+05	-3.35
73	9.91E+05	1.00E+06	1.00E+06	9.76E+05	-3.15
74	9.94E+05	1.00E+06	1.01E+06	9.74E+05	-3.69
75	9.97E+05	9.92E+05	1.01E+06	1.00E+06	-0.82
76	9.96E+05	9.98E+05	1.01E+06	1.01E+06	-0.16
77	9.97E+05	9.93E+05	1.01E+06	9.73E+05	-4.00
78	9.99E+05	9.98E+05	1.01E+06	9.77E+05	-3.89
79	9.94E+05	1.01E+06	1.01E+06	1.00E+06	-1.35
80	9.97E+05	9.96E+05	1.01E+06	9.75E+05	-3.71
81	9.97E+05	1.00E+06	1.01E+06	9.66E+05	-4.75
82	9.96E+05	1.01E+06	1.01E+06	9.91E+05	-2.11
83	9.96E+05	9.97E+05	1.01E+06	9.76E+05	-3.65
84	9.98E+05	9.99E+05	1.01E+06	9.64E+05	-5.07
85	1.00E+06	1.00E+06	1.01E+06	9.86E+05	-3.12
86	9.97E+05	1.00E+06	1.01E+06	9.98E+05	-1.54
87	9.98E+05	1.00E+06	1.01E+06	9.64E+05	-4.94
88	1.00E+06	1.00E+06	1.01E+06	9.74E+05	-4.16
89	1.00E+06	1.00E+06	1.01E+06	9.93E+05	-2.54
90	1.00E+06	9.98E+05	1.02E+06	9.62E+05	-5.56
91	1.004E+06	1.00E+06	1.02E+06	9.59E+05	-5.06
92	1.004E+06	1.01E+06	1.02E+06	9.90E+05	-3.03

EOI..

APPENDIX M

PROFESSIONAL PERSONNEL, INTERACTIONS AND PUBLICATIONS

The principal investigators for this study of the distributed-emission CFA were Dr. Joseph E. Rowe, Vice President for Technology, Harris Corporation, and Dr. Donald M. MacGregor, Senior Engineer, Harris SAI, Inc.

The basic data and much useful information about the five Raytheon CFA's were supplied by Mr. W. Griffin and Drs. G. MacMaster, L. Nichols and J. Skowron of Raytheon Company Microwave and Power Tube Division, Waltham, MA.

The SFD-261 information was provided by Mr. H. McDowell of Varian Associates, Beverly, MA, with whom many useful discussions were held at Varian on June 22, 1978 and subsequently by telephone.

Dr. A. Drobot of Science Applications, Inc., McLean, Virginia provided helpful advice about the modelling of the cathode emission and the modulator in the DECFA.

Harris SAI presented a paper describing the results of this contract at the Tri-Services Cathode Workshop at Rome Air Development Center, April 15-17, 1980. In April 1980 a short paper entitled "Computer Simulation of the Backward-Wave Distributed-Emission Crossed-Field Amplifier" was submitted for publication in IEEE Electron Device Letters.

END

FILMED

4-83

DTIC